Atomic-scale Modelling of Electro-catalytic Surfaces and Dynamic Electrochemical Interfaces

Hansen, Martin Hangaard

Publication date:
2016

Document Version
Publisher's PDF, also known as Version of record

Technical University of Denmark
Center for Atomic-scale Materials Design (CAMD)

Department of Physics
Fysikvej, bygning 307
DK-2800 Kongens Lyngby
Tel. +45 4525 3344

www.fysik.dtu.dk

Martin Hangaard Hansen

Atomic-scale Modelling of Electro-catalytic Surfaces and Dynamic Electrochemical Interfaces

DTU

Atomic-scale Modelling

of Electro-catalytic Surfaces and Dynamic Electrochemical Interfaces

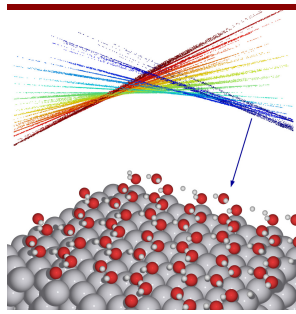

PhD Thesis
Martin Hangaard Hansen
May 2016

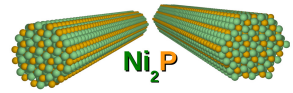

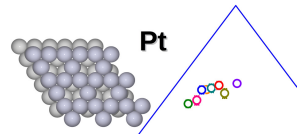

DTU Physics
Department of Physics

Preface

This dissertation is submitted in candidacy for the Ph.D. degree from the Technical University of Denmark, (DTU). The work was carried out between the 15th of May 2013 and the 14th of May 2016, mainly at the Department of Physics at DTU. The last year of work was done while based at the Nano-Science Center at the Chemical Institute, University of Copenhagen, as an external stay. A minor part of the work was done during an external stay at the Laboratory for Inorganic Synthesis at École Polytechnique Fédérale de Lausanne in Switzerland in the autumn of 2013.

The Ph.D. work has been supervised mainly by Professor Jan Rossmeisl, in part by Kristian S. Thygesen, and the part at EPFL was co-supervised by Professor Xile Hu. The work was funded by the Department of Physics at DTU and Innovation Fund Denmark via the NACORR project no. 12-132695.

Martin Hangaard Hansen
May, 2016

Acknowledgements

I would like to thank a few people for helping me in different ways during the last three years. First of all I thank Jan Rossmeisl, for giving me the opportunity to carry out this project, for his guidance, for our many and frequent discussions and for always being enthusiastic and creative. I have always found our meetings to be motivating. I would like to thank Xile Hu for hosting me at EPFL and Kristian Thygesen for our discussions. Other collaborators on the various projects, to whom I owe my gratitude are: Mårten Björketun, Rizwan Ahmed, María Escudero-Escribano, Ulrik Grønbjerg Vej-Hansen, Elisabeth T. Ulrikkeholm, Anders Filsøe Pedersen, Vladimir Tripkovic, Chengjun Jin, Paolo Malacrida, Amado Velázquez, Ligang Feng, Lucas Alexandre-Stern, Hendrik Bluhm, Jakob Schiøtz, Ifan Stephens and Ib Chorkendorff. I have enjoyed working with all of you. My work would not have been possible without my colleagues in supporting roles at DTU Physics: Marianne Ærsøe, Marcin Dulak, Ole Holm Nielsen, and Jens Jørgen Mortensen, for their help with everything from administration to technical support and guidance on the use of the ASE and GPAW software, and for leading the developing of that software, which I have used extensively for this work. I thank Alexander Bagger, Ivano Castelli, María Escudero-Escribano, Thomas A. A. Batchelor and Thomas Østergaard for helping me proof read the thesis. Other colleagues and office mates, who I had lots of good times with and who made the working environment excellent was Rasmus, Brian, Felipe, Simona, Thomas, Heron, Gregor, Carlos, Pablo, Michael M, Gerald, Michael B, Reza, Kristian Ø., Kirsten, Filip, Mohnish, Korina, Sten, Simone, Per, Manuel, Alexander, Ivano, Tom and Thomas. Last but not least I thank Inge, Carl, Lene, Simon, Christina, Christine, and Nanna for all their love and support, especially during the busy writing phase.

Abstract

This dissertation addresses numerical calculations on the atomic scale to study catalytic surfaces for electrochemistry. The first half of the thesis deals with calculations on the properties of catalytic surfaces, using well known methodology, whereas the second half of the thesis deals with the development of new methodology to explicitly include the electrolyte in the atomic scale calculations.

Chapter 3 presents calculations on contracted and reconstructed platinum surfaces, which are relevant for development of catalysts for proton exchange membrane fuel cells. Correlation of the results with experimental observations show that there is a natural limit to how far the reactivity of the catalysts can can be fine-tuned, exclusively using the strain effect, that is imposed by alloying with lanthanides.

In chapter 4, calculations are presented for several newly discovered catalysts for the hydrogen evolution reaction. The results show that molybdenum carbides and borides have reactive surfaces, which is not in consistency with their high catalytic activity. A possible active facet is suggested for the molybdenum boride. It is likely, however, that other unexplored active sites, surface terminations or phases are responsible for the observed catalytic activities. For nickel di-phosphide, which is another recently discovered catalyst for the hydrogen evolution reaction, it was possible to determine several facets and active sites, which have advantageous catalytic properties.

Chapter 5 presents the new methodology to calculate the structure of the electrolyte in the electrochemical interface. The strength of this methodology is that it makes fewer assumptions on the physics of the interface, while it takes a fundamental statistical mechanics approach. Large datasets of states for the electrolyte in contact with the surfaces of gold (111) and platinum (111) were calculated. Analysis methods were developed for determining the structure of the electrolyte as averages, which depend on pH and the electrode potential of the metal. The methodology remains under development, and it is expected that it will contribute with new insight to how pH and ionic chemical potentials affect the structure of the interface, to the benefit of future fundamental research in electrochemistry.

Resumé

Denne Ph.d.-afhandling omhandler numeriske beregninger på atomar skala til studie af katalysatorer til elektrokemiske reaktioner. De første kapitler beskæftiger sig alene med beregninger af katalysatorers overfladeegenskaber ved hjælp af kendt metodik, hvorimod kapitel 5 præsenterer en udvikling af metodikken til eksplicit at inkludere elektrolytten i de numeriske beregninger.

Kapitel 3 præsenterer beregninger på sammentrukne og rekonstruerede platin overflader, som er relevante for forskning i katalysatorer til polymer elektrolyt brændselsceller. Resultaterne afslører en naturlig grænse for hvor langt platin-overfladernes reaktivitet kan fin-tunes, alene ved det stræk eller sammentrykning af overfladens gitterstruktur, som kan opnås i legeringer med lanthanider.

I kapitel 4 beregnes overfladeegenskaber for en række nyopdagede katalysatorer til brintudviklingsreaktionen. Resultaterne viser at molybdænkarbider og -borider har meget reaktive overflader, hvilket ikke er konsistent med deres høje katalytiske aktivitet. Et muligt aktivt sæde er foreslået for molybdænborid. Det er dog sandsynligt at der endnu findes uopdagede aktive sæder, overfladetermineringer eller faser af materialerne, som kan være ansvarlige for de målte katalytiske aktiviter. For nikkeldifosfid, som er et andet nyopdaget materiale til katalyse af brintudviklingsreaktionen, lykkedes det at beregne flere facetter og katalytisk aktive sæder, som har fordelagtige katalytiske egenskaber. Ved et yderligere sæt beregninger viste det sig også at andre metalfosfider har disse fordelagtige egenskaber, som er en moderat bindingsenergi med atomart brint på metal-bro- eller metal-fosfor-bro geometrier.

I kapitel 5 præsenteres den nye metodik til at udregne strukturen af elektrolytten ved den elektrokemiske grænseflade. Metodikkens styrke består i at der laves færre antagelser om grænsefladens fysik og i at den benytter sig af en grundlæggende mekanisk statistisk tilgang. Store datasæt af tilstande for elektrolytten i kontakt med overfladerne af guld(111) of platin(111) blev udregnet. Analysemetoder blev udviklet til at bestemme den gennemsnitlige struktur af elektrolytten som gennemsnitsværdier, der afhænger af elektrolyttens pH og metallets elektrodepotential. Metodikken er fortsat under udvikling, og det er forventet at den kan levere en mere præcis indsigt i hvilken effekt pH og kemiske potentialer af ioner har på grænsefladens struktur til gavn for fremtidig forskning i elektrokemi.

Paper I: *Tuning the activity of Pt alloy electrocatalysts by means of the lanthanide contraction*

María Escudero-Escribano, Paolo Malacrida, Martin H. Hansen Ulrik G. Vej-Hansen, Amado Velázquez-Palenzuela, Vladimir Tripkovic, Jakob Schiøtz, Jan Rossmeisl, Ifan E. L. Stephens, Ib Chorkendorff

Science, April 1st (**2016**), 352, 6281.

Paper II: *Probing the nanoscale structure of the catalytically active overlayer on Pt alloys with rare earths*

Anders F. Pedersen, Elisabeth T. Ulrikkeholma, María Escudero-Escribanoa, Tobias P. Johansson, Paolo Malacrida, Christoffer M. Pedersen, Martin H. Hansen, Kim D. Jensen, Jan Rossmeisl, Daniel Friebel, Anders Nilsson, Ib Chorkendorff, Ifan E. L. Stephens

Nano Energy, (**2016**), Accepted.

Paper III: *Investigating the coverage dependent behaviour of CO on Gd/Pt(111)*

Elisabeth T. Ulrikkeholm, Martin Hangaard Hansen, Jan Rossmeisl, Ib Chorkendorff

(**2016**), In preparation.

Paper IV: *Widely available active sites on Ni_2P for electrochemical hydrogen evolution – insights from first principles calculations*

Martin H. Hansen, Lucas-Alexandre Stern, Ligang Feng, Jan Rossmeisl and Xile Hu

Physical Chemistry Chemical Physics, (**2015**), 17, 10823.

Paper V: Extract of: *Water at Interfaces*

Olle Bjorneholm, Martin Hansen, Andrew Hodgson, Li-Min Liu, David Limmer, Angelos Michaelides, Philipp Pedevilla, Jan Rossmeisl, Huaze Shen, Gabriele Tocci, Eric Tyrode, Marie-Madeleine Walz, Josephina Werner, Hendrik Bluhm

Chemical Reviews, (**2016**), Accepted.

Paper VI: *Towards first principles modeling of electrochemical electrode–electrolyte interfaces*
Malte Nielsen, Mårten E. Björketun, Martin H. Hansen, Jan Rossmeisl
Surface Science (2015), 631, 2–7.

Paper VII: *Finite Bias Calculations to Model Interface Dipoles in Electrochemical Cells at the Atomic Scale*
Martin Hangaard Hansen, Chengjun Jin, Kristian S. Thygesen, Jan Rossmeisl
The Journal of Physical Chemistry C, (**2016**), Accepted.

Paper VIII: *Grand Canonical Statistics of an Aqueous Electrochemical Interface from Dynamic Atomic-scale Calculations*
Martin Hangaard Hansen, Jan Rossmeisl
(**2016**), In preparation.

Contents

1. Introduction

1.1 Motivation

A continuing rise in population and in economic development is causing a rise in energy demand worldwide. The global energy system is based almost entirely on fossil fuels, which is a finite resource, and thus alternative sources of energy must eventually be developed to maintain the supply. Energy consumption is a prerequisite for economic activity and thus a dwindling energy supply will result in an economic decline.

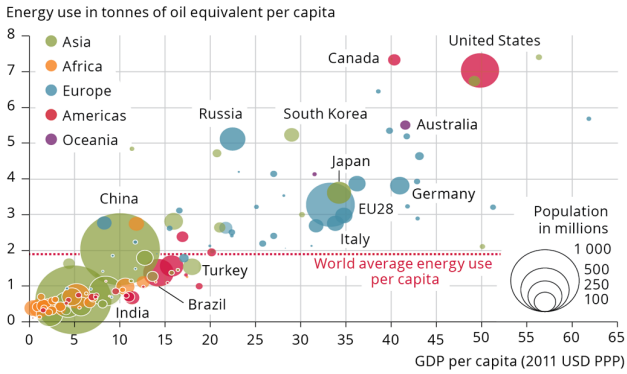

Figure 1.1: *Energy consumption per capita versus Gross Domestic Product per capita, (GDP), of countries. The size of the circles represent the population of the countries, and the color denote the region. Reproduced from the Environmental Energy Agency of the European Union*, EEA

There is naturally a strong correlation between the consumption of energy in a society and the wealth of that society, as shown in figure 1.1. The reason for this is that consumption of energy powers every activity going on in our society, and it is also fundamental to any activity that our society may wish to develop in the future. Energy supply and the security of energy supply is clearly a vital aspect of the security of economies and peoples.

The world wide energy consumption is growing at an increasing rate, and most rapidly in India and China, who currently do not consume very much energy per capita. If the living standards of all populations is to increase to approach that of wealthy countries, they can be expected to demand as much energy per capita as the wealthier countries,

which would cause the world wide energy consumption to triple in the process, (See Fig. 1.1).

Energy is a finite, conserved quantity by definition, so it cannot be created, but it can be transformed back and forth between various forms. *Potential energy* is found in the molecules in a fossil fuel, *kinetic energy* is associated with motion e.g. of a car or machinery, and heat is also a form of energy. Fundamentally, all conversion of energy is driven by the universe always changing to a more probable state, which provides the driving force for all energy conversion processes. Scientists and engineers have understood this better and better since the beginning of the industrialization, and applied their understanding to build technologies, that tap this driving force and provide the applications and services we presently depend on and enjoy. [1]

As shown in figure 1.2, most of the energy consumption has been in the form of either oil, gas or coal in the last century. [2]

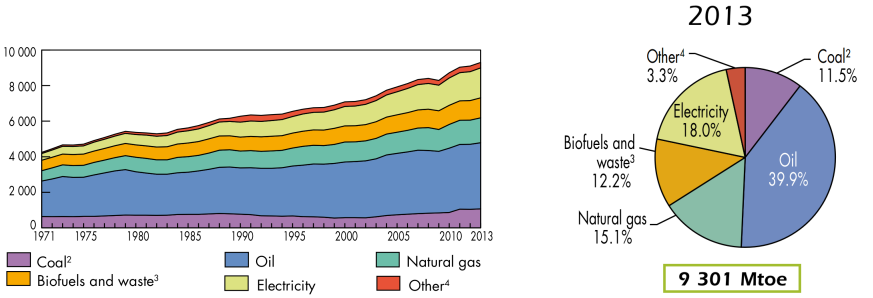

(a) *Historical development of energy consumption.*

(b) *Energy consumption in 2013.*

Figure 1.2: *Total world energy consumption in million tonnes of oil equivalent, (Mtoe). "Other" includes geothermal, wind, photovoltaic, solar thermal, ect. ©OECD/IEA* [2]

Oil accounts for the largest portion of the fossil fuels, due to its high energy content and because of its unique advantages for transportation and conversion into a wide variety of useful chemicals or energy-dense fuels. [3] Oil is mainly used to make fuels for combustion engines, which is shown in figure 1.3 under *Transport*, while plastics and medicines are in *Non-energy use* and take up a smaller part of the total world wide consumption.

Oil is gradually turning into a more limited resource, as reflected by the price of oil

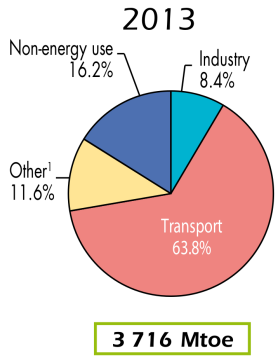

Figure 1.3: *Oil consumption by sector. "Transport", "Industry" and "Other" are energy uses, i.e. the oil is used in a form of fuel. "Other" include agriculture, public, residential and other non-specified energy uses. "Non-energy use" are medicine, plastics and other chemicals. ©OECD/IEA* [2]

products, shown in figure 1.4, although the world is not acutely running out of any type of fossil fuels, including oil. The resources are not distributed equally across regions, and some regions will likely be depleted before others. Some regions, including the European Union, are far from self-sufficient and the consequence is a dependency on import from fossil producing countries. The two biggest oil exporters are Saudi Arabia and Russia, the biggest gas exporters are Russia and Qatar, and the biggest coal exporters are China and India. In all three fossil categories, large European nations including Germany, the UK, France, Spain and Italy are among the top 10 importers in the world. [2] In the prospect of rising world wide energy demand and uncertainties about supply, the economy of Europe is particularly vulnerable to being drained by those imports, if the prices rise dramatically.

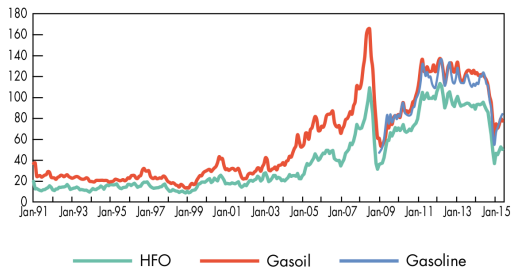

Figure 1.4: *Oil product spot prices in Rotterdam from 1990 to 2015. ©OECD/IEA* [2]

Besides the issues concerning the economy and security of energy supply, burning of

fossil carbon based material is causing a rapid rise in atmospheric carbon dioxide concentration, which threatens to destabilize the global climate. The effects on human societies of a destabilizing climate are hard to predict, but it does most likely not help the situation concerning security of supply. Thus, there are strong motivations for an acceleration of the transition towards reliance on sustainable energy sources.

The largest sustainable energy sources including hydro, wind and solar power comes in the form of electricity. Particularly solar has enormous potential as a source of primary sustainable energy[4,5], but historically, solar has taken up a rather small amount of the worlds energy supply. This is also reflected in the small share that electricity currently holds in the total consumption, (See Fig. 1.2), since sustainable energy sources are mainly used to produce electricity.

Wind and solar power are the fastest growing sources of energy, with growth rates in excess of 30% globally.[6] The growth in wind and solar power demands a subsequent growth in the electricity share of the energy consumption. To avoid too many conversion losses, that further prompts electrification of all possible applications. An additional advantage of electrification is that very large amounts of energy can be easily transmitted over long distances, given that the infrastructure is in place. The main concern in transitioning to rely on wind and solar power is the fact that it is intermittent and that it does not match electricity demand. This is illustrated by figure 1.5, where the wind power output plus the solar power output of Denmark has been plotted together with the total power consumption for December 2015. In this plot, daily and weekly variations in consumption are visible, and the reduced consumption is also clear during the holidays from December 24th to 26th. The wind and solar production is lower than the total consumption, most of the time, but occasionally it exceeds the total national consumption.

Since the amount of storage capability in the electricity system is rather low, the curves of *total* electricity production and consumption of course match. This is currently achieved by exporting the excess to neighbouring regions and meeting remaining demands by other power sources or import. In order to support a larger share of intermittent energy in the grid, regional infrastructures for transmitting electricity are being expanded in many regions of the world. A complete transition to renewable energy sources for electricity grids is not possible without expanding the energy storage capabilities.[7]

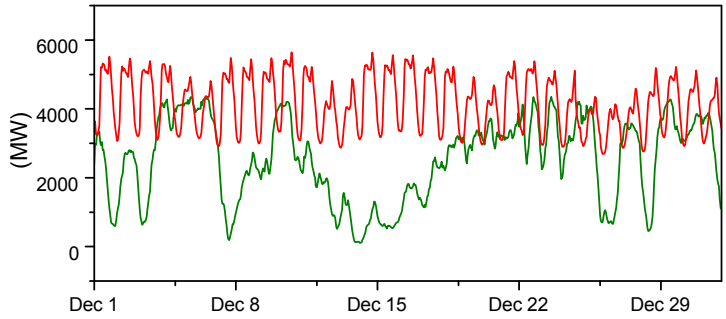

Figure 1.5: *Total electricity consumption of Denmark during December 2015, shown by the upper line in red, together with wind+solar power production in the same regions and time period, shown by the lower line in green. Based on wholesale market data from energinet.dk*

The part of the energy sector that poses the greatest challenges for transformation to a dependence on sustainable sources is the transport sector, which has to rely completely on stored energy. Currently there are no feasible technologies for producing carbon based fuels for conventional combustion engines, in a sustainable manner, on a world wide scale. It may one day become feasible to produce carbon based fuels using electrochemical cells, but this is not close to becoming a technology in the near future[8]. Closer to large scale applications are both the options of running on rechargeable batteries or on hydrogen. Arguably, the scaling of driving range versus weight and price is worse for batteries, compared to fuel cells running on hydrogen from pressurized tanks. On the other hand, electric vehicles have an advantage due to their efficiency and the low fixed cost associated with the systems of electric motors and batteries. Therefore there should be some range or vehicle size above which fuel cells are a cheaper solution than batteries. This point will depend on future developments of both technologies.[9]

Running on hydrogen is inherently carbon neutral, if the hydrogen is produced using electrochemical cells from sustainable sources. Hydrogen can be consumed in combustion engines or more efficiently in hydrogen fuel cells like the proton exchange membrane fuel cell, (PEMFC), and a sustainable hydrogen supply can eventually be based on excess power from renewable power sources.[10–13]

Toyota's introduction of a fuel cell powered sedan, with a price tag of approximately 600000 DKK $\approx$ 80000 is a recent demonstration of the feasibility or lack of same for PEM fuel cells.[14] The high price is partly rooted in the small number of vehicles produced, but

the manufacturing scalability of the hydrogen fuel cell is inhibited by its reliance on platinum catalysts, due to the scarcity and low world wide production volume of platinum.[15] This is the motivation for a great deal of research into fuel cell catalysis, including some of the work in this thesis.

1.2 Outline

The Ph.D. work has consisted of several subprojects, which can be divided in two categories: **1)** Existing computational modelling methods were used to calculate properties of surfaces that are interesting for catalysis in electrochemical cells. **2)** New methodology was developed and tested with the aim of extending the surface models to include the electrolyte explicitly in the calculations. The chapters are divided as follows:

1 Motivation: A brief overview of the global energy challenge was given, and the increasingly important role of electrochemical energy conversion was presented as the motivation for the Ph.D. study.

2 Theory: An introduction to fundamental concepts in electrochemistry, catalysis and density functional theory is given. It is described how density functional theory can provide insight on the atomic scale, which is useful for understanding and developing new catalytic systems.

3 Surfaces for Oxygen Reduction Reaction: Calculations were carried out to understand trends in the properties of recently discovered platinum-based catalysts, in perspective of fuel cell applications. A limit to the application of strain effects as an independent tuning parameter for Pt-alloy catalysts is identified. Several reconstructions of the platinum surface are found to increase reactivity, and thus to be undesired for any catalytic activity enhancement.

4 Catalyst surfaces for Hydrogen Electrodes: Recently discovered catalysts for the hydrogen evolution reaction, (HER), based on non-precious materials were investigated to elucidate the active sites. Among them, nickel phosphide was extensively studied, and Ni-Ni bridge geometries were found able to facilitate the HER reaction with low barriers for a possible Tafel pathway. A smaller study on other metal-phosphides, is presented which shows that the hydrogen binding energy is a good predictor for catalytic activity of HER on metal-phosphides, as it is known to be for transition metal catalysts.

5 Electrochemical Interface Model: Recently reported theory for pH in atomic scale simulations is applied, to develop a methodology for determining the structure of the electrochemical interface. This methodology includes liquid aqueous electrolyte explicitly and gold and platinum surfaces are used as case studies.

6 Conclusions and Outlook: A brief summary of the main conclusions from the thesis is given, and the outlook and suggestions for further continuation of the research is discussed.

2. Theory

Computational modelling is applied in this PhD work to study surfaces and interfaces, that are interesting for electrocatalysis in fuel cells and other applications. To understand the computational methods and how they can contribute to research in electrocatalysis, it is necessary to review some fundamental concepts in electrochemistry. In this chapter, the proton exchange membrane fuel cell is used as an example of an electrochemical cell, and the introduction is given with this system in mind, since the following chapter addresses surfaces relevant for catalysis in the PEMFC. Brief introductions to the PEMFC, electrochemistry, reaction rates, thermodynamics, and density functional theory is included in this chapter to give an overview on how computations on atomic scale models contributes with insight in the reactions taking place on the catalyst surfaces.

2.1 Proton Exchange Membrane Fuel Cell

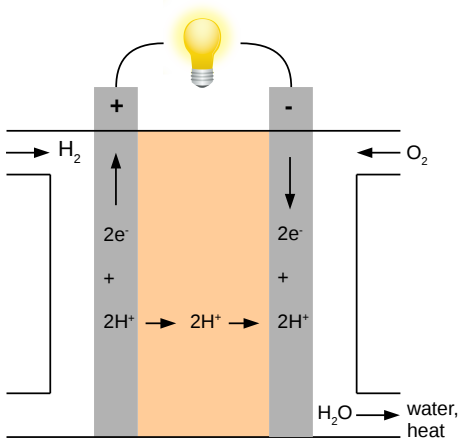

Figure 2.1: *The working principle of a proton exchange membrane hydrogen fuel cell (PEMFC). An electrolyser cell works via the same principle, but in reverse.*

The PEMFC produces electrical work and heat by converting hydrogen and oxygen

into water:

$$H_2 + \frac{1}{2}O_2 \rightarrow H_2O \tag{2.1}$$

There is a thermodynamic driving force for water to form from O_2 and H_2, which keeps the reaction running in the direction of water formation. This is exploited in a controlled process, which is sketched in figure 2.1. Hydrogen and oxygen are brought in contact via a membrane, which is proton conducting, but not permeable for gases and it is insulating for electrons.

At each side of the membrane, a porous electrode facilitates the chemical reaction between protons, electrons and the hydrogen or oxygen gas. In the left electrode in Figure 2.1, hydrogen is separated into protons and electrons and at the right electrode, protons and electrons reacts with oxygen gas and forms water. The proton path is ideally short circuited, and electrical work is tapped in the electronic circuit.

2.2 Electrochemistry

Electrochemical cells, including batteries and fuel cells consist of four main parts: Two electrodes, an electrolyte and the external circuit, connecting the electrodes (See Fig. 2.1).

Electrochemical reactions run at each electrode / electrolyte interface and drive ions trough the electrolyte and electrons through the external circuit. The power produced by the fuel cell is $U_{cell} \cdot I$, where I is the cell current and U_{cell} is the voltage between the electrodes. The output voltage at 100% efficiency, U^0_{cell}, between the electrodes is determined by the thermodynamic driving force, ΔG_{cell}, of the cell reaction by

$$\Delta G^0_{cell}/n = -U^0_{cell} \tag{2.2}$$

where n is the number of electrons in the reaction. [16] By convention, if ΔG^0_{cell} is negative, the cell reaction is spontaneous. For the PEMFC reaction (2.1), $\Delta G^0_{cell}/n = -1.23$ eV, so the fuel cell gives a power output. The measured cell voltage, particularly in PEMFC's [17], is often significantly smaller than U_{cell}, even at negligible cell currents, as illustrated by figure 2.2. Thus the cell is far from 100% efficient even at a low current. The fuel efficiency, ϵ, may be defined by $\epsilon = U_{cell}/U^0_{cell} = (U^0_{cell} - \eta_{cell})/U^0_{cell}$, where η_{cell} is the over-potential.

In order to understand efficiency losses, it is necessary to separate contributions from

each of the two electrode reactions, as well as from the membrane and external circuit. It often turns out (again the PEMFC is a good example [17]) that a large portion of the losses comes from poor catalysis of the electrochemical reactions at the electrode / electrolyte interfaces.

Each electrode is most often studied separately, while the other electrode is kept constant. An electrode under study is referred to as the working electrode, and the other is referred to as the reference electrode. Sometimes, a third electrode is included in experimental electrochemical cells in order to measure potential and current through separate channels.

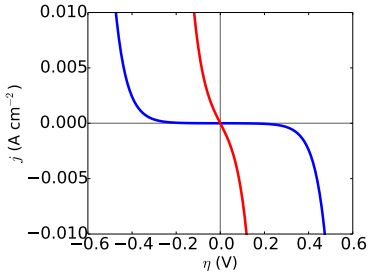

Figure 2.2: *Common characteristics of current, j, versus over-potential, η, of the working electrode.*

The electrochemical reaction at each electrode is called a half-reaction, and in the same spirit, one electrode-electrolyte junction is referred to as a half cell. The cell voltage is the difference between the half cell potentials:

$$U_{cell} = U_{right} - U_{left} \tag{2.3}$$

The cell over-potential, η_{cell}, is a sum of over-potentials from the serially connected electrodes and circuit $\eta_{right} + \eta_{left} + \eta_{\Omega}$, according to Kirchhoff's voltage law. An additional term, η_{diff}, may also result from diffusion resistance in the electrolyte. As protons are produced at the left electrode and consumed at the right electrode, resistance in the diffusion can result in a proton concentration gradient over the electrolyte. Such a gradient is measured as the diffusion over-potential, η_{diff}, because the equilibrium potential of each half cell, $U_{eq,half}$ shifts with changes in the concentrations according to the Nernst

equation:

$$U_{eq,half} = U^0_{half} - \frac{kT}{n} \ln \frac{a_R}{a_O} \tag{2.4}$$

where a_O is the activity of the reacting species and a_R is the activity of the product species. The indices are for *oxidised* and *reduced* species respectively. The over-potential associated with a reducing half electrode reaction is defined as[16]:

$$\eta = U_{half} - U_{eq,half} \tag{2.5}$$

and for the oxidising half reaction, the signs on the right side is reversed. Only cell potentials can be directly measured, so to deduce half cell potential of the working electrode, the potential of the reference electrode must be known. Reference electrodes are constructed to facilitate a fast surface reaction, to always maintain it's half cell reaction in equilibrium. In this way, the potential of this electrode is accurately defined by thermodynamics. An example of a reference is the hydrogen electrode, which keeps the equilibrium of the reaction:

$$\frac{1}{2} H_2 \leftrightarrow H^+ + e^- \tag{2.6}$$

The equilibrium of this reaction is dependent on the chemical potentials of protons as well as electrons. Therefore the standard hydrogen electrode potential, (SHE), is defined at pH = 0, and the reversible hydrogen electrode potential, (RHE), is defined at any pH.

According to the above mentioned definitions, the most efficient electrodes for fuel cell applications has the smallest possible over-potentials, at the highest possible current. The Butler-Volmer equation expresses the typically observed relationship between electrode current, j, and over-potential and concentrations of the oxidised and reduced species, [O] and [R]:

$$j = j_0 \left[[O] \exp\left(\frac{-(\alpha) F \eta}{RT} \right) - [R] \exp\left(\frac{(1-\alpha) F \eta}{RT} \right) \right] \tag{2.7}$$

where F is Faraday's constant, R is the gas constant, j_0, is the exchange current density and α is the transfer coefficient, which is usually between 0.3 and 0.7. The exchange current density, j_0, depend on the catalytic properties of the electrode interface. Take as an example the two I-V curves in figure 2.2, where one has a larger exchange current density than the other, and therefore show a smaller over-potential at a measurable current than the other. It turns out, that electrode over-potentials are governed mainly by the thermodynamics of molecules adsorbed on the catalyst surfaces and by the number of electrons transferred in the half reaction. This will be further explained, using the example of

the oxygen reaction, in chapter 3. The exchange current density, j_0, is equal to $-er_0$, where r_0 is the rate of the exchange reaction and e is the unit charge. The theory for reaction rates is very successful in linking experiments with fundamental understanding, as described in the following.

2.3 Reaction Kinetics and Catalysis

To rationalise an expression for the rate of an elementary chemical reaction, statistical mechanics can be applied. More specifically, transition state theory based on statistical mechanics has been proven to be rather successful at explaining reaction rates. Consider a molecule, which can find itself in the reactant ground state, in the product ground state or in an exited state of transition between the initial and final states. A 1-dimensional free energy landscape for the molecule is sketched in figure 2.3.

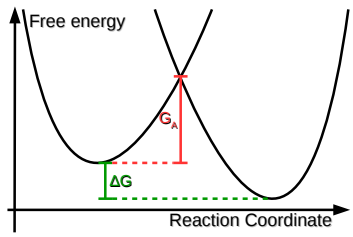

Figure 2.3: *Free energy landscape in transition state theory. The two curves show the free energy potential of the initial reactant state and the final product state. ΔG is the driving force of the reaction, and $G^\dagger$ is the activation free energy.*

The probability of finding the molecule in the transition state, is $Z^\dagger/Z$, where $Z^\dagger$ and Z are the partition functions of the transition state and the reactant, respectively, if they are in equilibrium. If the molecule is assumed to react once it has reached the transition state, the reaction rate is the attempt frequency times the probability to reach the transition state. The rate is written:

$$\frac{d[P]}{dt} = \nu \frac{Z^\dagger}{Z}[R] \tag{2.8}$$

where $[P]$ is the product concentration and $[R]$ is the reactant concentration. The attempt frequency, ν, can for example be $\frac{k_B T}{h}$ in the classical limit, where $k_B T \gg h\upsilon$ and υ is

the vibrational frequency for a reaction coordinate which is a single vibrational degree of freedom. This is in many cases a good approximation. From the partition functions, the Arrhenius equation can be derived, ending in the following result:

$$\frac{Z^\dagger}{Z} = \exp\left(-\Delta E^\dagger / k_B T\right) \exp\left(\Delta S^\dagger / k_B\right) \tag{2.9}$$

$$\frac{d[P]}{dt} = \nu \exp\left(-\Delta G^\dagger / k_B T\right)[R] \tag{2.10}$$

Thus, the rate depends exponentially on the free energy of the transition state.[18] Catalysts are essentially molecules or surfaces, which introduce alternative transition states for the reacting molecule. Transition states can be understood as saddle points in a free energy landscape, in which reactants move. Opening of a reaction path with a lower activation free energy, $\Delta G^\dagger$, result in an exponential speed-up of the reaction. For this reason, the vast majority of chemistry applied in industry is dependent of catalysts to make use of reactions feasible. Electrochemistry is no exception, in fact slow catalysis is the reason, that some fuel cell reactions are slow or do not run without a large over-potential, (this will be further explained in section 3.1.1). For the same reason, the loss of energy due to poor catalysis of important reactions also has great influence over the worlds energy consumption. It is of immense interest to chemists to characterize the transitions states of reactions, to understand catalysts and find better catalysts for interesting reactions. A large amount of effort goes into catalyst development using experimental and computational tools, in academia and in industry.

Reaction pathways and transition states are influenced by catalyst composition and by macroscopic conditions around the catalyst, such as temperature, pressure, electrode potentials and chemical potentials of molecules and surface species. In fact, catalysts are immensely complicated physical/chemical systems, which can be optimized and tailored on length scales from sub nano-meter to meters.[18]

The catalytic reactions in relation to electrochemistry, most often occur at a specific atomic geometry, referred to as a catalytic site, which provides the potential energy landscape with low barriers for the reaction. The reaction pathway usually involves adsorption of a reactant molecule on the catalytic site, exchange of ions with the electrolyte and electrons with the catalyst and then desorption of the resulting product molecule. As an example, take a catalysed hydrogen oxidation reaction in two elemental steps, where

$*$ denotes a site on the catalyst and * as a superscript denotes a molecule bound to the site:

$$H_2 \quad + \quad * \rightarrow H^* + H^+(aq) + e^-(m) \tag{2.11}$$

$$H^* \quad + \quad H^+(aq) + e^-(m) \rightarrow 2H^+(aq) + 2e^-(m) \tag{2.12}$$

$$\tag{2.13}$$

If the surface is not very reactive and molecules are unstable on the surface, adsorption events may be rare, and in that case, the rate of reaction 2.11 would be slow and act as a bottleneck. On the other hand, if the adsorbed hydrogen is too thermodynamically stable on the surface, it will rarely desorb, once it has adsorbed, which mean that a majority of sites will be occupied. Thus, catalytic sites and the conditions surrounding them, must be tailored, so that there is a high probability the sites will be free when a reactant molecule hits and they must facilitate a rapid rates of all steps on the surface and allow desorption, so the next reactant molecule can adsorb. Therefore adsorption energies play a central role in catalysis, as formulated more than a hundred years ago by Sabatier. [18,19]

Experimental efforts often turn to highly simplified model systems to separate effects each of the many important variables. Single crystal surfaces are excellent model systems for catalytic sites, since they can provide a macroscopic surface, which on the atomic scale is relatively uniform and ideally only consists of a single geometry that is repeated in the entire surface plane. Computational efforts often turn to atomic scale models and simulations to aid the understanding of the simplified model systems, including calculating adsorption energies of molecules on the extended surfaces from quantum mechanics. By continuously benchmarking computational results against well defined model system experiments, the computer models become increasingly reliable, while computations can aid the understanding of real model systems and thereby aid the development of design principles and new catalysts. [18,20]

2.4 Quantum Mechanics

As stated above, the energetics of molecules and adsorbates on a catalyst can be obtained from quantum mechanical calculations. In practice, a number of approximations, and implementation solutions have to be used when solving the quantum mechanical problems. This section introduces the method of density functional theory, (DFT), which used for

all the quantum mechanical computations in this thesis.

The calculations are based on the Schrödinger equation, which in principle holds the information needed to understand any system of electrons and nuclei, that is relevant for chemistry. The time-independent form of the equation can be written compactly as:

$$H\Psi_i(R,r) = E_i\Psi_i(R,r) \tag{2.14}$$

where $\Psi_i(R,r)$ are the eigenstates, E_i are the energy eigenvalues. The essence is that $\Psi_i(R,r)$ is the many particle wave function, which is a function of all the coordinates of the nuclei and the electrons. $\hat{H}$ is the full many particle Hamiltonian, which is written:

$$\begin{aligned}\hat{H} &= \underbrace{-\sum_{I=1}^{P}\frac{\hbar^2}{2M_I}\nabla_I^2 - \sum_{i=1}^{N}\frac{\hbar^2}{2m_i}\nabla_i^2}_{\text{kinetic energy}} + \underbrace{\frac{e^2}{2}\sum_{I=1}^{P}\sum_{J\neq 1}^{P}\frac{Z_I Z_J}{\mid \mathbf{R}_I - \mathbf{R}_J \mid}}_{\text{nuclei interaction}} \\ &+ \underbrace{\frac{e^2}{2}\sum_{i=1}^{N}\sum_{j\neq 1}^{N}\frac{Z_i Z_j}{\mid \mathbf{r}_i - \mathbf{r}_j \mid}}_{\text{electron interaction}} - \underbrace{e^2\sum_{I=1}^{P}\sum_{i=1}^{N}\frac{Z_I}{\mid \mathbf{R}_I - \mathbf{r}_i \mid}}_{\text{electron}-\text{nuclei interaction}}\end{aligned} \tag{2.15}$$

where I and J are indexes of the nuclei, i and j are indexes of the electrons, P is the number of nuclei, N is the number of electrons, M are nuclear masses, m is the electronic mass, Z are nuclear charges and e is the electronic charge. This equation is possible to solve for the hydrogen molecule, for the Helium atom, and that is basically it. For most problems it turns out to be unsolvable, analytically and even numerically. However, some approximations can be made. In this work, the preferred substitute for an exact solution is using density functional theory (DFT). In the following, a brief introduction to the approximations made in DFT is given.

2.4.1 Adiabatic approximation

The first simplification of the problem, is the adiabatic approximation. Since electrons are much lighter than the nuclei, it makes sense to decouple the electronic and nuclear degrees of freedom. In that way, one can treat the nuclei as stationary classical particles and find a solution to the instantaneous electronic problem. The full, time dependent many particle wave function can then be written as a product of the nuclear wave function and the

stationary electronic wave function:

$$\Phi_m(R,r,t) = \Theta_m(R,t)\Psi_m(R,r) \tag{2.16}$$

The nuclei are now treated as classical, which means their position expectation values are replaced by their positions. The nuclear equations of motion thereby reduces to the classical equations of motion. [21] The electrons now move in an external potential V_{ext} set up by the nuclei. That leads back to the Schrödinger equation, now with classical, stationary nuclei:

$$\left[-\frac{\hbar}{2m}\sum_j \nabla_j^2 - \sum_{j,l}\frac{Z_l e^2}{|r_j - R_l|} + \frac{1}{2}\sum_{j\neq j'}\frac{e^2}{|r_j - r'_j|}\right]\Psi = E\Psi \tag{2.17}$$

where Ψ is the all electron wave function. [22] This form has the consequence for the computational chemist, that nuclear positions are an input and the electronic structure is an output of each individual electronic structure calculation.

2.4.2 Many electron problem

The all electron wave function is still a function of all the electronic coordinates:

$$\Psi = \Psi(r_1, r_2, ..., r_N) \tag{2.18}$$

Using this wave function, the ground state can be calculated using the variational principle, which says that for any wave function Ψ:

$$\frac{<\Psi|H|\Psi>}{<\Psi|\Psi>} \leq E_0 \tag{2.19}$$

and E_0 is the ground state energy. That yields the ground state energy $E_0(\mathbf{R})$, as a function of just the input coordinates of the nuclei, thus revealing e.g. the energy of a transition state relative to that of a relaxed state of a molecule.

Instead of describing the all-electron wave function, it is useful to consider the electron density. The electron density of a single electron is given from it's wave function by:

$$\rho_j(\mathbf{r}) = |\psi_j(\mathbf{r})|^2 \tag{2.20}$$

The density is only a function in the three spacial dimensions. Therefore it can be expanded in a 3 dimensional grid, which is very useful for computer simulations. [22] The all electron density is also physical observable. Therefore it can be evaluated to provide understanding of phenomena, that are relevant for the chemistry, such as the electron transfer between surface and adsorbate ect.

Introducing the Hartree approximation, it is now assumed that every single electron is moving in the classical electrostatic potential from the nuclei and the other electron densities. The effective external potential for one electron is written:

$$V_{eff}(\mathbf{R},\mathbf{r}) = V_{ext}(\mathbf{R},\mathbf{r}) + \int \frac{\sum_{i\neq j}^{N} \rho_j(\mathbf{r'})}{|\mathbf{r}_i - \mathbf{r}_j|} d\mathbf{r}' \tag{2.21}$$

the $i \neq j$ condition in the sum assures, that an electron does not feel it's own potential. Using the variational principle, the ground state is found using a self consistency cycle in which an external potential is obtained from the electron density, the electron density is obtained from the single electron wave functions, and the wave functions are found by solving the single particle Schrödinger equation:

$$\left[-\frac{\hbar}{2m}\nabla^2 + V_{eff}(\mathbf{R},\mathbf{r})\right]\psi_i = E_i\psi_i \tag{2.22}$$

This solution works, if the many particle wave function can be written as a product of all the single particle wave functions:

$$\Psi(\mathbf{R},\mathbf{r}) = \prod_n \psi_n(\mathbf{r}) \tag{2.23}$$

of which every factor is a function of the three dimensional coordinates. [21]

Since electrons are Fermions, they should also obey the Pauli principle. The Pauli principle gives rise to exchange interaction, which is not yet included, because the Hartree single particle Hamiltonian only includes interaction with classical external potentials. Including the Pauli principle, the exact electron-electron interaction term may be written:

$$U_{ee} = \frac{1}{2}\int \frac{\rho(\mathbf{r})\rho(\mathbf{r'})}{|\mathbf{r}-\mathbf{r'}|} d\mathbf{r}d\mathbf{r'} + \int \frac{\rho(\mathbf{r})\rho(\mathbf{r'})}{|\mathbf{r}-\mathbf{r'}|}[g(r,r')-1]d\mathbf{r}d\mathbf{r'} \tag{2.24}$$

where $\rho(\mathbf{r})$ is the density of one electron at location $\mathbf{r}$ and $g(r,r')$ is the two body pair-correlation function, between the electrons, which includes the exchange and correlation

effects. The first term in 2.24 is the classical electrostatic interaction and the second term is the exchange-correlation contribution. Since the electron electron interaction is described separately, the Hamiltonian may be written as:

$$\hat{H} = \hat{T} + \hat{V} + \hat{U}_{ee} \tag{2.25}$$

where $\hat{T}$ and $\hat{V}$ are the potential and kinetic energy terms of non-interacting single electrons in the external potential (same as in equation 2.22), and $\hat{U}_{ee}$ is the electron-electron interaction.
Thomas-Fermi theory showed that the energy of the system can be calculated as a functional $E[\rho]$ of the electron density:

$$E[\rho] = T + V + E_H + E_X + E_C \tag{2.26}$$

The classical potential energies from ions, V, and from the electron density E_H are known exactly as functionals of the electron density. The exchange energy, E_X, and the non-interacting electronic kinetic energy, T, can be obtained from the non-interacting single electron orbitals, but the correlation energy, E_C is still unknown. For an infinite homogeneous electron gas, the exact solution to each of the terms of $E[\rho]$ was shown to be functionals of the density, using the constraint that the integrated electron density equals a finite number, N, electrons.

If the electron density varies very slowly for a different system of interest, it is therefore tempting to calculate the energy locally at a constant density in every point and integrate $E[\rho(\mathbf{r})]$ over the volume of the system. That leads to the local density approximation (LDA) to the energy functional. However, the real electron density and the single electron orbitals were not known for any real system of interest, and therefore it was not straightforward to find the correct electron density, $\rho[\mathbf{r}]$, at every point in space.[23] This problem is in part circumvented by the Hohenberg-Kohn theorems.

The first Hohenberg-Kohn theorem is a mathematical proof, that the electron density $\rho(\mathbf{r})$ uniquely determines the external potential. The second Hohenberg-Kohn theorem proves that the ground state many particle wave function is also uniquely determined by the density and that the energy can be found by a universal functional of the electron density.[24]

2.4.3 Density Functional Theory

The consequence of the H.K. theorems is that the variational principle can be applied to determine the unique ground state density.[22] The Kohn-Sham[25] equations do this using a self-consistency cycle, as will be explained in the following.

The first step in the Kohn-Sham self-consistency cycle (SCF) is to calculate the external potential, $V_{eff}(\mathbf{r})$, from an initial electron density:

$$V_{eff}(\mathbf{r}) = V_{ext}(\mathbf{r}) + \int \frac{\rho(\mathbf{r'})}{\mathbf{r} - \mathbf{r'}} d\mathbf{r'} + V_{XC}[\rho](\mathbf{r}) \tag{2.27}$$

The leading term on the right side in equation 2.27 is the classical potential from the ionic cores, and the second is the classical Hartree potential, whereas the $V_{XC}[\rho](\mathbf{r})$ is the potential from exchange and correlation, which will be further discussed in section 2.4.4. The external potential is inserted into the single electron Hamiltonian to solve:

$$\left[-\frac{\nabla^2}{2} + V_{eff} \right] \psi_i = E_i \psi_i \tag{2.28}$$

and obtain the single electron orbitals, ψ_i, and eigenvalues, E_i. For a system of N electrons the electronic density $\rho(\mathbf{r})$ is obtained by summing the densities of the N orbitals with lowest energies:

$$\rho = \sum_{i=1}^{N} |\psi_i|^2 \tag{2.29}$$

This density can then be inserted to obtain a new V_{eff} and start another iteration. The procedure iterates, until self-consistency is reached and the density and energy no longer changes in new iterations. As proven by the Hohenberg-Kohn theorems, the above procedure exactly determines the ground state density from any external potential, which is determined by atomic positions and number of electrons. This is the foundation for density functional theory, which is in principle exact except for the exchange-correlation contribution, $V_{XC}[\rho](\mathbf{r})$, in the effective potential.

2.4.4 Exchange and Correlation

The exchange correlation energy can be exactly written as:

$$E_{XC} = \frac{1}{2} \int \frac{\rho(\mathbf{r})\rho(\mathbf{r'})}{|\mathbf{r} - \mathbf{r'}|}[g(\mathbf{r} - \mathbf{r'}) - 1]d\mathbf{r}d\mathbf{r'} \tag{2.30}$$

where $g(\mathbf{r} - \mathbf{r'})$ is called the exchange-correlation hole. Basically $g(\mathbf{r} - \mathbf{r'})$ consists of the sum of the correlation hole, $g_C(\mathbf{r} - \mathbf{r'})$, and the exchange hole, $g_X(\mathbf{r} - \mathbf{r'})$, which are the contributions to the pair-potential on an electron at $\mathbf{r}$ from electron at $\mathbf{r'}$. The potential of exchange can be exactly calculated, but no exact solution has been found for the correlation part, except for the particular case of a uniform density.

The LDA functional, which was derived on an assumption of uniform electron density, may be used as a first approximation, but in real systems, the electron density varies dramatically on smaller and larger scales and is not uniform. The exchange and correlation terms are significant at long ranges, so LDA does not give very good results for most systems of interest for chemistry.[23]

LDA essentially corresponds to a first order gradient expansion of the energy functional in the density, using the assumption of constant density. Accepting that the electron density has gradients, a natural next step to go beyond LDA, is to more orders in the expansion. Adding one more term means that the local gradient of the density are also considered, but continuing the expansion to include even more terms is not necessarily feasible, because the sum is not monotonically convergent. Since the sum is not monotonically convergent, various approaches to a resummation of the series has been attempted to come up with a useful expression for E_{XC}. A class of these approaches writes a resummation in the form:

$$E_{XC}[\rho] = \int \rho(\mathbf{r})\epsilon_{XC}[\rho(\mathbf{r})]d\mathbf{r} + \int F_{XC}[\rho(\mathbf{r}), \nabla\rho(\mathbf{r})]d\mathbf{r} \tag{2.31}$$

This form (2.31) results in the semi-local functionals called the *generalized gradient approximation* (GGA), where F_{XC} and $\epsilon_{XC}[\rho(\mathbf{r})]$ can take various shapes, which satisfy different physical constraints from the exchange-correlation hole, although no one satisfies all the constraints. They can also be fitted to different training sets to reproduce atomization energies of molecules, geometries, ect.[21,23]

One of the most widely used versions of the GGA functionals is the Perdew-Burke-Ernzerhof, (PBE),[26] which was made to satisfy as many physical constraints as possible, omitting those that were expected to give the smallest contributions.
A revised PBE functional, the RPBE[27] is the most applied functional for calculations in this thesis. The reason for this choice is that the RPBE was been constructed to give the best results for chemisorption energies on metal surfaces and atomization energies of small molecules, which are central to the present work. In general, the GGA class are computationally efficient choices compared to a wide variety of more advanced XC functionals.

The GGA class functionals still do not include many-body correlations, also known as van der Waals potentials, and to include those, several van der Waals functionals have also been developed[28–30]. In their current implementation they demand somewhat more computational resources, and in this work they were therefore used to a smaller extend.

2.5 Implementation of DFT

This section deals with the implementation of DFT in the electronic structure code GPAW[31,32], which was used for most of the electronic structure calculations in this thesis. A central aspect of the choices in implementation is computational efficiency, which can be defined as the compromise of quality or accuracy of a result versus CPU hours spent.

Basis sets

In the GPAW code, three types of basis sets are available for the Kohn-Sham (KS) single particle wave functions in equation 2.28, and they were all used in different parts of the project. Usually, periodic boundary conditions are employed, and thus the wave functions should correspond to a solution that upholds translational periodicity of the unit cell, by being the product of a phase factor and a periodic function, according to the Bloch theorem[23,33]. The wave function can in principle be evaluated at an infinite number of k-points in the reciprocal unit cell, but the result will usually be converged by including a small number of k-points. The way to select the k-points, that is used in the GPAW implementation is the Monkhorst-Pack sampling[34], which selects points interpolated between the highest symmetry points.

Expanding the KS basis in a linear combination of plane waves, (PW), is an advantageous solution if periodic boundary conditions are employed and the unit cell dimensions are not too large. An expression for the wave functions, $\psi^{(\mathbf{k})}(\mathbf{r})_j$, with eigenstate j and k-vector $\mathbf{k}$, in which the periodic boundary conditions are satisfied is:

$$\psi^{(\mathbf{k})}(\mathbf{r})_j = \sum_{G=0}^{\infty} C_{j\mathbf{k}}(\mathbf{G})\phi_{\mathbf{G}}^{\mathbf{k}}(\mathbf{r}) \tag{2.32}$$

where $C_{j\mathbf{k}}(\mathbf{G})$ are the PW coefficients and $\mathbf{G}$ are the reciprocal lattice vectors. In principle, equation 2.32 produces a complete basis set, but the sum of coefficients must be truncated in some way. This is done so the waves with higher kinetic energy than a chosen cut-off are omitted, using the condition[23]:

$$\frac{\hbar^2}{2m} < E_{cut} \tag{2.33}$$

Another type of basis set is representing wave functions on a uniform three dimensional real space grid, where the values on the grid constitute the wave function and derivatives are calculated as finite differences.[32,35] This method is not as efficient as plane waves for small systems, but it does not need to transform entire wave functions between real space and reciprocal space, so parallelization beyond k-points is much easier than in PW mode. The only parameter to increase the size/accuracy of the real space basis set is the grid spacing and it converges towards a complete set, when decreasing the grid spacing. Therefore this mode can provide accurate solutions with better computational efficiency for larger systems.

Finally, the KS basis may be expanded in a linear combination of localized atomic orbitals, (LCAO).[36] This type of basis set can be expanded by adding more localized functions, but it does not converge systematically towards complete set, since different types of functions are added by choice. The localised basis functions are usually radial "zeta" functions and "polarisation" functions are functions to represent angular momentum.[37]

Core electrons

Near the atomic nuclei, a number of problems arises related to the diverging electrostatic potential or the nucleus. Core electrons may have high kinetic energies and thus wave

functions that oscillate extremely rapidly space, and so plane waves close to the cores electrons requires much higher energies than the valence electrons. On the other hand, only valence electrons are participating in chemical bonds, thus they are interesting for applications of DFT. Therefore it is advantageous to replace the core electrons with either a pseudo-potential or projector wave augmented functions[38,39], (PAW), both of which can be constructed once for every element from all-electron calculations. In GPAW, the PAW method is used to represent electronic cores. The PAW method relies on calculating the all electron wave functions of the core states for the isolated atoms, and then introduce a mapping between those and a pseudo wave function, which is smooth. Outside a certain radius around the nucleus, referred to as the augmentation sphere, the real all electron wave function is equal to the pseudo wave function. During solution of the eigenvalue problem in DFT, the pseudo wave functions and the pseudo electron density are used, while it is possible to transform into all electron wave functions and get the real all electron density.[32,38]

Forces and geometries

Energies of surfaces, molecules and chemisorbed species depend on the geometries, and they must be relaxed to the lowest energy state, to obtain the relevant energies for applications to thermodynamics.

A number of relaxation algorithms exist, which perturbs the atomic positions and geometries in different ways to locate minima. Methods for relaxing a smaller number of degrees of freedom always relies on forces from the electronic structure calculations. The first derivative of the energy from the converged electronic structure calculations is the Hellmann-Feynmann forces:

$$F_I = -\frac{\partial E^{DFT}(\mathbf{R})}{\partial \mathbf{R}_I} \tag{2.34}$$

$$= \int \rho(\mathbf{r}) \frac{\partial V_{ext}(\mathbf{r}-\mathbf{R}_I)}{\partial \mathbf{R}_I} + \sum_{J \neq I} \frac{\mathbf{R}_I - \mathbf{R}_J}{|\mathbf{R}_I - \mathbf{R}_J|^3} \tag{2.35}$$

where R is position and F_I denotes forces or positions of ion I. An additional term is added if the basis set is incomplete, e.g. if LCAO is used as basis set.[23,40]

A variety of iterative schemes use the forces to relax positions to the lowest local energy minimum, and then declare convergence when the force is smaller than some criterion deemed close enough to zero. It is a central problem for modelling atomic scale

systems, that the phase space of atomic positions has many degrees of freedom, and that the energy landscape can have many local minima. If the number of degrees of freedom is not too great, it is usually enough to try a few different starting configurations for a given state of some number of atoms, and assume that the lowest of the found minima is the global one. For most structure optimization problems in this thesis, a Broyden-Fletcher-Goldfarb-Shanno algorithm, (BFGS),[41–44] was used to find the local minima, and in a few cases the FIRE algorithm was used[45].

2.6 Thermodynamics from DFT

DFT can provide the ground state potential energy differences between molecules in various states on the surface or in the gas phase. Contributions for entropy and zero point energy can be obtained from standard thermodynamic tables or calculations, and they can be added to the potential energies to obtain free energy differences, including adsorption free energies.

Free energy differences are written in terms of differences in entropy, S and enthalpy, $H(T)$, which is further written in terms of the zero-point energies, ZPE, potential energies, E, and heat capacity in the following way:

$$\Delta G = \Delta H(T) - T\Delta S \tag{2.36}$$

$$\Delta H(T) = \Delta E + \Delta ZPE + \int_0^T C_P dT \tag{2.37}$$

In the Born-Oppenheimer approximation, the potential energies are the energy of the converged electronic structure, calculated using DFT. The entropy is normally obtained from thermodynamic tables, although vibrational, rotational, translational and electronic entropies can also be obtained from first principles.

Knowing the free energies of the micro states of different systems lets us apply statistical physics for calculating macroscopic properties of the system. This is can be done by taking the average of the property of all the micro states of the system weighted to their probability:

$$< A > \quad = \quad \sum_i A_i p_i \tag{2.38}$$

$$p_i = \frac{1}{Z}\exp\left(\Delta G_i/kT\right) \tag{2.39}$$

$$Z = \sum_i^{\infty}\exp\left(\Delta G_i/kT\right) \tag{2.40}$$

$$< A > = \frac{1}{Z}\sum_i A_i \exp\left(\Delta G_i/kT\right) \tag{2.41}$$

where $\Delta G_i = G_i - G_0$, and G_0 is the reference state.[33,46] In principle the number of states, i, is infinite, but the probability decays exponentially, and a cut-off for the partition function is therefore often used in practice. This can be done, if the states that are not counted can be assumed so rare that they are not relevant for the average, $< A >$. The states that are still included in the sum is sometimes referred to as *relevant states*.

Usually, adsorption energies are calculated at zero K and written:

$$\Delta G = \Delta E - T\Delta S + \Delta ZPE - n\mu_A \tag{2.42}$$

where μ_A is the chemical potential of the reference reservoir for atom A and n is a number of atoms that were added to the system. In the last equation, the first two terms only contain changes to the energy of the surface system. The reservoir is usually a gas at standard conditions or a bulk solid, for which the potential energy and zero-point energy can be obtained from DFT.

In the subject of this thesis, one of the most interesting reference states is the chemical potential of protons solvated in the electrolyte. However, there are many issues with calculating energetics of solvated molecules or ions, since solvation is often very long range and dynamic in nature and because systems that are not charge neutral cannot be handled with periodic boundary conditions. In the following, an introduction is given on how this is circumvented.

2.6.1 Computational Hydrogen Electrode

Calculating a free energy of electrosorption of an ion from solution requires a clever choice of reference, if one is to avoid modelling ions in solution explicitly. Such a choice of reference is introduced in this section.

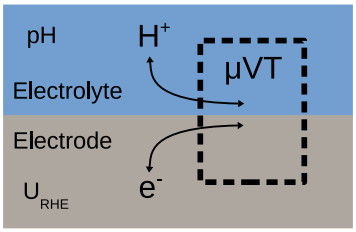

Figure 2.4: *Thermodynamics of adsorption should be understood using a grand canonical ensemble, due to the exchange of particles.*

The free energy of proton adsorption from solution is:

$$\Delta G = \Delta E + \Delta ZPE - T\Delta S - (\mu_{H^+} + \mu_{e^-}) \tag{2.43}$$

as in (2.42) where μ_{H^+} and μ_{e^-} are the chemical potentials of the protons in solution and electrons at the Fermi level of catalyst.

Since μ_{H^+} and μ_{e^-} cannot be used as references directly, it is necessary to relate them to a chemical potential of a species, which can be calculated from DFT. It is straight forward to calculate the energy of hydrogen in gas phase, so a reference that can be related to this is desirable. The hydrogen reference electrode maintains equilibrium between the hydrogen at standard conditions versus electrons + protons. Therefore the chemical potentials of these species at the reference electrode obey the relation: [47]

$$\mu_{H^+}^{ref} + \mu_{e^-}^{ref} = \mu_{H_2}/2 \tag{2.44}$$

The difference between the chemical potentials of electrons of the surface and the reference electrode can be measured in experiments, since the voltage U_{RHE} between the working electrode and the reversible hydrogen electrode is: [16]

$$U_{RHE} = -(\mu_{e^-} - \mu_{e^-}^{ref})/e \tag{2.45}$$

by inserting (2.44) into (2.45),

$$-eU_{RHE} = \mu_{e^-} - \mu_{H_2}/2 + \mu_{H^+}^{ref} \tag{2.46}$$

$$\mu_{e^-} = \mu_{H_2}/2 - \mu_{H^+}^{ref} - eU_{RHE} \tag{2.47}$$

If $\Delta F = \Delta E + \Delta ZPE - T\Delta S$, and 2.46 is inserted into (2.43),

$$\Delta G = \Delta F - \mu_{H^+} - (\mu_{H_2}/2 - eU_{RHE} - \mu_{H^+}^{ref}) \tag{2.48}$$

Usually it is assumed that μ_{H^+} is equal to $\mu_{H^+}^{ref}$. This holds if there is no gradient in chemical potential for the protons in solution, which is equivalent to an equilibrium situation, where diffusion is much faster than surface reactions. In that case, equation (2.48) reduces to

$$\Delta G = \Delta F - (\mu_{H_2} + eU_{RHE}) \tag{2.49}$$

This way of calculating the energy of electrosorption is referred to as the computational hydrogen electrode (CHE). In the usual formalism, $-eU_{RHE}$ is interpreted as a chemical potential, $\mu_{H^+ + e^-}$, for protons + electrons, with $H_2(g)$ at 1 atm as the reference chemical potential. This can be written:

$$\mu_{H^+ + e^-} = -eU_{RHE} = \mu_{e^-} - \mu_{e^-}^{ref} = \mu_{H^+} + \mu_{e^-} - \mu_{H_2}/2 \tag{2.50}$$

$$\Delta G = \Delta F - \mu_{H_2}/2 - \mu_{H^+ + e^-} \tag{2.51}$$

$$\Delta G = \Delta E + \Delta ZPE - T\Delta S - \mu_{H_2}/2 - \mu_{H^+ + e^-} \tag{2.52}$$

$$\tag{2.53}$$

The free energy, formulated using equation 2.52, is sketched in figure 2.5.

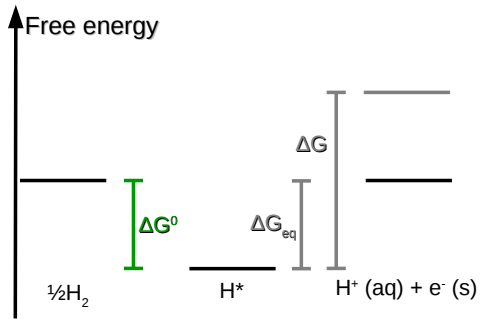

Figure 2.5: *The computational hydrogen electrode visualised for the electrosorption of protons. ΔG is obtained by calculating ΔG_{eq} and subtracting $\mu_{H^+ + e^-}$.*[48]

Figure 2.5 illustrates, how a DFT calculation of adsorbed hydrogen relative to H_2, leads to the electrosorption energy using $\mu_{H^+ + e^-}$. A requirement for the applicability

of the CHE, is that changing the electrode potential of the surface does not introduce a significant electric field contribution to the potential energy of the adsorbate. A standard DFT calculation with a slab and periodic boundary conditions would not capture such a contribution in the potential. However for most small molecules, this contribution has proven to be negligible.[49]

The CHE is extensively used in the following chapters of this thesis. Chapter 3 treats calculations of thermochemistry of intermediates for the oxygen reduction reaction on ideal, strained and reconstructed Pt(111) surfaces. The CHE is the key to understanding the over-potential of ORR and to understand, which materials properties should be addressed in the search for better catalysts for this reaction. Chapter 4 treats the hydrogen evolution, also using the CHE to evaluate several newly discovered catalysts. In chapter 5, the CHE scheme is further developed to account for electric field effects and pH effects at the interface.

3. Surfaces for Oxygen Reduction Reaction

This chapter presents DFT calculations to understand the trends in reactivity of contracted and reconstructed platinum surfaces in perspective to catalysis of the oxygen reduction reaction, (ORR). First, a brief introduction is given to the fundamentals of ORR and to recent results on platinum lanthanide alloys for ORR catalysis. Then computations are presented and discussed in relation to trends observed in the experimental studies on the newly discovered series of Pt-lanthanide materials. Some of work presented in this chapter is published in paper I, and some of the work is prepared for publication in paper II and III.

3.1 Introduction

ORR is the electrochemical half reaction which forms water from electrons, protons and oxygen:

$$O_2(g) + 4H^+ + 4e^- \rightarrow 2H_2O \tag{3.1}$$

It is fundamental for hydrogen fuel cells, and it is the process, which involves the largest efficiency loss in the PEM fuel cell. Therefore studies with the aim of developing new catalysts for this reaction is of high interest to the hydrogen fuel cell industry and to the fields involving surface science and electrocatalysis.

A great number of advances in understanding of the ORR have been made in the last decade or so, by computations and by surface science, spectroscopy and electrochemical experiments.[50,51] Design principles were developed, which suggested new candidate materials, and eventually the new understanding manifested itself in new experimental catalysts, which are mainly based on platinum alloys. There are still a great number of questions regarding the properties of these catalysts, the structure of the active surfaces, the stability of these and the features that make them better than other catalysts such as pure platinum. These questions must be answered in order to rationally optimize the catalysts and improve the design principles to search for even better catalyst candidates.

3.1.1 Fundamentals of the oxygen reduction reaction

The oxygen reduction reaction can be separated in four elementary protonation reactions. First, an oxygen molecule must adsorb on the catalyst. Then the first protonation reaction forms the hydroxyl intermediate:

$$O_2^* + 4H^+ + 4e^- \rightarrow HOO^* + 3H^+ + 3e^- \tag{3.2}$$

The second protonation step forms a water molecule and an atomic oxygen:

$$HOO^* + 3H^+ + 3e^- \rightarrow O^* + H_2O + 2H^+ + 2e^- \tag{3.3}$$

Theoretically, the second step can also end in a $H_2O_2^*$ state, but this is not a relevant pathway on platinum[52]. The third protonation forms the hydroxide intermediate:

$$O* + 2H^+ + 2e^- \rightarrow HO^* + H^+ + e^- \tag{3.4}$$

And the fourth step consumes hydroxide and forms water:

$$HO^* + H^+ + e^- \rightarrow H_2O^* \tag{3.5}$$

Using the computational hydrogen electrode, the free energy of each reaction step can be written:

$$\Delta G = \Delta G^0 + eU_{RHE} \tag{3.6}$$

where ΔG^0 is the free energy change at 0 V versus RHE and e is the unit charge. If any one of these reactions is significantly slower than the others, it can be assumed that this is rate-determining. Transition state theory (See section 2.3) predicts that the intermediate step with the slowest rate is the one with highest ΔG.

If written relative to the initial state, the free energy is:

$$\Delta G^{int}(U_{RHE}) = \Delta G^0 + neU_{RHE} \tag{3.7}$$

where n is the number of proton + electron pairs. The origin of the over-potential is evident, when equation (3.7) is used to plot $\Delta G(U_{RHE})$ for the full ORR reaction path (Fig. 3.1).

By increasing the over-potential sufficiently, ΔG for all four reaction steps become

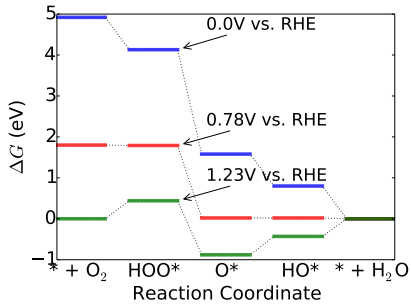

Figure 3.1: *Free energy diagram for ORR intermediates adsorbed on Pt(111) based on previous DFT calculations. Adapted from Karlberg et al.*[52] *with no field corrections.*

negative. The last step to become negative, as the over-potential is increased, is the potential determining step.[48]

From figure 3.1, it is appears that Pt(111) binds the O* and HO* intermediates too strongly and HOO* too weakly. The FCC(111) facets of platinum and Pt-alloys are nevertheless the most active surfaces known for ORR catalysis. By computational screening of transition metals for the binding energy of these intermediates, it was calculated, that substituting one metal for the next, the change in reactivity towards one intermediate scales linearly with the change in reactivity of the other intermediates. As long as the linear relation for FCC(111) surfaces hold, the number of degrees of freedom in optimizing the catalysts may be reduced to one. The binding energy of either adsorbate is therefore a good descriptor for reactivity and activity. Within the constraint of these scaling relations, a more optimized catalyst would bind the intermediates slightly weaker than Pt(111). In accordance with the Sabatier principle[19], the DFT calculations predict that there is an optimal reactivity, which mean that an excessive weakening of the oxygen binding energies, will again yield a lower catalytic activity.[48,52,53]

3.1.2 Trends in ORR activity

Platinum has the advantage as a catalyst material, that is relatively resistant to dissolution in the very acidic environment of the PEMFC electrolyte. Only a few other transition metals such as palladium and gold have enough stability in the conventional acid electrolytes. Therefore, numerous experimental and computational studies has been done on platinum-alloy catalysts, in attempts to improve activity, without compromising resistance to dissolution.[51,54–58].

Most platinum-transition metal alloys have low energies of alloying, which renders them vulnerable to segregation of the elements. However, platinum-yttrium and platinum-gadolinium was found to be more active catalysts than pure platinum while being more stable than transition metal alloys.[59]

Angle resolved XPS experiments[60] revealed that a thick platinum skin forms on the gadolinium alloy. Yttrium and gadolinium, are very reactive towards oxygen and the mechanism for the formation of the Pt-skin is most likely a leaching of the rare-earth element into solution, leaving the skin which then protects the alloy from contact with the electrolyte and further leaching. XRD measurements show that the bulk structure of the alloy has two alternating layers in the (001) planes. These are shown in Fig. 3.2.

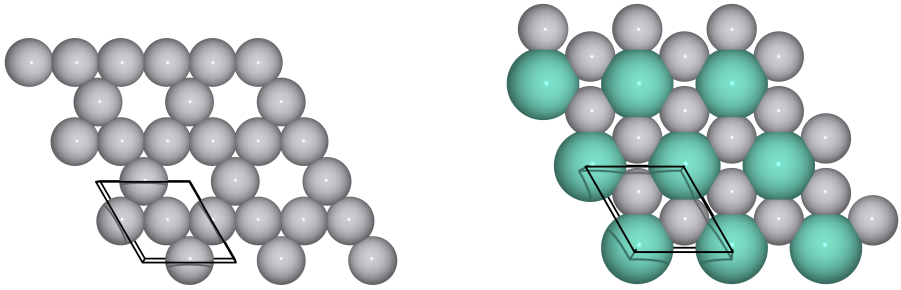

(a) *Kagomé layer. The structure is equal to an FCC(111) layer, where every fourth atom has been removed.*

(b) *Pt_2Gd layer.*

Figure 3.2: *Models of the two atomic layers in the Pt_5Gd unit cell. Small gray spheres represent platinum atoms and large cyan spheres represent gadolinium atoms. In the Pt_5Gd unit cell, the vacancies in the Kagomé layer are positioned over the Gd atoms in the Pt_2Gd layer.*

The vacancies in the Kagomé layer (Fig. 3.2a) have the same positions as the Gd atoms. Since gadolinium tends to leach out into the solution, it has been hypothesized that some Pt_5M (001)/overlayer interfaces are terminated by the Kagomé layer, providing a lattice match with the Pt(111) lattice. The Pt_5Gd (001) facet is 4.5% smaller than the Pt(111). The overlayer can therefore be a Pt FCC(111) layer with a contraction of around 4.5%. Electronic structure theory predicts that contracted surfaces are more noble[61], which would be beneficial to activity[48]. Since the Pt skin is several atomic layers thick, the change in activity is attributed mainly to strain effects, as opposed to ligand

effects.

3.1.3 Strain effect on Pt(111)

It turns out that many of the Pt-lanthanides can form the Pt_5Gd crystal structure. A systematic series of experimental studies on alloying platinum with lanthanides was therefore carried out in an attempt find the optimal Pt-lanthanide catalyst with a fine tuned lattice constant to get perfect reactivity. A correlation between the lattice parameters of platinum-lanthanide alloys and the catalytic activity of polycrystalline samples was observed.[58]

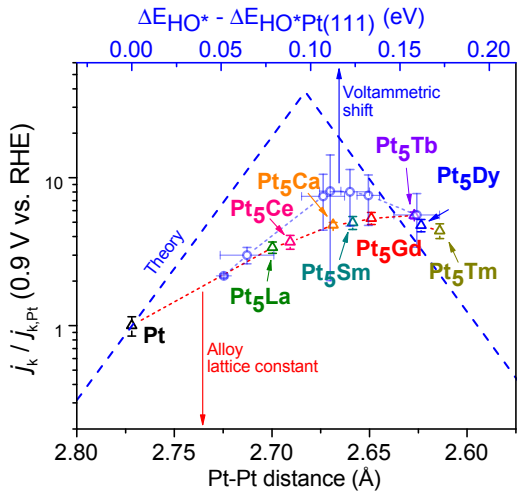

Figure 3.3: *The ORR activity of poly-crystalline platinum-lanthanide alloys plotted versus the Pt-Pt distance in the alloy*[58]*. The top axis is the OH binding energy constructed by transforming strain into OH binding from DFT calculations on Pt(111) surfaces with lattice contractions, (Shown in figure 3.4). The gray dataset in the background is from Cu/Pt(111) near-surface alloys*[57]*, where the OH binding energy was obtained from a voltammetric shift of the OH adsorption peak.*

Fig. 3.3 plots the measured activity vs. Pt-Pt distance trend for the Pt-lanthanides. Observing the trend for the Pt-lanthanides a maximum in activity is identified around the Pt-Pt distance of Pt_5Tb. It was not possible to accurately determine the OH binding energies on Pt-lanthanides from the electrochemical experiments, to construct the Sabatier volcano directly for the Pt-lanthanides. Therefore, activity vs. OH binding energy from

Cu/Pt(111) near surface alloys, (NSA's)[57], are co-plotted in Fig. 3.3. For the Cu/Pt(111) NSA's the change in OH binding energy could be quantified by experiments to make the Sabatier analysis. The study on near Cu/Pt(111) near surface alloys can thereby be used as a benchmark for the computed prediction of activity enhancement versus binding energy.

A linear fit to the change in calculated OH binding energy versus strain[58], was used to scale the ΔG_{OH} axis in figure 3.3. These OH adsorption energies are plotted vs. strain in 3.4.

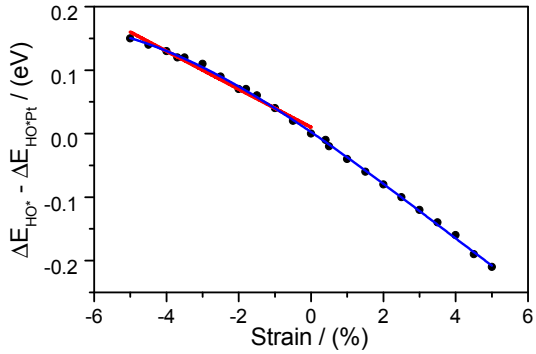

Figure 3.4: *Adsorption energies versus strain on Pt(111), by U. G. Vej-Hansen*[62]

Past DFT calculations predict, that the optimal OH binding is 0.1 eV weaker than on Pt(111)[63]. According to the calculated trend in OH binding versus strain, this shift in ΔG_{OH} corresponds to a contraction of around 3% (See Fig. 3.4). However, experiments in several past studies on different Pt alloys give a picture of an optimal OH binding that is 0.12 eV weaker than on Pt(111)[51,57]. This value is within the confidence range of the computed value of 0.1 eV. Micro kinetic models suggest an explanation to why the top of the experimental volcano is shifted and it explains why the optimum is lower than the peak. If there is a higher barrier for water formation from OH (reaction 3.5), than for OOH formation (reaction 3.2), the trend in activity enhancement on the strong binding side of the volcano will converge to a constant level as the surfaces become more noble, until OOH formation becomes rate limiting.[63]. Assuming that the Pt-skin lattice distances matches the (001) facet of the alloy, the optimum OH binding is 0.15 eV weaker than Pt(111), which corresponds to a strain closer to 5% (See Fig. 3.4). This would mean that the Pt-lanthanides up to Pt_5Tb are strong binding, and the Pt_5Dy and Pt_5Tm alloys

are too weak binding. The relation between activity, binding energy and strain, which can be characterized as skewed towards the weak binding side of the Sabatier volcano, is not unlike that reported by Strasser et al.[64] for dealloyed Cu-Pt nano particles. However, there is no clear explanation to why the optimum binding energy on Pt-lanthanides should be higher than for the Cu/Pt(111) near surface alloys. One possible reason is that the dependence of binding energy on the lattice strain is not reproduced very well by DFT calculations, and another is that the assumption of a Pt(111) skin matching the Pt-lanthanide alloy is not accurate.

Electrochemical measurements on the series of polycrystalline Pt-lanthanide alloys were able to quantify the binding energies towards hydrogen. Experiments by M. Escudero-Escribano et al.[58] show that the H adsorption peaks of the Pt-alloys are shifted towards more negative potentials than polycrystalline Pt, indicating a decreased reactivity towards hydrogen. This trend is in agreement with previous experimental and theoretical studies on contracted Pt surfaces by Hoster et al.[56] The experiments by M. Escudero-Escribano et al. also showed, however, that the alloys with smallest lattice parameters, (Pt_5Tm, Pt_5Tb and Pt_5Dy) were more reactive towards hydrogen than Pt_5Gd. The hydrogen binding energy is obtained from cyclic voltammetry experiments by noting the potential, at which a charge, corresponding to a certain coverage of hydrogen, has been transferred. That result is unexpected, given that hydrogen adsorbs on a Pt(111) overlayer, which matches the alloy, because a compressed overlayer would be more noble than pure Pt[61]. Small perturbations to the reactivity of Pt(111) tends to scale consistently for various intermediates, according to previous DFT calculations[65]. In that case, the perturbations to Pt(111) reactivity was due to ligand effects from near surface alloying with scandium and yttrium. Strain on the ideal Pt(111) surface is also expected to behave as a small perturbation, yielding scaling relations between OH and other molecules such as hydrogen. This relation is further explored in section 3.2.1, by relating adsorption energies of OH, hydrogen, and CO, calculated by DFT.

During degradation tests with 10000 potential cycles between 0.6 V and 1.0 V versus RHE, the activity of the Pt-lanthanides had degraded somewhat, depending on the alloy. After this, Pt_5Gd became the most active[58], while Pt_5Tb has degraded more. Keeping the assumption of a Pt(111) skin matching the lattice constant of the alloy, it so appears that the most noble surfaces degrade more that the more reactive surfaces.

The trend in degradation and the trend in reactivity towards hydrogen do not seem

consistent with a simple picture of regular Pt(111) over layers with varied lattice parameters depending on the lanthanide. Some unanswered questions are:

- What is the change in binding energy of oxygen species due to lattice contraction?
- What is the real lattice constant and structure of the Pt_5M surface layers?
- What is the d-band shift of the surfaces?

These questions should be answered to fully understand the trends in activity and stability of the Pt-lanthanide catalysts.

It is also possible, that the contracted surfaces reconstruct and that reconstructions govern the observed activity enhancement. Such effects are discussed in section 3.2.4 on the basis of DFT calculations and experiments. Further experimental investigations of the consequences of lanthanide alloying are also on-going, particularly using single crystal model systems. Before presenting new DFT calculations, a brief review of the latest results from model system experiments is given.

3.1.4 Model Systems

To study the structure of the Pt-lanthanide alloy surface layers, single crystal alloys have been made in ultra high vacuum, (UHV), with yttrium, (Y/Pt(111)), by Johansson et al.[66] and with gadolinium, (Gd/Pt(111)), by E. Ulrikkeholm et al.[67]

Low electron energy diffraction, (LEED), experiments show $\approx (2 \times 2)$ structures on both the Gd and the Y alloys when they were prepared and annealed, and not yet exposed to air or an electrolyte. This agrees with the hypothesis of a Pt_5M (001) surface terminated by a Kagomé layer (Fig. 3.2a). LEED also show that the Y/Pt(111) lattice appear to be 5% to 6% contracted and the Gd/Pt(111) appear to be 5.2% contracted.

The single crystal systems were also characterized in ultra high vacuum by temperature programmed desorption (TPD) experiments with CO. The Y/Pt(111)[66] and the Gd/Pt(111) showed clear differences in the TPD spectra compared to Pt(111). Two main differences are observed: **1)** the desorption spectrum shift down in temperature, indicating that CO is destabilised on the alloy surfaces. **2)** The desorption spectrum narrows and develops sharp peaks, as opposed to the spectrum of Pt(111), which is a broad soft feature. The CO binding energy can be estimated roughly from the shift in desorption temperature and the obtained temperature shift for for Y/Pt(111) was around 100K,

which corresponds to a shift of $\Delta\Delta E_{CO}^{des} \approx 0.28$ eV, and for the Gd/Pt(111) the shift was 197K, which corresponds to $\Delta\Delta E_{CO}^{des} \approx 0.55$ eV.[18,68]. DFT calculations presented in section 3.2.2 were carried out to provide an interpretation of the differences in the TPD spectra, based on the adsorption properties of CO on strained Pt(111) and to compare the measured desorption energies with calculated CO adsorption energies on contracted Pt(111) surfaces.

Exposure to air and electrolyte

After exposure to air, the single crystal samples were investigated by angle-resolved X-ray photoelectron diffraction (AR-XPS), which can provide a depth profile of the elemental composition in the few outermost atomic surface layers. The result is consistent with a one monolayer of Pt terminating the alloy[67]. After exposure to electrolyte and oxidising potentials, another AR-XPS experiment showed that a platinum skin of 3 to 4 monolayers had formed, just as previously observed for polycrystalline Pt-Gd alloys[60].

The samples were also studied with surface sensitive X-ray diffraction (SSXRD) by A. Pedersen et al. at SLAC[1] before and after exposure to electrolyte. The SSXRD experiments show crystalline order with domains rotated 60 degrees from each other. After electrochemical treatment, the SSXRD experiments revealed the same surface order, but now rotated 30 degrees from the Pt(111) substrate crystal.[67] This could be explained by a variety of surface structures, which were investigated further using DFT calculations, presented in section 3.2.4. The lattice constants obtained from the SSXRD were rather close to those of the relaxed platinum lattice. For Y/Pt(111) they were 1.4% contracted in the plane and 2.3% contracted out of the plane. The Gd/Pt(111) facets were only 0.3% contracted in the plane, but had an out-of plane tensile strain of up to 1.1%. One must keep in mind, that the SS-XRD experiments captures a mean of the surface, while there may be many domains present with varying reconstructions and lattice constants.

3.2 DFT Calculations

The main goals of the DFT calculations, which are presented in the following sections are **1)** To further understand the structure and behaviour of the catalyst surfaces, and **2)** To

[1]National Accelerator Laboratory, Menlo Park, CA, USA

evaluate the accuracy with which trends in reactivity versus strain are computed by DFT.

All DFT calculations presented in this section were carried out using the GPAW code[31,32], which uses projector augmented wave functions to represent atomic core electrons. The single electron Kohn-Sham[25] wave functions were represented using plane-waves with an energy cut-off of 800 eV. It is worth noting that a fine grid spacing for the density, (equivalent to a high density cut-off), is in order, when attempting to capture the differences in electronic structure from straining the unit cells. Otherwise, incremental changes in grid spacing or number of grid points may influence the accuracy of the calculated trends. For the present calculations the grid spacing was converged with the energy cut-off, which sets the default value of the grid spacing.

A k-point sampling[34] of 8×8 was used for unit cells at the size of an FCC(111) 2×2 super cell, and 6×6 or 6×8 k-points samplings were used for super cells of the size of FCC(111) 3×3, or 3×2, respectively. Exchange and correlation contributions were approximated with the RPBE functional[27], and a Fermi smearing of 0.1 eV was used to help convergence. The structures were relaxed until the maximum forces were below 0.05 eV/Å, using the BFGSLinesearch algorithm implemented in the atomic simulation environment, (ASE)[69].

3.2.1 Reactivity vs. Strain

DFT calculations show consistent relations between the change in reactivity towards OH, CO and H, due to strain as shown by figure 3.5. The binding energies were modelled with 1/4 ML coverage in 2×2 non-orthogonal unit cells with surfaces represented by 5 atomic layers, except for the energies for hydrogen adsorption, which is from U. G. Vej-Hansen et al.[58,62].

The trends show that strain can be regarded as a small perturbation to the reactivity of the Pt(111) surface, and that this perturbation scales between different adsorbates. Similar trends have been observed earlier, where the perturbation to the binding energies came from ligand effects[66] (as mentioned in section 3.1.3).

To compare the scaling trend with experiments, it can be used that, the binding energy of hydrogen is related to the voltammetric shift from cyclic voltammograms by

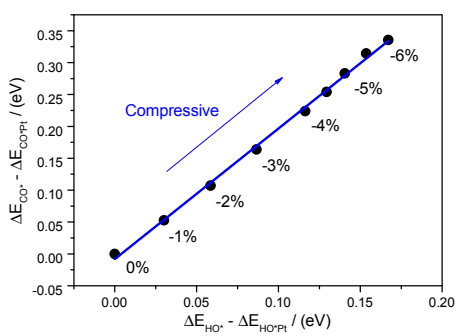

(a) *Shift in CO* adsorption energies vs. HO* adsorption energies. The fit has a slope of* ≈ 2.

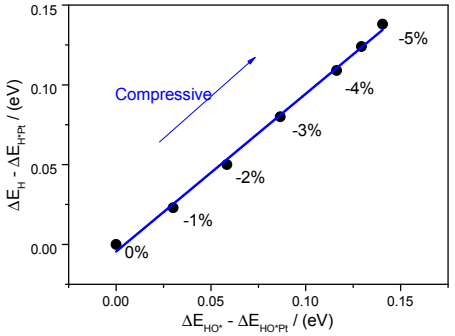

(b) *Shift in H* adsorption energies vs. HO* adsorption energies. The linear fit has a slope of* ≈ 1

Figure 3.5: *The shift in adsorption energies of CO* and H* due to lattice strain plotted versus the shift in the adsorption energy of HO*.*

the relation:

$$\Delta G_{H^*} - \Delta G_{H^*Pt} = -e\left(U_{H^*_{upd}} - U_{H^*_{upd}Pt}\right) \tag{3.8}$$

where $U_{H^*_{upd}}$ denotes the adsorption potential on one of the Pt-alloys, and $U_{H^*_{upd}Pt}$ is the adsorption potential on pure Pt. Considering the trend in the voltammetric shift for hydrogen adsorption on the polycrystalline Pt-lanthanides in light of the correlation between HO* binding and hydrogen binding, some kind of restructuring or relaxation of the surface, which affect the trends in surface reactivity is most likely occurring. The samples that should have the largest lanthanide contraction, (Pt_5Tb, Pt_5Dy and Pt_5Tm), relative to the rest of the series, bind hydrogen stronger, and are due to the DFT trend expected to be more reactive towards OH. Possible reasons for this is further discussed in the end of this chapter (Section 3.3). However, it is clear that Pt_5Tb, Pt_5Dy and Pt_5Tm are on the strong binding side to the Sabatier volcano.

A linear fit to OH binding energies versus strain yields a slope of -0.033 eV /%. Using this correlation the OH binding energy can be estimated from the strain obtained experimentally from SSXRD. To benchmark this relation, the OH binding energies can also be obtained from the voltammetric shift in OH adsorption region of the CV curves for Y/Pt(111) and Gd/Pt(111). Either adsorption energy can be correlated with ORR activity, as in past studies on Pt-Cu near surface alloys[57]. Figure 3.6 shows the ORR activity of the Y/Pt(111) and Gd/Pt(111) plotted against **1)** the ΔE_{OH} from the voltammetric shift and **2)** against the ΔE_{OH} from strain measurements and DFT.

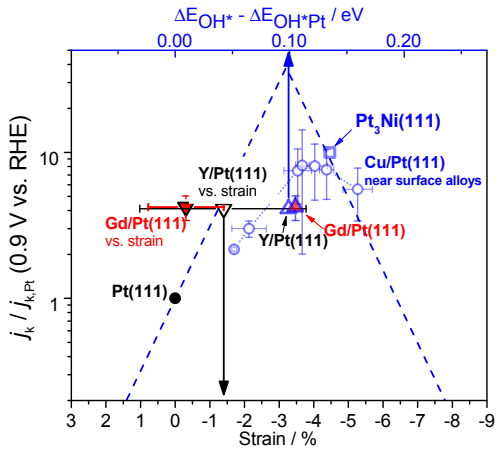

Figure 3.6: *Oxygen reduction Sabatier volcano as a function of lateral strain (lower x-axis) and OH binding energy (upper x-axis), relative to Pt(111). The relation between the strain and shift in OH binding energy is based on DFT calculations.*[58] *The blue dashed line is the thermodynamic Sabatier analysis, representing the upper limit to activity, neglecting additional kinetic barriers.*[63] *The activity of Y/Pt(111) and Gd/Pt(111) are plotted versus their measured strain on the bottom axis (down-triangles with black edge), and versus the voltametric shift on the top axis (up-triangles with blue edge). The error bar in the strain corresponds to the microstrain. For comparison, the blue circles represent the activity of the Cu/Pt(111) near surface alloys*[57] *and the square vacuum annealed $Pt_3Ni(111)$,*[55] *both plotted as a function of voltammetric shift for OH adsorption, which we assume to be equal to the shift in OH binding. The Gd/Pt(111) activity enhancement is based on several activity measurements of both Gd/Pt(111) and Pt(111) at 23°C, whereas the Y/Pt(111) activity enhancement is based on a single measurement of Y/Pt(111) and Pt(111) at 60°. Reprinted from Paper II*[67]

Finally, the correlation with CO binding energies may be compared with either electrochemical CO desorption experiments or temperature programmed desorption experiments. In the following, a more detailed study of CO adsorption is presented and compared to recent CO TPD experiments.

3.2.2 TPD with strain effects

The trend in CO binding energies versus strain may also be compared to TPD experiments to benchmark the accuracy of the DFT description of reactivity versus strain to experiments. In order to accomplish this, a set of simulations of the TPD spectra was carried out based on calculated trends in CO binding energies. These simulations are

presented in this section.

The adsorption/desorption energies of CO was calculated on Pt(111) in a detailed ensemble of coverages, θ, and with various lattice strains. The strain was in the range from -6% to 0%, and the CO coverages were 1/6, 2/9, 1/4, 1/3, 4/9, 1/2, 5/9 and 2/3 monolayers set up on surfaces represented with non-orthogonal 3×3, 2×2, or orthogonal or non-orthogonal 3×2 super cells. Several possible adsorbate surface arrangements were checked for the coverages 2/9, 1/3, 4/9 and 1/2.

The differential adsorption energy (See figure 3.7b) is defined as:

$$\Delta E^{diff}(\theta) = N \frac{\partial E^{int}(n, N)}{\partial n} = \frac{\partial E^{int}(\theta)}{\partial \theta} \tag{3.9}$$

where ΔG^{int} is the integral adsorption energy, which is:

$$\Delta E^{int}(n, N) = \left(E(n, N) - E_*(0, N) - n \cdot E_{CO(g)} \right) / N \tag{3.10}$$

Here n is the number of CO molecules on a surface with N surface atoms in the unit cell. If ΔE^{int} is plotted versus the coverage $\theta = n/N$, surface configurations with $\Delta E^{int}(\theta)$ above a line between any two other configurations will be unstable. In reality they will not exist, but the surface will have domains of the two other surface configurations, and the average $E^{int}(\theta)$ of the surface will be on the line between the stable points. Practically, $E^{int}(\theta)$ can be used to construct a phase diagram for the surface. The convex hull of the $E^{int}(\theta)$ ensemble is therefore used to select the relevant subset of integral free energies. The calculated $E^{int}(\theta)$ from DFT are shown in figure 3.7a together with an interpolation of the convex hull of $E^{int}(\theta)$.

In figure 3.7b the differential adsorption energy is shown. Notice that the differential energy of the unstrained surface increases gradually with increasing coverage. This trend is expected, since there is a positive interaction energy between the CO molecules. The differential adsorption energy in the low coverage limit is around 0.32 eV higher on the surface which is 6% contracted, compared to the one with a relaxed lattice constant. At $\theta = 1/4$, which is shown in figure 3.5a, the shift is 0.33, and for this unit cell size, the d-band shift of the clean surface is also shown in figure 3.14b. The current values corresponds to a weaker shift than previously reported values from DFT calculations on strained surfaces[70], which was up to 0.25 eV at just -3.2% strain.

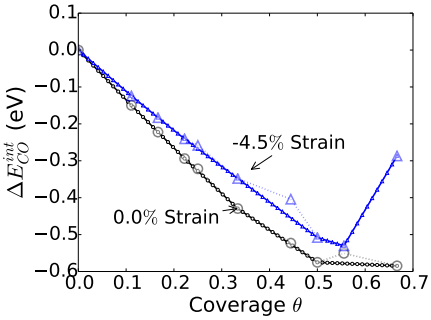

(a) *Integral adsorption energy $E^{int}(\theta)$ from DFT (large markers) and the linear interpolation of the convex hull of $E^{int}(\theta)$ (small markers).*

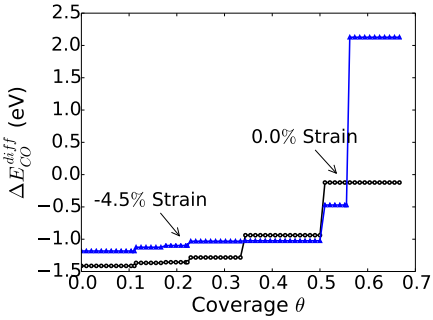

(b) *Differential adsorption energies.*

Figure 3.7: *Integral and differential adsorption energies of CO on relaxed Pt(111) and on Pt(111) with 6% compression.*

For the contracted surface, there is a much sharper increase in differential energy at $\theta = 0.5$ ML. The reason is most clearly understood from observing the integral binding energies, where the 0.5 ML configuration is very stable.

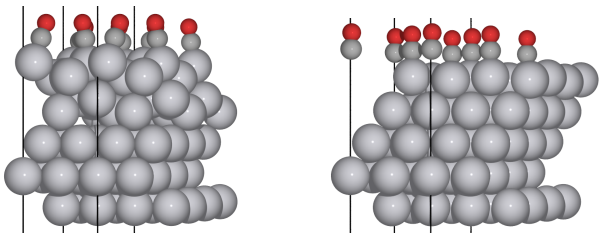

(a) *Side view of the system where the lattice is contracted 6%.*

(b) *Side view of the relaxed system.*

Figure 3.8: *Side view of compressed and relaxed Pt(111) surfaces covered with 0.5 ML CO in a 2×2 super cell.*

The relative stability of the 0.5 ML configuration comes from a subtle reconstruction of the Pt(111) facet. When CO adsorbates are on neighbouring Pt atoms in rows or lines across the surface, the Pt-atoms below are raised out of the plane, while the rest of the plane moves very slightly into the surface. This reconstruction is most pronouced on the

contracted surfaces as clearly observed from comparison between the structures in figure 3.8a and 3.8b. In some cases, the CO molecules point also towards each other on the more contracted surfaces, possibly adding another stabilizing effect.

In order to simulate TPD spectra, the desorption energy was calculated as minus the differential adsorption energy, i.e $E^{des}(\theta) = -E^{diff}(\theta)$. Two approaches to simulating the TPD spectra may be chosen: **1)** Most commonly, a lattice Monte Carlo-based simulation is chosen. Such a simulation randomly removes particles from sites on a grid, with probabilities based approximated desorption energies. These desorption energies are introduced through pair potentials with neighbouring particles, and they produce simulated spectra that resemble experiments.[71–73] However, it is tricky to include the line-reconstruction effect, because it requires identification of adsorbate-lines and the length of such groups would be an unknown parameter. It was not feasible to investigate this parameter further with DFT, so instead a more simple TPD simulation was performed: **2)** The TPD spectra can be assumed to follow first order desorption described by

$$-\frac{d\theta_s}{dT} = \frac{\nu}{\beta} \exp\left[-E_s^{des}/k_B T\right] \theta_s(T) \tag{3.11}$$

where β is the ramp rate (2 K / min) and ν is the attempt frequency, which is $\frac{k_B T}{h}$. In the simple approach to TPD-simulation, E_s^{des} is not explicitly a function of θ or T. Instead, the simulated spectra are the result of the summed contribution from each coverage, treated as distinct sites, s, each with a constant E_s^{des}. The per site coverage, θ_s, is a function of the temperature, which it enters as[74]

$$\theta_s(T) = \exp\left[F(T)\right] \tag{3.12}$$

$$F(T) = \frac{\nu}{\beta} \int_0^T \exp\left[-E_{des}/kT\right] dT \tag{3.13}$$

The disadvantage of this approach, compared to 1), is that configurational entropy is not included. However, it turns out that the main trends are still captured. Two examples of simulated TPD spectra are shown in figure 3.9.

The shift in E^{des} in the low coverage limit is around 0.32 eV, and therefore the right limit of the simulated desorption feature shifts by around 110°C. The overall trend from the computations are in accordance with the trends in the measured TPD spectra, which makes it likely that a similar phenomenon is responsible for the trends in the experiments.[75]. The shift in CO binding energy, measured by TPD is 0.55 eV, which larger

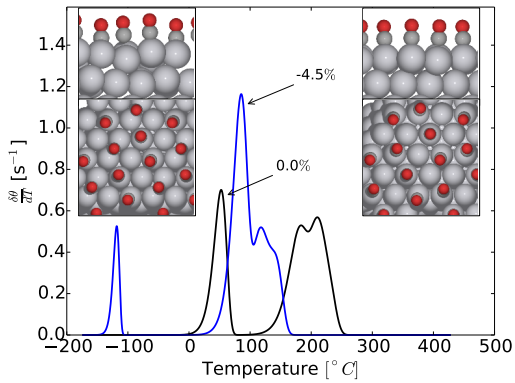

Figure 3.9: *TPD spectra simulated using equation 3.11, where adsorption energies are from DFT calculations on strained Pt(111) surfaces. The insets show views of the most stable configuration with 0.5 ML CO adsorbed, on surfaces with −4.5%s and 0% strain on the left and right, respectively. Notice how the CO molecules on the contracted surface have drawn Pt atoms out of the surface plane.*

than expected. As shown in figure 3.5a, the DFT calculations correlate a shift of 0.3 eV with approximately 5% contraction of the Pt(111) lattice, which is close to the contraction of the Pt-Pt distances in bulk Pt_5Gd. Previously reported TPD experiments on a strained surface with no ligand effects also shown larger shifts in binding energy than expected from DFT calculations [70].

The Pt-skin is most likely thinner on the lanthanide/Pt(111) samples in UHV, since they have not been exposed to an electrolyte, that can leach out the lanthanide from the outermost layers. Since gadolinium atoms were not included explicitly in the calculations, it is uncertain, what role Gd ligands may play on the adsorption energies. [75]

3.2.3 Stability of strained Pt

A thick Pt skin can to a first approximation be modelled as bulk Pt, under in-plane strain. A quick calculation was carried out to get the elastic properties for platinum in and out of the (111) plane.

From figure 3.10 it is observed, how much strain/contraction in the surface plane is compensated by contraction/strain out of the plane. The destabilisation due to strain is plotted in energy per atom in the inset. Taking Pt_5Gd as an example, a Pt bulk matching the strain of the alloy feels an increase of around 0.1 eV in potential energy per atom.

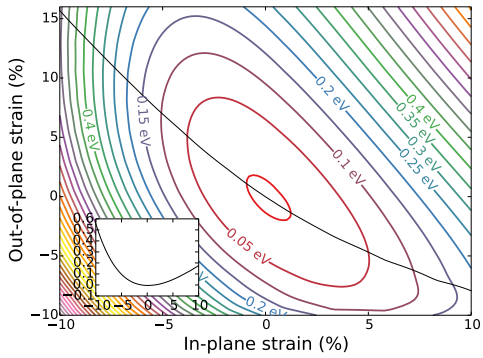

Figure 3.10: *Contour plot of the potential energy per atom of bulk Pt strained in the (111) plane and out of the plane. The black curve marks the most relaxed state, while constraining the in-plane lattice constant. The inset shows the potential energy vs. in-plane strain along the curve, where the out-of-plane strain is relaxed.*

A thick surface should therefore be more likely to relax the contraction, while forming defects and domains. Platinum skins of just a few atomic layers may be constrained from such reconstructions. In order to investigate platinum skins of just a few atomic layers, DFT calculations of reconstructed surfaces with varying in-plane strain were performed.

3.2.4 Reconstructed Surfaces

Reconstructed surfaces were modelled with up to three atomic surface layers. The layer representing termination of the bulk, i.e. the fourth layer from the surface, was a constrained Kagomé layer (See Fig. 3.2a).
The atomic structures were based on Pt(111) slabs with 6 atomic layers in 2×2 super cell. The bottom three layers were always constrained FCC(111) layers to represent the bulk crystal, while the top three layers were relaxed to represent the surface. The top three layers were varied in combinations of FCC(111) layers, Kagomé layers. A side view of the slab with two free Kagomé layers is given in figure 3.11.

A $\sqrt{3} \times \sqrt{3}$ reconstruction was also tried, since studies on Pt_5Ce and Pd_5Ce indicate that this structure might be present[76]. The modelled structure had two 30° rotated FCC(111) layers with 3/4th the normal atomic density, as shown in figure 3.13. These

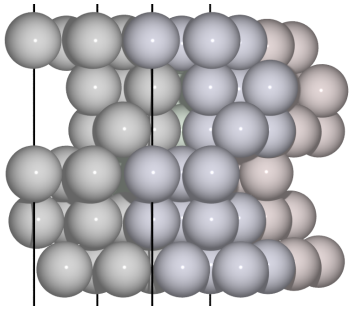

Figure 3.11: *This atomic surface model has a full FCC(111) layer on top of three Kagomé layers. The bottom three atomic layers were constrained to represent the bulk. All spheres represent Pt atoms, and the variation in color assigns the atoms to different repetitions of the unit cell.*

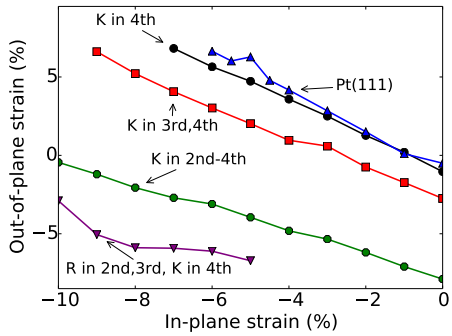

Figure 3.12: *Out-of plane strain versus in-plane strain of the outer two layers of relaxed surfaces. The K label is for Kagomé layer and the R label is for the rotated and strained $\sqrt{3} \times 3$ FCC layer.*

layers match the regular FCC(111) lattice with a Pt-Pt distance $2/\sqrt{(3)}$ times that of the FCC(111) lattice.

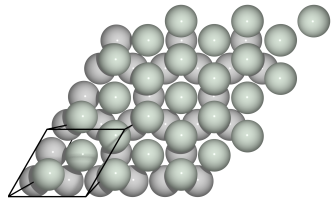

Figure 3.13: *Model of the rotated FCC(111) layer on top a regular FCC(111) layer. The rotated layer has a 30 degree angle and 3/4 of the atomic density, relative the FCC(111) layer.*

Surface geometries were relaxed using the BFGS LineSearch algorithm within ASE[69] until maximum forces on the atoms were less than 0.05eV/Å. Relaxation of regular FCC(111) surfaces usually reveal a small contraction of outermost one or two interplanar distances. Applying an in-plane contraction to the lattice result in an increase in the interplanar distances of the relaxed surface. This can be observed in Figure 3.12 for the top two atomic layers in the investigated surface structures. Comparing the different types

of layers, it appears that a lowered atomic density in the atomic surface layers also result in a contraction of the interplanar distances. Recent SSXRD experiments (See section 3.1.4) show rather large out-of plane contraction in Gd/Pt(111) samples with very modest in-plane contraction. This is in accordance with DFT results given the presence of Kagomé layers in the near-surface. In the following, the consequence for reactivity from the reconstructions is explored.

Reactivity

Figure 3.14a shows the adsorption energies of OH plotted versus strain, on the various reconstructed Pt surfaces and also an unmodified five layer Pt FCC(111) slab for reference. On most of the various surface structures, there is a clear trend of destabilization of the adsorbate as the contraction is increased.

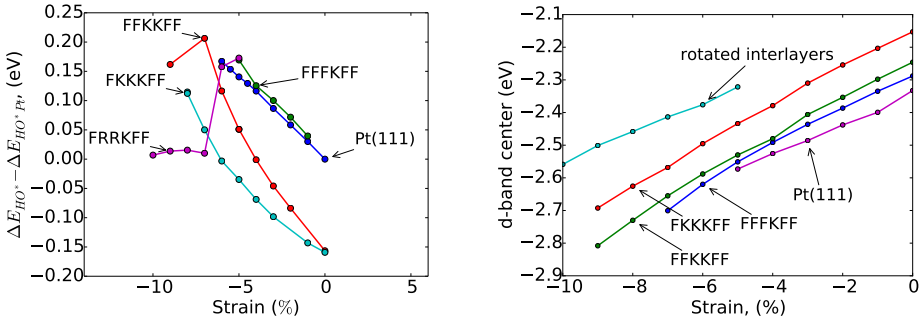

(a) *Adsorption energies versus strain.*

(b) *d-band centers of the top three atomic layers versus strain, from DFT calculations.*

Figure 3.14: *Calculated d-band centers and adsorption energies on reconstructed Pt(111) surfaces. The labels denote the type of layer ordered from the surface and down. F denotes regular FCC(111), K denotes Kagomé layers and R denotes the rotated and strained* $\sqrt{3} \times 3$ *FCC(111) layer.*

As shown in figure 3.14b, the d-band of the surface atoms consistently shifts down with more lattice contraction, for each of the structures. Changing the structure causes a d-band shift in itself, which seems to be correlated with the atomic density. These results are consistent with the d-band model[20,61]: As the lattice contracts, d-orbital overlap increase which strengthen the interaction and broadens the d-band. The d-band of Pt is almost fully occupied, and the occupation of the bands do not vary with strain. With this

constraint, the broadening of the d-band must lead to a down-shift of the d-band, which results in an increase in the filling of the anti-bonding states. Occupying the anti-bonding states result in a destabilization of the adsorbate binding to the surface.

It is evident from the binding energies in figure 3.14a, that the surface structures with regular FCC(111) termination tend to be the most noble. Surfaces with Kagomé layers in the near surface layers bind more strongly. The increase in reactivity is most likely due to an upward d-band shift due to lower atomic density in the Kagomé layers, which causes less d-band overlap.

Since all types of surface reconstructions considered here cause large increases in reactivity compared to Pt(111), the reconstructions would have a detrimental effect on catalytic activity. The most noble surface would be a regular FCC(111) structure with the highest possible amount of in-plane contraction.

3.3 Discussion

DFT calculations presented in section 3.2.4 show that surface reconstructions including near surface Kagomé layers and rotated layers cause a greatly increased reactivity, relative to the regular FCC(111) facet, even at larger compression values. This does not correlate well with the observation, that all the Pt-lanthanide alloys yields an enhanced ORR activity relative to Pt(111), because it is expected that a slightly more noble surface will be more active for ORR catalysis.

SSXRD experiments do not rule out the presence of Kagomé layers in the Pt skin, but they also suggest that exposure to electrochemistry causes a great deal of strain relaxation and domain formation on the surface. A small average contraction is still observed in the SSXRD experiments. This is in accordance with the expectations from computations, since the formation energy exhibits a harmonic potential in the strain/contraction space, meaning small strain or contraction only destabilizes by a very small amount while the energy increases quickly as strain or contraction increases beyond a certain threshold. A minority of domains with a moderate compressive strain may still be responsible for the enhanced ORR activity.

The most simple hypothesis on the optimum in activity enhancement around Pt_5Tb is that the Pt_5Tm and Pt_5Dy alloys are too weak binding. However, the hydrogen voltam-

metric shift indicates that these alloys are in fact more reactive than Pt_5Tb and the DFT calculations show that perturbations to the binding energy of H* scales with the perturbation to the binding energy of HO*. The voltammetric shift for hydrogen adsorption, that has been measured using cyclic voltammetry by M. Escudero-Escribano, may therefore be used to calibrate the estimation of OH binding energies and strain. This calibration of the strain and OH binding is plotted in figure 3.15.

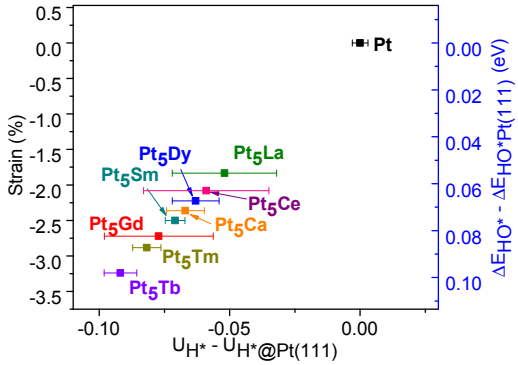

Figure 3.15: *Calibration of the OH binding energy and strain to the experimentally determined shift in hydrogen adsorption, $U_{H*upd} - U_{H_{upd}*Pt}$. Reprinted from paper I.*[58]

The right axis in figure 3.15 shows the estimated OH binding energies of the alloys, based on a transformation using the linear fit to the ΔE_{OH} versus ΔE_H, obtained from DFT. The H_{upd}-calibrated contraction values are all smaller than the values expected from a direct match of a Pt(111) skin on the (001) facets of the alloy lattices. Particularly, the alloys with the largest mismatch, exhibits the largest apparent strain relaxation. The mechanism of the strain relaxation still remains unclear. However it seems to be clear that there is a limit to how much strain and reactivity can be tuned by the strain effect alone. Since strain is correlated with reactivity towards both hydrogen and OH, the activity enhancement also correlates with both. The ORR activity enhancement is plotted versus the voltammetric shift of hydrogen adsorption in figure 3.16a and versus the calibrated strain in figure 3.16b. In plots, the top axis shows the calibrated OH binding energy, towards which the Sabatier volcano and the data from Cu/Pt(111) near surface alloys are plotted.

Assuming the reactivity toward hydrogen and OH are directly correlated to the strain under electrochemical conditions, the volcano contains all the Pt-lanthanides including

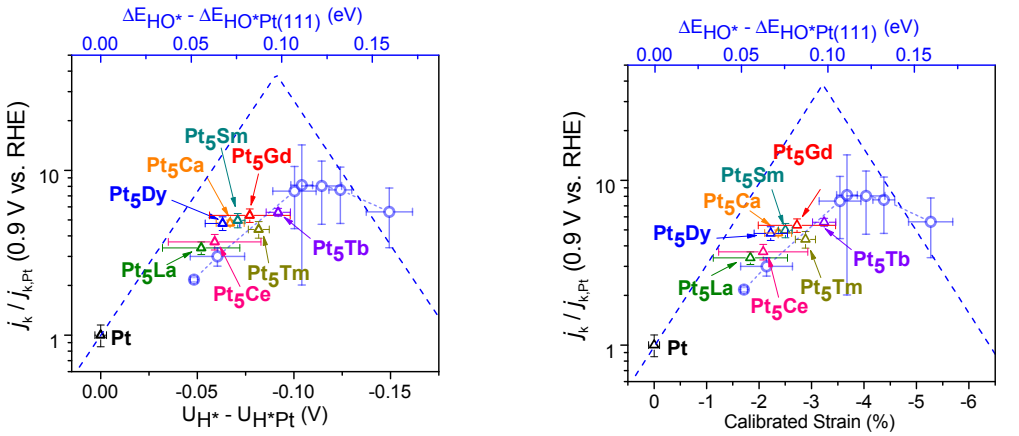

(a) *The voltametric shift for hydrogen adsorption is on the bottom axis.*

(b) *The strain, calibrated from the voltametric shift is on the bottom axis.*

Figure 3.16: *Sabatier volcano plots with oxygen binding energies estimated using DFT correlation to hydrogen binding energies and the hydrogen binding energy shift from experiments. Reprinted from paper I.*[58]

Pt_5Tm, Pt_5Dy on the strong binding leg. The correlation with the activity enhancement is close to the trend line of the Cu/Pt(111) near surface alloys. The electrochemical measurements, correlated with the trends in reactivity vs. strain obtained from DFT, therefore suggest that the limit for the strain effect has been reached around Pt_5Tb, by moving through the lanthanide series, and the limit with stability to cycling is reached around Pt_5Gd.

It is tempting to conclude an "optimal strain" around 3% from figure 3.16b, but the strain is based on the voltammetric shift, which is an average value over the polycrystalline sample, while the activity enhancement may come from a minority of domains with a different strain. The average strain, calibrated from the voltammetric shift and DFT is also not in agreement with the SSXRD experiments, but unfortunately it is not possible to conclude if either the DFT description of strain effects or the SSXRD experiments are subject to an error. The measurements of HO^* an H^* voltammetric shifts on single crystals tend to agree with the DFT predicted scaling in hydrogen binding energy versus OH binding energy. This adds confidence that the scaling between adsorption energies are accurately captured by DFT, although the strain values versus shift in adsorption energy may be less accurate. This is understandable from an electronic structure viewpoint, since the binding energies of all adsorbates is related to the shift in the d-band, while the

d-band changed by the orbital overlap due to lattice strain. A possible deviation may exist between real and computed d-band shift, and the amount of changed orbital overlap causing the shift.

3.4 Summary

The lanthanide elements have the property, that they can be used to tune the lattice constants of the bulk Pt-lanthanide alloy, on which a contracted platinum skin forms. DFT calculations shown that a contraction of the Pt surface cause a decrease in reactivity, in accordance with the d-band model, and this decrease in reactivity is beneficial for ORR catalytic activity. Extensive experimental efforts have been invested in understanding the Pt-lanthanide systems, and computational efforts have been applied to support the theory and understand the observed trends.

In this chapter, binding energies of H^*, HO^* and CO^* on strained and reconstructed Pt(111) surface models have been correlated with experimental trends in activity and reactivity for Pt-lanthanide alloys. These correlations show that it is likely that an amount of strain relaxation occurs in the Pt-skin so the entire skin do not match the alloy. The DFT calculations correlated with the enhanced activity also show is unlikely that the active sites on the surface has Kagomé layers or other reconstructed geometries in the near surface.

There is not complete accordance between all experimental trends and the computational trends in strain versus reactivity and activity, so as to quantify the amount of strain present in the Pt-skins. Particularly the SSXRD shows smaller average in-plane strain values, than calibrated from the voltammetric shift of hydrogen adsorption and DFT. It is possible that the size of the strain effect is not accurately captured by DFT.

Scaling between the perturbation to adsorption energies of different species due to strain, appear to show consistency between experiments and DFT calculations. This includes the correlation with electrochemical experiments and calculated H^* and HO^* binding, (See section 3.2.1).

The trend in binding energies of CO^* and simulated TPD spectra were compared to CO-TPD experiments, (See section 3.2.2). An experimentally observed tendency to narrowing and downward temperature shift of the TPD spectra with increasing contraction

was reproduced by the simulations. The shift in binding energy from TPD is 0.55 eV, whereas calculations predict a shift of only 0.2 eV to 0.3 eV at low CO coverages. The reason for this may is likely the presence of ligand effects, which are unaccounted for in the current DFT calculations.

3.5 Outlook

The DFT calculations presented in this chapter have only concerned effects from varying the catalyst surfaces. Water has not been included, and thus any strain or surface reconstruction effects that are coupled to the electrolyte have not been computed. It is usually done by including one or two relaxed layers of hexagonal water structure, to provide the hydrogen bonds, which usually account for a stabilization of 0.3 eV on the HO* intermediate. Meanwhile, improvements of the models are being developed and tested to include the electrolyte more explicitly, thereby modelling the entire interface instead of only the surface. More on this subject can be found in chapter 5.

Several questions on the structure of the Pt-lanthanide alloy surfaces and the reasons for their enhanced activity are still open. More experimental measurements of strain, d-band shift, reactivity, ect. are desired to benchmark the DFT calculations as well as to advance understanding of the catalyst surfaces. It is important to keep in mind, however, that a minority of surface sites can have optimal properties for catalysis and be responsible for most of the activity enhancement, while most UHV and electrochemical experiments only capture the average properties of the entire surface.

Despite the open questions, the known Pt-lanthanide catalysts are very promising for applications in PEM fuel cells. They have yet to be produced by up-scalable methods, however, that are suitable for industry. In addition, the existing design rule of lattice tuning suggest that ternary alloys of such as $Pt_{10}TbSm$, $Pt_{10}TbGd$ or $Pt_{10}GdSm$ could be even more active and stable than the alloys, that are already tested.

4. Catalyst Surfaces for Hydrogen Electrodes

4.1 Introduction

In this chapter, recently discovered catalysts for the hydrogen evolution reaction are investigated. At the time of initiation of the PhD work, a several new non-precious catalysts had been discovered for the hydrogen evolution reaction, (HER). Only a few years earlier, almost all useful catalysts for this reaction had been based on precious metals such as platinum. In addition, there are still no non-precious catalysts for the reverse reaction, the hydrogen oxidation reaction, (HOR), which is the half cell reaction on the hydrogen electrode in the PEM fuel cell. For fuel cell applications, it would be beneficial, if a non-precious catalyst could be found to work on the hydrogen side as well, so that the scarce platinum could be avoided.

Studying these HER catalysts using DFT calculations, therefore had one primary goal: To improve the understanding of the newly discovered non-precious HER catalysts, and identify active sites. Secondary interests was to study the reason, why the non-precious HER catalysts do not catalyse the hydrogen oxidation reaction, and possibly to search for alternative HER/HOR catalysts.

The reactivity of molybdenum di-carbide and mono-boride and nickel di-phosphide and a few other metal phosphides are addressed. First a brief introduction is given to the hydrogen evolution/oxidation reaction, and thereafter calculations and results are presented and discussed.

4.1.1 Fundamentals of hydrogen evolution and oxidation

The hydrogen evolution reaction, (HER), is the reverse of the hydrogen oxidation reaction, (HOR), which was visited in the introduction. HER is interesting for reverse operation of fuel cells, for industrial electrolysis and for solar hydrogen production [77,78]. It can be divided into three elementary reaction steps. The first is proton discharge, known as the

Volmer step:

$$H^+ + e^- + * \rightarrow H^* \tag{4.1}$$

The hydrogen desorption step is usually viewed as either the Heyrovski step (4.2)

$$H^+ + e^- + H^* \rightarrow H_2 \tag{4.2}$$

or the surface combination step, also known as the Tafel reaction: (4.3)

$$2H^* \rightarrow H_2 + 2* \tag{4.3}$$

The fundamental difference between the Heyrovski and the Tafel reactions is that only the Heyrovski reaction is an *electrochemical* elementary step. Experimental studies often conclude which one is rate limiting, through measurement of Tafel slopes, which are the slope of the log to the current, $log(j)$, plotted versus the over-potential, η. However this is a very indirect method, to determine what the rate limiting step is. In theory, the distinction between the Tafel and the Heyrovski does not always have to be clear-cut on the atomic scale, since the transition state in the Heyrovski step may be more or less in contact with the surface.

A prerequisite for a good catalyst is a moderate hydrogen binding energy, which can be understood by writing up the rate expressions for proton adsorption and hydrogen desorption.[79] This reveals that a binding free energy of 0.0 eV is optimal.

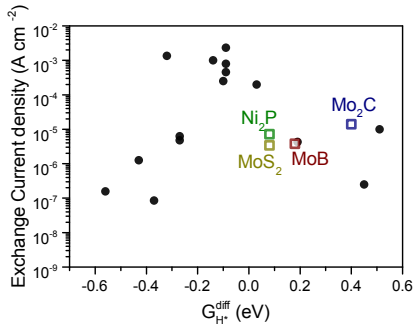

Figure 4.1: *Trends in Exchange Current Density versus hydrogen binding energy. The black dots are data compiled by Nørskov et al.,*[80] *and exchange current densities for Ni_2P, Mo_2C and MoS_2 are compiled by Morales et al.*[81–83]*, while binding energies for Ni_2P and Mo_2C are from this work, and binding energies for MoS_2 are from Hinnemann et al.*[84]

Plotting the measured exchange current densities from various catalysts versus the binding free energy for hydrogen on the catalysts also show a rough trend, as shown in figure 4.1. Noble metals such as platinum are the best catalysts. However, the noble metals are expensive and large scale application of would be challenged by the scarcity of these elements [85,86].

4.1.2 Computational Studies on HER

DFT has aided a higher understanding of trends in the electronic structure of the metal surfaces in a framework of simple electronic structure models [20]. The correlations between hydrogen binding energy, activity and the position of the transition metal catalysts in the periodic table was also understood in this framework [80].

The clear correlations and the understanding of the trends in electronic structure provided predictive power, so new hydrogen evolution catalysts could be developed. The first example of rational catalyst design appeared for HER, which was the edge site of MoS_2 [84]. It is also experimentally verified, that the HER rate scales with the number of available edges sites on MoS_2, and this corroborates the DFT result. [82] A large number of studies have been done on MoS_x based HER catalysts, and integration of them in devices for solar hydrogen production. Since only the edge site is active, a lot of nano engineering efforts can be spent optimizing the MoS_x HER catalysts. [87,88] MoS_2 is a reasonably active catalyst, although not as active as platinum and it is stable only in acid. It also does not catalyse the reverse reaction (HOR), which there are currently no non-precious catalysts for. The reason why the non-precious HER catalysts are not active for HOR is not entirely clear. The most simple explanation is that they are more reactive towards oxygen and OH, and that OH covers the surface above the equilibrium potential for hydrogen.

In practice, the free energies are calculated using a few adsorbate configurations with varying hydrogen surface coverages. The differential free energy, $\Delta G^{diff}(\theta_H)$, is the energy difference of adsorbing a single hydrogen. In analogy with section 3.2.2, the free adsorption energies are calculated at 0K using:

$$\Delta G^{diff}(\theta) = N\frac{\partial G_{int}(n,N)}{\partial n} = \frac{\partial G_{int}(\theta)}{\partial \theta} \tag{4.4}$$

$$\Delta G^{int}(\theta) = (G(n,N) - G_*(0,N) - n\cdot[G_{H_2(g)/2} - eU_{RHE}])/N \tag{4.5}$$

$$G = E + ZPE - TS \tag{4.6}$$

ΔG, are the free energy differences calculated using DFT and thermodynamic tables, $\theta_H = n/N$ is the hydrogen coverage, n is the number of atomic H on the surface and N is the number of surface atoms or sites.[89] The integral free energies are obtained from DFT calculations, and then filtered, so that only the relevant states are included in the ensemble for later analysis. In a plot of ΔG^{θ} versus θ, a point above a line connecting the any two other points will only represent an unstable state, since a surface with domains of the two other states will be lower in free energy. Therefore the relevant subset is found using the convex hull of $\Delta G^{int}(\theta)$. The differential energy is obtained by taking the derivative of the relevant subset of the integral energies, as written in equation 4.4.

In order to better understand the descriptor, it is helpful to review computational results on the binding energies of hydrogen on the two well known HER catalysts, Pt and MoS_2. Figures 4.2 shows the free energies calculated for the MoS_2 edge[84] and for Pt(111). Even though they are both active for HER, the difference between them is clear. Adsorbates do not show significant repulsive interaction on Pt(111), whereas there is a strong repulsive interaction for hydrogens at MoS_2. On Pt(111) the differential adsorption energy is close to zero regardless of coverage (between 0 ML and 1 ML). The minimum integral adsorption energy is 0.5 ML, and so it can be concluded that Pt(111) has a coverage around 0.5 ML at equilibrium.

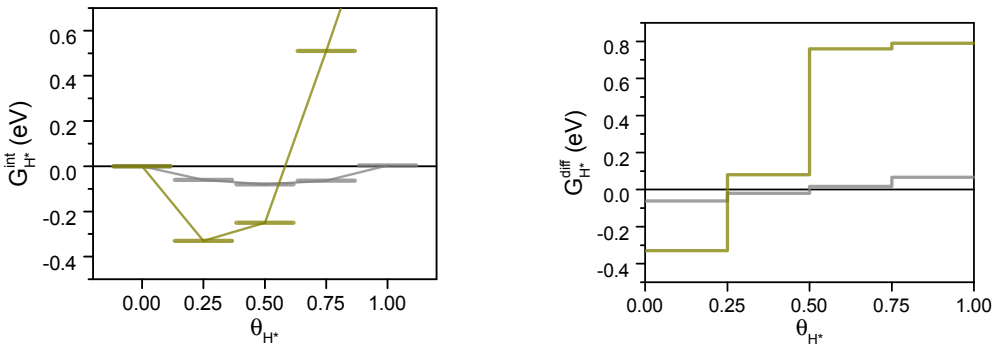

(a) Integral Free Energy

(b) Differential Free Energy

Figure 4.2: *The free energy of hydrogen adsorption on Pt(111) (Gray lines) and on MoS_2 (Yellow lines), the latter from Hinnemann et al.*[84]*, and the first calculated with GPAW in the real space basis mode. The integral free energy reveals the most stable coverage at equilibrium with H_2 (g), and the differential free energy shows the adsorption energy depending on the coverage.*

From the integral adsorption energy or MoS_2 is can be concluded that the surface has 1/4 ML coverage of hydrogens, and the differential adsorption energy between 1/4 ML and 1/2 ML is 0.08 eV. This is not far from the optimum, and since an over-potential stabilises ΔG^{diff} with $-eU_{RHE}$ [48], MoS_2 could have an over-potential as low as 0.08 V for HER.

Finding a material with the optimal differential binding energy is a required for an optimal catalyst, but not necessarily sufficient. The barriers between the elementary steps in reality limits the rate, although the activation energies may scale with one or more adsorption energies of the intermediates involved.

Determining, if the Tafel or Heyrovski mechanism dominates, is not trivial due to the difficulties in distinguishing the reaction steps through experiments and calculation of electrochemical reaction barriers correctly from first principles by have turned out to be very challenging [90]. It is known from experiments, that the pH may have a large effect on the barrier of electrochemical reaction steps such as proton adsorption [91]. This is an indication, that the theory must account for the pH effect on the electrochemical interface in order to make correct barrier calculations. Developing simulations that treat the full electrochemical interface explicitly in DFT, and accounts for pH effects is now a frontier in atomic scale modelling [92]. One such model is the topic of chapter 5 in this thesis.

This chapter

The following section presents calculations in search of the active site for HER catalysis on the molybdenum carbide and molybdenum boride surfaces. The approach was using integral binding energies to construct surface phase diagrams, thereby calculating the state of the surface under operating conditions. Then the differential hydrogen binding energy is used as a descriptor for activity. Section 4.3 present calculations with the same method which successfully identifies facets of the Ni_2P crystal, which have more optimal reactivity for hydrogen evolution, than the previously studied active sites. In addition to adsorption energies, activation barriers for the Tafel reaction are also calculated on the newly found facets. The last section (4.4) in this chapter presents a small screening study in search of other metal phosphide catalysts.

4.2 Molybdenum Carbide and Boride Catalysts

4.2.1 Background

Prior to the beginning of this PhD work, Vrubel et al.[93] demonstrated the HER activity of MoB and Mo_2C in both alkaline and in acid, which has been followed up by studies on different morphologies of Mo_2C.[94,95]. The exchange current densities were similar at pH = 0 and pH = 14 for both materials indicating that they have similar catalytic efficiency for proton and water reduction. The over potentials were between 210 mV and 240 mV, which is about 100 mV more than platinum. Compared to Molybdenum sulphides, the MoB and Mo_2C exhibits better stability in alkaline solutions, which makes them interesting for some applications. Equally high activities for HER in such wide pH range is not very common for HER catalysts.[96]

The active sites and mechanism are unknown for the two catalysts, but from the Tafel slopes, it was hypothesized that the rate was not limited by the Volmer reaction (4.1), in contrast to MoS_x thin film catalysts.[78] Energetics provided by DFT calculations could possibly provide an explanation using the differential binding energy as a descriptor for HER activity, as done in the past for transition metal surfaces.

The approach was to calculate the hydrogen adsorption energy on selected facets of the materials, which were active according to the experiments. The synthesized phases were β-Mo_2C which has the crystal structure space group P_{63} / mmc (number 194), and the cuboid α-MoB. The latter has the space group $I4_1/amd$ (number 141)[97]. Figure 4.3 shows the unit cells of β-Mo_2C and α-MoB.

A number of facets and terminations of these structures might be relevant for the investigation. The most close packed facets are usually the least reactive, and these were therefore selected for the calculations. Both structures may be terminated by either molybdenum or their respective alloy element. In both alkaline and acidic solutions the Mo_2C was reported to be inactive until after an initial activation period. The MoB catalyst required an activation period when in acidic solution, but not in alkaline solution. This could be an indication that the surface needs to be reconstructed or oxidised to form the active sites.

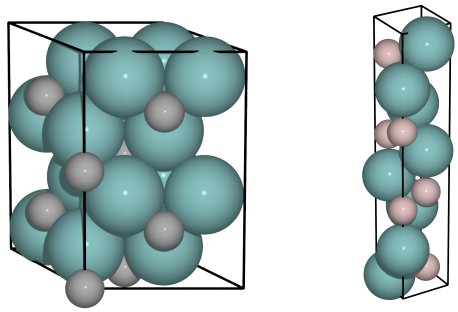

(a) β-Mo_2C (b) α-MoB

Figure 4.3: Unit cells of molybdenum carbide and molybdenum boride. Molybdenum atoms are represented by cyan spheres, carbon atoms by gray spheres and boride atoms are represented by pale pink spheres.

4.2.2 DFT Calculations

The procedure to understand the reactivity of these compounds were to first determine the surface coverage of hydrogen and oxygen under the relevant macroscopic conditions, and then use the differential free energy at the relevant coverage as a descriptor for activity. A surface phase diagram was constructed for each surface from all the states using integral free energies calculated using DFT and the computational hydrogen electrode. Now that states with oxide species are included in the ensemble, the integral free energies in figure were written:

$$\begin{aligned} \Delta G^{int} &= \Delta E + ZPE - TS - n_H \cdot G^0_{H_2}/2 \\ &- n_O \cdot (G^0_{H_2O} - G^0_{H_2}/2) + (n_H - 2 \cdot n_O) e U_{RHE} \qquad (4.7) \\ \Delta E &= E(n_O, n_H) - E(n_O = 0, n_H = 0) \qquad (4.8) \\ G^0_{H_2} &= (E_{H_2} + ZPE_{H_2} - TS_{H_2})/2 \qquad (4.9) \\ G^0_{H_2O} &= E_{H_2O} + ZPE_{H_2O} - TS_{H_2O} \qquad (4.10) \end{aligned}$$

The entropy of adsorbates on the surface was assumed to be negligible. The reference state for water was gaseous at 0.035 bar, which is in equilibrium with liquid water at standard conditions, and the zero point energies were taken from Nørskov et al. [80].

A phase diagram is shown for Mo_2C in figure 4.4, where G^{int} is plotted versus the potential versus RHE for the most stable surface configurations. Notice in the phase

diagrams, that the slopes of $G^{int}(U_{RHE})$ is due to the last term in equation 4.7 and the offsets are G^{int} at 0 V versus RHE.

Mo_2C (001) facet

In past DFT studies on this compound[98], the Mo2C (001) surface were calculated with a Mo-termination, based on previous theoretical and experimental studies[99]. The same close packed surface was used in the present work.

The surface was modelled using the 1×1 unit cell with oxygen coverages θ_O from 0 to 1.5 ML and hydrogen coverages from 0 to 2.5 ML. States with $\theta_O > 1$, had oxygen diffused into the interstitials below the outermost atomic surface layer. Combinations of oxidized surfaces with hydrogen present on top Molybdenum or as OH was also tried.

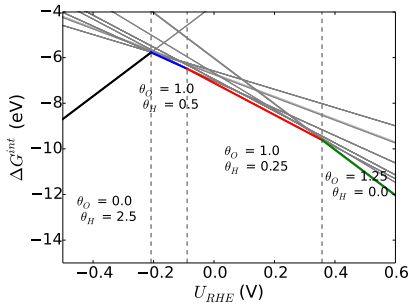

Figure 4.4: *Surface phase diagram of Mo_2C (001). The lines shows integral free energies, G^{int} of the most stable surface configurations as a function of potential versus RHE. The labels denote hydrogen and oxygen coverages, $\theta = n/N$, where $N = 4$ surface atoms.*

According to the calculated surface phase diagram in figure 4.8a, the surface is oxygen covered surface at 0 V versus RHE, with 1/4th of the oxygen atoms binding a hydrogen as shown in figure 4.5, left panel. Under oxidising conditions beyond +0.4 V versus RHE, oxygen atoms were also found to move into the interstitials under the first surface layer. The activation process observed for Mo_2C might be related to incorporation of oxygen atoms into these interstitials, and it would therefore be interesting to include states with an oxidised subsurface and various surface coverages of hydrogen and hydroxide, but currently this has not been investigated further.

At a potential of around -0.1 V versus RHE, the surface is reduced further, and at -0.2

V it becomes covered with hydrogen only. Such a sudden shift from a surface oxide to a surface hydride is typical for a very reactive surface, which would usually not be expected to be a great catalyst, but the hydrogen bind moderately on the adsorbed oxygen atoms. Besides, the coverage goes up to 2.5 ML around -0.2 V versus RHE, and there, the Tafel reaction most likely has a very low barrier.

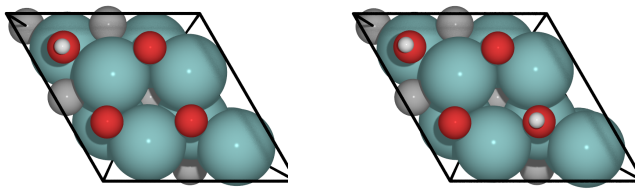

Figure 4.5: Top views of the Mo_2C at HER/HOR equilibrium conditions. The surface is covered with oxygen, but is protonated negative of 0.38 V versus RHE, and protonated further negative of -0.1 V versus RHE.

The differential free energy for hydrogen adsorption is plotted for the reduced and the oxidised Mo_2C (001) surfaces in figure 4.6 (a) and (b), respectively. Note in the plots of the differential binding energy, that not all states, considered there, are stable. The configuration with $\theta_H = 0$ and $\theta_O = 1$ does not appear in the phase diagram, because oxygen moves into the subsurface at a more negative potential than the 1ML. It only makes sense to consider the differential binding energies for configurations that appear in the phase diagram.

At the equilibrium potential, where the Mo_2C surface is oxidised the differential free energy of hydrogen adsorption shoots up from -0.1 to +0.4 eV, going from the low coverage state in figure 4.5 to a higher coverage. Thus, the over-potential for hydrogen evolution is expected to be around 0.4 eV. Observing the reduced surface, the differential free energy is around 0.3 eV at the most stable coverage.

Neither the reduced surface or the oxidised surface explains the low HER over-potentials, which have been reported to be only around 0.2 V.[93–95] Since the (001) facet is the most close packed on Mo_2C, it is not trivial to find another site that is expected to have lower reactivity on this compound. It is therefore more likely that another surface state or phase or another stoichiometry of the material is responsible for the catalytic activity. According to past computational studies[99], the mono-carbide, MoC, is reported to be less reactive, which makes it a likely candidate. More recent calculations by Michalsky et

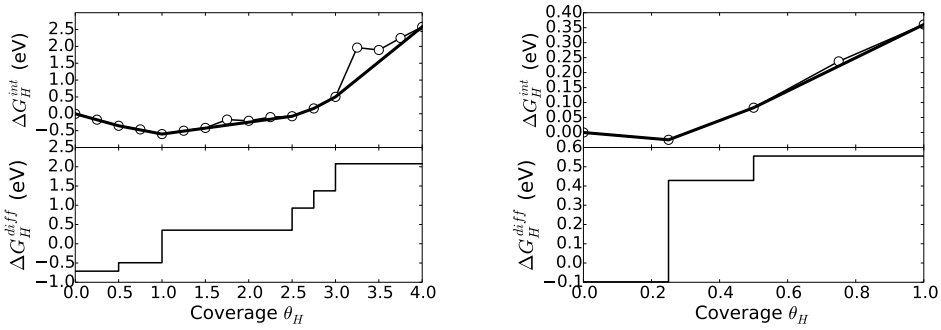

(a) *Mo_2C(001)* (b) *oxidised Mo_2C(001)*

Figure 4.6: Free energies of hydrogen adsorption on (a): a clean Mo_2C (001) surface and (b): the now with 1ML of O^* adsorbed.

al. suggest that the (101) facet is a more likely candidate although it has a differential binding energy of 0.34 eV, which is still too high evolve H_2 with an over-potential as low as 0.2 V[100]. There could be many other possibilities, however, so this has not been pursued further at this time. In parallel to the computations for Mo_2C, the MoB catalyst was also investigated, as presented in the following.

MoB (002) facet

The other active catalyst from the study by Vrubel et al.[93] was molybdenum mono-boride (MoB). The (001) facet has a dense Mo-B termination, and it was therefore chosen for the calculations.
A calculated Pourbaix diagram from the materials project[101] for Mo and B suggest, that MoB is not stable in aqueous solutions, since Boride can dissolve in the form of BH_4^-. Thus it was interesting to add a surface termination, where B atoms were removed, although this leaves a more open surface, which makes it more reactive.

A surface phase diagram were made for each of the two terminations. The phase diagram for the Mo-terminated facet, shown in figure 4.7, shows that the facet is covered with oxygen at equilibrium. The oxygen atoms are protonated only at potentials negative of -0.5 V versus RHE. For the B-terminated facet, the phase diagram in figure 4.8a shows a partially oxidised surface at potentials positive of -0.5 V versus RHE, but a completely hydrogen covered surface negative of -0.5 V versus RHE. The boride termination on the (002) facet leaves a more closed and less reactive Molybdenum surface.

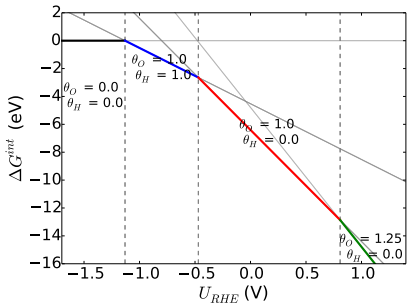

Figure 4.7: *Surface phase diagram of the Mo-terminated MoB (002)*

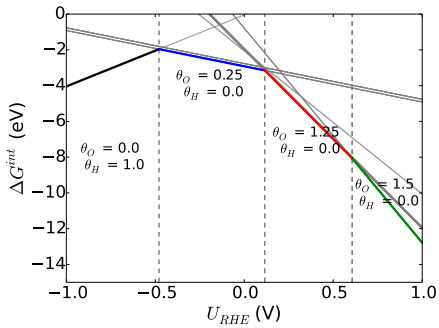

(a) *Surface phase diagram of the Boride terminated MoB (002)*

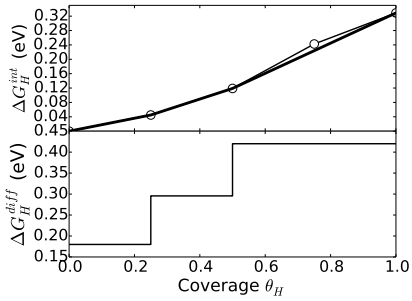

(b) *Free energies of hydrogen adsorption on the clean B-terminated MoB (001) surface.*

Figure 4.8: *Surface phase diagram and adsorption free energies for the B-terminated MoB.*

The differential binding energy is plotted in figure 4.8b, omitting the states with a non-zero oxygen coverage. These ΔG^{diff} are relatively small, around 0.18 eV at low coverages, which is consistent with the experimentally observed over-potentials on this material. However, it is not clear how the low coverage of oxygen adsorbates, that are stable in this part of the phase diagram will affect the energies. It may be possible to clarify this further by including larger unit cells and more coverages and configurations in the analysis, but it is also likely that the boride termination is unstable in aqueous environments. Boride dissolution could be hindered by a large activation energy, so it is possible, that boride terminated (002) facet is the active site. It is also possible that the neither the boride termination or the molybdenum termination are stable in solution, and

that the facet evolves HER, while being dissolved slowly. There are many other possible terminations of the α-MoB, which has not been investigated in this study, and besides, there are other phases, which could be contributing to the observed activity. In summary, the moderate hydrogen binding energy of the clean B-terminated facet may be the explanation for the high HER activity of this catalyst, but it is not possible to conclude with certainty, because this facet should be prone to dissolution.

4.2.3 Discussion

The phase diagrams clearly reflects, that the surfaces of the molybdenum mono-boride and di-carbide are quite reactive, since they are always covered with either hydrogen or oxygen in the aqueous environment.

It is also noted that the binding energies of hydrogen depends significantly on the coverage, even below $\theta_H = 0.5$ ML, and this means that there are repulsive adsorbate interactions. This is contrary to hydrogen adsorption on many transition metal surfaces [80], but similar to the behaviour of MoS_2 edges as calculated by Hinnemann et al. [84], (A comparison between Pt(111) and MoS_2 is shown in Fig. 4.2).
Using the differential binding energy as a descriptor, it appear that rather large overpotentials, above the observed ones, would be observed, when evolving hydrogen from the molybdenum compounds that were included in this study. Thus it is most likely that another active site or surface termination exists, which has yet to be identified. For Mo_2C it could be interesting to continue the investigation with a near surface oxide and/or partial coverages of HO^* and H^* on the (001) facet. For MoB, it would be interesting to try larger unit cells and co-adsorb ensembles of O^*, HO^* and H^*, to confirm whether the differential H^* binding is affected by co-adsorbed HO^* or O^*.

In addition, there may be other phases of both catalysts that could be responsible for the activity, than the majority phases. If these are to be investigated, the number of degrees of freedom for identifying the active site is quite large, since many surface terminations and surface compositions between Mo and the alloy elements may have to be screened in the search for the active site.

4.3 Nickel Phosphide for catalysis of HER

In this section, results on studies of Ni_2P and other phosphide-based HER catalysts are presented. In contrast to the results on MoB and Mo_2C, these calculations revealed sites with moderate differential binding energies for hydrogen on several facets of Ni_2P [102] and also on some other metal phosphides. The results on Ni_2P are published and included as Paper IV in this thesis.

Nickel phosphide attracted attention as a good hydrogen evolution catalyst after discovery by Schaak et al. [83]. There are several reasons why it is interesting to study in detail. One is that it has a small band gap with band edges near the $H_2/H^+ + e^-$ equilibrium potential, which makes it interesting for solar water splitting. [77] The second is that it was one of the best known non-precious HER catalysts. The most studied non-precious alternative, MoS_2, is demanding in efforts to fabricate active morphologies [88], because it is only active on the edge site [82,84]. Ni_2P seemed to be very active more or less regardless of the morphology [83,102–104], which may be an advantage if the catalyst are to be integrated in applications.

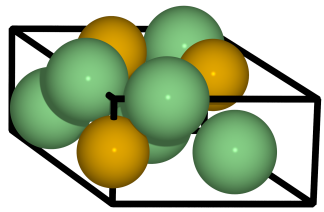

Figure 4.9: *The unit cell of Ni_2P. Phosfor atoms are represented by yellow spheres and nickel atoms are represented by slightly larger green spheres.*

Liu & Rodriguez [105] calculated the adsorption energies of HER intermediates on a number of Ni complexes and surfaces including $Ni_2P(0001)$. They concluded, that Ni_2P could be a good catalyst for HER in terms of both activity and stability. It was more recently that Popczun et al. [83] measured high catalytic activity for HER in acid from Ni_2P nano particles. The (0001) facet, which was believed to be the active site according to an "ensemble effect", binds hydrogen moderately in the hollow site. However, surface face diagrams analogous to the ones presented in the previous section would clarify that the hollow site would actually be occupied at equilibrium, and adsorption of hydrogen atoms to the Ni-P bridge would be rather unstable. Therefore the Tafel pathway would be

blocked on this facet, and only a Heyrovski pathway to the hollow site might be possible. Calculation of a Heyrovski pathway is hard to achieve accurately with existing methods [90].

This section presents calculations of hydrogen binding to several facets of Ni_2P, which show that the most active sites are in fact likely to be the $(11\bar{2}1)$, the $(11\bar{2}0)$ or the $(10\bar{1}0)$ facets, where bridge sites may facilitate the Volmer-Tafel pathway with over-potentials lower than on the (0001) facet. It is also shown that the barrier of the Tafel reaction can be indirectly overcome by increasing the over potential. The results have been published [102] and are included in paper IV in this thesis.
The bulk structure of Ni_2P (See figure 4.9) has alternating layers in the (0001) plane, which consists of Ni_3P_2 and Ni_3P. STM and DFT studies [106] have suggested that the most preferred (0001) surface termination is the Ni_3P_2, which was used in the past DFT calculations [105]. Later LEED and STM studies suggest, the metal sites are covered by P adatoms under oxidising conditions, while there may be exposed metal atoms under reducing conditions [106]. However, these studies were done in vacuum, and there are uncertainties as to how the surfaces are terminated in the aqueous environment.

4.3.1 DFT Calculations

The calculations were done with GPAW [31,32] using projector augmented wave functions to represent atomic cores and valence wave functions were represented on a real space grid with a spacing of 0.18 Å. Periodic boundary conditions were used in the plane and non-periodic boundary conditions were used out of the surface plane with a dipole correction [107]. The RPBE [27] functional was used to approximate exchange and correlation contributions to the effective potentials, and a Fermi smearing with 0.1 eV was applied to ensure convergence and the energies were extrapolated to 0 K in electronic temperature. Spin polarized calculations produced magnetic moments smaller than 0.001 for all atoms, and therefore further calculations were done in spin-paired mode to save CPU time.

The Ni_2P bulk structure was obtained from the Materials Project database [101,108–111] and then relaxed. The bulk lattice constants were converged to a = b = 5.948 Å, c = 3.408 Å. By X-ray diffraction these have been found to be a = 5.855 Å and c = 3.339 Å by Rodriguez et al. [112], so the error versus experiment is around 2%, which is commonly found, when using the RPBE functional for metals [27].

From the relaxed bulk lattice, the most low index facets were cut and the top one or

two surface layers were relaxed. Integral and differential binding energies were calculated for hydrogen in many different configurations, at various coverages, to make sure that the lowest energy configuration was found at every coverage.

Hydrogen on Ni_2P (0001)

The (0001) facet is the one that was previously calculated [105], but the calculations were done again, expanding with a few more adsorbate configurations to make sure the results on different facets were comparable and to compare the DFT results.

The slab was a 1×1 cell with 5 atomic layers so that the slab was symmetric, although the two layer types (See Fig. 4.9) means that it was not completely stochiometric. The k-point sampling for the Kohn-Sham wave functions was a 3×3 Monkhorst-Pack [34] sampling. A few surface calculations were carried out with and without adsorbates in spin-polarized mode, but as in bulk mode, magnetic moments converged to zero, and therefore all further calculations were done in spin-paired mode. The calculated potential energies of adsorption agree with the calculations on this facet by Liu & Rodriguez [105].

The hollow site with 3 Ni and a P atom below the center was the strongest adsorption site for the first hydrogen. After this was occupied, the next hydrogen atoms adsorbed on the NiP bridge sites of which there are 6 per unit cell. The relevant descriptor for activity is the differential free energy, ΔG^{diff}, as presented in the beginning of this chapter and this is presented in figure 4.10a together with the integral free energies.

The phase diagram in figure 4.10b is constructed by plotting the integral adsorption, G^{int}, energies of all calculated states versus U_{RHE}, which is the same methodology as in the previous section. Oxygen adsorption was also calculated on this facet, and it is therefore observed from the phase diagram, that oxidation of the surface is stable at potentials more positive than 0.1 V versus RHE. At equilibrium with hydrogen and water or in the potential range, where hydrogen evolution is favourable, a surface oxide is not stable. Instead, the phase diagram shows that the low coverage of hydrogen in the hollow sites is stable in a wide region around the equilibrium potential.

The differential adsorption energy of at higher hydrogen coverages is 0.4 eV, which indicate that the over-potential should be at least 0.4 V. The observed over-potential from Schaak et. al [83] is less than 0.2 V, so it was expected that other facets of Ni_2P

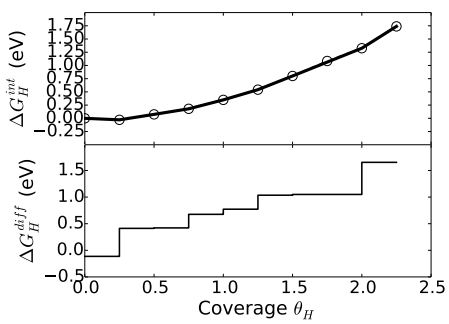

(a) *Free energies of hydrogen adsorption: The upper panel shows integral free energy, while the lower panel shows differential free energy.*

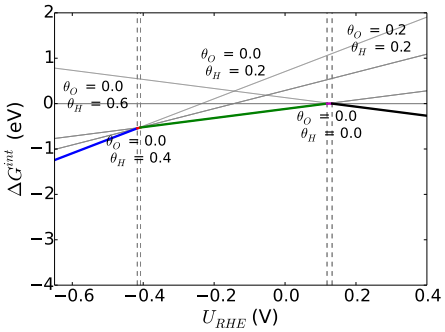

(b) *Surface phase diagram of Ni_2P (0001). The labels denote coverages, $\theta = n/N$, where $N = 5$ surface atoms.*

Figure 4.10: *Surface phase diagram and adsorption free energies on Ni_2P (0001).*

would be better for HER catalysis. In the following, the same analysis is presented for the other low-index facets of the Ni_2P crystal, which turned out to predict higher activity.

Hydrogen on Ni_2P $(11\bar{2}1)$

Another low index facet is the $(11\bar{2}1)$, which is very interesting because it also has a nickel hollow site, like the (0001), (See the top view in Fig. 4.11).

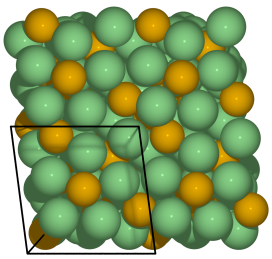

Figure 4.11: *Top view of the $(11\bar{2}1)$ facet of Ni_2P.*

The surface was represented by a three atomic layer slab in a 1×1 super cell, as shown in figure 4.11. The number of k-points was 2×2 in the plane and the grid spacing was 0.18 Å. The differential and average free energies are presented in figure 4.12a. Calculating a few adsorption energies with 3, 4 and 5 layer slabs, the differences were below 0.03 eV,

which is below the uncertainty attributed to DFT.

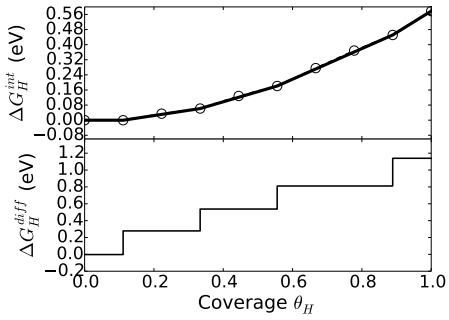

(a) *Free energies of hydrogen adsorption. The upper panel shows integral free energy, while the lower panel shows differential free energy.*

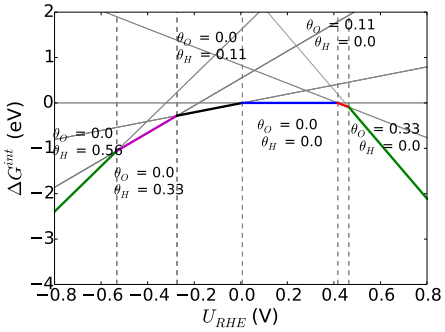

(b) *Surface phase diagram of Ni_2P $(11\bar{2}1)$. The labels denote surface coverages, $\theta = n/N$, where $N = 9$ surface atoms.*

Figure 4.12: *Surface phase diagram and adsorption free energies on Ni_2P $(11\bar{2}1)$*

From the phase diagrams, it can be concluded that the surface begins to accept atomic oxygen positive of +0.4V versus RHE, which is also the case for the (0001) facet. Atomic oxygen was checked on the $(11\bar{2}1)$, while configurations with HO* or combinations of H* and O* were omitted, but it is likely that OH adsorbates have the same stability as on the (0001), where they begin to adsorp positive of 0.1 V versus RHE.

Chemisorbed hydrogen is most stable in the hollow site, just as on Ni_2P (0001), and further adsorption resulted in occupancy of the nickel bridge sites consisting of the hollow site and one adjacent nickel atom. At HER/HOR equilibrium, the most stable coverage is $\theta_H = 1/9$, and at this coverage, the differential adsorption energy is 0.28 eV. Thus it can be concluded, that the $(11\bar{2}1)$ facet may catalyse HER via a Tafel mechanism with an over potential of 0.28 V.

Hydrogen on $(10\bar{1}0)$

Since nickel bridge sites were stable adsorption sites for hydrogen on the $(11\bar{2}1)$ facet, the $(10\bar{1}0)$ appeared to be more promising, since it contains continuous rows of adjacent nickel bridge sites, (See the top view in Fig. 4.13).

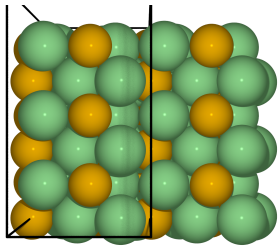

Figure 4.13: *Top view of the* $(10\bar{1}0)$ *facet of* Ni_2P

The $(10\bar{1}0)$ surface was represented by four atomic layer slabs in 1×2 and in 1×3 super cells, (the latter is marked by black lines in figure 4.13). The k-point sampling was 3×3 for the small super cell and 3×2 for the larger super cell.

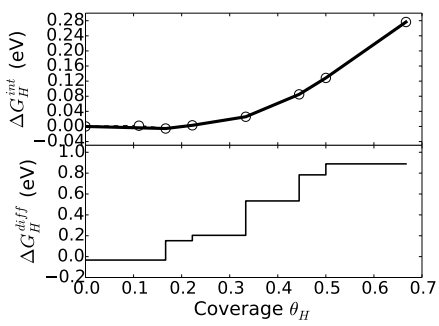

(a) *Free energies of hydrogen adsorption calculated in both a* 1×2 *and in a* 1×3 *super cell. The upper panel shows integral free energy, while the lower panel shows differential free energy.*

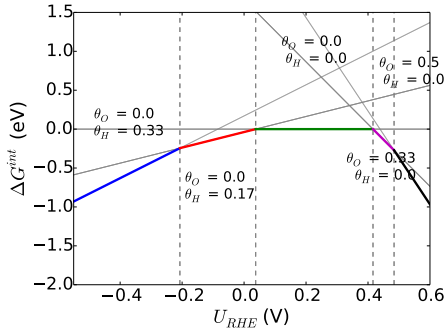

(b) *Surface phase diagram of* Ni_2P $(10\bar{1}0)$ *based on calculations in a* 1×2 *super cell. The labels denote coverages,* $\theta = n/N$*, where* $N = 6$ *surface atoms.*

Figure 4.14: *Surface phase diagram and adsorption free energies on* Ni_2P $(10\bar{1}0)$

The phase diagram in Figure 4.14b shows that the surface begins to accept atomic oxygen at potentials positive of +0.4V versus RHE, just like the two Ni_2P facets presented in the previous sections. Several configurations were checked to find the most stable adsorption sites, but configurations containing HO* or combinations of co-adsorbed H* and O* together were not included.

At HER/HOR equilibrium, a low coverage of 1/6 of hydrogen is stable on the surface as seen in the phase diagram in figure 4.14b, again in the nickel bridge sites. At this

coverage, the differential adsorption energy is 0.15 eV, which can be considered rather moderate and central on the HER volcano. Thus the calculations predict the $(10\bar{1}0)$ facet to be a good HER catalyst with an over-potential as low as 150 mV.

Hydrogen on Ni_2P $\pm(11\bar{2}0)$

The $\pm(11\bar{2}0)$ facets could be terminated in several ways, and the potential energies of every different way to cleave the crystal in the $\pm(11\bar{2}0)$ plane were therefore calculated by DFT, to find the minimum energy terminations. The stable $\pm(11\bar{2}0)$ surfaces can be characterized as corrugated, and the bridge sites can be present on crystal edges, such as in figure 4.17.

Adsorption energies of hydrogen were then calculated on only the most stable termination in each direction. Since oxygen adsorption on the previous three facets showed that the adsorption potentials were more positive than the HER/HOR equilibrium potential, oxides species were not included in the investigation of these last two facets.

The surfaces were represented by three atomic layer slabs in 1×2 super cells, and a k-point sampling of 3×2 was used for both.

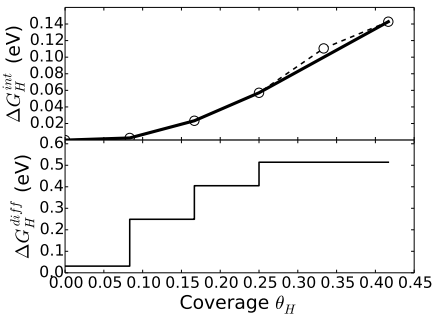

(a) *Free energies of hydrogen adsorption. The upper panel shows average free energy, while the lower panel shows differential free energy.*

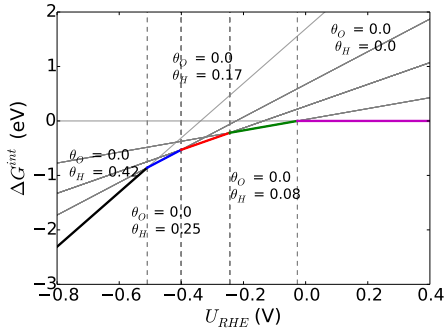

(b) *Surface phase diagram of Ni_2P $(11\bar{2}0)$. The labels denotes coverages, $\theta = n/N$, where $N = 12$.*

Figure 4.15: *Surface phase diagram and adsorption free energies on Ni_2P $(11\bar{2}0)$*

The phase diagram of Ni_2P $(11\bar{2}0)$, (See Fig. 4.15b), shows that a low hydrogen cover-

age around 1/12 is stable at 0V versus RHE, and the differential adsorption energy from this coverage is 0.25 eV. The most stable adsorption sites were again the nickel bridge sites.

The same crystal plane terminated in the opposite direction is the $(\overline{1}\overline{1}20)$ facet, and this is predicted to be the most active facet. The surface phase diagram of Ni_2P $(\overline{1}\overline{1}20)$, (See Fig. 4.16b), is very similar to Ni_2P $(11\overline{2}1)$, in that 1/12 coverage of hydrogen is stable at 0V versus RHE, but the differential adsorption energy is in this case just 0.08 eV.

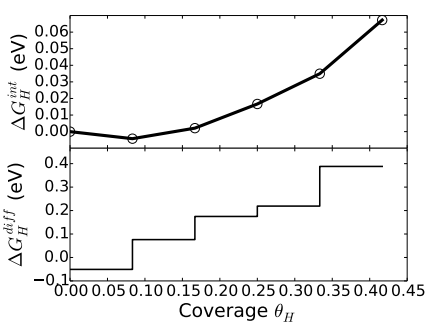

(a) *Free energies of hydrogen adsorption. The upper panel shows integral free energy, while the lower panel shows differential free energy.*

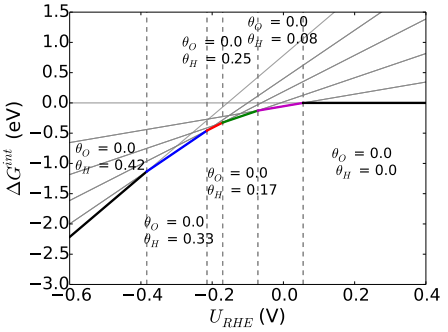

(b) *Surface phase diagram of Ni_2P $(\overline{1}\overline{1}20)$*

Figure 4.16: *Surface phase diagram and adsorption energies on Ni_2P $(\overline{1}\overline{1}20)$. The labels denote coverages $\theta = n/N$ with $N = 12$.*

4.3.2 Discussion

In literature, the prevailing theory on the high HER activity from Ni_2P has been that the hollow site on the (0001) is responsible for the activity [113]. The relevant configuration on the (0001) facet has the metal hollow sites occupied by hydrogen. The differential free energy to adsorp another hydrogen on the Ni bridge or Ni-P hollow site is almost 0.5 eV, which makes the Tafel pathway improbable on this facet. De-occupation of the hollow site via a Heyrovski step would be more likely at equilibrium.

However, on all the other investigated facets of Ni_2P, the Tafel pathway would be possible at over-potentials below 0.3 V. The differential free energies at the coverage relevant

at 0V versus RHE are compiled in table 4.1.

Facet	Coverage	ΔG^{diff}
(0001)	1/5	0.41 eV
$(11\bar{2}1)$	1/9 ML	0.28 eV
$(10\bar{1}0)$	1/6 ML	0.15 eV
$(11\bar{2}0)$	1/12 (0/12 ML)	0.25 eV (0.03 eV)
$(\bar{1}\bar{1}20)$	1/12 ML	0.08 eV

Table 4.1: *Differential free energies of adsorption for various facets of Ni_2P.*

Despite the low differential free energies, in some of the configurations, particularly for the $(\pm 11\bar{2}0)$ facets, the hydrogen atoms are placed rather far apart. Ordering the facets according to predicted activity from the differential adsorption energies gives $(\bar{1}\bar{1}20) > (10\bar{1}0) > (11\bar{2}0) > (11\bar{2}1) > (0001)$. With this order in mind, the nano wire morphology synthesized by Chen et al.[114] seemed to be close to optimal, as visualized in the model in figure 4.17.

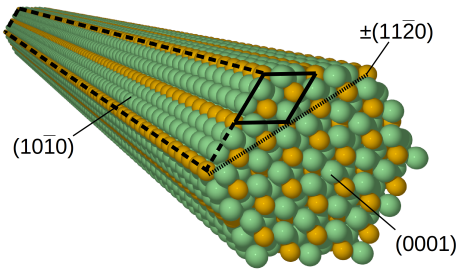

Figure 4.17: *Atomic-scale model of a Ni_2P nanowire grown in the [0001] direction.*

Due to the growth direction and large aspect ratio[114], this morphology would ideally not expose very many (0001) or $(11\bar{2}1)$ sites. It would however expose the facets, which propagate along the growth direction, such as the $(10\bar{1}0)$ and the $\pm(11\bar{2}0)$ facets. The most active facets were expected to be the $(10\bar{1}0)$ and the $(\bar{1}\bar{1}20)$ according to the DFT calculations. Experiments were therefore carried out by Hu et al. at EPFL to test, whether the nano wire morphology could yield increased HER activity compared to other morphologies.

The difficulty in quantifying the number of active sites in the sample meant, that it was not possible to determine with high precision, whether they expose more active sites than other known morphologies, such as the spherical nano particles[83]. In summary, the experiments showed high catalytic activity for HER from the nano wires, but it was not possible to prove a higher activity, than the spherical nano particles. The result that many different fabrication methods and morphologies of Ni_2P are active for HER, are in accordance with, but can not prove the DFT finding, that the active site is adjacent nickel bridge geometries, which can be found on several facets.[102]

Moving beyond the descriptor based approach, the Ni_2P catalyst was further investigated by calculating the barriers for the Tafel (surface recombination) reaction, to check whether this pathway is open. These results are discussed in the following.

4.3.3 Reaction barriers for surface combination

In search of better determination of the active site or facet, the barriers were calculated for the Tafel reaction using the nudged elastic band method, (NEB), with a climbing image. The NEB method creates a series of states which are interpolated images between an initial and a final state, after which it relaxes the images, while they are connected by a spring force.[115,116]. The climbing image reverses the component of the spring force parallel to the reaction coordinate, on the image with the highest energy, so that the image moves towards the saddle point in the potential energy landscape. This feature was activated after a few iterations of relaxation, to get a good guess as to which state was closest to the saddle point.[117]

Assuming a Tafel mechanism, the potential determining step have to be the adsorption of a second or third hydrogen to stable sites in vicinity to other H^*. On all the investigated facets, nickel bridge sites were the most stable.The initial states were the most stable states at equilibrium with hydrogen, where two hydrogen atoms were present on the surface. A guess for the final states for the Tafel step was found by applying a Hookean constraint between the H atoms in the initial state and relaxing to form a H_2 molecule in a nearby local minimum on the surface. The spring constant for the Hookean was set to 3 eV/Å^2 at distances larger than 0.9Å, and 0 at distances smaller than 0.9Å. Thereafter, the NEB calculation was carried out without the Hookean constraint. The final state usually turned out to be H_2 adsorbed on top a nickel atom.

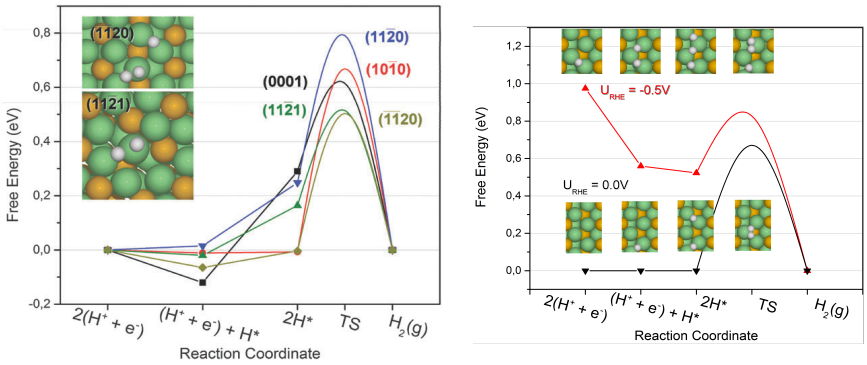

(a) *Tafel reaction barriers calculated at lowest or equilibrium coverages on the five different facets.*

(b) *Tafel reaction barriers at 0 V vs. RHE and at 0.5 V vs. RHE.*

Figure 4.18: *Barriers for the Tafel reaction on Ni_2P, calculated with the nudged elastic band method. Reprinted under CC license.*[102]

An interesting observation is seen, regarding the barriers on the same facet calculated different electrode potentials. Increasing the coverage, increases the adsorption energy due to repulsive adsorbate interactions, and the transition states found at higher coverages corresponding to higher over-potentials also increase in energy. However, in some cases they do not increase as much as the initial adsorbed state, as shown in figure 4.18b. This effectively means that increasing the over-potential electrochemically at some point creates equilibrium between protons+electrons and the transition state.

After calculating the Tafel barriers of the five investigated facets, shown in figure 4.18a, a reordering of the predicted activity is in order: $(\bar{1}\bar{1}20) > (11\bar{2}1) > (10\bar{1}0) > (11\bar{2}0) > (0001)$. It turns out that the energy of the transition states that were found, do not scale very accurately with the energies of the adsorbed states. This may be expected to be the case, if the geometry of the initial, and transition states are the same due to the scaling relations between adsorbates on different geometries[118,119], but in this case the geometries also have many variations, e.g. on the $(\bar{1}\bar{1}20)$ facet the final state is on a nickel row, which makes the ridge of this corrugated surface, and on the $(11\bar{2}1)$ and (0001) facets, the final state is on the nickel atoms, which sit around the hollow site. In best cases the barriers are around 0.5 eV, which is relatively modest compared to those reported for Pt(111)[89], where they are up to 0.85 eV, and thus it is not unlikely from the

computations that Ni_2P is active through a pure Tafel pathway.

The barrier calculations may explain why the Ni_2P nano wires did not yield an activity enhancement over the previously reported spherical nano particles. The nanowires are likely to have many more $(10\bar{1}0)$ facets than other morphologies due to the growth direction. The barrier calculations changed the order to the $(\bar{1}\bar{1}20)$ and $(11\bar{2}1)$ facets were both predicted to be more active that the $(10\bar{1}0)$ facet, and there is no reason why, there would be more of those on the nano wires, compared to other morphologies.

After the results explaining the activity of Ni_2P were done, a few calculations were carried out on other transition metal phosphides to check if other candidates could be discovered for HER, or even more interesting, for HOR catalysis. The descriptor for HOR catalysts is in principle the exact same as for the HER catalyst, namely the differential binding energy og hydrogen, since there are no other intermediates. It is therefore puzzling why the metal-sulfide, carbide and nickel phosphide catalysts are not active for HOR.

4.4 Other metal-phosphides

This section presents a small screening study for other metal phosphides, (FeP, Fe_2P, CoP, Co_2P, MnP, CrP and WP) for hydrogen evolution and hydrogen oxidation. The way in which phosphor stabilizes nickel in acid might also work on these metals and the electronic properties of the surface could prove even more favourable than Ni_2P. Surface phase diagrams and plots of the integral and differential free energies are available for each of these compounds in appendix 7.1, and the results are summarized in table 4.2.

The surfaces were modelled with four atomic layers, in 1×1 super cells for the monophospides, and in 1×2 super cells for the di-phosphides. The k-point sampling was 3×3 in all the calculations.

This limited screening study presented iron-monophosphide, (FeP), as the most promising material. The adsorption energies for FeP (100) are shown in figure 4.19a and the surface phase diagram for FeP (100) is shown in figure 4.19b.

Interestingly, hydrogen adsorps both on the phosphor and on the iron atoms in the FeP surface, which is in contrast to Ni_2P, where only the metal sites are moderately binding, and the phosphor atoms are not binding. The differential binding energies calculated at

Facet	Coverage	ΔG^{diff}
FeP (001)	2/4	0.00 eV
Fe_2P (10$\bar{1}$0)	2/6 ML	0.10 eV
CoP (001)	2/4	0.13 eV
Co_2P (10$\bar{1}$0)	3/6 ML	0.13 eV
MnP (001)	4/4	-0.06 eV
WP (001)	4/4	0.2 eV

Table 4.2: *The most stable surface coverages at the HER/HOR equilibrium potential, and the differential free energies of hydrogen adsorption at that coverage, for each of the transition metal phosphides that were included in the small screening study.*

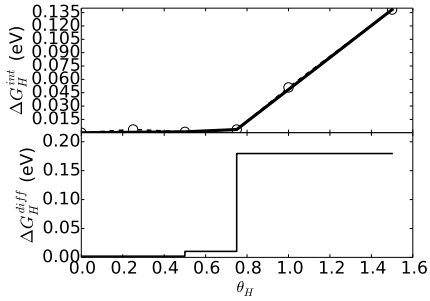

(a) *Free energies of hydrogen adsorption. The upper panel shows integral free energy, while the lower panel shows differential free energy.*

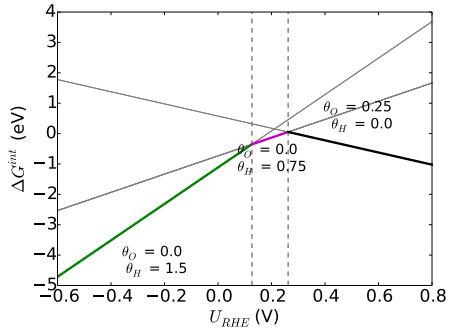

(b) *Surface phase diagram of FeP (100)*

Figure 4.19: *Surface phase diagram and free energies of hydrogen adsorption for FeP (100)*

equilibrium for a few metal-phosphides reveal that iron phoshides should evolve hydrogen with over-potentials around 200 mV, while tungsten and cobalt mono-phosphides might reduce that to 100 mV. Since the reactivity towards hydrogen on FeP (100) is favourable for HOR/HER, it was interesting to compute the barrier for the Tafel reaction. This is shown in figure 4.20. The transition state is only 0.14 eV above the 1/2 ML state, which is a rather low barrier, and it can therefore be concluded that the Tafel pathway is highly probable on this catalyst.

It is currently complicated to get accurate and reliable barriers for the Volmer-Heyrovski pathway, due to the charge transfer steps. Electrochemical charge transfer reactions were not investigated further in this study, because calculations of barriers for charge trans-

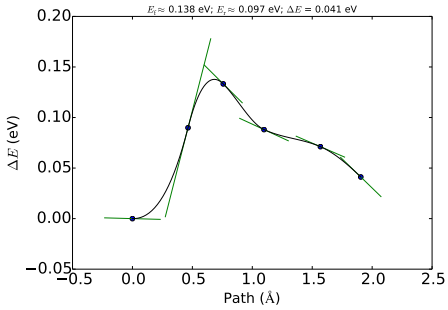

(a) *Potential energy barrier for the Tafel reaction on FeP.*

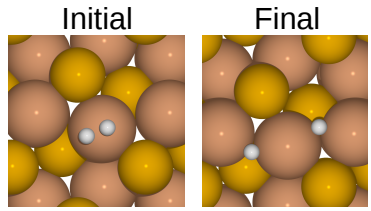

(b) *Views of the initial and final states, which correspond to the left and right points in (a). The small white spheres represent H atoms, the large brown spheres represent Fe atoms and the middle sized yellow spheres represent P atoms.*

Figure 4.20: *Results of the Nudged Elastic band calculation on the Tafel reaction on FeP.*

fer reactions are associated with some difficult problems. The free energy of transitions states involved in the electrode-electrolyte charge transfer reactions is dependent on the interface electric fields, interface dipole and on the water structure. Thereby, the free energy pathways of these reactions can not be obtained in with the usual methods. Many recent advances has been made towards developing methods for this goal[90,120–123], but a key element is still missing, which is more accurately characterizing the structure of the interface, particularly the electrolyte side, under operating conditions. This is the subject of chapter 5 in this thesis.

Meanwhile these computational studies were ongoing, several metal phosphides were being discovered in experimental screening, primarily by Schaak et al.[124–126]. These experiments demonstrate high activity from cobalt and iron phosphides[124]. More recently, a systematic study of the metal-phosphides for HER has reported that a bimetallic phosphide, FeCoP, shows the most optimal properties for hydrogen evolution[127].

So far all the non-precious catalysts, that have been discovered have been reported to be inactive for the hydrogen oxidation reaction, (HOR). The simplest explanation for the lack of HOR activity is that the surfaces become covered with oxide species are slightly

positive potentials versus RHE. Some of the computed surface phase diagrams, presented in this chapter indicate that this hypothesis is reasonable, since oxygen begins to adsorb from +0.2 V to +0.5 V. Further calculations of HO* binding to the metal phosphide surfaces will shed more light on this question.

4.5 Summary

Computational studies of the hydrogen adsorption energies on various facets on Ni_2P show that the (0001) facet, previously thought to be the active site, is most likely not. Several other facets of this compound have more moderate differential adsorption energies at the equilibrium coverage, particularly the $(\overline{1}\overline{1}20)$, $(11\overline{2}1)$ and $(10\overline{1}0)$ facets, which are all predicted to be active through the Tafel pathway and possibly also the Heyrovski pathway. The material is rather weak binding, in that the hydrogen coverage is always low at equilibrium.

Calculations of barriers for the Tafel reaction were carried out for a few different coverages. The activation free energy increases with increasing coverage, but the increase is smaller than the increase in binding energies. The consequence of this is that applying enough reducing over-potential will increase the equilibrium coverage to a point, where the adsorbates are added practically in the transition state.

Computed hydrogen binding energies correlate well with the trends in activity for the metal phosphides, and this adds confidence to the predictive power of computational screening methods.

4.6 Outlook

The hydrogen evolution reaction is one of the simplest electrochemical reactions, that is needed for the purpose of electrochemical energy conversion. It is a reaction that demands relatively little of a catalyst material, because the material only need to bind one surface intermediate optimally for optimal catalysis. This is reflected by the many new discoveries of catalysts for the reaction, many of which are made from abundant and inexpensive materials. It is too early, however, to say that the problem of identifying hydrogen evolution catalysts is solved. The requirements for the catalyst material is also that it

has sufficient long term stability, and many of the new catalysts do not have issues with stability. Other requirements also apply depending on the type of system, the catalyst should be integrated in, e.g. in some cases it should be active in alkaline solution. Therefore there are still lots of motivation for researching further into materials for this reaction.

For fuel cell applications, it would be advantageous if a non-precious hydrogen oxidation catalyst could be found. The reason for the lack of HOR activity in the non-precious HER catalysts has yet to be understood fully and further research into this problem is warranted, including studying the adsorption properties of HO^* on the metal-phosphide surfaces.

5. Electrochemical Interface Model

5.1 Introduction

The chapters up to this point have presented models of surfaces in perspective for electrocatalysis. Although the reactivity of surfaces and the ensembles and geometries of atomic sites on surfaces may be the only important properties for some catalytic reactions, for other reactions, the electrolyte part of the interface means everything, and this part has not been considered so far. There are some analytical and computational complications in modelling the atomic scale properties the electrode/electrolyte interface, but many advances and solutions have been developed in by many different groups in the recent decades. In this chapter, a methodology presented, which we are developing with the aim of giving predictive capability for calculation of the atomic structure of the interface, as a function of the electrode potential, of solution pH and chemical potentials of counter ions in solution, using a statistical physics approach.

Many observed phenomena in electrochemistry depend explicitly on the pH and chemical potentials of various counter ions. These observed phenomena also affect rates and selectivity of some important electrochemical reactions such as hydrogen evolution and CO reduction.[91,128,129] Electrochemical reactions always involve charge transfer reactions, which move charges between the electrolyte phase and the electrode. If these charge transfer reactions affect the rate, calculations of their activation barriers is a highly interesting prospect. Previous works[89,90,121,130,131] on this, have revealed several complications: **1)** The unit cell has a finite size and a constant amount of electronic charge, and it has been shown that varying the size and/or the amount of charge affects the energy landscape of the reactions dramatically. The first problem may be helped by extrapolation schemes with different sizes of unit cells[130] or by assuming a capacitor model.[132,133] More recent efforts to benchmark a simple capacitor model against the unit cell extrapolation scheme has been made.[122,123] **2)** The second issue is that structure of the aqueous electrolyte also affect the energy landscape of the reaction, and this structure changes the internal electric fields normal to the surface. Thus it will be necessary to be able to determine the structure of the electrolyte and how it depends on the surroundings, to calculate barriers and use transition state theory to predict reaction rates.

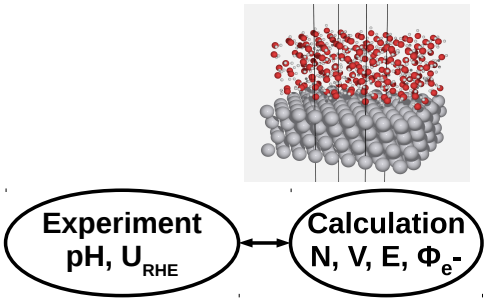

Figure 5.1: *The challenge in modelling the electrochemical interface. In the simulations, the number of particles, N, the volume, V, is fixed and the energy, E, is calculated. In experiments, the temperature, the pH, and electrode potentials are constant, but not the number of particles.*

The above mentioned problems are fundamentally due to a gap in our understanding the link between atomic scale systems and macroscopic systems. DFT calculations routinely model atomic-scale systems in the micro canonical ensemble where the volume, the particles and the energy are fixed, referred to as the NVE ensemble. In reality, the electrochemical interface is an open system, which exchanges ions, electrons and heat with the surrounding environment. Therefore it should arguably be modelled using a grand canonical ensemble, referred to as a μVT ensemble, in which the numbers of ions and electrons must be varied to find the relevant states. The model should also include the effect of pH and electrode potential, since it is known from experiments that they are important parameters.

The many previous advances toward the grand canonical modelling of the electrochemical interface can be categorized as follows:

1 The system exchanges electrons with a well defined reservoir, but not ions.[134–136] This is particularly interesting because of the ability to tune the chemical potential of electrons and thus act as a potentiostat. It is preferable if the macroscopic conditions can be an input to the calculation rather than an output, due to the efficiency problem of having to calculate different states each corresponding to one external condition. The unit cell can must be neutralized using charge densities placed various regions of the atomic scale simulation cell, e.g. as Gaussian distributions outside the double layer or as homogeneous background charges.[131]

2 External electric fields are imposed in the simulation using an external field added in the Poisson equation[49,52]. The external electric fields can be linked to electrode potential imposing the Fermi levels and orbital overlap of semi-infinite metal electrodes, using non-equilibrium Green's function theory[137]. It is an appealing idea, because a reference electrode is then explicitly included in the system, and this method is explored a bit further with calculations that are presented in section 5.3 and in paper VIII. The disadvantage of the current state of this method, is mainly that it is very demanding in computational resources and dynamics, force relaxation and variation of particle numbers is therefore not currently feasible.

3 Systems where both ions and electrons are exchanged[63,90]. The approach is in principle similar to the first category, but now all charges are explicit in the system, i.e. they are explicit protons and electrons, but in equal numbers to keep the unit cell charge neutral. Again, care must be taken to link the chemical potential of their reference reservoirs properly with pH and/or electrode potential. The electrode potential is normally linked by using a vacuum level as reference, in line with Trasatti's absolute electrode scale[90,120,138–141]. The computational hydrogen electrode, (CHE), is also put in this category, but only the link to the U_{RHE} i.e. the driving force is included in that, not a link to pH independently from electrode potential.

Another discussion of the various types of models related to this problem can also be found in a recent review included as paper VII in this thesis. A more general perspective on water interfaces can be found in paper VI.

Just prior to the beginning of this PhD work, a solution to the problem of linking pH to work function was published[120], which essentially was a generalization of the computational hydrogen electrode, and the methodology that has been used in this PhD work is based on this Generalized Computational Hydrogen Electrode, (GCHE).

The next section in this chapter reviews the GCHE and links the atomic scale to the ionic and electronic chemical potentials. Section 5.3 compares DFT calculations on extended slabs with finite bias simulations, thereby showing how the internal interface dipole must exactly fulfil the constraint to screen the external chemical potentials. Section 5.4 presents the expressions for the free energies depending on pH and work functions thereby

enabling the analysis of a μVT ensemble, and 5.5 shows how micro states can be sampled for the μVT ensemble using slab calculations with molecular dynamics. Finally, section 5.8 presents results from this methodology and compares the results with experiments.

5.2 Theory

5.2.1 Electronic and ionic chemical potentials

In section 2.6.1, it was shown that the free energy of an interface micro state can be written:

$$\Delta G^{int} = E(n) - E(n=0) - n(\mu_{H_2}/2 - eU_{RHE}) \tag{5.1}$$

It was also mentioned, that pH effects on the stability of adsorbates or interface structures are observed because their free energy depend on the interface electric field. This can be understood when the electrode potential is written in the form of equation 5.2, which will be derived in this section.

$$-eU_{RHE} = \phi_{SHE} + k_B T \cdot pH - \phi_{e^-} \tag{5.2}$$

Here ϕ is the work function of the interface in the micro state, and ϕ_{SHE} is the work function of the standard hydrogen electrode. Since the work function is a fixed property of a micro state, it is evident from this formulation, that particular atomic states only exist at particular electrode potentials and pH, and furthermore, that the free energy depends on the grand canonical variables. Deriving the method to model effects of the pH and electrode potential, essentially boils down to deriving equation 5.2 and assuming it is valid for every relevant micro state. This is done in the following.

To introduce the effect of interface dipoles on the binding energies of ions, it is instructive to reconsider the case for proton+electron insertion into the interface system. Instead of taking hydrogen gas or protons as the reference, the state of protons and electrons in vacuum at rest is now considered. The Born-Haber cycle in figure 5.2 shows the conservation of free energy, regardless of the pathway, for insertion into the interface system.

In vacuum at rest, the chemical potentials of the proton and electron are both determined by the electrostatic potential. The assumption of fast proton diffusion is applied

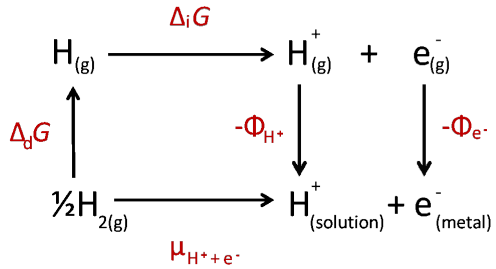

Figure 5.2: *Born-Haber cycle for insertion of protons + electrons into the interface system.*

again, just as in the computational hydrogen electrode. Thus, the protons have the same chemical potential, μ_{H^+}, everywhere in the electrolyte. Now consider the free energy difference for a proton taken from the electrolyte to a point in the vacuum. This difference is referred to as a proton work function, and it can be written:

$$\phi_{H^+} = \mu_{H^+}^{vacuum} - \mu_{H^+} \tag{5.3}$$

The pH is defined as $-\log_{10}(a_{H^+})$, where a_{H^+} is the activity of protons in solution. If $\mu_{H^+}^0$ is the proton chemical potential in a solution with pH $= 0$, then the following relates pH with the chemical potential, μ_{H^+}, of the protons in solution:

$$\mu_{H^+} = \mu_{H^+}^0 - k_B T \ln a_{H^+} = \mu_{H^+}^0 - 2.303 k_B T \cdot pH \tag{5.4}$$

If this is inserted into equation 5.3, the relation between pH and the proton work function is evident:

$$\phi_{H^+} = \mu_{H^+}^{vacuum} - (\mu_{H^+}^0 - 2.303 k_B T \cdot pH) \tag{5.5}$$

The vacuum level, which we use as reference can be infinitely far away in space, but in the DFT calculations it is convenient to use the vacuum level right outside the electrode as reference. To use this vacuum level as a reference for protons and electrons, it is necessary to be convinced that the vacuum levels must be equal right outside both electrodes. To check this, one can do thought experiment: A cavity is imagined immersed in an infinite electrolyte. Inside the cavity, there is only vacuum and all surfaces of the cavity are the vacuum-electrolyte surface. This is illustrated in figure 5.3.

The near field vacuum level is defined as the electrostatic potential at a point near the vacuum-electrolyte surface. A charge at rest in the near field vacuum feels a nearby

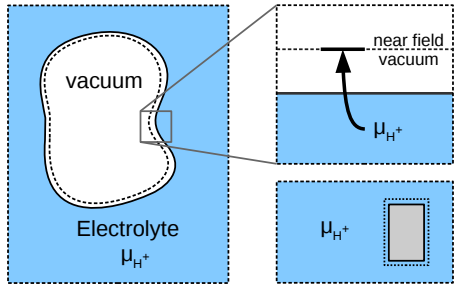

Figure 5.3: *Cavity in aqueous electrolyte. The work function for the proton is the difference in free energy between the state at rest in vacuum and the state in the electrolyte in equilibrium. Near the interface, the curvature is assumed infinitely small and a proton at rest would be in the electric field of an infinite surface.*

interface, extending infinitely. Equation 5.5 is now applied, where the vacuum level is the near field vacuum level. Assuming the vacuum-electrolyte interface dipole is identical everywhere along the vacuum-interface, ϕ_{H^+} is a constant. Since μ_{H^+} is constant everywhere in the electrolyte, $\mu_{H^+}^{vacuum}$ must also be constant anywhere along the dashed line in the cavity. The inset in the bottom right of figure 5.3 shows a metal immersed in the infinite electrolyte. Around the metal is an interface region which screens the surrounding solution from the metal. In the bulk, outside the screening region, the solution does not feel the metal at all. The electronic work function is now defined as the difference between the electron energy, $\mu_{e^-}^{vacuum}$, at rest in the near field and the Fermi in the metal, μ_{e^-}:

$$\phi_{e^-} = \mu_{e^-}^{vacuum} - \mu_{e^-} \tag{5.6}$$

If this is accepted, two electrodes can now be inserted in vicinity to the cavity. A voltmeter is in place to measure the voltage between the two electrodes. If one electrode is the hydrogen reference electrode, the voltage is denoted U_{RHE}. This situation is shown in figure 5.4, for pH = 0.

If the electrodes are sufficiently screened by a layer of electrolyte, the vacuum levels in each side of the cavity are equal. The near field position is the same for protons and for electrons. Thereby, the work functions of the two electrodes is linked to the electrode potential by

$$eU_{SHE} = \phi - \phi_{SHE} \tag{5.7}$$

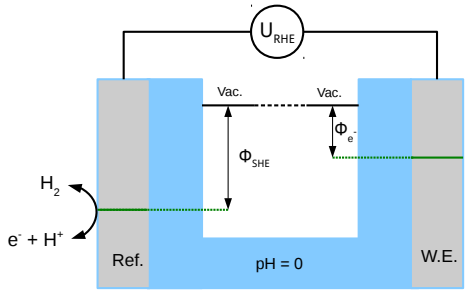

Figure 5.4: *Diagram of an electrochemical cell with a cavity in the electrolyte. The vacuum levels, near the vacuum/water interface around each electrode, are equal.*

In principle, it is therefore possible to relate the work function of an electrode to an absolute potential scale. This was argued by Trasatti[138] already back in the 1980's, and different variants of this idea has also been used in the past for DFT calculations with electrode/water systems[90,139–141], although not with constant μ for ions and using the link between the work function and the chemical potential for ions.

In the following section, DFT calculations are presented to show that the vacuum level is practical to use as an absolute reference. This is done by comparing simulations with semi-infinite electrodes (See Fig. 5.4) with regular slab/water calculations with a dipole correction. It turns out that the interface dipoles come out identically with the two methods.

5.3 DFT Calculation with Explicit Reference Electrode

This section presents a comparison between two types of calculations that link the interface dipole to electrode potential in two different ways. By doing so, it is shown that the absolute electrode scale relying on the work function and the internal dipole of the interface gives predicts the same atomic structures as the imposing the electrode potential using an explicit reference electrode and fixed external boundary conditions for the electric field. The results presented in this section are submitted for publication and included as Paper VII in this thesis.

The first method is DFT on an extended slab with water on one side. The system has periodic boundary conditions in the in-plane dimensions. In the out-of-plane direction, the system is centered with vacuum on either side and non-periodic boundary conditions are applied with a dipole correction, so the near field work function can be calculated. Various atomic structures set up various interface dipoles. The internal electric field from these structures, result in different work functions on the water side of the system. This is shown in figure 5.5.

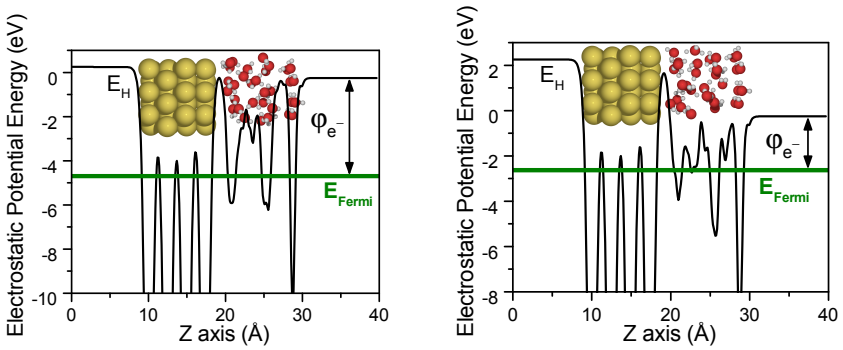

(a) $\phi_{e^-} = 4.44\ eV$. (b) $\phi_{e^-} = 2.43\ eV$.

Figure 5.5: *Slab/Water structures shown with the electrostatic potential energy, E_H, averaged in the XY plane. Due to screening in the metal, the work function on the slab/vacuum interfaces are identical, while the work function of the water interface depends on the net dipole of the interface structure.*

The second method is finite bias calculations, to evaluate the electrostatic potential energy under varying applied bias against a reference electrode, included explicitly in the calculation. The half cell atomic structures are placed opposite to each other with a layer of vacuum in between (See figure 5.6). On each surface, the layer of water sets up an interface dipole like in the previous DFT calculations. The calculation is carried out using non-equilibrium Green's function DFT (NEGF-DFT) [137].

NEGF-DFT is widely used in the molecular electronics community and it is usually applied to calculate electronic conductivity through atomic-scale systems. NEGF-DFT calculations employ periodic boundary conditions in the plane dimensions. Normal to the plane, the boundaries are infinite continuations of the three outermost FCC(111) layers of the electrodes. Instead of the usual wave functions, the NEGF-DFT calculations use

Green's functions, $f_G(E)$, which are written

$$f_G(E) = \left(E \cdot S - H_C - \sum_L (E) - \sum_R (E) \right)^{-1} \tag{5.8}$$

where E is the energy, S is the overlap, H_C is the Hamiltonian and $\sum_{L,R}$ are the self-energies of the left and right leads. The latter are obtained for the left and right leads from a calculation with periodic boundary conditions in all directions. For the central region, the electrostatic potential is obtained as usual from the Poisson equation, but now the left and right boundary conditions are set by the two leads. The Fermi levels of the leads are denoted μ_L and μ_R, and the bias, U, is controlled by setting $\mu_R = \mu_L + U$. As in regular DFT, a self-consistency cycle, ($f_G \rightarrow \rho(r) \rightarrow v(r) \rightarrow H_C \rightarrow f_G$), is used to converge the electronic structure. The electronic density $\rho(r)$ is obtained from $f_G(r, r; E)$ by integrating the diagonal.

The two types of calculations are compared in situations where equation 5.7 is fulfilled and where it is not fulfilled. In all situations, we keep the atomic structure on the left constant, but vary the atomic structure on the right and/or the bias U. In both types of DFT calculations, the electrostatic potential, E_H, averaged in the plane is written:

$$< E_H > (z) = \int_{x,y} E_H(x, y, z) dx dy \tag{5.9}$$

Three situations are imagined: Situation **1)** The voltage between the electrodes is 0 V and the interface structures are identical, and thus the interface dipoles are also identical. That is set up by using identical atomic structures for both interfaces. Situation **2)** A finite bias is applied, but the interface dipoles are identical. Situation **3)** A finite bias is applied and the interface dipoles are different.

Situation **1** is shown in figure 5.6. Here, no potential gradient is present in the vacuum between the electrolyte layers, since no bias is applied and the interface dipoles are identical. The interface dipoles are identical because, both atomic structures are identical. Figure 5.6 also shows the electrostatic potential of this slab/water structure, calculated by regular DFT with the dipole correction. This is also shown separately in figure 5.5a.

Situation **2** is shown in figure 5.7. The atomic structures and interface dipoles are unchanged from situation 1, but a bias of 2.01 V is applied between the electrodes. In

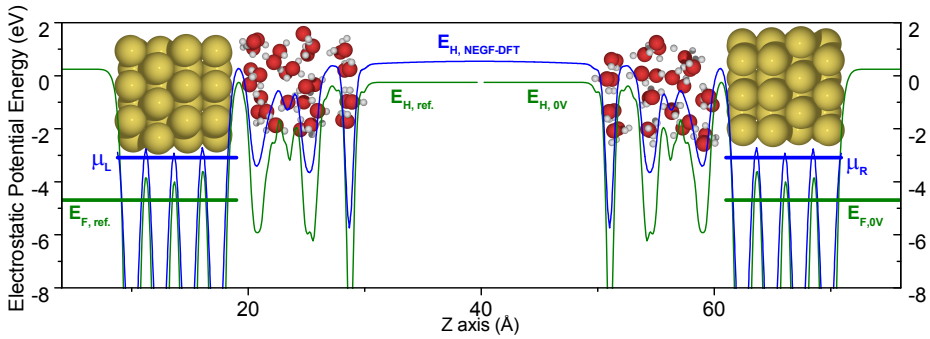

Figure 5.6: *Situation* ***1)*** *The electrostatic potentials, E_H, of the full cell NEFG-DFT calculation (blue line), and the reference half cell calculations (green lines, left and right). The Fermi levels is shown for each electrode with a thick line. The two electrodes are the same atomic structure which have a work function of 4.44 eV. Electronic chemical potentials μ_L, μ_R, from Transiesta are plotted with reference to the deformation potential, δ_E, averaged in a single atomic layer in the left electrode. $\delta_E = E_H - E_{NA}$, where E_H is the electrostatic potential and E_{NA} is the neutral atom potential from Transiesta.*

practice this is done in Transiesta[137] by setting $\mu_R = \mu_L + 2eV$. Because the interface dipoles are unchanged but the bias is changed, situation **2)** does not fulfil equation 5.7. The result of this, is that an electric field is present in the cavity between the electrodes. That means the chemical potential of a proton at the near field level outside either electrode would vary depending on which side of the electrolyte it is taken from, or that the protons at either side are not in equilibrium.

In situation **3)**, (See Fig. 5.8) the atomic structure on the right is exchanged with the one in figure 5.5b. The voltage is kept at 2.01V. Because the difference in work functions between the two electrodes (Calculated with regular DFT) are now the same as the applied bias times the unit charge, the electric field in the vacuum is zero. In other words, because situation **3)** fulfils equation 5.7, there is no field in the vacuum.

Full cell structures consistently result in an electric field in the vacuum layer, if the electrode potentials do not fulfil

$$eU = \phi - \phi_{ref} \tag{5.10}$$

where ϕ and ϕ_{ref} are the work functions of the atomic half cell structures. An electric field in the cavity is equivalent to a gradient in the chemical potential of protons through an electrolyte connecting the interface regions. On the other hand, atomic full cell structures

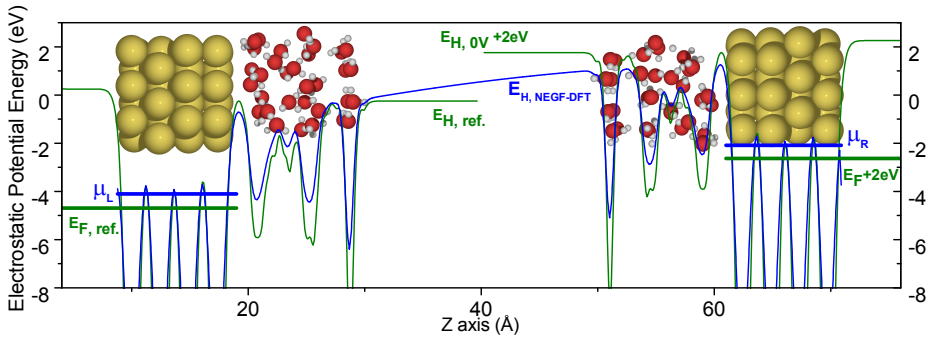

Figure 5.7: *Situation* ***2)*** *The same full cell atomic structure and half cell calculations as in figure 5.6. However the bias in the full cell calculation is now U = -2.01V. As observed on the electrostatic potential of the NEGF-DFT calculation (blue line), a non-zero electric field therefore remains between the electrodes due to the difference between μ_R and μ_L (shown as thick horizontal lines). The position of the potentials of the working electrode half cell (right) is such that the Fermi level (thick green line) is 2.01 eV higher than on the reference.*

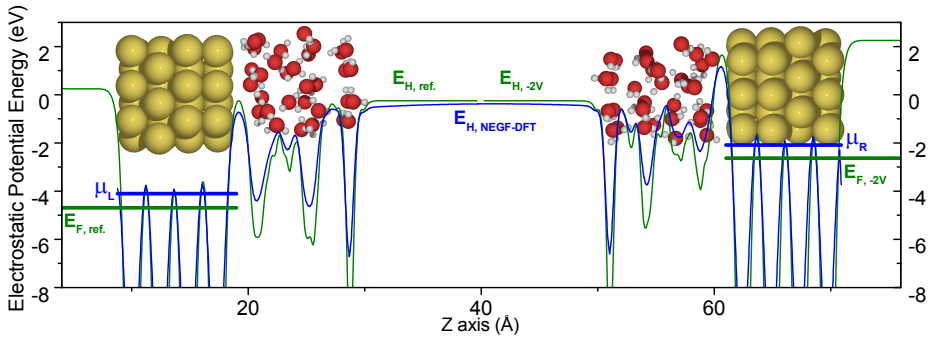

Figure 5.8: *Situation 3) The planar averaged electrostatic potentials, E_H, of the full cell calculation (blue line), and of the separate half cell calculations (green lines, left and right). The half cell electrostatic potentials are aligned to each other at the vacuum level outside the water layer. The Fermi levels are shown with thick horizontal lines for each structure. The working electrode (left) has a work function of 2.43 eV, whereas the reference electrode (right) has a work function of 4.44 eV. When applying $U = -2.01$ V, there is practically no electric field in the vacuum in this full cell calculation.*

that fulfil equation 5.10, accurately produces zero electric fields in the vacuum region.

In the situation, where fast diffusion can be assumed, and the protons are in thermodynamic equilibrium everywhere in the electrolyte, the above calculations clearly illustrate

that equation 5.10 is a constraint on the work function of the extended interface. Thus, knowing the work function from a slab/water structure, the U value which fulfils the thermodynamic constraints is known. This is very encouraging, because it is therefore possible to rely on half-cell calculations for studies of the interface under various applied bias and pH. This means there is no difference to using external or internal electric field as constraints on the interface atomic structure. Now that this is confirmed, we proceed with the derivation of pH-dependent free energy, ΔG, for the slab/water structures. Thereby the grand canonical ensemble can be formed and analysed to determine the structure of the interface from pH and U_{RHE}.

5.4 Generalized Computational Hydrogen Electrode

The pH of the solution governs the internal dipoles of the interface, since the work function and the U_{RHE} are both linked to the pH. This was shown in the previous section for the electrode potential and equation 5.5 shows how the proton work function is related to the pH. In this section, the pH dependence on the free energy is derived and it is shown how the grand canonical ensemble for the interface exchanging protons and electrons can be calculated.

The free energy of the interface with n protons + electrons inserted is generally:

$$\Delta G^{int} = E(n) - E(n=0) - n(\mu_{H^+} + \mu_{e^-}) - T\Delta S + \Delta ZPE \tag{5.11}$$

From the computational hydrogen electrode, we have:

$$\mu_{H^+} + \mu_{e^-} = \mu_{H_2} + eU_{RHE} \tag{5.12}$$

From the previous section the constraint linking bias and work functions is imposed:

$$eU_{RHE} = \phi_{e^-} - \phi_{e^-}^{ref} \tag{5.13}$$

At pH = 0, we have $\phi_{e^-}^{ref} = \phi_{SHE}$ from the definition of the standard hydrogen electrode. As a function of pH, the proton work function was shown in equation 5.5 to be:

$$\phi_{H^+}^{ref} = \phi_{H^+}^{0} + 2.303 k_B T \cdot pH \tag{5.14}$$

Since the vacuum level is the same for electrons and protons we have:

$$\phi_{e^-}^{ref} = \phi_{SHE} - 2.303 k_B T \cdot pH \tag{5.15}$$

Combining the above with equation 5.13, yields:

$$eU_{RHE} = \phi - (\phi_{SHE} - 2.303 k_B T \cdot pH) = -\mu_{H^+ + e^-} \tag{5.16}$$

Using this with equation 5.1, the relative free energy of an interface state can thereby be written

$$\Delta G^{int} = E(n) - E(n=0) - n\mu_{H_2}/2 - \phi_{SHE} + \phi_{e^-} + k_B T \cdot pH - T\Delta S + \Delta ZPE \tag{5.17}$$

The two last equations provides the relative free energy of each state as function of pH and potential, and thus it is the key to modelling the electrochemical interface.[120] So far the only ions that have been included are protons, but it is straight forward to include the ionic chemical potentials of counter ions. An example is therefore given in the following on how to account for counter ions in the free energy.

5.4.1 Counter ions

Calculating the free energy of adding other ions along with protons is now straightforward. Let's use chloride as an example. Chloride ions are only added to the interface system, while electrons are removed to keep the system charge neutral. Thus, the integral free energy of states with varying numbers of chlorides and hydrogens is:

$$G^{int} = E(n_H, n_{Cl}) - E(n_H = 0, n_{Cl} = 0) - n_H(\mu_{H^+ + e^-} + \mu_{H_2}/2) - n_{Cl}(\mu_{Cl^-} - \mu_{e^-}) \tag{5.18}$$

Chloride gas (Cl_2 (g)) is a system, which can be handled easily by DFT, and therefore it can be used as reference. The equilibrium potential of the reaction:

$$\frac{1}{2} Cl_2(g) \leftrightarrow Cl^-(aq) - e^-(m) \tag{5.19}$$

is at 1.36 V versus SHE, when the Cl ions in solution go to a 1M solution. Thus, for an electrode at 0 V versus SHE, the chemical potentials obey the following relation:

$$\mu_{Cl_2}/2 \quad = \quad \mu_{Cl^-}(1M) - (\mu_{e^-}^{SHE} - 1.36eV) \tag{5.20}$$

$$\mu_{Cl^-}(1M) \quad = \quad \mu_{Cl_2}/2 + (\mu_{e^-}^{SHE} - 1.36eV) \tag{5.21}$$

Inserting this into equation 5.18 leads to:

$$\begin{aligned} G^{int} &= E(n_H, n_{Cl}) - E(n_H = 0, n_{Cl} = 0) \\ &- n_H(\mu_{H^+ + e^-} + \mu_{H_2}/2) - n_{Cl}(\mu_{Cl_2}/2 + \mu_{e^-}^{SHE} - 1.36eV - \mu_{e^-}) \end{aligned} \tag{5.22}$$

Note that the electron reservoir is still only measured relative to the hydrogen electrode. The difference in chemical potentials of electrons at the working and the hydrogen electrode is the voltage, which is already known:

$$\mu_{e^-} - \mu_{e^-}^{SHE} = -eU_{SHE} = \phi_{SHE} - \phi \tag{5.23}$$

Inserting that leads to the useful expression for the free energy:

$$\begin{aligned} G^{int} &= E(n_H, n_{Cl}) - E(n_H = 0, n_{Cl} = 0) \\ &- n_H(\mu_{H^+ + e^-} + \mu_{H_2}/2) - n_{Cl}(\mu_{Cl_2}/2 + \phi - \phi_{SHE} - 1.36eV) \end{aligned} \tag{5.24}$$

Changing the chemical potential of chloride ions will enter as an additional term, so that we can define:

$$\mu_{Cl^- - e^-} \equiv \phi - \phi_{SHE} - 1.36eV + 2.3k_BT \ln \frac{a_{Cl}}{a_{Cl}^0} \tag{5.25}$$

where a_{Cl}^0 is the activity of Cl ions at 1M. An analogous expression can be made for any other counter ion, as long as the equilibrium potential versus SHE is known.

5.4.2 Discussion

The physical consequence of equation (5.16) and the expressions for the interface free energies, is that the U_{RHE} scales directly with the work function, given a constant pH. The other way around, given constant U_{RHE}, the dipole must change when varying the pH. Since the work function is directly linked to the interface dipole, one must expect that pH effects in the atomic scale electrochemical interface come from the interface dipole. [120]

Previously, the effect has appeared in calculations on relaxed atomic scale metal/water structures [120,142] and metal/oxide structures [143]. The conclusion was that at constant electrode potentials, the most stable configurations were oriented differently depending on the

pH or ionic chemical potential. However, these studies were proofs of concept based on rather small ensembles of structures, (around 100 states). The following sections of this chapter presents calculations with the aim of sampling many more states to further understand the capabilities of this methodology. Figure 5.9 shows plots of the free energies, G^{int}, of ensembles generated by molecular dynamics.

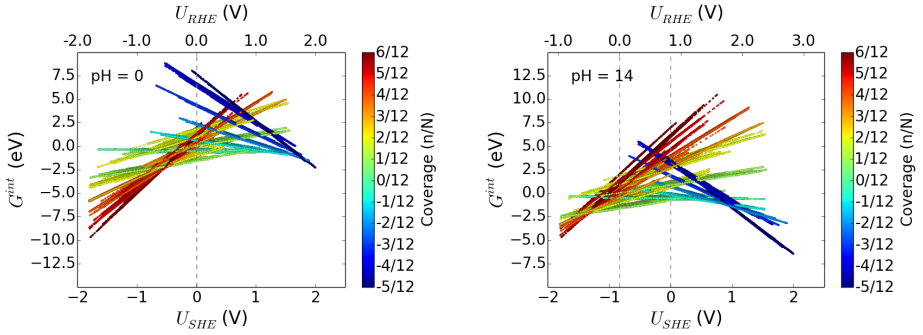

(a) pH 0 (b) pH 14

Figure 5.9: *Calculated G^{int} versus U_{SHE} and U_{RHE} (bottom and top axis respectively) for all atomic structure states, sampled from a molecular dynamics of the Au(111)/Water interface. n/N denotes the number of H atoms added to the neutral water system, and this value is shown for every state by color as indicated by the colorbar. The two plots show projections of G^{int} onto $pH = 0$ and $pH = 14$. The sample contains a total of 72000 states.*

With large ensembles of interface states, the statistical approach can be taken to calculate the quantities, that are of interest to understand the electrochemical interface. If this approach becomes feasible, it may prove to be a very powerful tool to understand atomic scale interface systems in details. Elaboration on the production of the larger ensembles of states is presented in section 5.5. Before that, a few examples are given of interesting quantities to characterize the structure of the interface.

5.4.3 Quantities Characterizing the interface

Quantities of interest could be any property of the interface at the atomic scale. Usually they are connected with an experimental observable, and thus they can be used to benchmark the simulations. In this section, just a couple of examples of observables that are used in the results section (5.8) are presented.

Excesses and surface coverage

The interface excess, usually denoted Γ, is the surface specific density of a species in one of the two phases of the interface region. Γ_{H^+} is the proton excess, also called the proton charge. The proton excess in a given micro state can be evaluated by counting the number of hydrogen atoms from a distance above the specifically adsorbed hydrogen, (around 1.9Å from the surface atoms), and to the top of the unit cell, subtracting two times the number of oxygen atoms. The resulting number of protons is normalized to the number of surface atoms, to obtain Γ.

Surface coverage is denoted θ and it denotes chemisorbed species. This defined as the number of excess atoms between the surface atoms and a distance of around 1.9Å (in the case of hydrogen). At this distance the density is usually zero. There is no difficulty in distinguishing specifically adsorbed hydrogen atoms from protons.

Geometry distribution functions

The interfacing electrolyte phase can be characterized by the distributions of various geometries. The typical geometries for characterizing water near a surface are distances between the surface and solvent atoms, distances between pairs of oxygen atoms or the angles between groups of three oxygen atoms. All of these can be evaluated by making histograms, with some normalization.

One of the most interesting quantities for characterizing the metal-water interaction is the distribution, $G(z)$, of distances between atoms and the surface. This quantity is interesting because it can reveal whether the surface is hydrophobic or hydrophilic, and how layered the water is near the surface. It is written as:

$$G(z) = \frac{1}{N^2 \rho \cdot X \cdot Y \cdot \delta z} \sum_{i}^{N} n(z) \tag{5.26}$$

where ρ is the average number density of the atom in water, X and Y are the dimensions of the unit cell, z is the distance from the surface and N is the number of states. The sum double counts all distances, so N^2 appears in the normalization.

The so-called pair-distribution function of the oxygen atoms, $G(r)$, is normalized to the number density of water molecules. It is therefore written:

$$G(r) = \frac{1}{N^2 \rho \delta V} \sum_{i}^{N} n(r) \tag{5.27}$$

Near a surface, some of the volume around each atom is occupied by surface. In addition, the number density is really a function of the distance to the surface. This function is basically $G(z)$, which is defined in the above. Therefore one can take two approaches to the normalization: **1)** The pair distribution is simply evaluated in the plane parallel to the surface, for atoms in a narrow distance interval from the surface. This 2-dimensional distribution is:[46]

$$G(r) = \frac{1}{N^2 \rho \cdot 2\pi r \delta r} \sum_{i}^{N} n_i(r) \tag{5.28}$$

This is the simplest solution to the problem, and it is used later in this thesis. The disadvantage, is that distances are not exactly reproduced, because their out of plane component is ignored. In experiments, to which the simulations would be compared, the real distances, including the out-of-plane component, would be the observable. The out-of-plane component is small, however, if the evaluation interval normal to the surface is much smaller than the pair-distances.

Approach **2)**: The distribution is calculated in all three dimensions, again in an interval close to the surface. The integration volume is a the shell of sphere, which is capped at the surface and at the maximum distance from the surface[144]. The problem with approach 2 is that it is hard to define exactly where the surface ends.

Both approaches are subject to the problem, that density is a function of the distance from the surface, and that they are only meaningful in a narrow interval. The boundaries of this interval is ambiguous. Surface sensitive experiments will most likely also have varying sensitivity at various distances from the interface. Approach 1 became preferred for it's simplicity, and because it does not depend on the distance from the atoms to the surface plane, which is ambiguous.

5.5 Generating micro states

In order to find the most relevant water structure out of every possible configuration, given the chemical potentials, it is in principle necessary to calculate the free energy of every water structure in the configuration space. Most first principles calculations of the properties of liquid water use molecular dynamics, due to it's advantageous efficiency in creating relevant structures.[145]

With a set of dynamics trajectories of equal temperature, each with a fixed number of hydrogens, the question arises: How many states should be sampled with each number of hydrogens, n to give the correct weight in the grand partition function and calculate the correct average $< n >$? Other types of grand canonical ensemble simulations are sampled with Monte Carlo algorithms. Unfortunately, directly guessing new states for a Monte Carlo algorithm is difficult for water, because of difficulty in finding stable positions for insertion of particles. For this project, it was therefore decided solve the problem by implementing a Monte Carlo algorithm, which walks between the states from the dynamics simulations, thereby constructing the grand canonical ensemble. More on the grand canonical ensemble is written in section 5.8.1.

In the following, the method that was applied for sampling states with molecular dynamics is presented.

Atomic Scale model

In every step in a molecular dynamics simulation, a DFT calculation provides the potential energy and the work function, which is used to find the relative free energies. The atomic slab model has periodic boundary conditions in the plane and non-zero boundary conditions out of the plane, with a vacuum region to get the work function. The surface is as usual represented by a slab of a few layers of metal atoms, while the electrolyte is represented by water molecules which are free to move in the dynamics. An artificial boundary have to be made to bound the electrolyte and keep it from desorption into the vacuum. In the present simulations, this boundary is represented by one constrained layer of water. This layer is a relaxed layer with zero net dipole normal to the plane, since the bulk electrolyte does not have any net dipole moment.

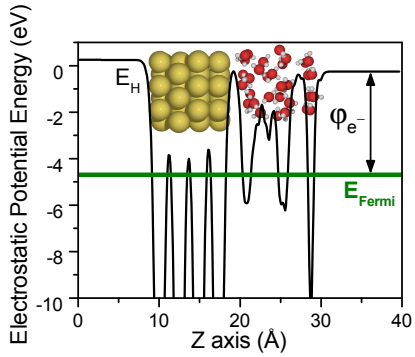

Figure 5.10: *Atomic slab/Water model shown with the electrostatic potential energy, E_H, averaged in the XY plane. The outermost layer is kept constrained, while the other water molecules are free to move in the molecular dynamics.*

5.5.1 Molecular Dynamics

A molecular dynamics algorithm solve the classical equations of motions for a set of particles, each of which have momenta and positions. If the particle index is i, the positions are, $\mathbf{x}_i$, the mass is m_i and the forces on the particle are $\mathbf{F}_i$. The equations of classical equation of motion is a set of second order differential equations which are written

$$m_i \mathbf{a}_i(x_i) = \mathbf{F}_i(x_i) \tag{5.29}$$

The forces, $\mathbf{F}_i$, may in principle be obtained from classical conservative force fields or, as in the present context, from electronic structure calculations. Solving equation 5.29 is done numerically in every time step.[146] The dynamics algorithm of choice in the present work is based on the Verlet.

The Verlet algorithm can be obtained from a third order Taylor expansion of the positions at timestep $t - h$ and at time step $t + h$, where h is the size of the time step. These are written:

$$\mathbf{x}_i(t-h) = \mathbf{x}_i(t) - h\mathbf{v}_i(t) + \frac{h^2\mathbf{a}_i(t)}{2} - \frac{h^3\mathbf{b}_i(t)}{6} \tag{5.30}$$

$$\mathbf{x}_i(t+h) = \mathbf{x}_i(t) + h\mathbf{v}_i(t) + \frac{h^2\mathbf{a}_i(t)}{2} + \frac{h^3\mathbf{b}_i(t)}{6} \tag{5.31}$$

where $\mathbf{v}_i(t)$ are the velocities, $\mathbf{a}_i(t)$ are the accelerations and $\mathbf{b}_i(t)$ are the third order derivatives of $\mathbf{x}_i(t)$ with respect to time. By subtracting them from each other, the

position in the next time step is obtained in a second order form:

$$\mathbf{x}(t+h) = 2\mathbf{x}(t) + h\mathbf{v}(t) + h^2\mathbf{a}(x(t)) \tag{5.32}$$

where the velocities, $\mathbf{v}(t)$ are:[146]

$$\mathbf{v}(t) = [\mathbf{x}(t+h) - \mathbf{x}(t-h)]/2h \tag{5.33}$$

and the velocities in the next time step, $\mathbf{v}(t+h)$, can be calculated using:

$$\mathbf{v}(t) = h\frac{\mathbf{a}(t) + \mathbf{a}(t+h)}{2} \tag{5.34}$$

The Velocity Verlet utilizes the following procedure[147,148]:

1 Calculate $\mathbf{x}(t+h)$ from equation 5.32

2 Calculate $\mathbf{a}(t+h)$ from forces at $(\mathbf{x}(t+h))$

3 Calculate $\mathbf{v}(t+h)$ from equation 5.34

Forces are commonly calculated using classical force fields, due to their computational efficiency. However, the work function is needed for every state to calculate the free energy, and the details of the chemical interactions between electrode and electrolyte molecules are of interest. Therefore the forces are obtained through DFT calculations in the present work. Molecular dynamics with forces obtained from DFT calculations is commonly referred to as ab initio molecular dynamics, (AIMD).

Two general classes of AIMD exist. Born-Oppenheimer molecular dynamics (BOMD) completely decouples the motion of the atomic nuclei from that of the electrons and it uses e.g. the Velocity Verlet while calculating the forces from a DFT calculation in every time step. The second class is the Car-Parinello (CPMD), in which the nuclei are still classical, and the Kohn-Sham wave functions are not converged in every time step. Instead, the electron density is propagated in a classical manner where it has a fictitious mass and it is included in the equations of motions.[149] CPMD requires very small time steps to be effective, and this may be particularly beneficial, if time-dependent quantities are of interest, since small time steps are then needed anyway. Finally, it is also possible to implement quantum nuclei, although the computational cost of this increases too much for our present goals. More on the state of the art in simulating water dynamics can be found in a review by A. Hassanali.[150] The following sections presents the parameters for the

dynamics, and section 5.6 presents the parameters for the electronic structure calculations.

Only static observables are evaluated as explained in section 5.4.3, and the MD algorithm is only used as a means to generate unique micro states. Although CPMD is faster than BOMD with a plane wave basis set, it is not implemented with an LCAO basis, which also improve efficiency. For the calculations in this thesis, BOMD dynamics with the LCAO basis sets were used.

The various quantities, which are obtained from weighted averages may be well defined after averaging over smaller or larger time scales. For example, the average distance between H and O atoms in water can be obtained by averaging over a few oscillation periods and sampling longer than that will not change the average. Water translation and reorientation has longer characteristic time scales, and larger structural changes occur over even longer time scales. The dynamics algorithm will have to generate a sufficient number of states to obtain and preserve the averages of interest. In addition, the states are weighted with the probability, which is given by:

$$p_i = \frac{1}{Z} \exp\left(-G^{int}/k_B T\right) \tag{5.35}$$

The energy distribution of the states in the ensemble is thus also important. States with much higher energies than the most stable ones will be irrelevant in the grand canonical scheme, and generation of such states is therefore essentially a waste of time. Thus, the algorithm has to generate many unique micro states, preferably with Boltzmann distributed total energies.

Obtaining a useful accuracy and speed of production is not trivial, since a long list of parameters needs to be fine tuned. One of the most essential of these is the time step, which is explained below. Other important parameters are the thermostat, (Discussed in section 5.5.2), and those of the electronic structure calculation, which are addressed in section 5.6.

Time step

Water is an intrinsically difficult system for molecular dynamics simulations because the relative difference in mass between the hydrogen atoms and the oxygen atoms means they move on different time scales. It is therefore a challenge to get a long enough sampling

time to translate water molecules, while describing the hydrogen stretching motion with sufficient accuracy. The consequence of not resolving the all time scales finely enough is noise in the total energy. This can be observed in figure 5.11, where the total energy of trajectories with various sizes of the time step are compared.

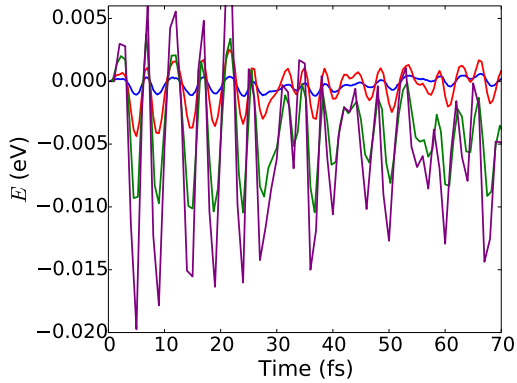

Figure 5.11: *The total energy plotted vs. time for various sizes of the timestep. The magenta line with the largest oscillations is with a timestep of 1 fs, the blue line with the smallest oscillation has a timestep of 0.25 fs, and the red and green lines have time steps of 0.5 fs and 0.75 fs respectively.*

Usually, the noise root mean square of the total energy grows linearly with the time step in a Velocity Verlet simulation[146]. It can be observed, that the simulation with time steps larger than 0.5 fs have noise on the order of k_BT. Previous AIMD dynamics simulations of water[151] with GPAW, used a constraint to fix the O-H bond lengths to eliminate the fast O-H stretching mode from the simulation, thus allowing a time step of up to 2 fs. Constraints could not be used in this project, since protons and hydroxides would have to be included in the simulations, and their interaction with the surface would be affected dramatically by constraints. However, the surface itself was kept constrained. For sampling runs for the grand canonical analysis, the most efficiency was obtained with a time step 0.5 fs.

5.5.2 Temperature

The total internal energy E_{tot} is the sum of the kinetic and potential energies

$$E_{tot} = E_{kin} + E_{pot} \tag{5.36}$$

During a simulation, the total energy is constantly exchanged between kinetic E_{kin} and potential energy E_{pot}, but the total energy stays constant, if the forces are calculated with enough accuracy. Therefore the simulation is in the micro canonical ensemble, where the number of particles, the volume and the energy is conserved, (constant NVE). In reality, the system of interest has a constant temperature, usually 300K.

For the micro system, temperature is given by the equipartition theorem:

$$\frac{3}{2}k_B NT =< E_{kin} > \tag{5.37}$$

where N is the number of particles.[152]

There are several methods for setting the temperature of the simulation. One may simply use a starting configuration for the system with momenta corresponding to the desired temperature and propagate a Velocity Verlet, which conserves the total energy and thereby also the average temperature. However, when starting the simulation, an equilibration of the system always takes place.
A finite amount of energy is often exchanged between kinetic and potential energy during initial equilibration and the set temperature is not exactly obtained. Since the grand canonical analysis (See section 5.4) have to include states with varying numbers of particles, the ensemble must be constructed from many trajectories. For this reason, all the trajectories should have exactly equal average temperatures. As evident from equation 5.37, an offset in average temperature of just a few K can cause one trajectory to be several $k_B T$ more stable than others. A thermostat can be introduced to obtain and keep the same set temperature in all the trajectories. Thermostats aim to employ dynamics in the canonical ensemble (NVT), where number of particles, volume and temperature is conserved. On average, the total energy is also conserved in the NVT ensemble, if the system is in equilibrium.

5.5.3 Canonical ensemble dynamics

There are a wide variety of thermostats for controlling the temperature of the dynamics. Common to them all is that they exchange energy with the system through a weak coupling. The coupling strength is set through one or more tunable parameters and it generally has to be strong enough, so the average set temperature is obtained without equilibrating for too long. At the same time, it has to be weak enough that it is only a

very small perturbation to the dynamics, i.e. it has to equal the NVE dynamics, in the weak coupling limit. Too strong thermostats often result in large fluctuations in the total energy and the temperature.

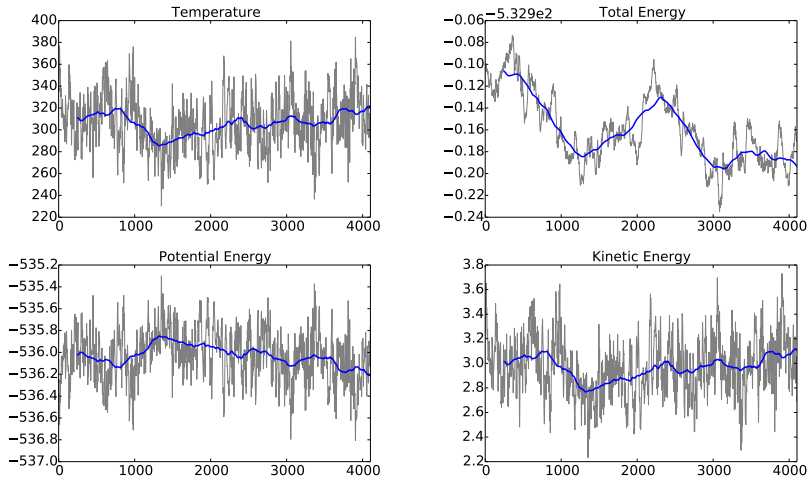

Figure 5.12: *T, E_{kin}, E_{pot} and E_{total} plotted vs. time for a an example dynamics trajectory. The gray line is the actual tractory and the blue line is the average over 500 time steps. Each time step is 0.5 fs and a Berendsen thermostat with a characteristic time constant of 1000 fs was applied to obtain the set temperature of 300K. A significant drift is still present in this trajectory.*

The Berendsen thermostat[153] controls the temperature by rescaling all particle velocities in every time step with the factor:

$$\lambda(t) = \sqrt{1 + \frac{\Delta t}{\tau_B}\left(\frac{T_{set}}{T(t)} - 1\right)} \tag{5.38}$$

where T_{set} is the desired temperature, $T(t)$ is the temperature at time step t and τ_B is the characteristic time constant of the thermostat. This thermostat reproduces the water structure well for water with time constants larger than 100 fs[154]. However, the total energy fluctuations can easily become larger than $k_B T$, and to avoid this a τ_B of around 500 fs is needed.

Other thermostats, such as the Langevin and the Nosé-Hoover, add some terms to the forces instead of rescaling velocities. In the Langevin thermostat, the first additional

term is a friction force, which slows movement and a second term adds small fluctuations to the forces, which heat up the system. These two terms keep each other in balance at the set temperature.

The Nosé-Hoover thermostat only adds a friction force, but the friction coefficient varies from negative to positive, depending on the measured temperature, so that it speeds up particles, when the temperature is too low and it slows down particles when the temperature is too high. The friction coefficient acts as an additional degree of freedom, which exchanges energy with a heat bath. This thermostat is shown analytically to imitate the canonical distribution [152].

The Berendsen thermostat was the most used thermostat in the present work, due to it's efficiency in equilibrating temperature and in dampening temperature and total energy oscillations. For the Berendsen thermostat, there is only one parameter to converge, which is the characteristic time constant, τ_B. When testing τ_B, it is impossible to distinguish total energy drift from energy exchanged by the thermostat. The time step and other parameters should therefore be tested first and optimized with the thermostat switched off, i.e. with the Velocity Verlet only.

5.6 Electronic Structure

A number of choices of methods and parameters are important for the electronic structure calculations. The information, which must be obtained from the electronic structure is most importantly the energy of every state and the forces to propagate the dynamics simulations. To obtain the free energy, we additionally need the work functions of every state. In the following, different choices of parameters and methods for the electronic structure calculations are discussed in perspective of obtaining this information efficiently.

5.6.1 Work function

An essential quantity for the model is the work function measured outside the electrolyte layer. After each step in the MD simulation, the work function of the state was stored along with the energy, atomic numbers and positions ect. in an ASE database file [69]. The database can be searched to extract the needed data, to monitor the dynamics or to carry

out *a posteriori* analysis. An example of the work function in a dynamics trajectory is plotted in figure 5.13.

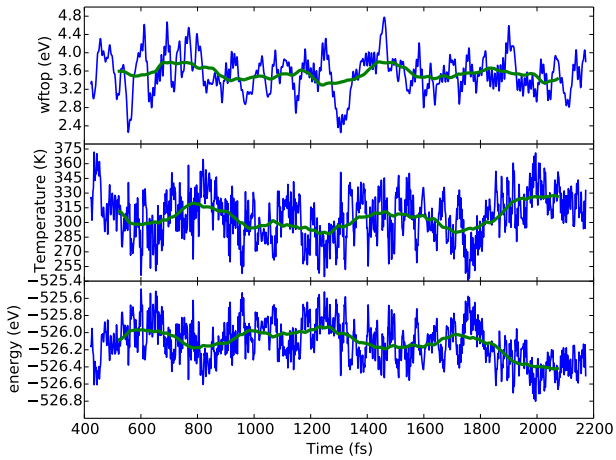

Figure 5.13: *Top panel: work function versus time. Bottom panel: potential energy versus time. This trajectory is a Water/Au(111) interface at 300K. The green line is the averaging over 400 fs.*

The work function is directly linked to the absolute electrode potential (equation 5.10), which means that the states that are relevant at a certain electrode potential must have the corresponding work function. Therefore it is fortunate that the work function varies rapidly enough in the the dynamics to obtain states in all of the potential range. It also does not appear that there is a strong correlation between work function and potential energy.

Convergence criteria

The Kohn-Sham self consistency cycle, (SCF), in the electronic structure calculation stops when self-consistency is achieved. The self-consistency criterion is when the difference in electronic energy and the maximum difference electronic density is with less than some value, when comparing with the previous SCF step.

The size of the convergence criteria are essentially the size of the error in the energy and the density. For the purpose of molecular dynamics, these electronic structure errors appear random, and they add inconsistency to the forces and thereby to the dynamics.

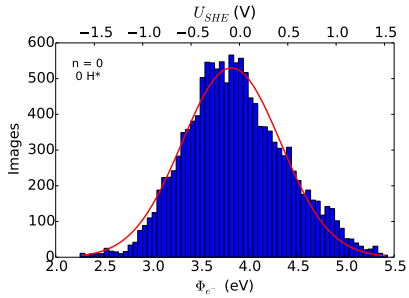

Figure 5.14: *Histogram of work functions of a Water/Au(111) interface, from the subset of structures with no chemisorbed species and no protons in the double layer.*

This inconsistency can break energy conservation and cause a drift to the total energy as shown with varying convergence criteria for the energy in Figure 5.15a and for the density in Figure 5.15b.

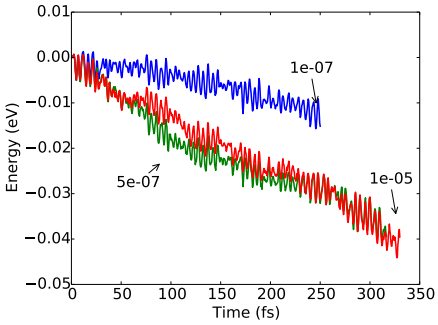

(a) *Convergence criteria for the energy marked by the labels. The density convergence criterion was* $2 \cdot 10^{-5}$ *Å*$^{-3}$.

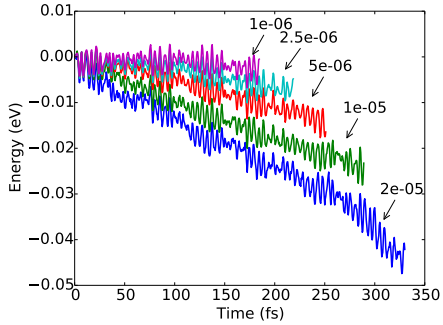

(b) *Convergence criteria for the density marked by the labels. The energy convergence criterion was* 10^{-6} *eV.*

Figure 5.15: *The total energy plotted vs. time, for trajectories calculated with various convergence criteria. The dynamics is a Velocity Verlet with a 0.5 fs time step.*

It is clear from tests of the convergence criteria, that the cost of reducing drift is quite high in terms of number of states sampled. In previous studies[151] of water using the GPAW code[31] the energy convergence criterion was set to 10^{-7} eV. In the present work, the convergence criteria of the density was used to control the drift/speed compromise, since it from Figure 5.15 appears that this more directly controls the drift. Although a thermostat was used, which compensates for any cooling or heating of the system over a

longer time scale, a lower drift may help to avoid oscillations. A value of $2 \cdot 10^{-5}$ Å^{-3} or $1 \cdot 10^{-5}$ Å^{-3}, was assessed to be the best compromise, and those values were used for the simulations.

k-point sampling

Exact absolute binding energies are not a priority in the development stage of the interface model, so time can be saved by using a sparse k-point sampling. However, if too few k-points are used for the simulation, i.e. less than a Monkhorst-Pack [34] sampling of 3×3, for a 3×4 FCC(111) super cell, then the metal has a small band gap, (See figure 5.16a).

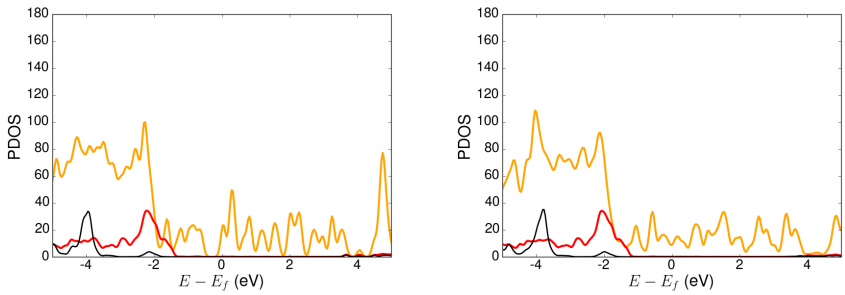

(a) *PDOS with* 2×2 *k-points.* (b) *PDOS with* 3×3 *k-points.*

Figure 5.16: *Projected Density of States (PDOS) calculated for the Au(111)/Water interface in a* 3×4 *FCC(111) super cell, with two different k-point samplings. The yellow line is the projection onto the atomic orbitals of gold, the red line is for oxygen and the black lines is for hydrogen.*

An important feature of a model of the electrochemical interface, is that it captures charge transfer between the metal and water in a realistic way [155]. This is because any charge transfer between the metal and water changes the work function of the interface structure, which should correspond to a chemical potential.
In addition, it is important that the metal slab efficiently screens the dipole moments and charges, so that the work function on the vacuum side of the metal stays constant. This is necessary, so adding or removing electrons to/from the system has the same energy with respect to the vacuum levels and so the work function scales directly with the interface dipole. As shown in figure 5.16b, 3×3 k-points is the most sparse k-point sampling in which the surface is still metallic.

Kohn Sham basis

Localized atomic orbitals (LCAO) were used as Kohn-Sham basis sets for all the dynamics simulations. Presently, the more complete basis sets, FD and plane waves are prohibitively expensive to use for generating large enough ensembles. LCAO represent a minimal basis set and are the computationally efficient choice, and they still reproduce geometries and energies to an acceptable level. The number of basis functions and the grid spacing determines the accuracy of this type of basis set. More on basis sets is written in section 2.5.
The basis set effect on geometries can be observed, in a test simulation, which was done with a rather coarse grid spacing of 0.25 Å. The distribution of ionic, $g(z)$, distances to the surface clearly reveals the effect from the coarse grid spacing.

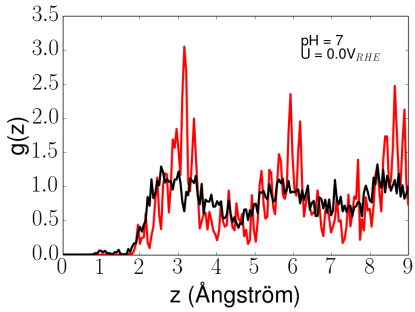

Figure 5.17: *Example of a distribution of ionic distances to a Pt(111) surface, calculated with a grid spacing of 0.25Å. The black line shows the hydrogen distribution and the red line shows oxygen distribution. A periodic noise in the distribution is visible, which comes from the eggbox error due to the coarse grid spacing.*

In figure 5.17 shows $g(z)$ for hydrogen a periodic noise is visible, which has a period equal to the grid spacing. This is a result of eggbox error, which is variation in the energy depending on atomic positions, relative to the grid points. The larger the grid spacing, the larger the error is, and in this test it was large enough to affect the interface structure averages. Later simulations used a grid spacing of 0.2 or 0.18, which is sufficient to avoid egg-box errors (This is evident when comparing Fig. 5.19a with Fig. 5.17).

Work functions also depend on the basis set, because the distribution of electronic density at the vacuum interface is affected if the basis set is insufficient. Usually, the electron spill-out is too small if the basis set is insufficient at the surface. That affects

the vacuum interface dipole, which in the end lowers the work function. This tendency is tested by a few single point calculations of relevant water structures spanning the potential range. The calculations are repeated with finite differences (FD mode) and localized basis functions (LCAO mode)[37]. The calculation is also done for the clean slab and for the template with a constrained top water layer.

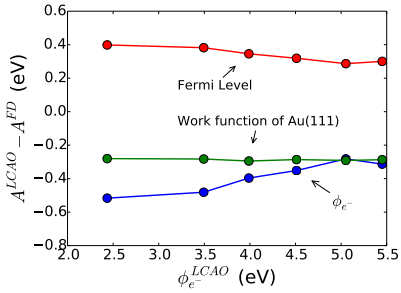

Figure 5.18: *The basis set error, evaluated by calculating the difference between results with LCAO basis sets and grid (FD) basis sets.*

As shown in Figure 5.18, LCAO mode systematically underestimates Au(111) work functions, on the backside of the slabs, by 0.29 eV ± 0.01 eV and water/vacuum interface work functions are underestimated by 0.3 eV to 0.5 eV. The experimental value for the work function of gold is between 5.2 eV and 5.3 eV,[156,157] and in FD mode the result is 5.23 eV ± 0.01 eV, so for the more complete FD basis set, work function values are expected to be reasonable. Since LCAO mode is used to sample structures with MD, a correction for underestimation of the work functions may be in order. To get a better benchmark of water structures with the corresponding electrode potential, ϕ_{SHE} is therefore corrected, and tentatively set to 3.9 eV, instead of the experimental value of 4.44 eV. More discussion on the distribution of work functions will follow in the results in section 5.8.2.

5.7 Water Structure

The main purpose of the methodology is to determine the structure of the interface, as a function of pH and electrode potentials. This is obtained by calculating the grand canonical averages, (at constant μVT), as outlined in section 5.4.

The structures presented from the various individual constant NVT ensembles can naturally not be correlated with any particular pH or electrode potential. However, pinning out the structures at various individual NVT ensembles is of interest for several reasons: **1)** Understanding the features in the distribution functions from the NVT ensembles are useful to identify effects of surface coverage or the presence of protons. That is necessary to separate those effects from the effects of electrode potentials and pH, (i.e. effects coming from the interface dipole). **2)** It makes it possible to compare the computations with other atomic scale simulations of water on interfaces. So the results from the NVT or μVT ensembles contains water structures, which are expected to be relevant and comparable to other simulations.

For this purpose, a set of simulations were made, in which the sample counts around 400000 states with a timestep of 1 fs, using the Berendsen thermostat[153] with a characteristic time constant of 500 fs. Correlation of structure averages to the initial conditions is always a concern in AIMD simulations, since the time scales that can be included are limited. Each coverage, included in this data set, was represented by 6 to 12 trajectories with different starting configurations. This arguably reduces the concern of correlation to the initial conditions, although each trajectory only contained sampling time between 4 ps and 8 ps. The starting configurations were water structures relaxed in combinations of up and down pointing layers stacked a-a or a-b, which were generated from relaxed water layers taken from previous works.[120,158] Addition or removal of protons from these configurations were done by adding or removing hydrogen to/from the water molecules closest to the surface and running a structure optimization before starting the molecular dynamics.

Only a single k-point was used for the 3×4 Au(111) super cell, the grid spacing was 0.2 Å and RPBE[27] was used for the exchange-correlation contribution to the energy. The surface was represented by four constrained layers of metal atoms and the electrolyte by 24 water molecules and 8 constrained water molecules as the top layer. 24 water molecules correspond to three hexagonal layers, if the structures were relaxed to form frozen water layers. The numbers of hydrogens n included were from -4 to +4, with or without at least one proton for the $n \geq 0$ subsets, and in some cases up to three protons were included.

Clean surface

This section evaluates the distribution functions characterizing the average water structures and how they vary at different amounts of protons and surface species. Before carrying out the grand canonical analysis of the water structure, it is useful to observe the distributions in the canonical ensemble in order to understand the features and what molecular structures they project.

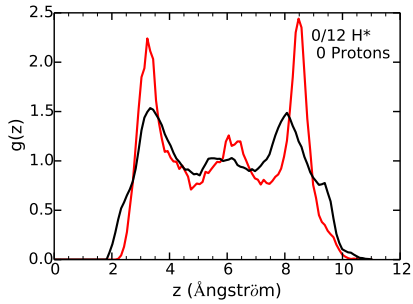

(a) *Pure water, no protons or chemisorbed species.*

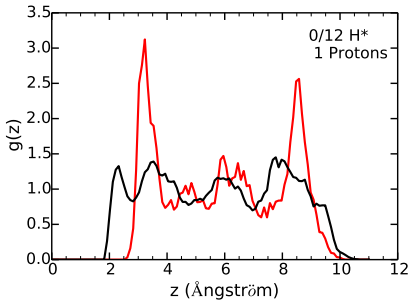

(b) *One proton, no chemisorbed species.*

Figure 5.19: *Distributions of ions versus distance to the Au(111) surface layer. The red line is the average density of oxygen ions and the black line is average density of hydrogen ions. They are unweighed averages from dynamics simulations of water/Au(111) in a* 3×4 *super cell, with* 1×1 *k-points in the plane, and 1 fs time steps.*

The first observation from the distribution of ions versus distance to the surface is that the water is layered. The confined volume between the surface and the constrained top layer cause three distinct layers of oxygen atoms. The oxygen atom density between the layers is not zero, but it is up to four times smaller than the center of the peaks. The layering of the hydrogen ions is much less distinct, with a ratio from peak to valley up to around 2. There is also a wide empty region from the surface to the water molecules, and a somewhat soft and gradual increase of atomic density from 2Å and out, showing that chemisorption does not take place.

In the first water layer, there is some density of hydrogens closer than the edge of the oxygen ion density, which is attributed to water molecules pointing one or both H-down. The distances of the first peak of hydrogens and the first peak for oxygens coincide, suggesting there is also a large number of water molecules with a hydrogen pointing parallel to the surface.

As evident from comparing figures 5.19 a) and b), introducing a proton causes a drastic change in the hydrogen features from the water nearest to the surface. The feature just outside 2Å, seem to be the most pronounced change when adding the proton. It may be explained by molecules pointing one H-down, due to attraction from the image charge on the metal from the extra proton. The first oxygen peak is around 1Å from the H-down peak, indicating that many molecules point one H-down, while hydrogen peak that was overlapping appear to be displaced slightly outward. This outward displacement is in accordance with many one H-down pointing water molecules, since the 120 degree angle will cause the other hydrogen to point up with a 30 degree angle corresponding to a position around 0.3Å outside the oxygen peak.

The clearest change in the oxygen distribution (red lines) is the new peak just below 5 Å, which should most likely be attributed either to a preferred position of the hydronium ion or to the solvation shell of the hydronium ion, if it prefers the first layer near the interface.

The effect of adding the proton also causes some more subtle changes in the oxygen pair-distribution functions, plotted in figure 5.20.
The oxygen pair distribution function for pure water near the surface, (See figure 5.20a),

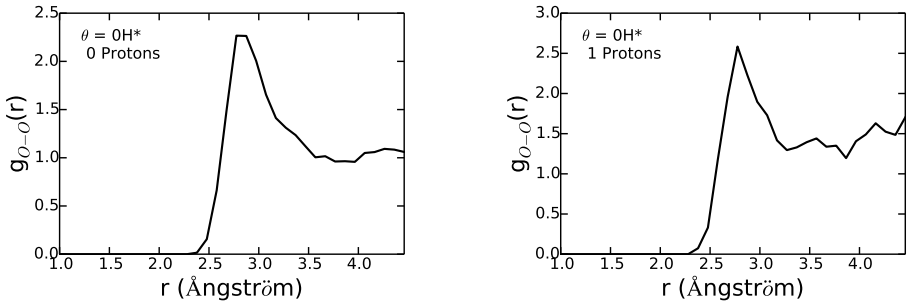

(a) *Pure water, no protons or chemisorbed species.*

(b) *One proton, no chemisorbed species.*

Figure 5.20: *Oxygen ion pair distribution functions in the plane, between 2.8Å and 3.8Å from the Au(111) surface atoms.*

reveals a clear nearest neighbour peak at 2.8Å. This is in resemblance to a high density liquid phase, which have many broken hydrogen bonds, and thus is not very ordered laterally[144]. This is in accordance with previous reports of disordered water structures on

noble metal surfaces in AIMD simulations[159].

The effect on the pair-distributions of adding a proton is rather weak. A slight sharpening of the first shell, and appearance of some soft peaks around 3.5Å and 4.2Å is visible in figure 5.20b. Previous simulations by Tuckerman et al.[160] show that protons produces shorter first O-O distances in the both Zundel ($H_5O_2^+$) or Eigen ($H_9O_4^+$) groups, while the O-H bonds are longer. Both Eigen and Zundel groups produces a peak in the O-O pair distribution between 4.0Å and 4.5Å, which may suggest that the peak observed at 4.2Å in the present study comes from those structures.

Hydrogen covered surface

AIMD simulations of water on hydrogen covered surfaces by A. Großet al.[159,161] show that the lateral ordering of the water layer on Pt(111) can become stronger due to a mono layer of hydrogen coverage. In the present simulations on Au(111), only up to 1/3 ML was considered. Yet, a similar effect is still visible.

Observing the distribution of hydrogens from the surface, shown in figure 5.21a, the adsorbates in hollow sites, at around 0.9 Å, are distinguishable from those in bridge sites or on top sites, at around 1.5 Å, (checked manually from a few individual images). Outside the distances corresponding to chemisorption, the first water layer resembles that with no chemisorbed species, (The latter is shown in Fig. 5.19a). A density of hydrogen is present closer than the oxygen density, indicating some H-down pointing water molecules. The gap between adsorbates and closest molecules is very small, but this is most likely only because the surface coverage is far below 1 ML. Reaction events were only caught in the early non-equilibrated parts of the trajectories, in which large forces or high temperature made them probable.

The layering of both hydrogen and oxygen is quite strong on the surface with a hydrogen coverage, indicating a stronger surface/electrolyte interaction. The central layer is particularly pronounced. The confined volume of the water was not varied, as hydrogens were added or removed, and thus one possible reason for the more pronounced layering is that the added surface hydrogens effectively take some volume from the water, which gets compressed a little more.

As observed from figure 5.21, adding a proton to the water layer completely dissolves

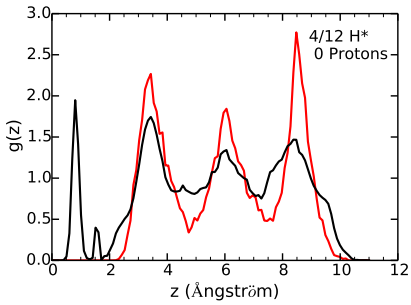

(a) *Pure water,* $\theta_H = 1/3$.

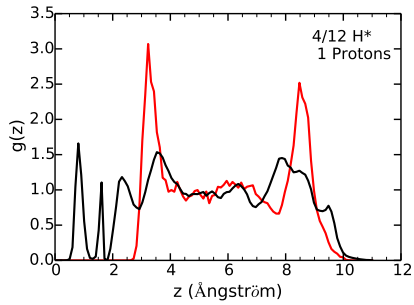

(b) *One proton included in the electrolyte layer,* $\theta_H = 1/3$.

Figure 5.21: *Distributions of ions versus distance to the gold(111) surface. The red line is the average density of oxygen ions and the black line is average density of hydrogen ions.*

the second layer for the oxygens, while the hydrogens order into a H-down peak and a peak close slightly outside the first layer of oxygens. As for the clean surface, the governing effect on the structure is probably the electronic counter charge to the proton, which sits on the metal surface and attracts the hydrogen ends of the water molecules.

Oxide covered surface

Introduction of oxidised species, (HO* or O*) on the surface causes great changes to the interface water structure, as seen in figure 5.22. The $g(z)$ for oxygen identifies atomic oxygens adsorbed in hollow sites at a distance of around 1.4Å from the surface plane, and it identifies HO* on top sites at around 2.0Å to 2.1Å, as derived by comparing snapshots with the distributions. Water molecules were not found specifically adsorbed on the Au(111) surface.

The layering of the water outside the surface is rather weak, except from a the boundary to the constrained layer. Even at the electrode interface, a the main peak is only due to chemisorbed species. Outside this layer, a soft peak is present around 3.5Å. It is at the same distance as the peak from water outside the the clean surfaces, so it is probably present over surface atoms that are not covered with adsorbates. These water molecules may donates and/or accept hydrogen bonds with the adsorbed HO*. This peak disappears completely, when the coverage is increased to $n/N = -5/12$, which may be an indication that there is no more space for any water molecules at the surface. The density

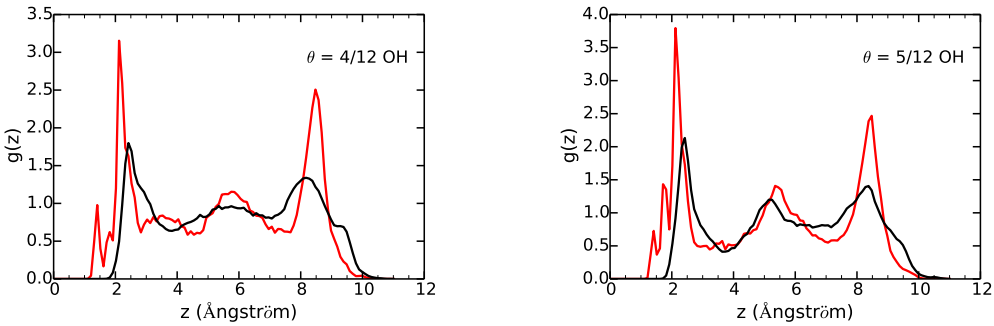

(a) *Pure water*, $\Gamma_H = -1/3$. (b) $\Gamma_H = -5/12$.

Figure 5.22: *Distributions of ions versus distance to the gold(111) surface. The red line is the average density of oxygen ions and the black line is average density of hydrogen ions.*

of oxygens or hydrogens does not go to zero above the HO* species at any coverage, and a continuous network of hydrogen bonds is most likely still there, even at 5/12 ML HO*.

The first peak of the hydrogen density $g(z)$ is slightly outside the first oxygen peak, indicating that HO* points a bit outwards. There is a second, very soft peak, which is slightly inside the oxygen peak of the second water layer, indicating that there are more donations of hydrogen bonds from the second water layer to the first, than the other way around.

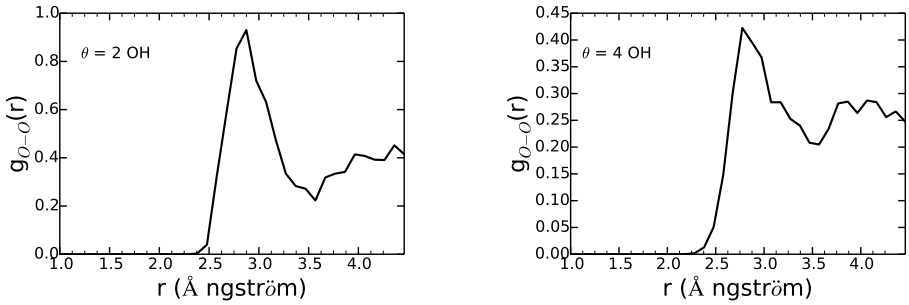

(a) $\theta_{OH} = 1/6$. (b) $\theta_{OH} = 1/3$.

Figure 5.23: *Oxygen ion pair distribution functions in the plane, between 3.0Å and 4.0Å from the Au(111) surface atoms.*

Examining pair-distribution function of the water layer outside from 3Å to 4Å, right

outside the HO* layer, shows a clearly distinguished second coordination shell, when the coverage is higher than 1/12 ML, as shown in figure 5.23. It still has a high density liquid characteristic, but the lateral ordering of the water has increased and formed more hydrogen bonds. It thus appear that an intermediate HO* coverage have an ordering effect on the water layer due to hydrogen bonds with the adsorbed HO*. At 1/12 ML HO*, the second shell is not clearly visible, and the $g(r)$ function looks much like that of the clean surface/water, and at 5/12, the layer of water has almost disappeared from the $g(z)$ function.

Discussion

Several of the features in the distribution functions could be explained by comparing the peak positions with distances in snapshots from the trajectories. All of the structure averages are only projections of the water structures, but no one of them give the complete picture. To improve the picture and further test the various identified structures, it would be beneficial to evaluate other geometries including the O-H pair distributions and the angles in triangles between three oxygen atoms ect. Developing tools for calculating these properties, however, are not the scope of this study, and there are various other projects on such tools[162], which can be taken in use at a later time.

For all plots of the distributions of ionic distances to the surface, $g(z)$, to the surface, it is observed that outermost part of the water structure remains almost invariant no matter the coverage, and presence of protons. This indicate that whatever is present at the interface, including distribution of electronic charge, is mostly screened by the two first layers of water.

Each coverage was represented by samples corresponding to at least 25 ps, by combining several trajectories. As seen in the oxygen pair distribution functions, $g(r)$ and the out-of-plane position distributions, $g(z)$, the peaks are very well defined, and the noise is low. The simulations presented in this section were run with just a single k-point, which makes the calculations a lot faster, than sampling with multiple k-points. Unfortunately, it is expected that the screening effects in the metal are affected significantly by running with less than 3×3 k-points in the plane as shown in section 5.6.1, and therefore another ensemble was generated for the following thermodynamics analysis on Au(111)/Water with a 3×3 k-point sampling.

In the following, results from the grand canonical analysis is presented to study the grand canonical thermodynamics including dependencies on pH and electrode potential.

5.8 Grand Canonical Analysis

5.8.1 Au(111)/Water

The results presented here for Au(111)/Water was calculated in with a four layer Au(111) slab in an orthogonal 3×4 super cell with 24 free water molecules and 8 molecules constrained as the top layer. Exchange-correlation contributions were approximated by the RPBE functional[27], the grid spacing was 0.18 Å and the k-point sampling was $3 \times 3 \times 1$. The dynamics had 0.5 fs time steps and the Berendsen thermostat[153] had a characteristic time constant of 1000 fs. The sample trajectories were 2 to 3 ps long after 1 to 2 ps equilibration. The main results on Au(111)/Water and the methodology are prepared for publication and included as Paper VIII in this thesis.

Adsorption Free Energies

The free energies of adsorption or proton insertion can be obtained as statistical averages. There is no simple method, however, for calculating the entropy contributions to the free energies in the electrolyte layer. The configurational entropy is therefore neglected for hydrogens added to the interface for the time being. This assumption is usually applied to chemisorbed species, where the entropy is small anyway, and here it is extended to the interface in lack of a proper estimate. Eventually, a correction for entropy should be included in some way or another. The entropy term might add a significant stabilization for protons in the electrolyte layer, so one should keep in mind that the free energies reported here for proton insertion may be over-estimated.

Using equation 2.41, the interface free energies were calculated for each coverage:

$$< G^{int}(n, \phi, pH) >= \frac{1}{N} \sum_{i}^{N} G_i^{int}(n, \phi, pH) \exp\left(-G_i^{int}(n, \phi, pH)/k_B T\right) \tag{5.39}$$

The differential adsorption energy is obtained just like in the previous two chapters, by

differentiating the integral energy with respect to n:

$$< \Delta G^{diff}(\phi, pH) > = \frac{\partial < \Delta G^{int}(n, \phi, pH) >}{\partial n} \quad (5.40)$$

$$= < G^{int}(n, \phi, pH) > - < G^{int}(n-1, \phi, pH) > \quad (5.41)$$

For the Au(111)/Water interface at $U_{RHE} = 0$ V, the adsorption free energies of hydrogens and HO* is shown in Figure 5.24.

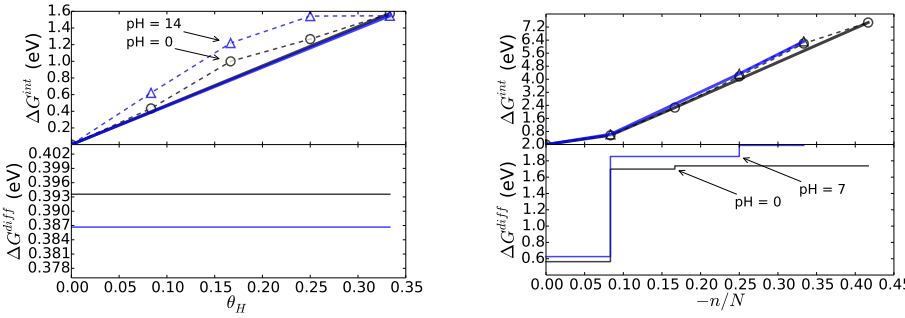

(a) *The average free energies of hydrogen adsorption.*

(b) *Average free energies of HO* formation by proton desorption.*

Figure 5.24: *Average free energy differences at 0 V vs. RHE. The top panels show the integral free energies, and the bottom panel shows differential free energies.*

Each integral free energy value is essentially an averages over a subset of states which has the work function corresponding to the pH and U_{RHE}, from a trajectory with a certain number of hydrogens added or removed. Keeping this in mind, while regarding the adsorption energy for hydrogen versus coverage, it appear that the trajectories with 1/12 ML to 3/12 ML are higher in energy than the one at 4/12 ML. The reason for this trend may be because the repulsive interaction for adsorbed hydrogen for some reason does not increase beyond a certain coverage. It can also, however, be because of small differences in temperature in the trajectories, which are rather short. The 3 ps trajectories are barely enough to get the total energies equilibrated, and in addition, the states that are relevant at any given potential and pH is only a subset of the total ensemble. To rule out such errors, tools for estimation of the correlation in the trajectories should be implemented, so it could be quantified how much the various properties, including the free energy is correlated with the starting configuration in the sample.

Differential adsorption energy also barely changes due to pH, although the trajectories with hydrogen coverages $\theta_H = 1/12$ ML to θ_H 3/12 ML show clear differences. Differences in energy at different pH come from a dependence of the average total energies on the work function.

Since the differences are taken in a work function interval, the differential energies will naturally only be accurate in potential intervals, where there are enough states sampled for both coverage n and $n-1$. To illustrate this, differential free energies of proton insertion are therefore plotted together with the histogram of number of states in each bin in figure 5.25.

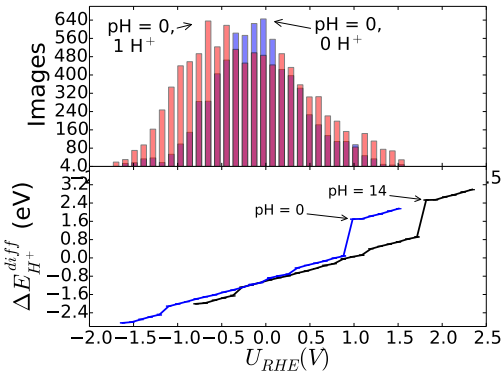

Figure 5.25: *The free energy of proton insertion plotted for pH = 0 and pH = 14. The top panel shows two histograms overlayed, both of which show the number of states at pH = 14 at the work function corresponding to the U_{RHE}, on the first axis. The left hand histogram in red color counts states with one proton included, and the right hand blue histogram counts states with no protons included.*

The plots of free energies show some sharp steps around the boundaries of the potential interval, where the statistics are less reliable, e.g. around $U_{RHE} = 1.0$ V in figure. To see the origin of this step, we can try and take a look at the different contributions to the free energy, which include the averaged kinetic energies and the averaged potential energies. These are shown in figure 5.26, and they have been evaluated as averages, still weighted to their probabilities, which includes the free energy:

$$< E^{int}(n,\phi,pH) > \quad = \quad \frac{1}{N}\sum_{i}^{N} E_i^{int}(n,\phi,pH)\exp\left(-G_i^{int}(n,\phi,pH)/k_BT\right) \quad (5.42)$$

$$< E^{diff}(n, \phi, pH) > \quad = \quad < E^{int}(n, \phi, pH) > - < E^{int}(n-1, \phi, pH) > \qquad (5.43)$$

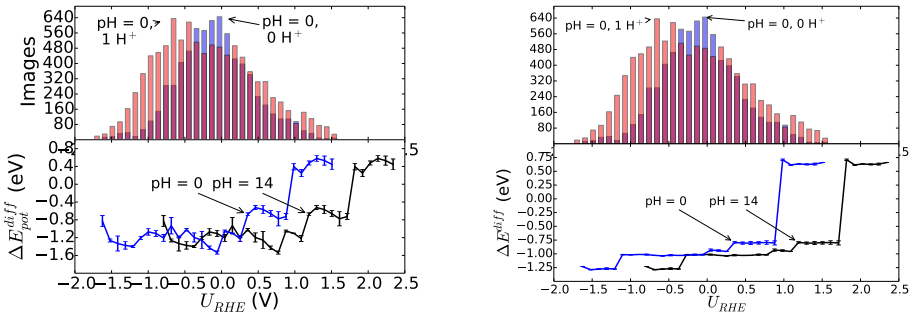

(a) *The potential energy of proton insertion*

(b) *The total energy of proton insertion*

Figure 5.26: *Energies for proton insertion plotted for pH = 0 and pH = 14, as functions of U_{RHE}. The top panels show histograms overlayed, which show the number of states at pH = 14, at the work function corresponding to the U_{RHE}, on the first axis. The left hand histogram in red color counts states with one proton included, and the right hand blue histogram counts states with no protons included.*

The potential energy averages, in figure 5.26a have quite large error bars, which come from the large exchange between kinetic and potential energy, which can be observed in figure 5.13 for one trajectory. In the total energy in Figure 5.26 the noise in the potential energy has been cancelled out, but the jump around 1 V versus SHE, has not. These steps also occur in other plots of differential adsorption energies for the proton, but they will probably move outward and disappear if the sampling is improved. The calculations presented in this chapter is, however, mainly a proof of concept, and further sampling and calculations of various other systems of interest can wait until the methodology for analysing and mining the data is more optimized.

The free energies of adsorption, and particularly of proton insertion, that are presented in this section may be difficult to compare directly with experiments, no matter how accurately they can be calculated. In addition to evaluating the free energy differences, it is therefore also interesting to evaluate numbers or coverages of the various species at different potentials as weighted averages from the grand canonical ensembles. Plotting the surface coverages versus potentials produce the Gibbs isotherms, and if they are differentiated, simulated differential capacitances is the result. They can be compared directly with experiments, and in the following it will therefore be shown how they can

be obtained.

Grand Canonical Partition Function

With a set of dynamics trajectories of equal temperature, each with a fixed number of hydrogens, the question arises: How many states should be sampled with each number to give the correct weight in the grand partition function and calculate the correct Gibbs isotherms? Other types of grand canonical ensembles are routinely sampled with Monte Carlo algorithms to obtain the equilibrium number of atoms. Unfortunately, directly guessing new states for a Monte Carlo algorithm is complicated for water, because of difficulty in finding stable positions for insertion of particles. For now, it was therefore decided solve the problem by implementing a Monte Carlo algorithm, which walks between the states from the dynamics simulations, thereby constructing the grand canonical ensemble with the correct weighting to number of hydrogens.

Metropolis Monte Carlo (MC) algorithms essentially calculates the probability weight function for the states in an ensemble. The approach is to walk stepwise from micro state to micro state, adding states to the ensemble in a manner, so the occurrence of states is distributed according to the probability weight function.

Each cycle of the algorithm chooses a random trial step, X_{t+1}. If the trial step has lower free energy than the present step, X_t, the trial state is accepted. If the trial step has a higher free energy, it is accepted with the probability $p_{t\to t+1}$

$$p_{t\to t+1} = \frac{\exp\left(G_{t+1} - G_t\right)}{k_B T} \tag{5.44}$$

It has been proven, that the resulting set of states are distributed with the probability weight function.[163]

To "anneal" the ensemble from the molecular dynamics trajectories, trial steps are chosen to increase or decrease the number of particles at equal attempt probabilities. The trial step can also conserve the number of particles. Thereby the equilibrium between particle count in the annealed ensemble is established[164].

Figures 5.27 show the free energies versus electrode potentials at pH = 0 and pH = 14, in (a) and (b), respectively for states of the annealed ensembles. The "raw" ensembles before the Monte Carlo annealing are shown in figure 5.9.

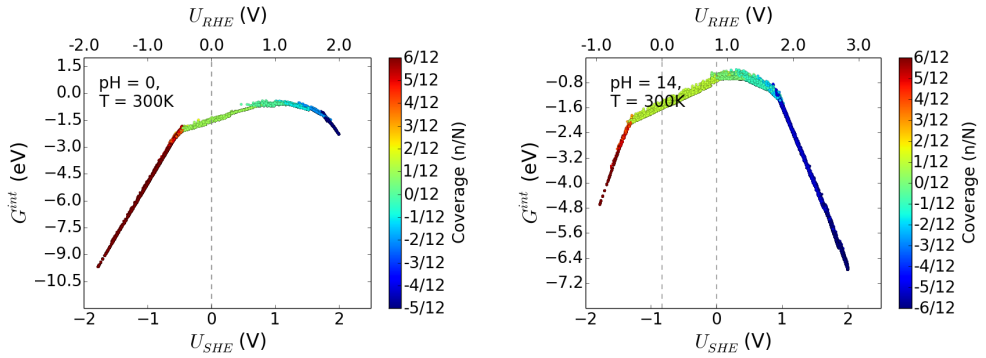

(a) $pH = 0$ (b) $pH = 14$

Figure 5.27: *Calculated G^{int} versus U_{SHE} and U_{RHE} (bottom and top axis respectively) for all atomic structure states, sampled from molecular dynamics and annealed to 300K with a Grand Canonical Monte Carlo sampling. n/N denotes the number of H atoms added to the neutral water system, and this value is shown for every state by color as indicated by the colorbar. The two plots show projections of Gint onto pH 0 and pH 14.*

Each state may appear multiple times, if it has a high probability of occurrence. Notice also the boundaries of the annealed ensemble. It is practical to cut the lower and upper boundaries for the work function in the raw ensembles and remove states outside the interval. Otherwise some numbers of hydrogens may be represented at the edges, with the most stable number being unrepresented, resulting in wrong results. This can also be observed from the histograms of work functions that reveal that the number of states in each work function bin is much smaller near the upper and lower boundaries. If the work function interval is limited by the band gap of the electrolyte, it may be possible to enlarge the gap using DFT+U, according to a study on relaxed water layers. [155]

After a grand canonical ensemble with the correct probability weight has been created, calculation of an average, $< A >$, reduces to:

$$< A > (\phi, pH) = \frac{1}{N} \sum_{i}^{N} A_i(\phi, pH) \tag{5.45}$$

where N is the number of micro states in each work function bin of the annealed ensemble. The following section present properties of the interface obtained by this method for Pt(111)/Water and Au(111)/Water interfaces.

Au(111)/Water

Previous computations have provided surface phase diagrams for several metals based on relaxed surface structures[49]. Here, the surface coverages are calculated as averages and presented in the form of Gibbs isotherms. Inserting Γ_{H^+} and n into equation 5.45 and plotting the averages versus U_{RHE} gives the Gibbs isotherms at each pH. These are shown in figure 5.28.

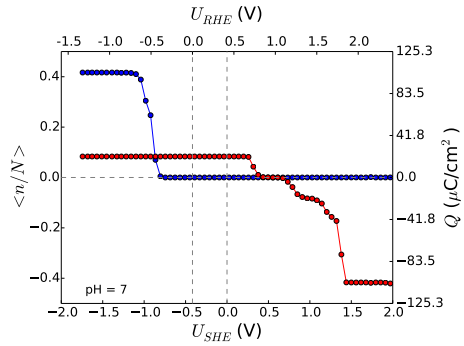

(a) *pH = 0. The blue data is the contribution from adsorbed hydrogen and the red data is $< n/N > - < theta_H >$, which is the contribution from solvated protons in the electrolyte layer above $< n/N >= 0$, and the contribution from oxidised species below $< n/N >= 0$.*

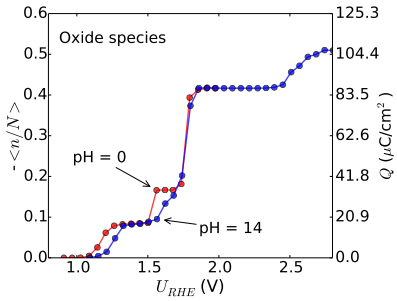

(b) *The coverage of oxidised species versus U_{RHE}, plotted for pH = 0 and pH = 7.*

Figure 5.28: *Simulated Gibbs Isotherms of hydrogen in the interface system. To separate (Γ_{H^+}) from (θ_H), the numbers of hydrogens above and below a distance of 1.8Å from the surface were counted separately.*

The plateaus for a hydrogen covered surface, a clean surface and the oxidised surface are clearly visible in the Gibbs isotherms, in figure 5.28a. The interval with a clean surface is quite wide, as was also the result when relaxed structures[49]. The negative part of $< n/N >$ is due to hydrogen deficient states, which have oxidised species on the surface. A zoomed view of this part is plotted in figure 5.28b. Since the isotherms for pH = 0 and pH = 14 are on top of each other, a pH dependence is not evident despite of the small differences in the free energies at pH = 0 and pH = 14. The $- < n/N >$ curve in figure 5.28b shows some plateaus, which indicate that there are destabilizing adsorbate interactions between the oxidised species at some coverages. If the adsorbates stabilized each other at all coverages, the curve would increase suddenly from 0 to the maximum coverage.

To compare with experiments, the differential capacitances are found by differentiating the isotherms. If it is assumed that all electrons inserted into the system, including the ones screening a solvated proton contributes to the measured current, differentiating $e < n/N >$ gives the differential capacitances:

$$Q = e < n/N > \tag{5.46}$$

$$C = | \frac{dQ}{dU} | \tag{5.47}$$

In cyclic voltammetry experiments, the differential capacitance can be obtained from the measured current, j, and the scan speed, v:

$$C = \frac{j}{v} \tag{5.48}$$

In figure 5.29, C is plotted together with experimental data at the relevant conditions, from cyclic voltammetry, (forward scan).

It is clear that the experimentally measured capacitances are consistently larger than the computed capacitances, and in the region above 1.6 V versus RHE, the currents correspond to many monolayers of charges. This is because Au surfaces are known to grow many layers of surface oxides at the most oxidising potentials [168], and that is not included in the present model.

In the reducing region, hydrogen evolution begins before the surface can be covered. DFT calculations suggest that atomic hydrogen on Au(111) is unstable and will instead form H_2 [80]. The features of the computed capacitances are so far in agreement with existing literature, as shown in figure 5.29. At intermediate potentials, where nothing is adsorbed, CV experiments show a small current from free charge that is transferred due screening charges in the electrode. The contribution to this charge from screening of protons is already counted in this methodology. Counter ions have not been included in the ensembles at the present stage, but they can be added to the ensemble in the future.

Another contribution to the free charge is screening of dipole moments in the double layer. It does not seem that this free charge can be accounted for directly in the present method. However, it is possible to find a potential of *minimum* free charge, as discussed further in section 5.8.2.

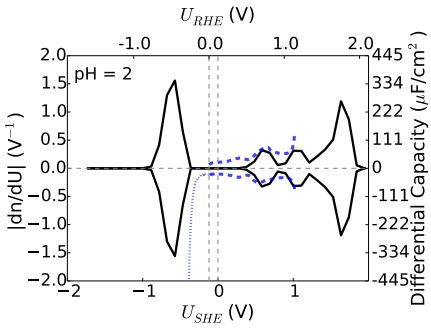

(a) *Black line: Computed differential capacitances at pH = 2. Blue dashed lines: Experimetal differential capacitances from CV's in 0.01M HClO4 by Hamelin et al.*[165] *in the oxidising region.*

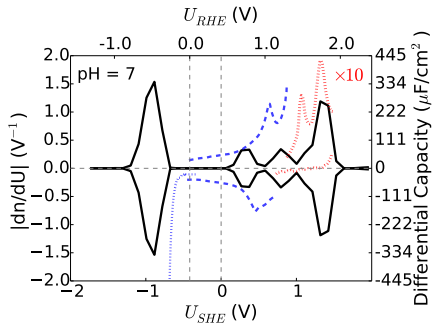

(b) *Black line: Computed differential capacitance at pH = 7. Blue dashed lines: Experimetal differential capacitances from CV's in 0.1M $NaClO_4$ by Hamelin et al.*[166] *in the oxidising region. The high potential regions, marked by red dotted lines are very large and are therefore divided by 10 in the plot.*

Figure 5.29: *Specific capacities from numerical differentials of the isotherms in figures 5.28. This is the differential capacity which is observable in by intergrating the charge transferred as a function of potential in an electrochemical I-V curve. In both plots, the experimental current in the HER region has been taken from Wang et al.*[167]*, (in 0.5M H_2SO_4, plotted versus RHE).*

To take a closer look at the computed proton insertion and hydrogen adsorption regions, zoomed views of the Gibbs isotherms are shown in figure 5.30.

The expectation for the proton isotherm is a dependence on work function and thereby on pH, based on past studies on relaxed water structures[90,120,141,142]. Electrochemical experiments show more and less pH-dependent behaviour of various counter ions[169], and inclusion of some of those counter ions could show more pH dependent behaviour than the protons.

When looking at figure 5.28, the pH dependence is not very large. A possible reason for this can be that the proton either does not have it's full charge in the simulations because the electrode may not have taken the extra electron. To investigate this, it could be interesting to evaluate the average charge density profile normal to the surface. The electron density profile may also be an experimental observable that the calculations could

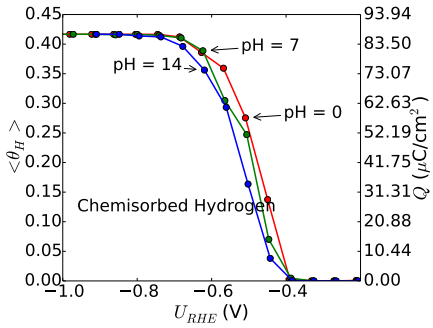

(a) θ_H versus U_{RHE}, plotted for pH = 0, 7 and 14.

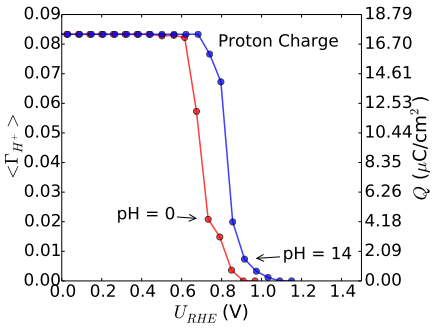

(b) Γ_{H^+} versus U_{RHE}, plotted for pH = 0, 7 and 14.

Figure 5.30: *Simulated Gibbs isotherms of hydrogen in the interface system.*

be benchmarking towards.[170] Presently, the electron density profile and electrostatic potential profiles have not been saved for every state, since it will greatly affect the size of the databases. Another possibility is that the most stable states with a proton, is when it is located very close to the surface, and most of the variation in the electric field due to pH is outside of the location of the proton. To clarify this, it could be interesting to separate subsets of states with the proton located in different regions of the electrolyte or to add other ions. The latter will may require a better sampling, since it requires another subdivision of the dataset.

In the following a further discussion of the behaviour of free charge and the potentials of zero charge will be addressed for both Au(111)/water interface.

5.8.2 Potentials of zero charge

The potential of zero free charge and of zero total charge are both of interest for benchmarking the calculations with electrochemical experiments. The total charge σ_{Total} is obtained from experiments through integration the current in the cyclic voltammograms, and thus it is electronic charge transferred to the electrode surface. From our first principles methodology, some contributions of the charge can also be calculated. The total charge, σ_{Total}, can be written as:

$$\sigma_{Total} = \sigma_F - F\theta_H + F\theta_{OH} \tag{5.49}$$

where $F\theta$ is attributed to electrosorption of a species denoted by the subscript.[171] The free charge is σ_F, which is observed in CV experiments as the capacitive current from metal electrodes in aqueous media. The surface charge, could be calculated, but not the free charge. The free charge may be divided into two contributions:

$$\sigma_F = \sigma_{dl} + \sigma_{dip} \tag{5.50}$$

where σ_{dl} is attributed to screening of ions in the double layer. The electro-neutrality condition then states that:

$$\sigma_{dl} = F\Gamma_{OH^-} - F\Gamma_{H^+} \tag{5.51}$$

The proton charge, Γ_{H^+}, and the hydroxide ion charge Γ_{OH^-} may also be calculated by the DFT method. The remaining contribution is σ_{dip}, which is interpreted as the charge which screens the dipoles in the double layer. It does not appear that σ_{dip} can be accounted for directly in the current methodology, but in the following we show how the potential of *zero* dipole charge may be calculated.

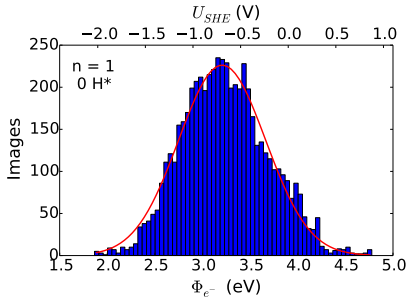

Figure 5.31: *Histogram of work functions of the subset of states with no chemisorbed species and 1 proton in the electrolyte layer. The maximum is at a work function of 3.21 eV*

As shown in figure 5.31 the distribution of work function tends to fit a normal distribution. The reason for this is most likely that water molecules rotate almost freely and thus that the sum of their dipole moments in the out of plane directions follow a random walk. It is therefore hypothesized that the distribution of work functions shows the maximum entropy of the interface.

Experiments by Climent et al.[172–174] use laser induced potential transients to measure potentials of maximum entropy, (PME), on gold and platinum single crystal surfaces.

Briefly explained, the experiment heats the surface up with a microsecond pulse from an infra-red laser. The heating temporarily shifts the equilibrium state of the interface to one with a higher entropy, and that causes a reorientation of the interface dipole. A potential transient is measured, in the experiment which decays within a few microseconds, as the interface re-equilibrates with the surroundings. From the electrocapillary equation the following relation can be derived for an ideal polarizable electrode [175,176]:

$$\frac{\partial U}{\partial T}_{q} = -\frac{\partial \Delta S}{\partial q}_{T} \tag{5.52}$$

where q is charge and U is the electrode potential. Measuring ΔU, equation 5.52 is then used to identify the potential of zero potential transient with the potential of maximum entropy.

For the Au(111) surface the PME has been reported to be around 0.2 V vs SCE, measured in 0.1 M HCl + 0.1 M H_2SO_4. This value corresponds to 0.42V versus SHE. [173]

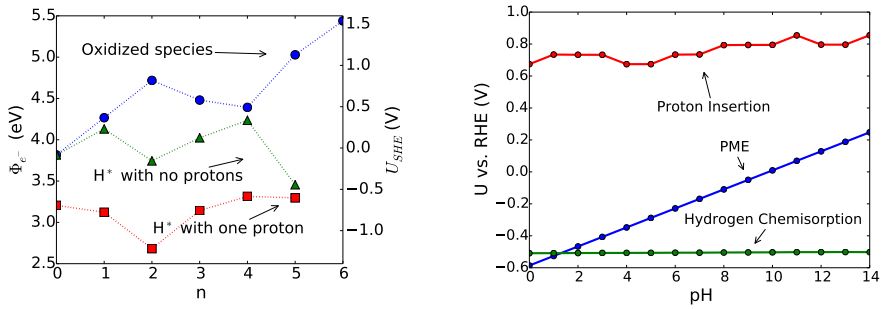

(a) *The position of the peaks of the work function distribution, as a function of number of chemisorbed species, hydrogens, (n), or oxides species, (−n), denoted by the annotation.*

(b) *The calculated potentials of zero proton charge, hydrogen adsorption, and the peak of the potential of maximum entropy, plotted versus pH. The electrode potential scale is related to the work function by assuming $\phi_{SHE} = 3.9$ eV.*

Figure 5.32: *Calculated behaviour of potentials of maximum entropy*

The calculated work function distributions have different positions for the maximum, depending on the numbers of hydrogens or protons, as shown in figure 5.32a. Distributions on which this figure is based can be found in appendix section 7.2.1. The 0.2 V value reported by Climent et al. [173] is at a much more positive potential than the peak of the distributions indicate, although that depends on what the value of ϕ_{SHE} is, since

the electrode potential is related to the work function by $eU_{SHE} = \phi - \phi_{SHE}$.

In section 5.6.1, it was also shown that the DFT calculations with an LCAO basis set underestimated the work functions compared to a real space grid based basis set, by up to 0.5 eV. Assuming that the real ϕ_{SHE} is 4.44 eV, the value for ϕ_{SHE} was tentatively set to 3.9 eV due to the correction for the incomplete basis set. The correction brings the result closer to a value in agreement with the laser induced potential transient experiments, but there is still a difference of around 0.3 eV assuming $n = 0$.

In the following, results will be presented for the Pt(111)/Water interface using the same methodology, as presented in the previous sections of this chapter.

5.8.3 Pt(111)/Water

Calculations for the Pt(111)/Water interface was carried out using the BEEF-vdW functional[30] to approximate the exchange and correlation contributions, including van der Waals contributions. This particularly improves the description of water structures[151], but in it's current implementation that comes at some computational cost.

The surface was represented by a four layer Pt(111) slab in an orthogonal 3×4 super cell and the electrolyte was represented by 24 moving water molecules and 8 constrained water molecules as the top boundary. The grid spacing was 0.2 Å and a single k-point was used. The following analysis of the Pt(111) water interfaces uses the experimental value of 4.44 eV for ϕ_{SHE}.

Oxidising conditions

As done for the Au(111)/Water interface in section 5.8.1, Gibbs isotherms are presented below for the Pt(111)/Water interface.

Pt(111) is a more reactive surface, so the overview of the isotherms in figure 5.33a shows a narrower region, where nothing is on the surface, from around 0.2V to 0.5V versus RHE. This interval is slightly narrower than the one obtained with relaxed interface structures[49], due to the lower potential for OH adsorption. The reason for this is most likely that there are more ways, the water network can form hydrogen bonds with

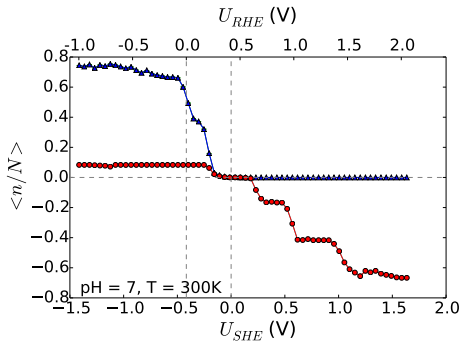

(a) *pH = 0. The blue triangles is the contribution from adsorbed hydrogen and the red circles is $< n/N > - < \theta_H >$, which is the contribution from solvated protons in the electrolyte layer above 0, and the contribution from oxidised species below 0.*

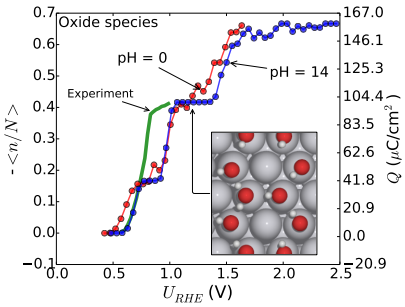

(b) *θ_H versus U_{RHE}, plotted for pH = 0 and pH = 14. The inset shows the chemisorbed layer in the most stable image found at 1.2 V versus RHE, at pH = 14. The green line is the isotherm deduced from CV experiments.*[55,177]

Figure 5.33: *Simulated Gibbs Isotherms of hydrogen in the interface system. To separate (Γ_{H^+}) from (θ_H), the numbers of hydrogens above and below a distance of 1.8Å from the surface were counted separately.*

the adsorbed OH. The number of particles included in the ensemble for Pt(111)/Water went from $\theta_H \in [0; 9/12]$, and for all of these states one or zero protons were included. Oxide species were included up to the equivalent of 3/4 ML OH, so $n/N \in [-8/12; 10/12]$.

Note that the coverage of oxide species go almost straight to $5/12 \approx 0.4$ ML around 1.0 V versus RHE, as seen in figure 5.33b. This behaviour is in good accordance with experiments, but to our knowledge, a configuration with 5/12 ML HO* has not previously been reported from ab initio calculations despite efforts to do so.[177] This finding gives additional confidence, that dynamics simulations are an efficient choice for searching the structure space.

In the following, a closer look is taken at the structure averages, in order to better understand which new structures, that are responsible for the result for the Gibbs isotherm in the oxidising potential region. First, it is necessary to take a look at the distribution of atomic distances to the surface, which is plotted in figure 5.34. A sharp peak from adsorbed oxygen species is present in all the distributions of oxygen atoms. Outside that, is a peak corresponding to a layer that donates and/or accepts hydrogen bonds with the adsorbed HO*, but it is only present at 0.8 V and not at 1.2 V. In light of hte This

may indicate that the structure 5/12 ML HO* structure forms a more complete bonding network on its own, with less interaction with the electrolyte.

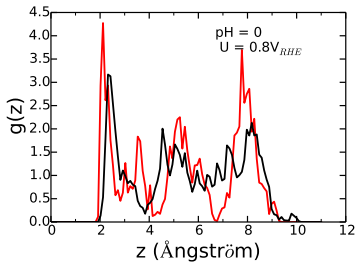

(a) *pH = 0, U = 0.8V vs. RHE*

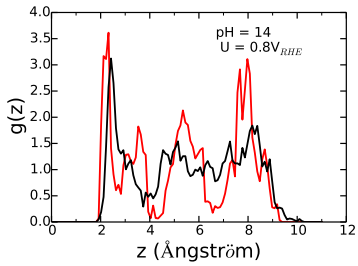

(b) *pH = 14, U = 0.8V vs. RHE*

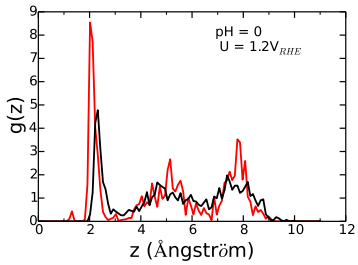

(c) *pH = 0, U = 1.2V vs. RHE*

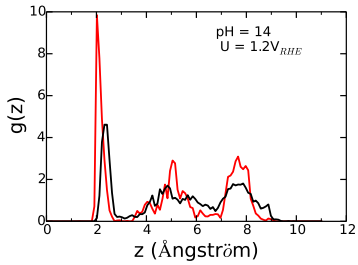

(d) *pH = 14, U = 1.2V vs. RHE*

Figure 5.34: *Distributions of ions versus distance to the Pt(111) surface. The red line is the average density of oxygen ions and the black line is average density of hydrogen ions. The ensemble is the subset of states with work functions corresponding to 0V ±0.2 V vs. RHE at the specified pH.*

To take a closer look at the chemisorbed layer, the oxygen pair distribution functions are shown in figure 5.35. The first oxygen peak for the chemisorbed layer is located around 2.1 Å from the surface, and planar oxygen pair distribution functions were therefore evaluated in a 1Å interval centered around this peak.

The oxygen pair distances have rather sharp features with zero density after the peak. The latter particularly reveals that the first layer structures are ice-like. The peak maxima are centered around 2.7Å, which is the usual distances between adsorbed OH and water, where the water molecule donates, and the OH accepts a hydrogen bond. Slightly longer distances, around 3.0 Å are characteristic of OH donating the hydrogen bond to the oxygen of an adsorbed water molecule.[178] The peaks from the present simulations

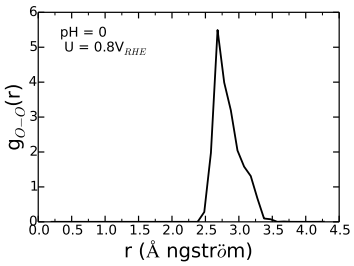

(a) *pH = 0, U = 0.8V vs. RHE*

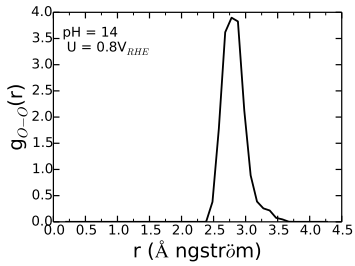

(b) *pH = 14, U = 0.8V vs. RHE*

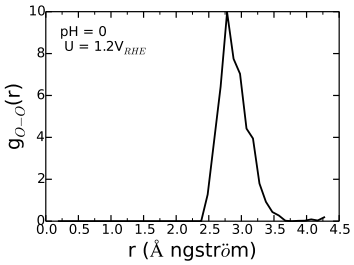

(c) *pH = 0, U = 1.2V vs. RHE*

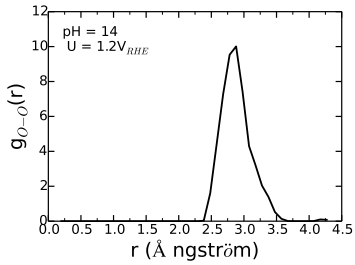

(d) *pH = 14, U = 1.2V vs. RHE*

Figure 5.35: *Oxygen pair distribution functions in the plane in an intervl from 1.6Å to 2.6Å from the surface atoms. The ensemble is the subset of states with work functions corresponding to the specified U_{RHE} ±0.2 V at the specified pH.*

seem broad enough to include all of these structures, but there is a clear shift in the peak maximum as the potential is increased from 0.8 V to 1.2 V versus RHE. Changes due to potential is most likely just founded in the increased OH coverage. A small shift in the peak is also present for increasing pH. A peak shift by varying pH can only be founded in the ensemble of structures with the work function corresponding to that pH and potential. Since, at constant U_{RHE}, it thus appears there is a pH effect on the structures, and capturing such effects is the one of the main goals of testing this methodology.

Reducing conditions

Looking closer at the hydrogen chemisorption isotherm, in figure 5.36a), the isotherms are close to the ones calculated from relaxed structures.[179] Just as for Au(111), no pH dependence is expected, because the potential energy of hydrogen adsorption is rather independent on electric fields on the atomic scale[49].

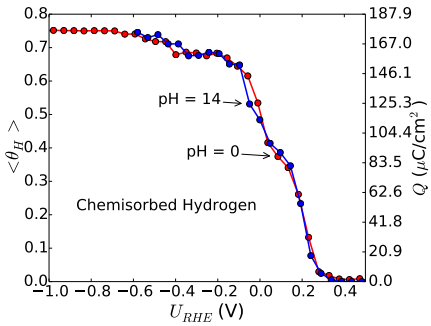

(a) θ_H versus U_{RHE}, plotted for pH = 0, 7 and 14.

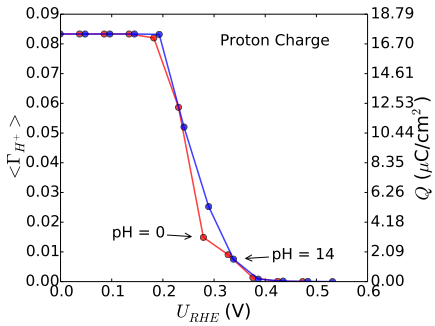

(b) Γ_{H^+} versus U_{RHE}, plotted for pH = 0, 7 and 14.

Figure 5.36: *Simulated Gibbs isotherms of hydrogen in the interface system.*

Recent cyclic voltammetry experiments on polycrystalline platinum [180] show pH-dependent binding energies, while past studies on single crystal surfaces have concluded that there is not pH-dependence, i.e. that the adsorption/desorption potentials are constant on the RHE scale [181–183] for Pt(111). Experimental studies also show that hydrogen stability on steps depends on pH [183], which may also play a role in the results on polycrystalline platinum.

The isotherm for proton insertion into the electrolyte layer again only shows a weak pH dependence. As mentioned in section 5.8.1, the reason for this may be that the variation in the interface dipole most often takes place outside the location of the proton, or it can be because the proton does not have its full charge in the calculations. This warrants further investigation.

5.9 Discussion

The presented methodology reproduces a wide variety of outputs in terms of properties of the electrochemical interface, which have previously been reported in many individual computational studies. Those outputs are the adsorption energies, Gibbs isotherms, simulated cyclic voltammograms, distribution functions characterising the water structure, and most stable structures, all from the same database of structures, energies and work functions. The foundation for obtaining all the quantities of interest is the ensemble of states and their free energies depending on pH and electrode potential.

The input to this methodology contains fewer than usual assumptions, which are:

1 The electrolyte is in equilibrium.

2 The interface region is in equilibrium with the surroundings.

3 The system size is large enough to include all screening effects, to conserve charge neutrality and to maintain the link between work function and absolute electrode potential.

The latter assumption is the most difficult to one to corroborate, but fulfilling it is essentially nothing more than a matter of the size of the atomic model.

Other inputs to the calculation are an extended metal surface structure or facet, such as Pt(111), a system size in given by the unit cell and the amount of electrode layers and explicit electrolyte included. From there, one can in principle press play and wait for the ensemble to be formed for subsequent analysis. In practice it is obviously not that simple, however, since maintaining an efficient sampling is demanding on computational resources and optimization of parameters while monitoring the trajectories.

The methodology remains under development and the end goal of providing a fully accurate representation of the interface regions is still not realized. Initially, the goal has merely been to provide a proof of concept and then to incrementally develop the capabilities of the methodology. The foremost of these capabilities is capturing pH effects, which has been successful to a limited degree so far.

A few challenges have been identified for obtaining more accurate representations of the interface systems. They are all related to the fact that a very large number of calculations of micro states is required for gaining accurate results, since many trajectories with varying surface coverages and excesses of ions must be included in the ensemble. This is combined with the time it takes to get large well equilibrated ensembles from the molecular dynamics, which are sensitive to the size of the size of time steps, to the thermostat in the MD and to the convergence criteria in the DFT calculations. It is not that demanding on to achieve well defined water geometries as shown in section 5.7. Getting accurate energetics is usually more challenging due to a requirement of better k-point sampling and basis sets. The accuracy of work functions is also an issue that is important to consider, although an uncertainty of ± 0.1 eV in the work function may

be acceptable for proof of concept purposes. The accuracy of work functions and the distribution of charges in metal or electrolyte may both be affected by the choice of basis sets. It should be considered whether Car-Parinello dynamics are feasible, since they may make it feasible to use plane wave basis sets, but it will require an implementation where the Fermi level and work function can be extracted.

Generally the challenge is to get a large enough sample, while maintaining a high accuracy on the calculation of the electronic structure.

5.10 Summary

The methodology, which is being developed has the present disadvantage of being demanding on time and computational resources. In order to calculate properties as averages, a large number of states is needed - at least a few thousands in the ensemble that is of interest. The dynamics produce states in the entire range of work functions, and if only a narrow interval of electrode potentials is of interest, the remaining states are unused. Essentially this is a consequence of the lack of a "potentiostat" - a means to input electrode potential rather than measuring it.

Getting an efficient and proper sampling for forming the grand canonical ensemble from Born-Oppenheimer molecular dynamics, (BOMD), requires a lot of fine tuning of various parameters, which are discussed in section 5.5 and 5.6. The LCAO basis sets are the minimal and efficient choice for this purpose, but they have a consequence on accuracy on work functions. The MD time step should be small enough so that noise in the total energy is much smaller than $k_B T$, but also not too large in order to equilibrate the ensemble within the possible sampling time. For these simulations, 0.5 fs was found to be a good compromise. The thermostat should maintain the temperature and minimize fluctuations in the total energy. The Berendsen thermostat with a time constant of 1000 fs was found to be quite stable and well suited. The convergence criterion on the density in the DFT should be small enough that the drift is minimized, and when a thermostat is used it should be small enough to avoid fluctuations in temperature and total energy. Avoiding drift completely comes at a great cost in speed, so rather large values around 10^{-5} Å^{-3} were used.

The main advantages of the methodology, which is being developed is that it makes

fewer assumptions on the physics of the interface. No capacitor model was invoked, only models within thermodynamics and definitions from electrochemistry. Secondly, no other method captures this many features of the electrochemical interface on the atomic scale in one combined representation, to the best of our knowledge.

So far, only quite small and subtle pH effects have been found, and only in a few cases have the cause been clear. The subtle variations in the structures of the water-oxide species on the Pt(111) surface seems to be a direct effect of pH. The potential of maximum entropy has Nernstian behaviour, i.e. it shifts on the RHE scale by $2.3k_BT$ per pH. Identifying this with the distribution of the net dipole moment resulting from the dynamics, may also prove to be an important fundamental result.

6. Conclusion and Outlook

6.1 Conclusion

This thesis consists of several projects related to electrochemistry. In chapter 3 and chapter 4, the well known methodology of DFT calculations combined with the computational hydrogen electrode was used to study the reactivity of various metal surfaces and correlate the results to the trends in activity and reactivity of electro-catalysts.

The recently discovered Pt-lanthanide catalysts form a series, in which the reactivity can be tuned using the lanthanide contraction. The Pt-lanthanides are quite stable, and it is hoped that they can be further optimized for applications in proton exchange membrane fuel cells. The platinum-skin on the surface of these catalysts is a complicated system, on which there are still many open questions. In chapter 3, correlations between experimentally observed trends with the computed trends suggested that there is a limit to how much the strain effect can be exploited to fine tune the reactivity of catalyst surfaces, and that this limit is reached around Pt_5Tb.

In chapter 4, several recently discovered catalysts for hydrogen evolution were studied to understand the active sites and state of the surface. It was shown, that some low index facets of molybdenum carbide and boride are very reactive, and the computations predict that they are oxidised under reaction conditions. The low index facets of Mo_2C were found to be unsuited for HER or HOR catalysis, which suggest that there are still undiscovered active sites, surface states or phases to be found in these materials. The (002) facet on MoB bind hydrogen moderately enough to be a good HER catalyst.

Low index facets of Ni_2P were also studied to elucidate the active site for HER catalysis. This study found that Ni_2P is slightly binds hydrogen slightly weaker than the optimum, and that a significant repulsive surface interaction exists between adsorbed hydrogen. The most optimal adsorption energies were found on the nickel bridge sites on the various facets and on the edges of the crystal structure, (See section 4.3). Calculations on a series of other phosphide catalysts revealed that they do not all work through the metal sites, but in fact the best catalysts adsorb hydrogen on both P and metal sites. Meanwhile, some of these phosphides were discovered independently, mainly by experimental

efforts. It builds confidence, that the design principles for HER on metals are also useful for the metal phosphides. It also shows that experimental screening studies to develop new catalysts are still keeping up with their computational counterparts, especially in the case where catalysts are active on many exposed facets.

Chapter 5 presents a method development project, which aims to advance the understanding of the structure of the electrochemical interface. Molecular dynamics was used to generate a database of structures for the water interface with platinum(111) and with gold(111), at various surface coverages of hydrogen and oxide species, and with or without protons in the water layer. An *a posteriori analysis* was then developed to extract various quantities of interest from the databases, in order to describe the atomic scale interface as a function of pH and electrode potential. The analysis method is a combination of the generalized computational hydrogen electrode with a Monte Carlo algorithm to calculate the proper weight functions of the grand canonical ensemble, as functions of pH and electrode potential. The methodology is powerful because it makes fewer assumptions on the fundamental physics of the interface than any other presently known method, while capturing pH effects. It's main limitation is the same as any atomic scale simulation method, that it is limited in possible system sizes and time scales by computational costs.

6.2 Outlook

There are reasons to be optimistic about the prospects of doing first principles calculations on the atomic scale properties of the electrochemical interface system. Many open questions are still standing on the physics that can be captured by the presented methodology. The biggest obstacle to progress is the cost versus accuracy of the computations, but a few more years of Moore's law may ease the burden significantly and make the presented methodology feasible for more widespread applications. The new understanding obtained from the calculations may in the future aid the electrochemists in understanding the complicated phenomena of various interfaces for fuel cells, electrolysers, batteries, solar-electrochemical devices, ect. With some luck and effort, this methodology may also aid development of rational design principles for new catalyst/electrolyte combinations.

It is fundamentally difficult to develop highly active electro-catalysts, and even more so, when catalysis of reactions including multiple electron transfers and intermediates are desired. Thus, advances of fundamental understanding and simulation capabilities of the

electrochemical interface are in great demand in this field of research. Breakthroughs in the field of electrocatalysis will prove beneficial, for the purpose of developing energy storage and conversion technologies, that are needed for a sustainable energy infrastructure. The challenges of solving the problems in electro-catalysis are indeed great, but there are also great rewards, if the solutions can contribute to make the energy system more sustainable. Applications of electrochemical energy conversion may eventually prove vital to the continued development of modern society.

Bibliography

[1] Charles Kittel and Herbert Kroemer. *Thermal physics*. Macmillan, 1980.

[2] OECD/IEA. Key world energy statistics, 2015. URL http://www.iea.org/t&c.

[3] Jens R. Rostrup Nielsen. Fuels and energy for the future: The role of catalysis. *Catalysis Reviews*, 46(3-4):247–270, 2004. doi: 10.1081/CR-200036716. URL http://dx.doi.org/10.1081/CR-200036716.

[4] Nathan S. Lewis. Toward cost-effective solar energy use. *Science*, 315(5813):798–801, 2007. ISSN 0036-8075. doi: 10.1126/science.1137014. URL http://science.sciencemag.org/content/315/5813/798.

[5] Timothy R. Cook, Dilek K. Dogutan, Steven Y. Reece, Yogesh Surendranath, Thomas S. Teets, and Daniel G. Nocera. Solar energy supply and storage for the legacy and nonlegacy worlds. *Chemical Reviews*, 110(11):6474–6502, 2010. doi: 10.1021/cr100246c. URL http://dx.doi.org/10.1021/cr100246c. PMID: 21062098.

[6] A. Demirbas. Global renewable energy projections. *Energy Sources, Part B: Economics, Planning, and Policy*, 4(2):212–224, 2009. doi: 10.1080/15567240701620499. URL http://dx.doi.org/10.1080/15567240701620499.

[7] Bruce Dunn, Haresh Kamath, and Jean-Marie Tarascon. Electrical energy storage for the grid: A battery of choices. *Science*, 334(6058):928–935, 2011. ISSN 0036-8075. doi: 10.1126/science.1212741. URL http://science.sciencemag.org/content/334/6058/928.

[8] Evgenii V. Kondratenko, Guido Mul, Jonas Baltrusaitis, Gaston O. Larrazabal, and Javier Perez-Ramirez. Status and perspectives of co2 conversion into fuels and chemicals by catalytic, photocatalytic and electrocatalytic processes. *Energy Environ. Sci.*, 6:3112–3135, 2013. doi: 10.1039/C3EE41272E. URL http://dx.doi.org/10.1039/C3EE41272E.

[9] Frederick T. Wagner, Balasubramanian Lakshmanan, and Mark F. Mathias. Electrochemistry and the future of the automobile. *The Journal of Physical Chemistry Letters*, 1(14):2204–2219, 2010. doi: 10.1021/jz100553m. URL http://dx.doi.org/10.1021/jz100553m.

[10] Dr Ulrich Eberle and Dr Rittmar von Helmolt. Sustainable transportation based on electric vehicle concepts: a brief overview. *Energy Environ. Sci.*, 3:689–699, 2010. doi: 10.1039/C001674H. URL http://dx.doi.org/10.1039/C001674H.

[11] Ulrich Eberle, Bernd Muller, and Rittmar von Helmolt. Fuel cell electric vehicles and hydrogen infrastructure: status 2012. *Energy Environ. Sci.*, 5:8780–8798, 2012. doi: 10.1039/C2EE22596D. URL http://dx.doi.org/10.1039/C2EE22596D.

[12] George W Crabtree, Mildred S Dresselhaus, and Michelle V Buchanan. The hydrogen economy. *Physics Today*, 57(12):39–44, 2004.

[13] Gregorio Marbán and Teresa Valdés-Solís. Towards the hydrogen economy? *International Journal of Hydrogen Energy*, 32(12):1625 – 1637, 2007. ISSN 0360-3199. doi: http://dx.doi.org/10.1016/j.ijhydene.2006.12.017. URL http://www.sciencedirect.com/science/article/pii/S0360319906006276.

[14] Toyota Danmark A/S. personal communication, 2015.

[15] Alison Cowley. Platinum 2013 interim review. *Johnson Matthey*, pages 1–36, 2013.

[16] A.J. Bard and L.R. Faulkner. *Electrochemical Methods: Fundamentals and Applications*. Wiley, 2000. ISBN 9780471043720. URL https://books.google.dk/books?id=kv56QgAACAAJ.

[17] Hubert A. Gasteiger, Shyam S. Kocha, Bhaskar Sompalli, and Frederick T. Wagner. Activity benchmarks and requirements for pt, pt-alloy, and non-pt oxygen reduction catalysts for PEMFCs. *Fuel processing and PEM Fuel Cells: advanced cata;ysts, adsorbents and electrocatalysts*, 56(1):9–35. ISSN 0926-3373. doi: 10.1016/j.apcatb.2004.06.021. URL http://www.sciencedirect.com/science/article/pii/S0926337304004941.

[18] I. Chorkendorff and J.W. Niemantsverdriet. *Concepts of Modern Catalysis and Kinetics*. Wiley, 2006. ISBN 9783527605644. URL https://books.google.dk/books?id=p34rVviEVWsC.

[19] Paul Sabatier. Hydrogénations et déshydrogénations par catalyse. *Berichte der deutschen chemischen Gesellschaft*, 44(3):1984–2001, 1911. ISSN 1099-0682. doi: 10.1002/cber.19110440303. URL http://dx.doi.org/10.1002/cber.19110440303.

[20] B. Hammer and J.K. Nørskov. Theoretical surface science and catalysis—calculations and concepts. In Helmut Knozinger Bruce C. Gates, editor, *Advances in Catalysis*, volume Volume 45, pages 71–129. Academic Press.

ISBN 0360-0564. URL http://www.sciencedirect.com/science/article/pii/S0360056402450134.

[21] S. Wilson. *Handbook of Molecular Physics and Quantum Chemistry: Molecules in the physico-chemical environment: spectroscopy, dynamics and bulk properties*. Handbook of Molecular Physics and Quantum Chemistry: Spectroscopy, Dynamics and Bulk Properties. Molecules in the Physico-chemical Environment. Wiley, 2003. ISBN 9780471623748. URL https://books.google.dk/books?id=44MhAQAAMAAJ.

[22] W. Kohn. Nobel lecture: Electronic structure of matter—wave functions and density functionals. *Rev. Mod. Phys.*, 71:1253–1266, Oct 1999. doi: 10.1103/RevModPhys.71.1253. URL http://link.aps.org/doi/10.1103/RevModPhys.71.1253.

[23] J. Kohanoff. *Electronic Structure Calculations for Solids and Molecules: Theory and Computational Methods*. Condensed matter physics, nanoscience and mesoscopic physics. Cambridge University Press, 2006. ISBN 9780521815918. URL http://books.google.dk/books?id=v2ElZFCKeBsC.

[24] P. Hohenberg and W. Kohn. Inhomogeneous electron gas. *Phys. Rev.*, 136:B864–B871, Nov 1964. doi: 10.1103/PhysRev.136.B864. URL http://link.aps.org/doi/10.1103/PhysRev.136.B864.

[25] W. Kohn and L. J. Sham. Self-consistent equations including exchange and correlation effects. *Phys. Rev.*, 140:A1133–A1138, Nov 1965. doi: 10.1103/PhysRev.140.A1133. URL http://link.aps.org/doi/10.1103/PhysRev.140.A1133.

[26] John P. Perdew, Kieron Burke, and Matthias Ernzerhof. Generalized gradient approximation made simple. *Physical Review Letters*, 77(18):3865–3868. URL http://link.aps.org/doi/10.1103/PhysRevLett.77.3865.

[27] B. Hammer, L. B. Hansen, and J. K. Nørskov. Improved adsorption energetics within density-functional theory using revised perdew-burke-ernzerhof functionals. *Physical Review B*, 59(11):7413–7421. URL http://link.aps.org/doi/10.1103/PhysRevB.59.7413.

[28] M. Dion, H. Rydberg, E. Schröder, D. C. Langreth, and B. I. Lundqvist. Van der waals density functional for general geometries. *Phys. Rev. Lett.*, 92:246401, Jun 2004. doi: 10.1103/PhysRevLett.92.246401. URL http://link.aps.org/doi/10.1103/PhysRevLett.92.246401.

[29] Kyuho Lee, Éamonn D. Murray, Lingzhu Kong, Bengt I. Lundqvist, and David C. Langreth. Higher-accuracy van der waals density functional. *Phys. Rev. B*, 82: 081101, Aug 2010. doi: 10.1103/PhysRevB.82.081101. URL `http://link.aps.org/doi/10.1103/PhysRevB.82.081101`.

[30] Jess Wellendorff, Keld T. Lundgaard, Andreas Møgelhøj, Vivien Petzold, David D. Landis, Jens K. Nørskov, Thomas Bligaard, and Karsten W. Jacobsen. Density functionals for surface science: Exchange-correlation model development with bayesian error estimation. *Phys. Rev. B*, 85:235149, Jun 2012. doi: 10.1103/PhysRevB.85.235149. URL `http://link.aps.org/doi/10.1103/PhysRevB.85.235149`.

[31] J. J. Mortensen, L. B. Hansen, and K. W. Jacobsen. Real-space grid implementation of the projector augmented wave method. *Physical Review B*, 71(3):035109. URL `http://link.aps.org/doi/10.1103/PhysRevB.71.035109`.

[32] J. Enkovaara, Carsten Rostgaard, Jens Jørgen Mortensen, Jingzhe Chen, M. Dulak, Lara Ferrighi, Jeppe Gavnholt, Christian Glinsvad, V. Haikola, and H. A. Hansen. Electronic structure calculations with GPAW: a real-space implementation of the projector augmented-wave method. *Journal of Physics: Condensed Matter*, 22(25): 253202.

[33] C. Kittel. *Introduction to Solid State Physics*. Wiley, 2004. ISBN 9780471415268. URL `https://books.google.dk/books?id=kym4QgAACAAJ`.

[34] Hendrik J. Monkhorst and James D. Pack. Special points for brillouin-zone integrations. *Physical Review B*, 13(12):5188–5192. URL `http://link.aps.org/doi/10.1103/PhysRevB.13.5188`.

[35] E. L. Briggs, D. J. Sullivan, and J. Bernholc. Real-space multigrid-based approach to large-scale electronic structure calculations. *Phys. Rev. B*, 54:14362–14375, Nov 1996. doi: 10.1103/PhysRevB.54.14362. URL `http://link.aps.org/doi/10.1103/PhysRevB.54.14362`.

[36] Otto F. Sankey and David J. Niklewski. *Ab initio* multicenter tight-binding model for molecular-dynamics simulations and other applications in covalent systems. *Phys. Rev. B*, 40:3979–3995, Aug 1989. doi: 10.1103/PhysRevB.40.3979. URL `http://link.aps.org/doi/10.1103/PhysRevB.40.3979`.

[37] A. H. Larsen, M. Vanin, J. J. Mortensen, K. S. Thygesen, and K. W. Jacobsen. Localized atomic basis set in the projector augmented wave method. *Phys. Rev. B*,

80:195112, Nov 2009. doi: 10.1103/PhysRevB.80.195112. URL http://link.aps.org/doi/10.1103/PhysRevB.80.195112.

[38] P. E. Blöchl. Projector augmented-wave method. *Phys. Rev. B*, 50:17953–17979, Dec 1994. doi: 10.1103/PhysRevB.50.17953. URL http://link.aps.org/doi/10.1103/PhysRevB.50.17953.

[39] Peter E. Blöchl, Clemens J. Först, and Johannes Schimpl. Projector augmented wave method:ab initio molecular dynamics with full wave functions. *Bulletin of Materials Science*, 26(1):33–41. ISSN 0973-7669. doi: 10.1007/BF02712785. URL http://dx.doi.org/10.1007/BF02712785.

[40] P. Pulay. Ab initio calculation of force constants and equilibrium geometries in polyatomic molecules. *Molecular Physics*, 17(2):197–204, 1969. doi: 10.1080/00268976900100941. URL http://dx.doi.org/10.1080/00268976900100941.

[41] CG Broyden. The convergence of single-rank quasi-newton methods. *Mathematics of Computation*, 24(110):365–382, 1970.

[42] R. Fletcher. A new approach to variable metric algorithms. *The Computer Journal*, 13(3):317–322, 1970. doi: 10.1093/comjnl/13.3.317. URL http://comjnl.oxfordjournals.org/content/13/3/317.abstract.

[43] Donald Goldfarb. A family of variable-metric methods derived by variational means. *Mathematics of computation*, 24(109):23–26, 1970.

[44] David F Shanno. Conditioning of quasi-newton methods for function minimization. *Mathematics of computation*, 24(111):647–656, 1970.

[45] Erik Bitzek, Pekka Koskinen, Franz Gähler, Michael Moseler, and Peter Gumbsch. Structural relaxation made simple. *Phys. Rev. Lett.*, 97:170201, Oct 2006. doi: 10.1103/PhysRevLett.97.170201. URL http://link.aps.org/doi/10.1103/PhysRevLett.97.170201.

[46] H. Gould and J. Tobochnik. *Statistical and Thermal Physics: With Computer Applications*. Princeton University Press, 2010. ISBN 9780691137445. URL https://books.google.dk/books?id=0mpJmAEACAAJ.

[47] Daniel ben Avraham. H. gould and j. tobochnik: Statistical and thermal physics. *Journal of Statistical Physics*, 140(5):1022–1023. ISSN 0022-4715. doi: 10.1007/s10955-010-0035-4. URL http://dx.doi.org/10.1007/s10955-010-0035-4.

[48] J. K. Nørskov, J. Rossmeisl, A. Logadottir, , L. Lindqvist, J. R. Kitchin, T. Bligaard, and H. Jónsson. Origin of the overpotential for oxygen reduction at a fuel-cell cathode. *The Journal of Physical Chemistry B*, 108(46):17886–17892, 2004. doi: 10.1021/jp047349j. URL `http://dx.doi.org/10.1021/jp047349j`.

[49] Jan Rossmeisl, Jens K. Nørskov, Christopher D. Taylor, Michael J. Janik, and Matthew Neurock. Calculated phase diagrams for the electrochemical oxidation and reduction of water over pt(111). *The Journal of Physical Chemistry B*, 110 (43):21833–21839, . ISSN 1520-6106. doi: 10.1021/jp0631735. URL `http://dx.doi.org/10.1021/jp0631735`.

[50] NM Markovic, TJ Schmidt, V Stamenkovic, and PN Ross. Oxygen reduction reaction on pt and pt bimetallic surfaces: a selective review. *FUEL CELLS-WEINHEIM-*, 1(2):105–116, 2001.

[51] Ifan E. L. Stephens, Alexander S. Bondarenko, Ulrik Grønbjerg, Jan Rossmeisl, and Ib Chorkendorff. Understanding the electrocatalysis of oxygen reduction on platinum and its alloys. *Energy & Environmental Science*, 5(5):6744–6762, . ISSN 1754-5692. doi: 10.1039/C2EE03590A. URL `http://dx.doi.org/10.1039/C2EE03590A`.

[52] G. S. Karlberg, J. Rossmeisl, and J. K. Norskov. Estimations of electric field effects on the oxygen reduction reaction based on the density functional theory. *Phys. Chem. Chem. Phys.*, 9:5158–5161, 2007. doi: 10.1039/B705938H. URL `http://dx.doi.org/10.1039/B705938H`.

[53] J. Rossmeisl, A. Logadottir, and J.K. Nørskov. Electrolysis of water on (oxidized) metal surfaces. *Chemical Physics*, 319(1–3):178 – 184, 2005. ISSN 0301-0104. doi: http://dx.doi.org/10.1016/j.chemphys.2005.05.038. URL `http://www.sciencedirect.com/science/article/pii/S0301010405002053`. Molecular Charge Transfer in Condensed Media - from Physics and Chemistry to Biology and Nanoengineering in honour of Alexander M. Kuznetsov on his 65th birthday.

[54] Vojislav Stamenkovic, Bongjin Simon Mun, Karl J. J. Mayrhofer, Philip N. Ross, Nenad M. Markovic, Jan Rossmeisl, Jeff Greeley, and Jens K. Nørskov. Changing the activity of electrocatalysts for oxygen reduction by tuning the surface electronic structure. *Angewandte Chemie*, 118(18):2963–2967, . ISSN 1521-3757. doi: 10.1002/ange.200504386. URL `http://dx.doi.org/10.1002/ange.200504386`.

[55] Vojislav R. Stamenkovic, Ben Fowler, Bongjin Simon Mun, Guofeng Wang, Philip N. Ross, Christopher A. Lucas, and Nenad M. Marković. Improved oxygen reduction activity on pt$_3$ni(111) via increased surface site availability. *Science*, 315(5811):493–497, . URL http://www.sciencemag.org/content/315/5811/493.abstract.

[56] Harry E. Hoster, Otávio B. Alves, and Marc T. M. Koper. Tuning adsorption via strain and vertical ligand effects. *ChemPhysChem*, 11(7):1518–1524, 2010. ISSN 1439-7641. doi: 10.1002/cphc.200900500. URL http://dx.doi.org/10.1002/cphc.200900500.

[57] Ifan E. L. Stephens, Alexander S. Bondarenko, Francisco J. Perez-Alonso, Federico Calle-Vallejo, Lone Bech, Tobias P. Johansson, Anders K. Jepsen, Rasmus Frydendal, Brian P. Knudsen, Jan Rossmeisl, and Ib Chorkendorff. Tuning the activity of pt(111) for oxygen electroreduction by subsurface alloying. *Journal of the American Chemical Society*, 133(14):5485–5491, . ISSN 0002-7863. doi: 10.1021/ja111690g. URL http://dx.doi.org/10.1021/ja111690g.

[58] María Escudero-Escribano, Paolo Malacrida, Martin Hangaard Hansen, Ulrik Grønbjerg Vej-Hansen, Amado Velázquez-Palenzuela, Vladimir Tripkovic, Jakob Schiøtz, Jan Rossmeisl, Ifan E. L. Stephens, and Ib Chorkendorff. Tuning the activity of pt alloy electrocatalysts by means of the lanthanide contraction. *Science*, 352(6281):73–76, 2016. ISSN 0036-8075. doi: 10.1126/science.aad8892. URL http://science.sciencemag.org/content/352/6281/73.

[59] J Greeley, I E L Stephens, a S Bondarenko, T P Johansson, H a Hansen, T F Jaramillo, J Rossmeisl, I Chorkendorff, and J K Nørskov. Alloys of platinum and early transition metals as oxygen reduction electrocatalysts. *Nature chemistry*, 1 (7):552–556, 2009. URL http://dx.doi.org/10.1038/nchem.367.

[60] Maria Escudero-Escribano, Arnau Verdaguer-Casadevall, Paolo Malacrida, Ulrik Grønbjerg, Brian P. Knudsen, Anders K. Jepsen, Jan Rossmeisl, Ifan E. L. Stephens, and Ib Chorkendorff. Pt5gd as a highly active and stable catalyst for oxygen electroreduction. *Journal of the American Chemical Society*, 134(40):16476–16479, 2012. doi: 10.1021/ja306348d. URL http://dx.doi.org/10.1021/ja306348d. PMID: 22998588.

[61] M. Mavrikakis, B. Hammer, and J. K. Nørskov. Effect of strain on the reactivity

of metal surfaces. *Physical Review Letters*, 81(13):2819–2822. URL http://link.aps.org/doi/10.1103/PhysRevLett.81.2819.

[62] Ulrik Grønbjerg Vej-Hansen, Jakob Schiøtz, Ifan Stephens, and Jan Rossmeisl. *Structure, activity, and stability of platinum alloys as catalysts for the oxygen reduction reaction.* PhD thesis, 2015.

[63] Jan Rossmeisl, Egill Skúlason, Mårten E. Björketun, Vladimir Tripkovic, and Jens K. Nørskov. Modeling the electrified solid–liquid interface. *Chemical Physics Letters*, 466(1):68–71, . ISSN 0009-2614. doi: 10.1016/j.cplett.2008.10.024. URL http://www.sciencedirect.com/science/article/pii/S0009261408013754.

[64] Peter Strasser, Shirlaine Koh, Toyli Anniyev, Jeff Greeley, Karren More, Chengfei Yu, Zengcai Liu, Sarp Kaya, Dennis Nordlund, Hirohito Ogasawara, et al. Lattice-strain control of the activity in dealloyed core–shell fuel cell catalysts. *Nature chemistry*, 2(6):454–460, 2010.

[65] T. P. Johansson, E. T. Ulrikkeholm, P. Hernandez-Fernandez, P. Malacrida, H. A. Hansen, A. S. Bandarenka, J. K. Nørskov, J. Rossmeisl, I. E. L. Stephens, and I. Chorkendorff. Pt skin versus pt skeleton structures of pt3sc as electrocatalysts for oxygen reduction. *Topics in Catalysis*, 57(1):245–254, 2013. ISSN 1572-9028. doi: 10.1007/s11244-013-0179-y. URL http://dx.doi.org/10.1007/s11244-013-0179-y.

[66] T. P. Johansson, E. T. Ulrikkeholm, P. Hernandez-Fernandez, M. Escudero-Escribano, P. Malacrida, I. E. L. Stephens, and I. Chorkendorff. Towards the elucidation of the high oxygen electroreduction activity of PtxY: surface science and electrochemical studies of y/pt(111). *Physical Chemistry Chemical Physics*, 16(27):13718–13725. ISSN 1463-9076. doi: 10.1039/C4CP00319E. URL http://dx.doi.org/10.1039/C4CP00319E.

[67] M. Escudero-Escribano T. P. Johansson P. Malacrida C. M. Pedersen M. H. Hansen Kim D. Jensen J. Rossmeisl D. Friebel A. Nilsson I. Chorkendorff I. E. L. Stephens A. F. Pedersen, E. T. Ulrikkeholm. Probing the nanoscale structure of the catalytically active overlayer on pt alloys with rare earths. *Nano Energy*, 2016. Accepted.

[68] Martin Ruff, Naoki Takehiro, Ping Liu, Jens K. Nørskov, and R. Jürgen Behm. Size-specific chemistry on bimetallic surfaces: A combined experimental and theoretical study. *ChemPhysChem*, 8(14):2068–2071, 2007. ISSN 1439-7641. doi: 10.1002/cphc.200700070. URL http://dx.doi.org/10.1002/cphc.200700070.

[69] Sune R. Bahn and Karsten W. Jacobsen. An object-oriented scripting interface to a legacy electronic structure code. *Computing in Science & Engineering*, 4(3):56–66. URL http://scitation.aip.org/content/aip/journal/cise/4/3/10.1109/5992.998641.

[70] A. Schlapka, M. Lischka, A. Groß, U. Käsberger, and P. Jakob. Surface strain versus substrate interaction in heteroepitaxial metal layers: Pt on ru(0001). *Phys. Rev. Lett.*, 91:016101, Jun 2003. doi: 10.1103/PhysRevLett.91.016101. URL http://link.aps.org/doi/10.1103/PhysRevLett.91.016101.

[71] S. Raaen and A. Ramstad. Monte-carlo simulations of thermal desorption of adsorbed molecules from metal surfaces. *Energy*, 30(6):821 – 830, 2005. ISSN 0360-5442. doi: http://dx.doi.org/10.1016/j.energy.2004.03.101. URL http://www.sciencedirect.com/science/article/pii/S0360544204001872. Second International Onsager Conference.

[72] N.V. Petrova and I.N. Yakovkin. Monte carlo simulation of {CO} and o coadsorption and reaction on pt(1 1 1). *Surface Science*, 578(1–3):162 – 173, 2005. ISSN 0039-6028. doi: http://dx.doi.org/10.1016/j.susc.2005.01.031. URL http://www.sciencedirect.com/science/article/pii/S0039602805000865.

[73] J.-S. McEwen, S.H. Payne, H.J. Kreuzer, M. Kinne, R. Denecke, and H.-P. Steinrück. Adsorption and desorption of {CO} on pt(1 1 1): a comprehensive analysis. *Surface Science*, 545(1–2):47 – 69, 2003. ISSN 0039-6028. doi: http://dx.doi.org/10.1016/j.susc.2003.08.040. URL http://www.sciencedirect.com/science/article/pii/S0039602803011257.

[74] Yun-Hang Hu, Hui-Lin Wan, Khi-Rui Tsai, and Chak-Tong Au. Computer simulation of derivative TPD. *Thermochimica Acta*, 274:289–301. ISSN 0040-6031. doi: 10.1016/0040-6031(95)02709-2. URL http://www.sciencedirect.com/science/article/pii/0040603195027092.

[75] J. Rossmeisl-I. Chorkendorff E. T. Ulrikkeholm, M. H. Hansen. Investigating the coverage dependent behavior of co on gd/pt(111). 2016. Submitted.

[76] Vladimir Tripkovic, Jian Zheng, Gian Andrea Rizzi, Carla Marega, Christian Durante, Jan Rossmeisl, and Gaetano Granozzi. Comparison between the oxygen reduction reaction activity of pd5ce and pt5ce: The importance of crystal structure. *ACS Catalysis*, 5(10):6032–6040. doi: 10.1021/acscatal.5b01254. URL http://dx.doi.org/10.1021/acscatal.5b01254.

[77] Brian Seger, Ivano E. Castelli, Peter C. K. Vesborg, Karsten W. Jacobsen, Ole Hansen, and Ib Chorkendorff. 2-photon tandem device for water splitting: comparing photocathode first versus photoanode first designs. *Energy Environ. Sci.*, 7: 2397–2413, 2014. doi: 10.1039/C4EE01335B. URL `http://dx.doi.org/10.1039/C4EE01335B`.

[78] Daniel Merki, Stéphane Fierro, Heron Vrubel, and Xile Hu. Amorphous molybdenum sulfide films as catalysts for electrochemical hydrogen production in water. *Chemical Science*, 2(7):1262–1267, 2011.

[79] Roger Parsons. The rate of electrolytic hydrogen evolution and the heat of adsorption of hydrogen. *Transactions of the Faraday Society*, 54:1053–1063, 1958.

[80] Jens Kehlet Nørskov, Thomas Bligaard, Ashildur Logadottir, JR Kitchin, JG Chen, S Pandelov, and U Stimming. Trends in the exchange current for hydrogen evolution. *Journal of The Electrochemical Society*, 152(3):J23–J26, 2005.

[81] Carlos G. Morales-Guio, Lucas-Alexandre Stern, and Xile Hu. Nanostructured hydrotreating catalysts for electrochemical hydrogen evolution. *Chem. Soc. Rev.*, 43:6555–6569, 2014. doi: 10.1039/C3CS60468C. URL `http://dx.doi.org/10.1039/C3CS60468C`.

[82] Thomas F. Jaramillo, Kristina P. Jørgensen, Jacob Bonde, Jane H. Nielsen, Sebastian Horch, and Ib Chorkendorff. Identification of active edge sites for electrochemical h2 evolution from mos2 nanocatalysts. *Science*, 317(5834):100–102, 2007. ISSN 0036-8075. doi: 10.1126/science.1141483. URL `http://science.sciencemag.org/content/317/5834/100`.

[83] Eric J. Popczun, James R. McKone, Carlos G. Read, Adam J. Biacchi, Alex M. Wiltrout, Nathan S. Lewis, and Raymond E. Schaak. Nanostructured nickel phosphide as an electrocatalyst for the hydrogen evolution reaction. *Journal of the American Chemical Society*, 135(25):9267–9270, 2013. doi: 10.1021/ja403440e. URL `http://dx.doi.org/10.1021/ja403440e`. PMID: 23763295.

[84] Berit Hinnemann, Poul Georg Moses, Jacob Bonde, Kristina P. Jørgensen, Jane H. Nielsen, Sebastian Horch, Ib Chorkendorff, , and Jens K. Nørskov*. Biomimetic hydrogen evolution: mos2 nanoparticles as catalyst for hydrogen evolution. *Journal of the American Chemical Society*, 127(15):5308–5309, 2005. doi: 10.1021/ja0504690. URL `http://dx.doi.org/10.1021/ja0504690`. PMID: 15826154.

[85] Peter C. K. Vesborg and Thomas F. Jaramillo. Addressing the terawatt challenge: scalability in the supply of chemical elements for renewable energy. *RSC Advances*, 2(21):7933–7947. doi: 10.1039/C2RA20839C. URL http://dx.doi.org/10.1039/C2RA20839C.

[86] E. Kemppainen, A. Bodin, B. Sebok, T. Pedersen, B. Seger, B. Mei, D. Bae, P. C. K. Vesborg, J. Halme, O. Hansen, P. D. Lund, and I. Chorkendorff. Scalability and feasibility of photoelectrochemical h2 evolution: the ultimate limit of pt nanoparticle as an her catalyst. *Energy Environ. Sci.*, 8:2991–2999, 2015. doi: 10.1039/C5EE02188J. URL http://dx.doi.org/10.1039/C5EE02188J.

[87] Anders B. Laursen, Soren Kegnaes, Soren Dahl, and Ib Chorkendorff. Molybdenum sulfides-efficient and viable materials for electro - and photoelectrocatalytic hydrogen evolution. *Energy Environ. Sci.*, 5:5577–5591, 2012. doi: 10.1039/C2EE02618J. URL http://dx.doi.org/10.1039/C2EE02618J.

[88] Jesse D. Benck, Thomas R. Hellstern, Jakob Kibsgaard, Pongkarn Chakthranont, and Thomas F. Jaramillo. Catalyzing the hydrogen evolution reaction (her) with molybdenum sulfide nanomaterials. *ACS Catalysis*, 4(11):3957–3971, 2014. doi: 10.1021/cs500923c. URL http://dx.doi.org/10.1021/cs500923c.

[89] Egill Skúlason, Vladimir Tripkovic, Mårten E. Björketun, Sigrídur Gudmundsdóttir, Gustav Karlberg, Jan Rossmeisl, Thomas Bligaard, Hannes Jónsson, and Jens K. Nørskov. Modeling the electrochemical hydrogen oxidation and evolution reactions on the basis of density functional theory calculations. *The Journal of Physical Chemistry C*, 114(42):18182–18197. ISSN 1932-7447. doi: 10.1021/jp1048887. URL http://dx.doi.org/10.1021/jp1048887.

[90] Egill Skulason, Gustav S. Karlberg, Jan Rossmeisl, Thomas Bligaard, Jeff Greeley, Hannes Jonsson, and Jens K. Norskov. Density functional theory calculations for the hydrogen evolution reaction in an electrochemical double layer on the pt(111) electrode. *Phys. Chem. Chem. Phys.*, 9:3241–3250, 2007. doi: 10.1039/B700099E. URL http://dx.doi.org/10.1039/B700099E.

[91] Ram Subbaraman, Dusan Tripkovic, Dusan Strmcnik, Kee-Chul Chang, Masanobu Uchimura, Arvydas P. Paulikas, Vojislav Stamenkovic, and Nenad M. Markovic. Enhancing hydrogen evolution activity in water splitting by tailoring li+-ni(oh)2-pt interfaces. *Science*, 334(6060):1256–1260, 2011. ISSN 0036-8075. doi: 10.1126/science.1211934. URL http://science.sciencemag.org/content/334/6060/1256.

[92] Malte Nielsen, Mårten E. Björketun, Martin Hangaard Hansen, and Jan Rossmeisl. Towards first principles modeling of electrochemical electrode–electrolyte interfaces. *Surface Science*, 631:2 – 7, 2015. ISSN 0039-6028. doi: http://dx.doi.org/10.1016/j.susc.2014.08.018. URL `http://www.sciencedirect.com/science/article/pii/S0039602814002453`. Surface Science and Electrochemistry - 20 years later.

[93] Heron Vrubel and Xile Hu. Molybdenum boride and carbide catalyze hydrogen evolution in both acidic and basic solutions. *Angewandte Chemie*, 124(51):12875–12878, 2012. ISSN 1521-3757. doi: 10.1002/ange.201207111. URL `http://dx.doi.org/10.1002/ange.201207111`.

[94] W.-F. Chen, C.-H. Wang, K. Sasaki, N. Marinkovic, W. Xu, J. T. Muckerman, Y. Zhu, and R. R. Adzic. Highly active and durable nanostructured molybdenum carbide electrocatalysts for hydrogen production. *Energy Environ. Sci.*, 6:943–951, 2013. doi: 10.1039/C2EE23891H. URL `http://dx.doi.org/10.1039/C2EE23891H`.

[95] Peng Xiao, Ya Yan, Xiaoming Ge, Zhaolin Liu, Jing-Yuan Wang, and Xin Wang. Investigation of molybdenum carbide nano-rod as an efficient and durable electrocatalyst for hydrogen evolution in acidic and alkaline media. *Applied Catalysis B: Environmental*, 154–155:232 – 237, 2014. ISSN 0926-3373. doi: http://dx.doi.org/10.1016/j.apcatb.2014.02.020. URL `http://www.sciencedirect.com/science/article/pii/S0926337314001131`.

[96] X. Hu H. Vrubel. *Molybdenum Based Electrocatalysts for Hydrogen Evolution in Water*. PhD thesis, 2013.

[97] Roland Kiessling. The crystal structures of molybdenum and tungsten borides. *Acta Chem. Scand*, 1:893, 1947.

[98] Ping Liu, José A Rodriguez, Takeshi Asakura, João Gomes, and Kenichi Nakamura. Desulfurization reactions on ni2p (001) and α-mo2c (001) surfaces: Complex role of p and c sites. *The Journal of Physical Chemistry B*, 109(10):4575–4583, 2005.

[99] Ping Liu and José A. Rodriguez. Effects of carbon on the stability and chemical performance of transition metal carbides: a density functional study. *The Journal of Chemical Physics*, 120(11), 2004.

[100] Ronald Michalsky, Yin-Jia Zhang, and Andrew A. Peterson. Trends in the hydrogen evolution activity of metal carbide catalysts. *ACS Catalysis*, 4(5):1274–1278, 2014. doi: 10.1021/cs500056u. URL `http://dx.doi.org/10.1021/cs500056u`.

[101] Shyue Ping Ong, Anubhav Jain, Geoffroy Hautier, Michael Kocher, Shreyas Cholia, Dan Gunter, David Bailey, David Skinner, Kristin A Persson, and Gerbrand Ceder. The Materials Project, 2011. URL http://materialsproject.org/.

[102] Martin Hangaard Hansen, Lucas-Alexandre Stern, Ligang Feng, Jan Rossmeisl, and Xile Hu. Widely available active sites on ni2p for electrochemical hydrogen evolution - insights from first principles calculations. *Phys. Chem. Chem. Phys.*, 17:10823–10829, 2015. doi: 10.1039/C5CP01065A. URL http://dx.doi.org/10.1039/C5CP01065A.

[103] Ligang Feng, Heron Vrubel, Michael Bensimon, and Xile Hu. Easily-prepared dinickel phosphide (ni2p) nanoparticles as an efficient and robust electrocatalyst for hydrogen evolution. *Phys. Chem. Chem. Phys.*, 16:5917–5921, 2014. doi: 10.1039/C4CP00482E. URL http://dx.doi.org/10.1039/C4CP00482E.

[104] Zonghua Pu, Qian Liu, Chun Tang, Abdullah M. Asiri, and Xuping Sun. Ni2p nanoparticle films supported on a ti plate as an efficient hydrogen evolution cathode. *Nanoscale*, 6:11031–11034, 2014. doi: 10.1039/C4NR03037K. URL http://dx.doi.org/10.1039/C4NR03037K.

[105] Ping Liu and José A. Rodriguez. Catalysts for hydrogen evolution from the [nife] hydrogenase to the ni2p(001) surface: the importance of ensemble effect. *Journal of the American Chemical Society*, 127(42):14871–14878, 2005. doi: 10.1021/ja0540019. URL http://pubs.acs.org/doi/abs/10.1021/ja0540019. PMID: 16231942.

[106] Donghui Guo, Yuta Nakagawa, Hiroko Ariga, Shushi Suzuki, Kumiko Kinoshita, Takeshi Miyamoto, Satoru Takakusagi, Kiyotaka Asakura, Shigeki Otani, and S.Ted Oyama. {STM} studies on the reconstruction of the ni2p $(10\bar{1}0)$ surface. *Surface Science*, 604(17–18):1347 – 1352, 2010. ISSN 0039-6028. doi: http://dx.doi.org/10.1016/j.susc.2010.03.024. URL http://www.sciencedirect.com/science/article/pii/S0039602810001202.

[107] Lennart Bengtsson. Dipole correction for surface supercell calculations. *Physical Review B*, 59(19):12301–12304. URL http://link.aps.org/doi/10.1103/PhysRevB.59.12301.

[108] Anubhav Jain, Shyue Ping Ong, Geoffroy Hautier, Wei Chen, William Davidson Richards, Stephen Dacek, Shreyas Cholia, Dan Gunter, David Skinner, Gerbrand

Ceder, and Kristin a. Persson. The Materials Project: A materials genome approach to accelerating materials innovation. *APL Materials*, 1(1):011002, 2013. ISSN 2166532X. doi: 10.1063/1.4812323. URL http://link.aip.org/link/AMPADS/v1/i1/p011002/s1&Agg=doi.

[109] E. Larsson. An X-ray investigation of the Ni-P system and the crystal structures of Ni P and Ni P2. *Arkiv foer Kemi*, 23:335–365, 1965.

[110] G. Bergerhoff, R. Hundt, R. Sievers, and ID Brown. The inorganic crystal structure data base. *Journal of Chemical Information and Computer Sciences*, 23(2):66–69, 1983. doi: 10.1021/ci00038a003. URL http://pubs.acs.org/doi/abs/10.1021/ci00038a003.

[111] FIZ Karlsruhe. Inorganic Crystal Structure Database. URL http://icsd.fiz-karlsruhe.de.

[112] José A. Rodriguez, Jae-Yong Kim, Jonathan C. Hanson, Stephanie J. Sawhill, and Mark E. Bussell. Physical and chemical properties of mop, ni2p, and monip hydrodesulfurization catalysts: time-resolved x-ray diffraction, density functional, and hydrodesulfurization activity studies. *The Journal of Physical Chemistry B*, 107 (26):6276–6285, 2003. doi: 10.1021/jp022639q. URL http://pubs.acs.org/doi/abs/10.1021/jp022639q.

[113] Peng Xiao, Wei Chen, and Xin Wang. A review of phosphide-based materials for electrocatalytic hydrogen evolution. *Advanced Energy Materials*, 5(24):n/a–n/a, 2015. ISSN 1614-6840. doi: 10.1002/aenm.201500985. URL http://dx.doi.org/10.1002/aenm.201500985. 1500985.

[114] Yuanzhi Chen, Houde She, Xiaohua Luo, Guang-Hui Yue, and Dong-Liang Peng. Solution-phase synthesis of nickel phosphide single-crystalline nanowires. *Journal of Crystal Growth*, 311(4):1229 – 1233, 2009. ISSN 0022-0248. doi: http://dx.doi.org/10.1016/j.jcrysgro.2008.11.094. URL http://www.sciencedirect.com/science/article/pii/S0022024808013432.

[115] Graeme Henkelman and Hannes Jónsson. Improved tangent estimate in the nudged elastic band method for finding minimum energy paths and saddle points. *The Journal of Chemical Physics*, 113(22), 2000.

[116] B.J. Berne, G. Ciccotti, and D.F. Coker. *Classical and Quantum Dynamics in Condensed Phase Simulations*. 1998. ISBN 9789814496056. URL https://books.google.dk/books?id=UoTVCgAAQBAJ.

[117] Graeme Henkelman, Blas P. Uberuaga, and Hannes Jónsson. A climbing image nudged elastic band method for finding saddle points and minimum energy paths. *The Journal of Chemical Physics*, 113(22):9901–9904. URL http://scitation.aip.org/content/aip/journal/jcp/113/22/10.1063/1.1329672.

[118] F. Abild-Pedersen, J. Greeley, F. Studt, J. Rossmeisl, T. R. Munter, P. G. Moses, E. Skúlason, T. Bligaard, and J. K. Nørskov. Scaling properties of adsorption energies for hydrogen-containing molecules on transition-metal surfaces. *Phys. Rev. Lett.*, 99:016105, Jul 2007. doi: 10.1103/PhysRevLett.99.016105. URL http://link.aps.org/doi/10.1103/PhysRevLett.99.016105.

[119] S. Wang, V. Petzold, V. Tripkovic, J. Kleis, J. G. Howalt, E. Skulason, E. M. Fernandez, B. Hvolbaek, G. Jones, A. Toftelund, H. Falsig, M. Bjorketun, F. Studt, F. Abild-Pedersen, J. Rossmeisl, J. K. Norskov, and T. Bligaard. Universal transition state scaling relations for (de)hydrogenation over transition metals. *Phys. Chem. Chem. Phys.*, 13:20760–20765, 2011. doi: 10.1039/C1CP20547A. URL http://dx.doi.org/10.1039/C1CP20547A.

[120] Jan Rossmeisl, Karen Chan, Rizwan Ahmed, Vladimir Tripkovic, and Marten E. Bjorketun. pH in atomic scale simulations of electrochemical interfaces. *Physical Chemistry Chemical Physics*, 15(25):10321–10325, . ISSN 1463-9076. doi: 10.1039/C3CP51083B. URL http://dx.doi.org/10.1039/C3CP51083B.

[121] Egill Skúlason. Modeling electrochemical reactions at the solid-liquid interface using density functional calculations. *Procedia Computer Science*, 51:1887 – 1896, 2015. ISSN 1877-0509. doi: http://dx.doi.org/10.1016/j.procs.2015.05.431. URL http://www.sciencedirect.com/science/article/pii/S1877050915012399. International Conference On Computational Science, {ICCS} 2015Computational Science at the Gates of Nature.

[122] Karen Chan and Jens K. Nørskov. Electrochemical barriers made simple. *The Journal of Physical Chemistry Letters*, 6(14):2663–2668, 2015. doi: 10.1021/acs.jpclett.5b01043. URL http://dx.doi.org/10.1021/acs.jpclett.5b01043. PMID: 26266844.

[123] Karen Chan and Jens K. Nørskov. Potential dependence of electrochemical barriers from ab initio calculations. *The Journal of Physical Chemistry Letters*, 7(9):1686–1690, 2016. doi: 10.1021/acs.jpclett.6b00382. URL http://dx.doi.org/10.1021/acs.jpclett.6b00382. PMID: 27088442.

[124] Juan F. Callejas, Joshua M. McEnaney, Carlos G. Read, J. Chance Crompton, Adam J. Biacchi, Eric J. Popczun, Thomas R. Gordon, Nathan S. Lewis, and Raymond E. Schaak. Electrocatalytic and photocatalytic hydrogen production from acidic and neutral-ph aqueous solutions using iron phosphide nanoparticles. *ACS Nano*, 8(11):11101–11107, 2014. doi: 10.1021/nn5048553. URL `http://dx.doi.org/10.1021/nn5048553`. PMID: 25250976.

[125] Eric J. Popczun, Carlos G. Read, Christopher W. Roske, Nathan S. Lewis, and Raymond E. Schaak. Highly active electrocatalysis of the hydrogen evolution reaction by cobalt phosphide nanoparticles. *Angewandte Chemie*, 126(21):5531–5534, 2014. ISSN 1521-3757. doi: 10.1002/ange.201402646. URL `http://dx.doi.org/10.1002/ange.201402646`.

[126] Joshua M. McEnaney, J. Chance Crompton, Juan F. Callejas, Eric J. Popczun, Carlos G. Read, Nathan S. Lewis, and Raymond E. Schaak. Electrocatalytic hydrogen evolution using amorphous tungsten phosphide nanoparticles. *Chem. Commun.*, 50:11026–11028, 2014. doi: 10.1039/C4CC04709E. URL `http://dx.doi.org/10.1039/C4CC04709E`.

[127] Jakob Kibsgaard, Charlie Tsai, Karen Chan, Jesse D. Benck, Jens K. Norskov, Frank Abild-Pedersen, and Thomas F. Jaramillo. Designing an improved transition metal phosphide catalyst for hydrogen evolution using experimental and theoretical trends. *Energy Environ. Sci.*, 8:3022–3029, 2015. doi: 10.1039/C5EE02179K. URL `http://dx.doi.org/10.1039/C5EE02179K`.

[128] Ana Sofia Varela, Wen Ju, Tobias Reier, and Peter Strasser. Tuning the catalytic activity and selectivity of cu for co2 electroreduction in the presence of halides. *ACS Catalysis*, 6(4):2136–2144, 2016. doi: 10.1021/acscatal.5b02550. URL `http://dx.doi.org/10.1021/acscatal.5b02550`.

[129] Ana Sofia Varela, Matthias Kroschel, Tobias Reier, and Peter Strasser. Controlling the selectivity of {CO2} electroreduction on copper: The effect of the electrolyte concentration and the importance of the local ph. *Catalysis Today*, 260:8 – 13, 2016. ISSN 0920-5861. doi: http://dx.doi.org/10.1016/j.cattod.2015.06.009. URL `http://www.sciencedirect.com/science/article/pii/S0920586115003594`. Surface Analysis and Dynamics (SAND).

[130] M. Otani and O. Sugino. First-principles calculations of charged surfaces and inter-

faces: A plane-wave nonrepeated slab approach. *Physical Review B*, 73(11):115407. URL http://link.aps.org/doi/10.1103/PhysRevB.73.115407.

[131] Jean-Sébastien Filhol and Matthew Neurock. Elucidation of the electrochemical activation of water over pd by first principles. *Angewandte Chemie International Edition*, 45(3):402–406. ISSN 1521-3773. doi: 10.1002/anie.200502540. URL http://dx.doi.org/10.1002/anie.200502540.

[132] Nicéphore Bonnet and Nicola Marzari. First-principles prediction of the equilibrium shape of nanoparticles under realistic electrochemical conditions. *Phys. Rev. Lett.*, 110:086104, Feb 2013. doi: 10.1103/PhysRevLett.110.086104. URL http://link.aps.org/doi/10.1103/PhysRevLett.110.086104.

[133] Ian T. McCrum and Michael J. Janik. ph and alkali cation effects on the pt cyclic voltammogram explained using density functional theory. *The Journal of Physical Chemistry C*, 120(1):457–471, 2016. doi: 10.1021/acs.jpcc.5b10979. URL http://dx.doi.org/10.1021/acs.jpcc.5b10979.

[134] N. David Mermin. Thermal properties of the inhomogeneous electron gas. *Phys. Rev.*, 137:A1441–A1443, Mar 1965. doi: 10.1103/PhysRev.137.A1441. URL http://link.aps.org/doi/10.1103/PhysRev.137.A1441.

[135] A. Y. Lozovoi, A. Alavi, J. Kohanoff, and R. M. Lynden-Bell. Ab initio simulation of charged slabs at constant chemical potential. *The Journal of Chemical Physics*, 115(4), 2001.

[136] Nicéphore Bonnet, Tetsuya Morishita, Osamu Sugino, and Minoru Otani. First-principles molecular dynamics at a constant electrode potential. *Phys. Rev. Lett.*, 109:266101, Dec 2012. doi: 10.1103/PhysRevLett.109.266101. URL http://link.aps.org/doi/10.1103/PhysRevLett.109.266101.

[137] Mads Brandbyge, José-Luis Mozos, Pablo Ordejón, Jeremy Taylor, and Kurt Stokbro. Density-functional method for nonequilibrium electron transport. *Physical Review B*, 65(16):165401. URL http://link.aps.org/doi/10.1103/PhysRevB.65.165401.

[138] Trasatti, Sergio. The absolute electrode potential: an explanatory note (recommendations 1986). *Pure and Applied Chemistry*, 58(7):955, 1986. ISSN 13653075. doi: 10.1351/pac198658070955. URL //www.degruyter.com/view/j/pac.1986.58.issue-7/pac198658070955/pac198658070955.xml.

[139] Yu Cai, , and Alfred B. Anderson. The reversible hydrogen electrode: potential-dependent activation energies over platinum from quantum theory. *The Journal of Physical Chemistry B*, 108(28):9829–9833, 2004. doi: 10.1021/jp037126d. URL http://dx.doi.org/10.1021/jp037126d.

[140] Christopher D. Taylor, Sally A. Wasileski, Jean-Sebastien Filhol, and Matthew Neurock. First principles reaction modeling of the electrochemical interface: Consideration and calculation of a tunable surface potential from atomic and electronic structure. *Physical Review B*, 73(16):165402. URL http://link.aps.org/doi/10.1103/PhysRevB.73.165402.

[141] Sebastian Schnur and Axel Groß. Challenges in the first-principles description of reactions in electrocatalysis. *Catalysis Today*, 165(1):129 – 137, 2011. ISSN 0920-5861. doi: http://dx.doi.org/10.1016/j.cattod.2010.11.071. URL http://www.sciencedirect.com/science/article/pii/S0920586110008187. Theoretical Catalysis for Energy Production and Utilization: from First Principles Theory to Microkinetics.

[142] Eriko Watanabe, Jan Rossmeisl, Mårten E. Björketun, Hiroshi Ushiyama, and Koichi Yamashita. Atomic-scale analysis of the ruo2/water interface under electrochemical conditions. *The Journal of Physical Chemistry C*, 120(15):8096–8103, 2016. doi: 10.1021/acs.jpcc.5b12448. URL http://dx.doi.org/10.1021/acs.jpcc.5b12448.

[143] Zhenhua Zeng, Martin Hangaard Hansen, Jeffrey P. Greeley, Jan Rossmeisl, and Mårten E. Björketun. Ab initio thermodynamic modeling of electrified metal–oxide interfaces: Consistent treatment of electronic and ionic chemical potentials. *The Journal of Physical Chemistry C*, 118(39):22663–22671, 2014. doi: 10.1021/jp507519a. URL http://dx.doi.org/10.1021/jp507519a.

[144] Sarp Kaya, Daniel Schlesinger, Susumu Yamamoto, John T. Newberg, Hendrik Bluhm, Hirohito Ogasawara, Tom Kendelewicz, Gordon E. Brown, Lars G. M. Pettersson, and Anders Nilsson. Highly compressed two-dimensional form of water at ambient conditions. *Scientific Reports*, 3:1074. URL http://dx.doi.org/10.1038/srep01074.

[145] I-F. W. Kuo, J. I. Siepmann J. VandeVondele C. J. Mundy, M. J. McGrath, M. Sprik, J. Hutter, and F. Mohamed M. Krack M. Parrinello B. Chen, M. L. Klein. Liquid water from first principles: investigation of different sampling approaches. *The Journal*

of Physical Chemistry B, 108(34):12990–12998, 2004. doi: 10.1021/jp047788i. URL http://dx.doi.org/10.1021/jp047788i.

[146] HJC Berendsen and WF Van Gunsteren. Practical algorithms for dynamic simulations. *Molecular-dynamics simulation of statistical-mechanical systems*, pages 43–65, 1986.

[147] William C. Swope, Hans C. Andersen, Peter H. Berens, and Kent R. Wilson. A computer simulation method for the calculation of equilibrium constants for the formation of physical clusters of molecules: Application to small water clusters. *The Journal of Chemical Physics*, 76(1), 1982.

[148] Ernst Hairer, Christian Lubich, and Gerhard Wanner. Geometric numerical integration illustrated by the stömer-verlet method. *Acta Numerica*, 12:399–450, 5 2003. ISSN 1474-0508. doi: 10.1017/S0962492902000144. URL http://journals.cambridge.org/article_S0962492902000144.

[149] R. Car and M. Parrinello. Unified approach for molecular dynamics and density-functional theory. *Phys. Rev. Lett.*, 55:2471–2474, Nov 1985. doi: 10.1103/PhysRevLett.55.2471. URL http://link.aps.org/doi/10.1103/PhysRevLett.55.2471.

[150] Ali A. Hassanali, Jérôme Cuny, Vincenzo Verdolino, and Michele Parrinello. Aqueous solutions: state of the art in ab initio molecular dynamics. *Philosophical Transactions of the Royal Society of London A: Mathematical, Physical and Engineering Sciences*, 372(2011), 2014. ISSN 1364-503X. doi: 10.1098/rsta.2012.0482. URL http://rsta.royalsocietypublishing.org/content/372/2011/20120482.

[151] Andreas Møgelhøj, André K. Kelkkanen, K. Thor Wikfeldt, Jakob Schiøtz, Jens Jørgen Mortensen, Lars G. M. Pettersson, Bengt I. Lundqvist, Karsten W. Jacobsen, Anders Nilsson, and Jens K. Nørskov. Ab initio van der waals interactions in simulations of water alter structure from mainly tetrahedral to high-density-like. *The Journal of Physical Chemistry B*, 115(48):14149–14160, 2011. doi: 10.1021/jp2040345. URL http://dx.doi.org/10.1021/jp2040345. PMID: 21806000.

[152] Nosé Shuichi. Constant temperature molecular dynamics methods. *Progress of Theoretical Physics Supplement*, 103:1–46, 1991. doi: 10.1143/PTPS.103.1. URL http://ptps.oxfordjournals.org/content/103/1.abstract.

[153] H. J. C. Berendsen, J. P. M. Postma, W. F. van Gunsteren, A. DiNola, and J. R. Haak. Molecular dynamics with coupling to an external bath. *The Journal of Chemical Physics*, 81(8), 1984.

[154] Anirban Mudi and Charusita Chakravarty. Effect of the berendsen thermostat on the dynamical properties of water. *Molecular Physics*, 102(7):681–685, 2004. doi: 10.1080/00268970410001698937. URL http://dx.doi.org/10.1080/00268970410001698937.

[155] Mårten E. Björketun, ZhenHua Zeng, Rizwan Ahmed, Vladimir Tripkovic, Kristian S. Thygesen, and Jan Rossmeisl. Avoiding pitfalls in the modeling of electrochemical interfaces. *Chemical Physics Letters*, 555(0):145–148. ISSN 0009-2614. doi: 10.1016/j.cplett.2012.11.025. URL http://www.sciencedirect.com/science/article/pii/S0009261412013310.

[156] Georges Valette. Hydrophilicity of metal surfaces. *Journal of Electroanalytical Chemistry and Interfacial Electrochemistry*, 139(2):285 – 301, 1982. ISSN 0022-0728. doi: http://dx.doi.org/10.1016/0022-0728(82)85127-9. URL http://www.sciencedirect.com/science/article/pii/0022072882851279.

[157] J. Lecoeur, J.P. Bellier, and C. Koehler. Comparison of crystalographic anisotropy effects on potential of zero charge and electronic work function for gold 111, 311, 110 and 210 orientations. *Electrochimica Acta*, 35(9):1383 – 1392, 1990. ISSN 0013-4686. doi: http://dx.doi.org/10.1016/0013-4686(90)85010-K. URL http://www.sciencedirect.com/science/article/pii/001346869085010K.

[158] Rizwan Ahmed and Jan Rossmeisl. *First Principle simulations of electrochemical interfaces - a DFT study*. PhD thesis, 2015.

[159] Axel Groß, Florian Gossenberger, Xiaohang Lin, Maryam Naderian, Sung Sakong, and Tanglaw Roman. Water structures at metal electrodes studied by ab initio molecular dynamics simulations. *Journal of The Electrochemical Society*, 161(8): E3015–E3020, 2014.

[160] M. Tuckerman, K. Laasonen, M. Sprik, and M. Parrinello. Abinitio molecular dynamics simulation of the solvation and transport of hydronium and hydroxyl ions in water. *The Journal of Chemical Physics*, 103(1):150–161. URL http://scitation.aip.org/content/aip/journal/jcp/103/1/10.1063/1.469654.

[161] Tanglaw Roman and Axel Gross. Structure of water layers on hydrogen-covered pt electrodes. *Catalysis Today*, 202:183 – 190, 2013. ISSN 0920-5861. doi: http://dx.doi.org/10.1016/j.cattod.2012.06.001. URL http://www.sciencedirect.com/science/article/pii/S0920586112004178. Electrocatalysis.

[162] M. Ceriotti, 2016. URL https://github.com/epfl-cosmo/pamm.

[163] S.E. Koonin and D.C. Meredith. *Computational Physics: Fortran Version*. Addison-Wesley, 1998. ISBN 9780201386233. URL https://books.google.dk/books?id=xAnh4qiSuYQC.

[164] John P. Valleau and L. Kenneth Cohen. Primitive model electrolytes. i. grand canonical monte carlo computations. *The Journal of Chemical Physics*, 72(11):5935–5941. URL http://scitation.aip.org/content/aip/journal/jcp/72/11/10.1063/1.439092.

[165] Antoinette Hamelin, M.J. Sottomayor, F. Silva, Si-Chung Chang, and Michael J. Weaver. Cyclic voltammetric characterization of oriented monocrystalline gold surfaces in aqueous alkaline solution. *Journal of Electroanalytical Chemistry and Interfacial Electrochemistry*, 295(1):291–300. ISSN 0022-0728. doi: 10.1016/0022-0728(90)85023-X. URL http://www.sciencedirect.com/science/article/pii/002207289085023X.

[166] A. Hamelin. Note on the behaviour of the (111) gold face in electrolytic solutions. *Journal of Electroanalytical Chemistry and Interfacial Electrochemistry*, 210(2):303 – 309, 1986. ISSN 0022-0728. doi: http://dx.doi.org/10.1016/0022-0728(86)80583-6. URL http://www.sciencedirect.com/science/article/pii/0022072886805836.

[167] Tanyuan Wang, Lu Liu, Zhiwei Zhu, Pagona Papakonstantinou, Jingbo Hu, Hongyun Liu, and Meixian Li. Enhanced electrocatalytic activity for hydrogen evolution reaction from self-assembled monodispersed molybdenum sulfide nanoparticles on an au electrode. *Energy Environ. Sci.*, 6:625–633, 2013. doi: 10.1039/C2EE23513G. URL http://dx.doi.org/10.1039/C2EE23513G.

[168] A. Hamelin. Cyclic voltammetry at gold single-crystal surfaces. part 1. behaviour at low-index faces. *Journal of Electroanalytical Chemistry*, 407(1):1–11. ISSN 1572-6657. doi: 10.1016/0022-0728(95)04499-X. URL http://www.sciencedirect.com/science/article/pii/002207289504499X.

[169] Donald D. Bode Jr., Terrell N. Andersen, and Henry Eyring. Anion and ph effects on the potentials of zero charge of gold and silver electrodes. *The Journal of Physical Chemistry*, 71(4):792–797, 1967. doi: 10.1021/j100863a002. URL http://dx.doi.org/10.1021/j100863a002.

[170] P. S. Pershan. Review of the highlights of x-ray studies of liquid metal surfaces. *Journal of Applied Physics*, 116(22):222201, 2014. doi: http://dx.doi.org/10.1063/1.4902958. URL http://scitation.aip.org/content/aip/journal/jap/116/22/10.1063/1.4902958.

[171] A.N. Frumkin and O.A. Petrii. Potentials of zero total and zero free charge of platinum group metals. *Electrochimica Acta*, 20(5):347 – 359, 1975. ISSN 0013-4686. doi: http://dx.doi.org/10.1016/0013-4686(75)90017-1. URL http://www.sciencedirect.com/science/article/pii/0013468675900171.

[172] Victor Climent, Barry A. Coles, and Richard G. Compton. Laser induced current transients applied to a au(111) single crystal electrode. a general method for the measurement of potentials of zero charge of solid electrodes. *The Journal of Physical Chemistry B*, 105(43):10669–10673, . ISSN 1520-6106. doi: 10.1021/jp012402e. URL http://dx.doi.org/10.1021/jp012402e.

[173] Víctor Climent, Barry A. Coles, and Richard G. Compton. Laser-induced potential transients on a au(111) single-crystal electrode. determination of the potential of maximum entropy of double-layer formation. *The Journal of Physical Chemistry B*, 106(20):5258–5265, . ISSN 1520-6106. doi: 10.1021/jp020054q. URL http://dx.doi.org/10.1021/jp020054q.

[174] Nuria García-Aráez, Víctor Climent, and Juan M. Feliu. Potential-dependent water orientation on pt(1 1 1) stepped surfaces from laser-pulsed experiments. *Electrochimica Acta*, 54(3):966–977. ISSN 0013-4686. doi: 10.1016/j.electacta.2008.08.016. URL http://www.sciencedirect.com/science/article/pii/S0013468608009997.

[175] J.A. Harrison, J.E.B. Randles, and D.J. Schiffrin. The entropy of formation of the mercury-aqueous solution interface and the structure of the inner layer. *Journal of Electroanalytical Chemistry and Interfacial Electrochemistry*, 48(3):359 – 381, 1973. ISSN 0022-0728. doi: http://dx.doi.org/10.1016/S0022-0728(73)80369-9. URL http://www.sciencedirect.com/science/article/pii/S0022072873803699.

[176] V.A. Benderskii and G.I. Velichko. Temperature jump in electric double-layer study. *Journal of Electroanalytical Chemistry and Interfacial Electrochemistry*, 140(1):1 – 22, 1982. ISSN 0022-0728. doi: http://dx.doi.org/10.1016/0368-1874(82)85295-7. URL http://www.sciencedirect.com/science/article/pii/0368187482852957.

[177] Jan Rossmeisl, Gustav S. Karlberg, Thomas Jaramillo, and Jens K. Norskov. Steady state oxygen reduction and cyclic voltammetry. *Faraday Discussions*, 140(0):337–346, . ISSN 1359-6640. doi: 10.1039/B802129E. URL http://dx.doi.org/10.1039/B802129E.

[178] T. Schiros, L. Å. Näslund, K. Andersson, J. Gyllenpalm, G. S. Karlberg, M. Odelius, H. Ogasawara, L. G. M. Pettersson, , and A. Nilsson. Structure and bonding of the water−hydroxyl mixed phase on pt(111). *The Journal of Physical Chemistry C*, 111(41):15003–15012, 2007. doi: 10.1021/jp073405f. URL http://dx.doi.org/10.1021/jp073405f.

[179] G. S. Karlberg, T. F. Jaramillo, E. Skúlason, J. Rossmeisl, T. Bligaard, and J. K. Nørskov. Cyclic voltammograms for h on pt(111) and pt(100) from first principles. *Phys. Rev. Lett.*, 99:126101, Sep 2007. doi: 10.1103/PhysRevLett.99.126101. URL http://link.aps.org/doi/10.1103/PhysRevLett.99.126101.

[180] Wenchao Sheng, Zhongbin Zhuang, Minrui Gao, Jie Zheng, Jingguang G Chen, and Yushan Yan. Correlating hydrogen oxidation and evolution activity on platinum at different ph with measured hydrogen binding energy. *Nature communications*, 6, 2015.

[181] Jorge Mostany, Enrique Herrero, Juan M. Feliu, and Jacek Lipkowski. Determination of the gibbs excess of h and OH adsorbed at a pt(1 1 1) electrode surface using a thermodynamic method. *Journal of Electroanalytical Chemistry*, 558:19–24. ISSN 1572-6657. doi: 10.1016/S0022-0728(03)00372-3. URL http://www.sciencedirect.com/science/article/pii/S0022072803003723.

[182] Nuria Garcia-Araez, Victor Climent, and Juan Feliu. Potential-dependent water orientation on pt(111), pt(100), and pt(110), as inferred from laser-pulsed experiments. electrostatic and chemical effects. *The Journal of Physical Chemistry C*, 113(21):9290–9304. ISSN 1932-7447. doi: 10.1021/jp900792q. URL http://dx.doi.org/10.1021/jp900792q.

[183] Maria J.T.C. van der Niet, Nuria Garcia-Araez, Javier Hernández, Juan M. Feliu, and Marc T.M. Koper. Water dissociation on well-defined platinum surfaces: The electrochemical perspective. *Catalysis Today*, 202:105 – 113, 2013. ISSN 0920-5861. doi: http://dx.doi.org/10.1016/j.cattod.2012.04.059. URL `http://www.sciencedirect.com/science/article/pii/S092058611200346X`. Electrocatalysis.

7. Appendix

7.1 Metal Phosphides

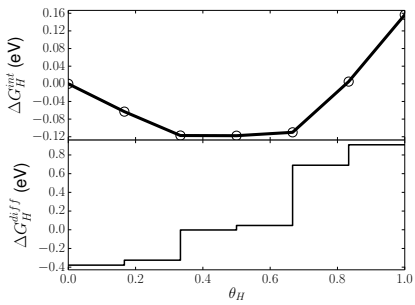

(a) *Free energies of hydrogen adsorption. The upper panel shows integral free energy, while the lower panel shows differential free energy.*

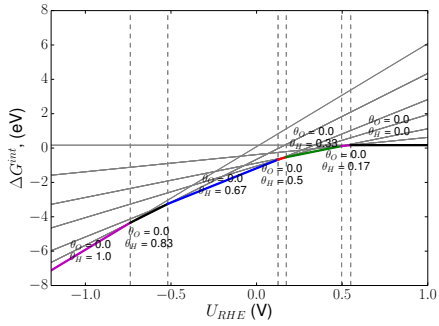

(b) *Surface phase diagram of Co_2P $(10\bar{1}0)$*

Figure 7.1: Results on Co_2P.

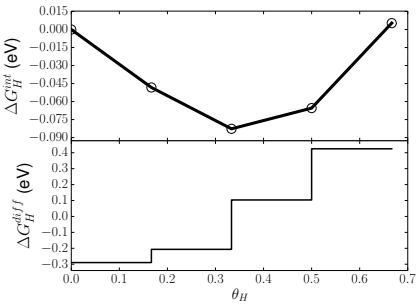

(a) *Free energies of hydrogen adsorption. The upper panel shows integral free energy, while the lower panel shows differential free energy.*

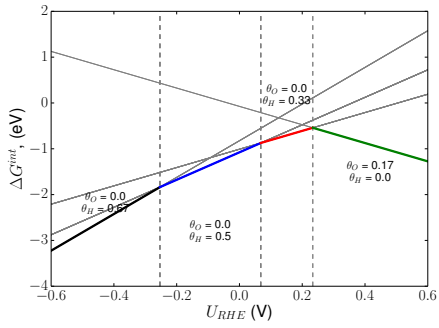

(b) *Surface phase diagram of Fe_2P $(10\bar{1}0)$*

Figure 7.2: Results on Fe_2P.

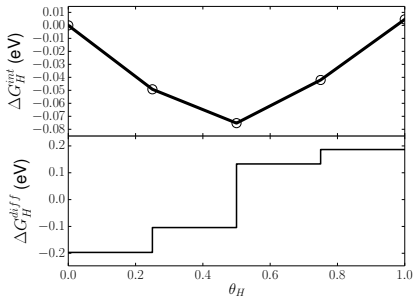

(a) *Free energies of hydrogen adsorption. The upper panel shows integral free energy, while the lower panel shows differential free energy.*

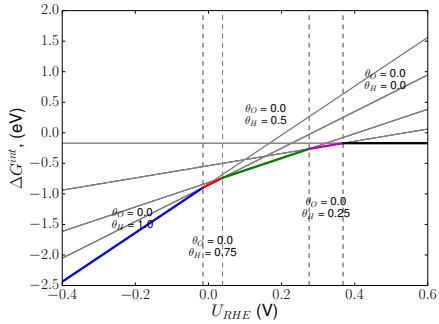

(b) *Surface phase diagram of CoP (100)*

Figure 7.3: Results on CoP.

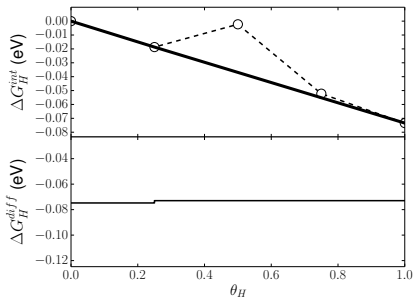

(a) *Free energies of hydrogen adsorption. The upper panel shows integral free energy, while the lower panel shows differential free energy.*

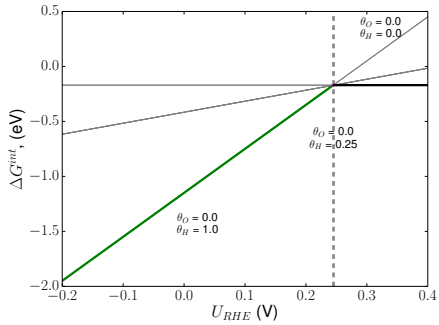

(b) *Surface phase diagram of MnP (100)*

Figure 7.4: Results on MnP.

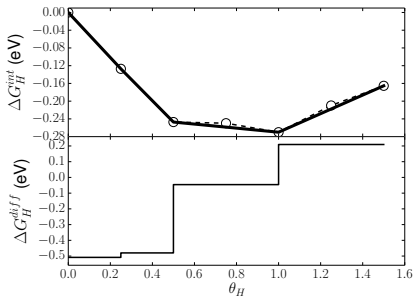

(a) *Free energies of hydrogen adsorption. The upper panel shows integral free energy, while the lower panel shows differential free energy.*

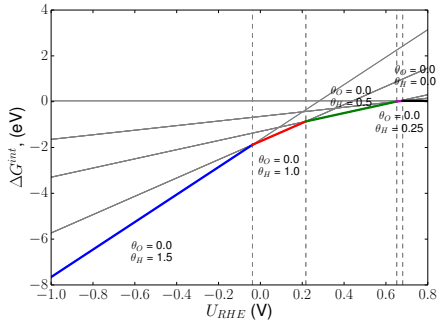

(b) *Surface phase diagram of WP (100)*

Figure 7.5: Results on WP

7.2 Water Structure

7.2.1 Au(111)/Water

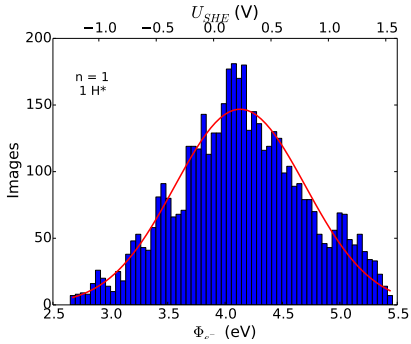

(a) 1/12 ML H*

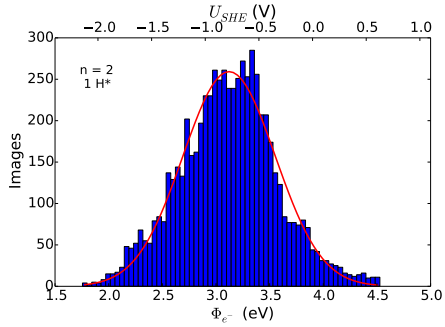

(b) 1/12 ML H* and 1 Proton

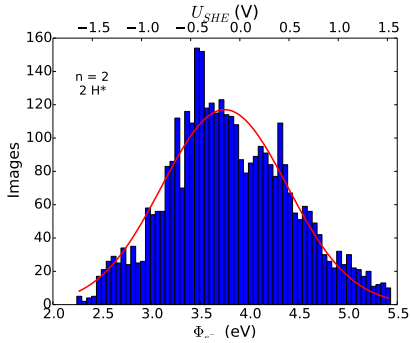

(c) 1/6 ML H*

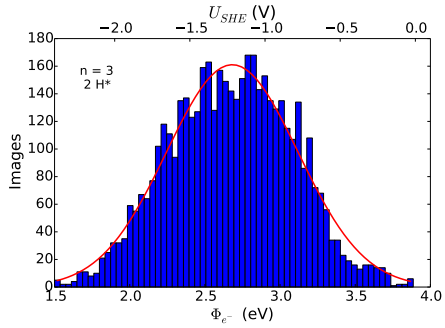

(d) 1/6 ML H* and 1 Proton

Figure 7.6: Histogram of work functions from constant N, V and T subsets of the ensemble.

8. Included Publications

Paper I

Tuning the activity of Pt alloy lanthanide contraction

María Escudero-Escribano, Paolo Malacrida, Martin H. Hansen Ulrik G. Vej-Hansen, Amado Velázquez-Palenzuela, Vladimir Tripkovic, Jakob Schiøtz, Jan Rossmeisl, Ifan E. L. Stephens, Ib Chorkendorff

Science, April 1st (**2016**), 352, 6281

that its concentration-dependent behavior and values correspond to a crystallization transition that is consistent with that found in other condensed matter systems (*28*). A thermal expansion of ~0.01°C^{-1} of the lattice (fig. S8) stems from the decrease of an average NLC elastic constant K and quadrupolar elastic forces as temperature increases (K decreases by a factor of ~3 when the composite is heated from room temperature to ~34°C) (*22*).

Nanorods can be electrically concentrated and ordered starting from dilute initial dispersions (fig. S9), similar to the crystallization of hard sphere–like colloids when subjected to electrophoretic or dielectrophoretic forces (*29*). The triclinic crystal order is facilitated by applying 300 to 900 mV to transparent electrodes on inner substrates of the cell, which is lower than the threshold voltage needed for NLC switching. In response to these dc fields, the positively charged nanorods slowly move toward a negative electrode as a result of electrophoresis and eventually form a crystal as their concentration uniformly increases (fig. S9). These low voltages also facilitate uniform alignment of crystalline nuclei and healing of defects; in addition, they induce a giant electrostriction of the triclinic lattice, with ~25% strain at fields of 0.03 V μm^{-1} (fig. S8B). Because NLC is switched at ~1 V (*9*, *21*), colloidal crystal lattice orientations can be reconfigured while following the rotation of the director, although these processes are slow and complex. Electric fields, confinement in thin cells (thicknesses ≤15 μm) that are incompatible with an integer number of primitive cells in the colloidal crystal, variations in nanorod concentrations that exceed the range accommodated by an equilibrium triclinic lattice, and temperature changes control the primitive cell parameters (table S1) and prompt the formation of defects ranging from edge dislocations (fig. S11) to vacancies and grain boundaries (*2*, *22*, *30*).

We have introduced a highly tunable and reconfigurable colloidal system with competing long-range elastic and electrostatic interactions that lead to triclinic pinacoidal lattices of orientationally ordered nanorods. This unexpected triclinic crystallization of semiconductor particles at packing factors <<1% shows potential for the self-assembly of a wide variety of mesostructured composites on device-relevant scales, which can be tuned by weak external stimuli such as low-voltage fields and very small temperature changes. The control of particle charging allowed for tuning of the triclinic lattice periodicity between 0.5 and 1.6 μm, a range which can be extended by tuning the strength of electrostatic interactions through doping or deionizing NLCs (*10*–*13*) or through using nematics with different properties. Considering that dipolar and other multipolar elastic colloidal interactions in NLCs can be introduced and guided by controlling the boundary conditions at particle surfaces, and given that the control of NLC elastic constants may alter the angular dependencies of these interactions (*22*), our study sets the stage for explorations of mesoscopic colloidal positional and orientational ordering that can enable the engineering of material properties through spontaneous ordering of nanoparticles.

REFERENCES AND NOTES

1. H. N. W. Lekkerkerker, R. Tuinier, *Colloids and the Depletion Interaction* (Springer Netherlands, 2011).
2. P. M. Chaikin, T. C. Lubensky, *Principles of Condensed Matter Physics* (Cambridge Univ. Press, 1995).
3. V. N. Manoharan, *Science* **349**, 1253751 (2015).
4. P. F. Damasceno, M. Engel, S. C. Glotzer, *Science* **337**, 453–457 (2012).
5. B. Senyuk *et al.*, *Nature* **493**, 200–205 (2013).
6. P. Poulin, H. Stark, T. C. Lubensky, D. A. Weitz, *Science* **275**, 1770–1773 (1997).
7. S. Sacanna, W. T. M. Irvine, P. M. Chaikin, D. J. Pine, *Nature* **464**, 575–578 (2010).
8. M. R. Jones *et al.*, *Nat. Mater.* **9**, 913–917 (2010).
9. Q. Liu, Y. Yuan, I. I. Smalyukh, *Nano Lett.* **14**, 4071–4077 (2014).
10. B. Liu *et al.*, *Nat. Commun.* **5**, 3092 (2014).
11. S. K. Sainis, J. W. Merrill, E. R. Dufresne, *Langmuir* **24**, 13334–13337 (2008).
12. A. Yethiraj, A. van Blaaderen, *Nature* **421**, 513–517 (2003).
13. M. F. Hsu, E. R. Dufresne, D. A. Weitz, *Langmuir* **21**, 4881–4887 (2005).
14. T. C. Lubensky, D. Pettey, N. Currier, H. Stark, *Phys. Rev. E* **57**, 610–625 (1998).
15. R. W. Ruhwandl, E. M. Terentjev, *Phys. Rev. E* **55**, 2958–2961 (1997).
16. S. Ramaswamy, R. Nityananda, V. A. Raghunathan, J. Prost, *Mol. Cryst. Liq. Sci. Technol. A* **288**, 175–180 (1996).
17. C. P. Lapointe, T. G. Mason, I. I. Smalyukh, *Science* **326**, 1083–1086 (2009).
18. J. C. Loudet, P. Barois, P. Poulin, *Nature* **407**, 611–613 (2000).
19. A. Nych *et al.*, *Nat. Commun.* **4**, 1489 (2013).
20. F. Wang *et al.*, *Nature* **463**, 1061–1065 (2010).
21. H. Mundoor, I. I. Smalyukh, *Small* **11**, 5572–5580 (2015).
22. Materials and methods are available as supplementary materials on *Science* Online.
23. N. Bogdan, F. Vetrone, G. A. Ozin, J. A. Capobianco, *Nano Lett.* **11**, 835–840 (2011).
24. D. E. Sands, *Introduction to Crystallography* (Dover Publications, 2012).
25. D. B. Conkey, R. P. Trivedi, S. R. P. Pavani, I. I. Smalyukh, R. Piestun, *Opt. Express* **19**, 3835–3842 (2011).
26. C. A. S. Batista, R. G. Larson, N. A. Kotov, *Science* **350**, 1242477 (2015).
27. V. D. Nguyen, S. Faber, Z. Hu, G. H. Wegdam, P. Schall, *Nat. Commun.* **4**, 1584 (2013).
28. R. W. Cahn, *Nature* **413**, 582–583 (2001).
29. R. C. Hayward, D. A. Saville, I. A. Aksay, *Nature* **404**, 56–59 (2000).
30. I. I. Smalyukh, O. D. Lavrentovich, *Phys. Rev. Lett.* **90**, 085503 (2003).

ACKNOWLEDGMENTS

This research was supported by the U.S. Department of Energy, Office of Basic Energy Sciences, Division of Materials Sciences and Engineering, under award ER46921, contract DE-SC0010305 with the University of Colorado–Boulder. We acknowledge the use of electron microscopy facility at the National Institute of Standards and Technology, Boulder, and thank A. Sanders for the help with imaging. We thank P. Ackerman, Q. Liu, T. Lee, and T. Lubensky for discussions.

SUPPLEMENTARY MATERIALS

www.sciencemag.org/content/352/6281/69/suppl/DC1
Materials and Methods
Figs. S1 to S11
Table S1
Movie S1
References (*31*–*39*)

14 December 2015; accepted 26 February 2016
10.1126/science.aaf0801

ELECTROCATALYSIS

Tuning the activity of Pt alloy electrocatalysts by means of the lanthanide contraction

María Escudero-Escribano,[1,2]* Paolo Malacrida,[1] Martin H. Hansen,[3,4] Ulrik G. Vej-Hansen,[1,3] Amado Velázquez-Palenzuela,[1] Vladimir Tripkovic,[3,5] Jakob Schiøtz,[1,3] Jan Rossmeisl,[3,4] Ifan E. L. Stephens,[1,6]* Ib Chorkendorff[1]*

The high platinum loadings required to compensate for the slow kinetics of the oxygen reduction reaction (ORR) impede the widespread uptake of low-temperature fuel cells in automotive vehicles. We have studied the ORR on eight platinum (Pt)–lanthanide and Pt-alkaline earth electrodes, Pt_5M, where M is lanthanum, cerium, samarium, gadolinium, terbium, dysprosium, thulium, or calcium. The materials are among the most active polycrystalline Pt-based catalysts reported, presenting activity enhancement by a factor of 3 to 6 over Pt. The active phase consists of a Pt overlayer formed by acid leaching. The ORR activity versus the bulk lattice parameter follows a high peaked "volcano" relation. We demonstrate how the lanthanide contraction can be used to control strain effects and tune the activity, stability, and reactivity of these materials.

To reduce the Pt loading at the cathode of polymer electrolyte membrane fuel cells (PEMFCs), researchers have intensively studied alloys of Pt with late transition metals such as Ni or Co as oxygen reduction reaction (ORR) electrocatalysts (*1*–*6*). Catalysts exhibiting even greater activity and stability could be designed through the identification of the descriptors that control the performance (*7*–*10*). One single descriptor controls ORR activity, the ΔE_{OH} binding energy, by way of a Sabatier volcano: An ΔE_{OH} ~0.1 eV weaker than Pt(111) yields the optimum value (*11*). Other indirect descriptors related to ΔE_{OH} include the d-band center (*12*), the Pt-Pt

interatomic distance (*4*) and the generalized coordination number (*8*). Stability is a multiparametric challenge, hence requiring several descriptors, such as the alloying energy E_a (*11*, *13*), and dissolution potential (*14*, *15*).

Our earlier studies identified alloys of Pt and rare earths, in particular Pt_xY and Pt_xGd, as active and stable catalysts for oxygen reduction, both in the bulk polycrystalline (*11*, *16*) and nanoparticle (NP) form (*17*, *18*). The exceptionally negative E_a of Pt–rare earth alloys should increase their resistance to degradation (*11*, *13*). In contrast, more commonly studied ORR alloys, such as Pt-Ni or Pt-Co, typically degrade in long-term tests via dealloying (*19*, *20*). Nevertheless, new forms of Pt-Ni–based catalysts achieve exceptional activity and stability during short-term accelerated degradation tests (*5*, *21*, *22*). Nonetheless, engendering long-term stability in fuel cells (*20*) may require materials that are inherently less prone to dealloying. Because the rare earth (e.g., Y or Gd) is unstable against dissolution, a Pt overlayer is formed on the surface, as shown on Fig. 1, A and B. We showed that on Pt_xGd and Pt_xY NPs, the bulk compressive strain correlated strongly with increased ORR activity; this result suggested that the bulk strain is imposed onto the Pt surface atoms, weakening ΔE_{OH} (*23*). These observations led us to conjecture that other Pt-lanthanide alloys, exhibiting more optimal levels of compression, would reach the peak of the Sabatier volcano. Here, we show how the decreased radius of the lanthanides with increased filling of the f-shell—i.e., the lanthanide contraction—provides us with a route to engineer such compression. We have systematically studied activity and stability trends of Pt_5La, Pt_5Ce, Pt_5Sm, Pt_5Gd, Pt_5Tb, Pt_5Dy, Pt_5Tm, and Pt_5Ca, using a combination of experiments and theory to explain our observations.

We evaluated the electrocatalytic properties of sputter-cleaned polycrystalline Pt_5M electrodes by rotating disk electrode (RDE) voltammetry in O_2-saturated 0.1 M $HClO_4$. We chose a Pt:M ratio of 5:1 because we could obtain a consistent series of alloys with the same structure, allowing for a systematic investigation. Furthermore, it corresponds to the phase that is most Pt-rich and stable (*16*). At 0.9 V, Pt_5Tb is the most active polycrystalline Pt-based catalyst reported. All of the materials exhibited activity enhancement by a factor of 3 to 6 over pure Pt (see figs. S5 and S6 and table S1 in the supplementary materials). The overall electrocatalytic ranking of ORR activity of polycrystalline Pt alloys is shown in fig. S6: $Pt_5Tb > Pt_5Gd \sim Pt_3Y > Pt_5Sm > Pt_5Ca \sim Pt_5Dy > Pt_5Tm > Pt_5Ce > Pt_5Y \sim Pt_5La >> Pt$ (*6*, *11*, *16*), demonstrating that these alloys accelerate the ORR more effectively than other polycrystalline Pt alloys. Pt_3Co and Pt_3Ni alloys prepared this way exhibited enhancement only by a factor of 2 (*12*, *24*). Accelerated stability tests consisting of 10,000 consecutive cycles between 0.6 and 1.0 V versus a reversible hydrogen electrode (RHE) were performed after the initial ORR activity measurements. The electrochemical experiments are summarized in figs. S3 to S11. Figure 1C reports the ORR activities before and after the stability test for all the Pt alloys and pure Pt. Apart from Pt_5Ca (which has a lower E_a), all of the Pt-lanthanide alloys retained enhancement by a factor of 3 over pure Pt after the accelerated stability test. Notably, Pt_5Gd exhibited a residual activity that was 5 times as great as that of pure Pt.

We characterized the structure and chemical composition of the electrocatalysts by x-ray diffraction (XRD) and x-ray photoelectron spectroscopy (XPS) in order to explain our experimental observations. All of the alloys formed stable intermetallic compounds with a hexagonal structure (figs. S1 and S2 and table S1), in agreement with previous reports (*25*). The XRD data suggest that the polycrystalline alloys may show different degrees of preferential orientation in the bulk (figs. S1 and S2). However, by presputtering the electrodes, we minimize any differences in surface orientation between the samples under investigation. Moreover, based on Watanabe and coworkers' in situ scanning tunneling microscopy measurements on sputter-deposited Pt-Fe (*26*), we expect the acid-leached Pt overlayers to be dominated by (111) terraces, typically the most stable facet termination (*27*). Most of the elements in the bulk Pt_5M alloy form a so-called kagome layer (*6*, *16*) (Fig. 2 and fig. S16), with a nearest-neighbor Pt-Pt distance $d_{Pt\text{-}Pt} = a/2$. The lattice parameter a and hence $d_{Pt\text{-}Pt}$ decreased from left to right in the lanthanide series (Fig. 2).

Figure 3, A and B, show the angle-resolved XPS (AR-XPS) depth profiles on sputter-cleaned Pt_5Tb before and after electrochemical measurements. For each of the alloys, the Pt to M ratio increased substantially, especially at the most surface-sensitive angles, as shown for Pt_5Tb on Fig. 3C, after initial electrochemistry measurements, confirming the formation of a Pt overlayer. The depth profile of Fig. 3B showed that, even after accelerated stability tests, this structure was maintained, demonstrating the stability of these materials upon potential cycling.

To quantitatively interpret our XPS data (for details, see section S4 of the supplementary materials and figs. S12 to S15), we evaluated the mean Pt overlayer thickness for the alloys. Figure 3D shows how it varied for both the initial ORR activity and after stability tests as a function of the bulk lattice parameter a. The overlayer thickness after the initial testing varied little between the different alloys. However, after stability tests, the mean Pt overlayer generally increased from Pt_5La to Pt_5Tb [Pt_5Ca lies out of the scale; the initial Pt:M ratios for Pt_5Ca, Pt_5Sm, and Pt_5Dy were in fact higher than those expected from the nominal bulk stoichiometry (fig. S13), thus inhibiting a precise calculation of the overlayer thickness]. This difference could explain the anomalous behavior of

[1]Center for Individual Nanoparticle Functionality (CINF), Department of Physics, Technical University of Denmark, 2800 Lyngby, Denmark. [2]Department of Chemical Engineering, Stanford University, Stanford, CA 94305, USA. [3]Center for Atomic-Scale Materials Design (CAMD), Department of Physics, Technical University of Denmark, 2800 Lyngby, Denmark. [4]Nano-Science Center, Department of Chemistry, University of Copenhagen, 2100 Copenhagen, Denmark. [5]Department of Energy Conversion and Storage, Technical University of Denmark, 4000 Roskilde, Denmark. [6]Department of Mechanical Engineering, Massachusetts Institute of Technology, Cambridge, MA 02139, USA.
***Corresponding author. E-mail: ibchork@fysik.dtu.dk (I.C.); ifan@fysik.dtu.dk (I.E.L.S.); maria.escudero@fysik.dtu.dk (M.E.-E.)**

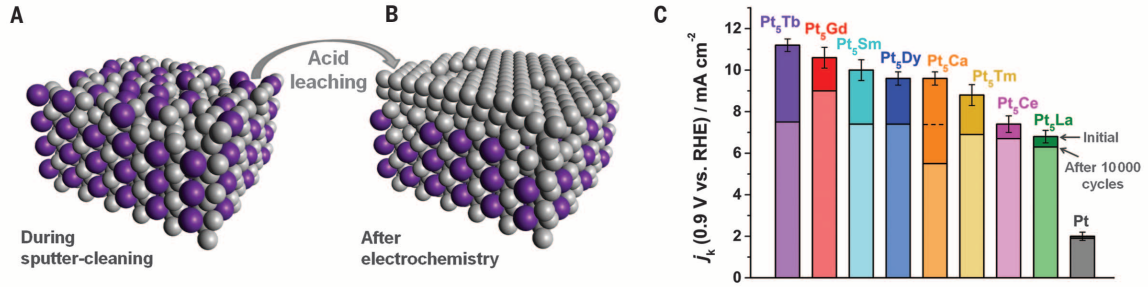

Fig. 1. Schematic views and electrochemical properties of polycrystalline Pt_5M (M = lanthanide or alkaline earth metal) electrocatalysts. Three-dimensional view of the Pt_5M structure (**A**) during sputter-cleaning and (**B**) after electrochemistry. (**C**) Kinetic current density, j_k, of Pt_5M and Pt at 23°C, 1600 revolutions per minute in O_2-saturated 0.1 M $HClO_4$, before and after a stability test consisting of 10,000 cycles between 0.6 and 1.0 V versus RHE at 100 mV s^{-1}. The activity of Pt_5Ca after the stability test has been normalized considering the increase of area after the test (see section S3.4 in the supplementary materials). The value normalized by the geometric area (dotted line) is shown for comparison.

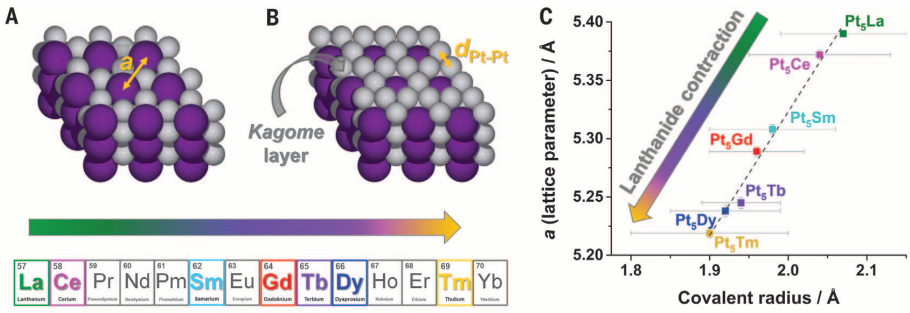

Fig. 2. Structure of Pt_5M. (**A** and **B**) Schematic view of the bulk structure of a Pt_5M (illustrated for Pt_5Tb), showing Pt_5Tb terminated by (A) a Pt and Tb intermixed layer and (B) a Pt kagome layer. Purple spheres represent Tb atoms, and gray spheres represent Pt atoms. Under ORR conditions in an acidic environment, one to two layers of M will be leached out, leaving three to five layers of Pt, as shown on Fig. 1B. (**C**) Relation between the lattice parameter *a* of Pt_5M measured by XRD (table S1) and the covalent radius of the lanthanide atoms (*31*). The dotted line shows the linear fit. The upper part of the figure shows the lanthanide contraction across the lanthanide series, the covalent radii decreasing in the same direction as d_{Pt-Pt}. The error in *a* corresponds to the uncertainty in the fit (table S1), whereas the error in the covalent radius corresponds to the estimated standard deviation from (*31*).

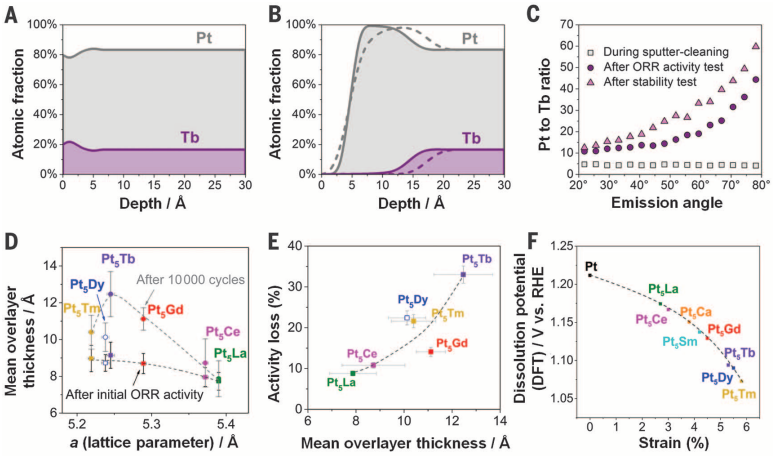

Fig. 3. XPS profiles before and after electrochemistry and Pt overlayer thickness as a function of the lattice parameter and activity loss. (**A and B**) AR-XPS profiles of polycrystalline Pt_5Tb (A) as prepared and (B) after initial ORR activity (solid line) and after stability test (dashed line). (**C**) Pt to Tb atomic ratios in Pt_5Tb from AR-XPS during sputter cleaning, after ORR initial activity, and after stability test. (**D**) Estimated average thicknesses of the Pt overlayer for Pt_5Tm, Pt_5Dy, Pt_5Tb, Pt_5Gd, Pt_5Ce, and Pt_5La after initial ORR activity and after stability test (taken from Fig. 1C), as a function of *a* lattice parameter [Pt_5Dy is shown as a hollow symbol to demarcate it as an outlier, likely because its as-prepared composition was inconsistent with that of the bulk (fig. S13)]. (**E**) Percentage of activity loss after stability test as a function of the Pt overlayer thickness. (**F**) Slab stability represented as dissolution potential versus the strain of the Pt overlayer on Pt_5M (from experimental lattice parameter *a*).

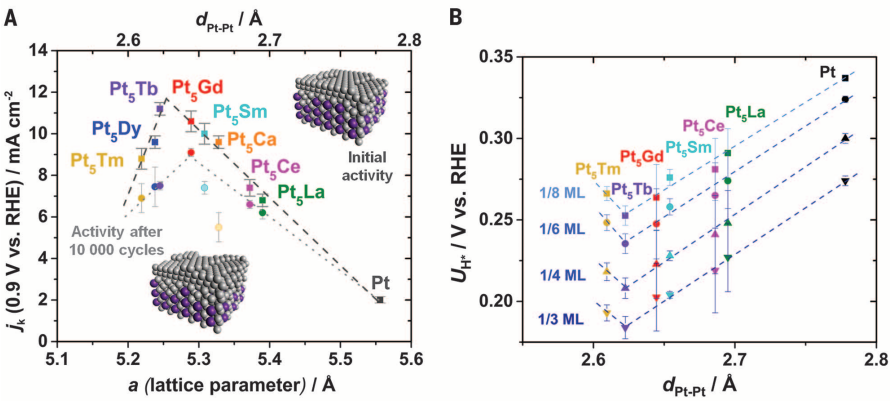

Fig. 4. Experimental volcano-type relationships between activity, H adsorption, and Pt-Pt distance. (**A**) Kinetic current density at 0.9 V (taken from Fig. 1C) on polycrystalline Pt_5M electrocatalysts versus the lattice parameter *a* of bulk Pt_5M (lower axis) and bulk d_{Pt-Pt} (upper axis), respectively. The figure shows the kinetic current density, j_k, of the alloys after the initial ORR activity (dark gray squares) and after 10,000 cycles of the stability test (colored circles). The dotted and dashed lines represent the experimental trends resulting after initial ORR activity and after stability, respectively. The activity of Pt_5Ca after 10,000 cycles has been normalized to account for the increase of area after the stability test. (**B**) Relation between the potential necessary to adsorb 1/8, 1/6, 1/4, and 1/3 monolayers (ML) of H (U_H) from the cyclic voltammograms (CVs) in the H adsorption region in N_2-saturated 0.1 M $HClO_4$ on Pt_5M (Fig. S5) and d_{Pt-Pt}.

these alloys, relative to the overall trend. The activity loss also correlates with the thickness of the overlayer (Fig. 3E) (*3*). Our density functional theory (DFT) calculations on the stability of different Pt overlayers, expressed as dissolution potential, show that the stability decreases as the compressive strain increases (Fig. 3F)—i.e., strain is a stability descriptor. We attribute the apparent thickening of the Pt overlayer with cycling to surface diffusion processes (*28*); bulk diffusion of lanthanide atoms through the overlayer will be strongly impeded by the strength of E_a (*13*). The strain-induced destabilization of the Pt overlayer could facilitate surface mobility (*28*), providing a channel for the dissolution of any residual lanthanide atoms in close vicinity to the surface. In summary, Fig. 3, D to F, shows that the overlayer thickness, activity losses, and thermodynamic stability are all a function of the bulk lattice parameter: Increased strain destabilizes the Pt overlayer and thus accelerates surface diffusion.

Figure 4A is a plot of the ORR activity as a function of the lattice parameter, a and $d_{Pt\text{-}Pt}$. Notably, all nine compounds, including the Pt-lanthanides and Pt_5Ca, follow the same volcano-type trend, with Pt_5Gd and Pt_5Tb at the apex. Because ΔE_{OH} is likely correlated with $d_{Pt\text{-}Pt}$ (*3*), the most trivial explanation for this trend is that the plot represents a Sabatier volcano: Alloys on the left bind OH too weakly, whereas on the right hand they bind ΔE_{OH} too strongly (as described by the DFT calculations in figs. S17 and S18). Alternatively, beyond a certain level of bulk strain, the overlayer could be unstable, causing the $d_{Pt\text{-}Pt}$ of the overlayer to relax toward a much lower level of surface strain. On single crystals, the destabilization is manifested as a positive shift in the "reversible" voltammetric peak for OH adsorption (*1*, *10*); however, we do not observe this shift on our polycrystalline materials, presumably because of hysteresis (electrochemical "irreversibility") or possibly coadsorption of OH and O. Conversely, the lanthanide contraction results in a clear voltammetric shift for the H adsorption region (figs. S3 and S4), plotted on Fig. 4B, which resembles the activity volcano, with Pt_5Tb exhibiting the maximum destabilization of adsorbed H. Notably, we also observe a linear relation between the experimental activity and the potential shift in the H adsorption (fig. S7).

Our DFT calculations on strain-activity-reactivity relations (section S5.4) suggest that Pt_5Tb, which is the most active electrocatalyst, should exhibit ~3% compression, approaching the optimum OH binding energy of the Sabatier volcano (*11*). By comparing our activity data and the voltammetric shift in H adsorption to the DFT predictions, we can conjecture that Pt-lanthanide alloys with a shorter $d_{Pt\text{-}Pt}$ than Pt_5Tb form a more relaxed overlayer (figs. S19 to S21]. More generally, our observations suggest that strain effects can only weaken the binding of H and OH to a certain extent. More appreciable destabilization of reaction intermediates can be afforded by ligand effects (*1*, *10*). The implementation of these catalysts in fuel cells will require scalable synthesis methods yielding high surface catalysts. Nonetheless, we have already demonstrated that Pt_xGd NPs exhibited an outstanding activity of 3.6 Å/mg Pt at 0.9 V RHE in liquid half cells (*18*, *29*) (fig. S6B), only surpassed by Pt_3Ni nanoframes (*21*) and Mo-doped Pt_3Ni nanoparticles (*22*). Careful tuning of the NP composition—for instance, by synthesizing ternary Pt-Gd-Tb alloys, in combination with a judicious choice of annealing treatment (*21*, *22*, *30*)—could yield record-breaking catalytic activity and stability over the long term in real devices.

REFERENCES AND NOTES

1. V. R. Stamenkovic *et al.*, *Science* **315**, 493–497 (2007).
2. H. A. Gasteiger, S. S. Kocha, B. Sompalli, F. T. Wagner, *Appl. Catal. B* **56**, 9–35 (2005).
3. P. Strasser *et al.*, *Nat. Chem.* **2**, 454–460 (2010).
4. S. Mukerjee, S. Srinivasan, M. P. Soriaga, J. McBreen, *J. Electrochem. Soc.* **142**, 1409–1422 (1995).
5. B. Han *et al.*, *Energy Environ. Sci.* **8**, 258–266 (2015).
6. I. E. L. Stephens, A. S. Bondarenko, U. Grønbjerg, J. Rossmeisl, I. Chorkendorff, *Energy Environ. Sci.* **5**, 6744 (2012).
7. J. K. Nørskov *et al.*, *J. Phys. Chem. B* **108**, 17886–17892 (2004).
8. F. Calle-Vallejo *et al.*, *Science* **350**, 185–189 (2015).
9. J. Suntivich, K. J. May, H. A. Gasteiger, J. B. Goodenough, Y. Shao-Horn, *Science* **334**, 1383–1385 (2011).
10. I. E. L. Stephens *et al.*, *J. Am. Chem. Soc.* **133**, 5485–5491 (2011).
11. J. Greeley *et al.*, *Nat. Chem.* **1**, 552–556 (2009).
12. V. R. Stamenkovic, B. S. Mun, K. J. J. Mayrhofer, P. N. Ross, N. M. Markovic, *J. Am. Chem. Soc.* **128**, 8813–8819 (2006).
13. U. G. Vej-Hansen, J. Rossmeisl, I. E. L. Stephens, J. Schiøtz, *Phys. Chem. Chem. Phys.* **18**, 3302–3307 (2016).
14. L. Tang *et al.*, *J. Am. Chem. Soc.* **132**, 596–600 (2010).
15. E. F. Holby, W. Sheng, Y. Shao-Horn, D. Morgan, *Energy Environ. Sci.* **2**, 865–871 (2009).
16. M. Escudero-Escribano *et al.*, *J. Am. Chem. Soc.* **134**, 16476–16479 (2012).
17. P. Hernandez-Fernandez *et al.*, *Nat. Chem.* **6**, 732–738 (2014).
18. A. Velázquez-Palenzuela *et al.*, *J. Catal.* **328**, 297–307 (2015).
19. K. J. J. Mayrhofer, K. Hartl, V. Juhart, M. Arenz, *J. Am. Chem. Soc.* **131**, 16348–16349 (2009).
20. L. Dubau *et al.*, *Appl. Catal. B* **142-143**, 801–808 (2013).
21. C. Chen *et al.*, *Science* **343**, 1339–1343 (2014).
22. X. Huang *et al.*, *Science* **348**, 1230–1234 (2015).
23. M. Mavrikakis, B. Hammer, J. K. Nørskov, *Phys. Rev. Lett.* **81**, 2819–2822 (1998).
24. V. Stamenkovic *et al.*, *Angew. Chem. Int. Ed.* **45**, 2897–2901 (2006).
25. V. Ohm *et al.*, *J. Alloy. C* **238**, 95–101 (1996).
26. L. J. Wan, T. Moriyama, M. Ito, H. Uchida, M. Watanabe, *Chem. Commun.* **2002**, 58–59 (2002).
27. L. Vitos, A. V. Ruban, H. L. Skriver, J. Kollar, *Surf. Sci.* **411**, 186–202 (1998).
28. J. Erlebacher, D. Margetis, *Phys. Rev. Lett.* **112**, 155505 (2014).
29. C. M. Pedersen *et al.*, *Electrochim. Acta* **179**, 647–657 (2015).
30. D. Wang *et al.*, *Nat. Mater.* **12**, 81–87 (2013).
31. B. Cordero *et al.*, *Dalton Trans.* **2008**, 2832–2838 (2008).

ACKNOWLEDGMENTS

The Center for Individual Nanoparticle Functionality is sponsored by the Danish National Research Foundation (DNRF54). We gratefully acknowledge EU FP7's initiative Fuel Cell and Hydrogen Joint Undertaking's project CathCat (GA 303492), as well as Danish Strategic Research's project NACORR (12-133817), for funding this work. M.E.-E. is the recipient of a Sapere Aude: DFF-Research Talent grant from the Danish Council for Independent Research. I.E.L.S. is the recipient of the Peabody Visiting Associate Professorship from the Department of Mechanical Engineering at Massachusetts Institute of Technology. We thank C. D. Damsgaard for assistance setting up the XRD measurements and O. Hansen for critically reading the manuscript. The authors declare competing financial interests: Intellectual property pertaining to the materials presented in this Report is protected by three patents (CA2877617-A1, WO2014079462-A1, and CA2767793-A1).

SUPPLEMENTARY MATERIALS

www.sciencemag.org/content/352/6281/73/suppl/DC1
Materials and Methods
Figs. S1 to S21
Table S1
References (*32*–*65*)

17 November 2015; accepted 11 February 2016
10.1126/science.aad8892

ICE SHEETS

Antarctic Ice Sheet variability across the Eocene-Oligocene boundary climate transition

Simone Galeotti,[1]* Robert DeConto,[2] Timothy Naish,[3,4] Paolo Stocchi,[5] Fabio Florindo,[6] Mark Pagani,[7] Peter Barrett,[3] Steven M. Bohaty,[8] Luca Lanci,[1] David Pollard,[9] Sonia Sandroni,[10] Franco M. Talarico,[10,11] James C. Zachos[12]

About 34 million years ago, Earth's climate cooled and an ice sheet formed on Antarctica as atmospheric carbon dioxide (CO_2) fell below ~750 parts per million (ppm). Sedimentary cycles from a drill core in the western Ross Sea provide direct evidence of orbitally controlled glacial cycles between 34 million and 31 million years ago. Initially, under atmospheric CO_2 levels of ≥600 ppm, a smaller Antarctic Ice Sheet (AIS), restricted to the terrestrial continent, was highly responsive to local insolation forcing. A more stable, continental-scale ice sheet calving at the coastline did not form until ~32.8 million years ago, coincident with the earliest time that atmospheric CO_2 levels fell below ~600 ppm. Our results provide insight into the potential of the AIS for threshold behavior and have implications for its sensitivity to atmospheric CO_2 concentrations above present-day levels.

The establishment of the Antarctic Ice Sheet (AIS) is associated with an approximate +1.5 per mil increase in deep-water marine oxygen isotopic ($\delta^{18}O$) values beginning at ~34 million years ago (Ma) and peaking at ~33.6 Ma (*1*–*3*), with two positive $\delta^{18}O$ steps separated by ~200,000 years. The first positive isotopic step primarily reflects a temperature decrease (*4*); the second isotopic step has been interpreted as the onset of a prolonged interval of

Paper II

Probing the nanoscale structure of the catalytically active overlayer on Pt alloys with rare earths

Anders F. Pedersen, Elisabeth T. Ulrikkeholma, María Escudero-Escribano, Tobias P. Johansson, Paolo Malacrida, Christoffer M. Pedersen, Martin H. Hansen, Kim D. Jensen, Jan Rossmeisl, Daniel Friebel, Anders Nilsson, Ib Chorkendorff, Ifan E. L. Stephens

Nano Energy, (**2016**), Accepted.

Probing the nanoscale structure of the catalytically active overlayer on Pt alloys with rare earths

Anders F. Pedersen[a,1], Elisabeth T. Ulrikkeholm[a,1], María Escudero-Escribano[a,b], Tobias P. Johansson[a], Paolo Malacrida[a], Christoffer M. Pedersen[a], Martin H. Hansen[c], Kim D. Jensen[a], Jan Rossmeisl[c], Daniel Friebel[d], Anders Nilsson[d], Ib Chorkendorff[a], Ifan E. L. Stephens[a,e*]

[a]Department of Physics, Center for Individual Nanoparticle Functionality, Building 312, Technical University of Denmark, 2800 Lyngby, Denmark
[b]Department of Chemical Engineering, Shriram Center, 443 Via Ortega, Stanford University, Stanford, CA 94305, USA
[c]Department of Chemistry, Univeristy of Copenhagen, Universitetsparken 5, 2100, Copenhagen, Denmark
[d]SLAC National Accelerator Laboratory, 2575 Sand Hill Road, MS31, Menlo Park, CA 94025, USA
[e]Massachusetts Institute of Technology, Department of Mechanical Engineering, 77 Massachusetts Avenue, Cambridge, MA 02139 USA

***Corresponding author:** ifan@fysik.dtu.dk

Abstract

Pt_xY and Pt_xGd exhibit exceptionally high activity for oxygen reduction, both in the polycrystalline form and the nanoparticulate form. In order to understand the origin of the enhanced activity of these alloys, we have investigated thin films of these alloys on bulk Pt(111) crystals, *i.e.* Y/Pt(111) and Gd/Pt(111). These surfaces exhibit a 4-fold improvement over Pt(111). We observe the formation of a thick Pt overlayer after the electrochemical measurements, both on Y/Pt(111) and Gd/Pt(111). Using surface sensitive X-ray diffraction we revealed that crystalline closely packed Pt overlayers were formed. The diffraction experiments showed that the strain and crystallinity of the overlayers are strongly dependent on the electrochemical treatment, and in general show lateral compression.

***Keywords*: Electrocatalysis, Pt-alloys, Pt(111), Oxygen Reduction, Diffraction**

[1] **These authors contributed equally to this work.**

1 Motivation

Polymer electrolyte membrane fuel cells (PEMFCs) are highly promising as a low emission source of power for portable applications, in particular automotive vehicles.[1] However, as a consequence of the slow kinetics of the oxygen reduction reaction (ORR) PEMFCs require a copious amount of Pt to catalyse the reaction. In order for PEMFCs to be scaled up beyond the niche market they occupy today, the amount of Pt needs to be decreased by up to an order of magnitude.[2-4] Arguably the most viable route to achieve this goal is to alloy Pt with other, less noble metals, thus improving the catalytic activity. Most investigations pertaining to Pt ORR alloys over the past two decades have focussed on alloying Pt with late transition metals such as Fe, Co and Ni.[5-9] These catalysts exhibit significant initial improvements in activity over pure Pt, but tend to degrade over time.[10, 11] The cause of the degradation is the leaching out of the less noble solute component into the acidic electrolyte, a process known as dealloying.[12, 13] Recent advances show that the stability of bimetallic Pt catalysts can be enhanced significantly, at least during short term tests.[7, 8, 14, 15] Nonetheless, it still remains to be seen whether these catalysts can survive long term tests in fuel cells.[16]

Earlier studies on Pt and Pt alloys suggest that the active site is located on the closely packed (111) surface.[17-20] According to a model based on density functional theory (DFT) calculations, the catalytic activity for oxygen reduction shows a *Sabatier*-volcano dependence on the binding to the key reaction intermediate, HO^* (where HO^* denotes a hydroxyl group adsorbend on an active site).[21] The optimal catalyst should exhibit moderate binding to HO^*, neither too strong nor too weak, with a binding to HO^* around ~0.1 eV weaker than Pt(111). Alloys such as Pt_3Ni or Pt_3Co exhibit improved activity because they exhibit closer to optimal binding of HO^*.[22] The first surface layer of these alloys is composed of pure Pt, as the solute metal will be unstable against dissolution to the electrolyte.[6, 23] Scanning tunnelling microscopy experiments indicated that pure Pt overlayers on acid-leached Pt alloys have smooth (111)-like surfaces.[24] The overlayer exhibits weakened binding to HO^* through ligand or strain effects. Ligand effects are due to the direct interaction of the Pt surface atoms with the underlying atoms of the non-noble metal in the second atomic layer.[25, 26] Similarly, a compressive lateral strain to the surface can also bring about a weakening of the binding of HO^*, by raising the position of the d-band centre relative to the *Fermi* level.[27]

Alloys of Pt and late transition metal have a negligible alloy formation energy.[22] This, in turn causes low bulk diffusion barriers,[28] which could explain their apparent susceptibility to degradation by dealloying.[12, 13, 16] Given these limitations, we embarked on a series of investigations to search for active and stable Pt alloys for the ORR. A DFT-based screening study identified Pt_3Sc and Pt_3Y to be particularly promising candidates.[22] We anticipated that they would have enhanced kinetic stability against dealloying as a result of their highly negative alloying energy, *i.e.* a strong bond between Pt and Sc or Y.

Based on the preditions from DFT, we tested bulk sputter-cleaned polycrystalline electrodes of Pt_3Sc and Pt_3Y in rotating disk electrode (RDE) measurements in 0.1 M $HClO_4$. Relative to Pt, Pt_3Y exhibited > 6 times improvement in ORR activity over polycrystalline Pt, constituting the most active catalyst ever prepared in this manner[22]. We tested a number of smooth polycrystalline electrodes of Pt rare earth alloys, exhibiting equivalent values of the alloying energy to Pt_3Y, mostly of the Pt_5M composition (where M = Y, Ce, La, Gd).[29, 30] The most active amongst these was Pt_5Gd, which exhibited activity just as high as Pt_3Y.[31] Moreover, we also found that model, mass-selected nanoparticles of Pt_xY and Pt_xGd exhibited an exceptionally high mass activity of up to 3.6 A/mg Pt at 0.9 V with respect to a reversible hydrogen electrode (RHE).[32, 33] During the course of 10,000 cycles between 0.6 and 1.0 V the nanoparticulate catalysts lose around 30 % of their activity. However, most of the activity losses occur between 0 and 1,000 cycles.[33] This suggests that during the first 1,000 cycles, the catalyst reaches a metastable, partially dealloyed state (the thermodynamically stabilised state would be a pure Pt particle with all the rare earth component dissolved into solution).

We initially predicted the high activity of Pt_3Y would be contingent on the formation of a specific structure with a single atom-thick Pt overlayer and at least 25 % Y in the second atomic layer.[22] On the basis that Y is larger than Pt, we expected the overlayer would be under tensile strain. Hence, a thick pure Pt overlayer would bind reaction intermediates stronger than a pure Pt surface, putatively the opposite effect required for an enhancement in ORR activity. Thus, according to our understanding at the time, a ligand effect from subsurface Y was essential to outweigh the effect of the tensile strain imposed onto the surface Pt atoms. Consequently, it came to our surprise to find that X-ray photoelectron spectroscopy (XPS) measurements of the electrodes, performed post-ORR, suggested that

the Pt overlayer was at least 3-4 atoms thick on Pt_3Y [29] and other Pt_5M alloys.[30] We later corroborated our XPS observations with elemental analysis based on transmission electron microscopy on nanoparticulate Pt_xY.[32] The key to understanding our observations came by analysing the bulk structure of the polycrystalline Pt_5M alloys, as deduced from X-ray diffraction (XRD). They form an unusual $CaCu_5$ structure that accommodates alloy components with different atomic radii in a way that is very different from FCC and HCP alloys, which have uniform bond lengths.[30, 34] Despite the larger size of M, relative to Pt, the closest Pt-Pt nearest neighbour distance in the core is smaller than that of pure Pt.[31] According to our DFT calculations, the 3-4 atom thick Pt overlayer concealing Pt_5M would be equivalent to a compressed closely packed pure Pt overlayer.[31] This notion is also consistent with our extended X-ray absorption fine structure (EXAFS) measurements, which showed that even after exposure to ORR conditions, the nanoparticles of Pt_xY and Pt_xGd remained under compressive strain. Moreover, the surface specific ORR activity showed an exponential dependence on the degree of compressive strain:[32, 33] this is exactly the trend we would expect, should we consider the strain to be imposed from the core on the catalytically active surface atoms.

Despite having established that the catalyst activity was strongly correlated to the bulk lattice strain, the structure of the overlayer remained elusive. To this end, following the precedent set by earlier combined surface science- and electrochemistry studies of Pt-based ORR catalysts,[18, 26, 35-37] we prepared single crystalline surfaces of Pt and rare earths. We were unable to source bulk single crystals of these specific alloys. Instead we formed alloy thin films by vacuum depositing ~200 Å Y or Gd on Pt(111) single crystal substrates. UHV and XRD measurements show that these structures exhibit a in-plane compression of 5 % to 6 %.[38, 39] The Gd/Pt(111) structures exhibit similar structural motifs to those of the $CaCu_5$ structure we observed in the polycrystalline alloys.[31, 38] The alloy film followed the orientation of the Pt(111) substrate half the time, otherwise it was rotated by 30˚. Upon testing the Y/Pt(111) electrode for the ORR, we measured an activity of 7.9 mA cm^{-2}, representing a 4-fold improvement over Pt(111) at 60 °C.[39] Significant leaching resulted in the formation of a ~1 nm thick Pt overlayer, similar to what we observed on the polycrystalline and nanoparticulate samples. Thus we consider the structures formed in vacuum to be precursors to the active phase.

In this paper, we report the electrochemical activity of Gd/Pt(111) for the ORR. Moreover, we use surface X-ray diffraction[40] to elucidate the strain in the electrochemically formed Pt overlayer on both Y/Pt(111) and Gd/Pt(111). We rationalise our trends with DFT calculations. By doing so we provide a fundamental link between the previously observed bulk strain and the nanoscale surface strain that controls the catalysis of oxygen reduction.

2 Experimental setup

2.1 Sample preparation and characterisation in ultra high vacuum

We have provided a full description of the UHV preparation of Y/Pt(111) and Gd/Pt(111) elsewhere.[38, 39] In brief, the sample preparation and initial characteriation were performed in a UHV chamber with a base pressure of 10^{-10} Torr. The chamber is equipped with standard UHV surface science techniques such as XPS, ion scattering spectroscopy (ISS), low-energy electron diffraction (LEED), and a quadrupole mass spectrometer for temperature programed desorption (TPD). ISS is performed using He^+ ions accelerated over an acceleration voltage of 1.2 kV. For the XPS experiments the K_α radiation of a Mg anode was used (1253.4 eV).

Non-destructive depth profiles of the surface were made using Angle Resolved XPS (AR-XPS). These experiments were carried out in another UHV chamber, hence the sample was exposed to air prior to these experiments. The electron analyser of this system allows to collect separate XPS signals for different emission angles, and in particular 16 angle intervals between 20 and 80 degrees from the surface normal. After subtraction of a *Shirley* type background and integration of the Pt 4f and Y 3d (or Gd 4d) peak areas, the XPS signals were processed using the simulation tool, ARProcess (Thermo Avantage software), which uses a maximum entropy method combined with a genetic algorithm to define the depth profiles: Emission angles over 65° were omitted to minimise the effects of elastic scattering.

The samples were based on Pt(111) single crystals (MaTecK GmbH, Germany, 5 mm diameter and 3 mm thick). They were mounted with a hairpin shaped tungsten wire onto the feed-through on the manipulator end. The temperature was measured using a type K thermocouple. The samples could be

resistively heated and cooled using liquid nitrogen. The main chamber is equipped with four metal evaporators and a quartz crystal microbalance (QCM), which makes it possible to evaporate metals on the surface of the sample at a well-known evaporation rate. The evaporators were made by cutting flakes of a Gd (Alfa Aesar, 99.9 %, 0.127 mm thick) or Y (Goodfellow, 99.9 %, 0.15 mm thick) foil and attaching them to a coil shaped 0.25 mm 99.95 % tungsten wire. Separate crystals were used for the rotating ring disk electrode measurements and the synchotron based XRD measurements. However, they were prepared under identical conditions.

2.2 Electrochemical methods

The electrochemical rotating ring disk electrode (RRDE) measurements on Gd/Pt(111), Y/Pt(111) and Pt(111) single crystalline electrodes were performed using RRDE assemblies provided by Pine Instruments Corporation. We used a VMP2 potentiostat (Bio-Logic Instruments), controlled by a computer with EC-Lab software. A standard two-compartment glass cell was used, which was equipped with a water jacket attached to a hot water bath to control the temperature. All glassware was cleaned for 24 h in a "piranha" solution consisting of a 3:1 mixture of 96 % H_2SO_4 and 30 % H_2O_2, followed by multiple runs of heating (to 85-90 °C) and rinsing with ultrapure water (Millipore Milli-Q, 18.2 MΩ cm, TOC < 5 ppb). All electrochemical experiments were carried out in 0.1 M $HClO_4$. The counter electrode (CE) was a Pt wire (Chempur 99.9 %, 0.5 mm diameter) and, the reference electrode (RE), a Hg/Hg_2SO_4, K_2SO_4 (0.6 M) (Schott instruments), was separated from the working electrode (WE) compartment by a ceramic frit. All the potentials in the text are referenced to the reversible hydrogen electrode (RHE), and are corrected for Ohmic losses, measured by fitting the high frequency impedance spectra taken typically from 500 kHz to 100 Hz. 0 V *vs*. RHE was established by performing the hydrogen oxidation and evolution reactions (HOR and HER, respectively) on a Pt electrode by means of cyclic voltammetry (CV) in H_2-saturated 0.1 M $HClO_4$ at 50 mV s^{-1} and 1600 rpm. The value for conversion to the RHE was taken as the average intersection with the potential axis of the anodic and cathodic curves. The RRDE was immersed into the electrochemical cell under potential control of ~0.1 V *vs.* RHE into a N_2-saturated (N5, Air Products) electrolyte. The ORR activity measurements were conducted in an electrolyte saturated with O_2 (N5, Air Products) at 1600 rpm and 50 mV s^{-1}.

Prior to the electrochemical measurements, the Pt(111) single crystal was flame-annealed according to the *Clavilier's* method.[41] Pt(111) was annealed for a few minutes (2-10 min) in the flame of Liquefied Petrolium Gas (LPG) for 5 min and cooled in a reducing 1:1 H_2/Ar atmosphere until room temperature (typically 5 min). The electrode surface was then protected by a droplet of ultrapure water, mounted in RRDE assembly and transferred to the electrochemical cell.

2.3 Synchrotron X-ray diffraction

X-ray diffraction measurements were performed on Gd/Pt(111) and Y/Pt(111) both in the as-prepared state, and after electrochemical conditioning. The X-ray diffraction experiments on the Y/Pt(111) and Gd/Pt(111) single crystalline alloys were carried out at the Stanford Synchrotron Radiation Lightsource (SSRL) at beam lines 1-5 and 7-2. The Y/Pt(111) crystal was measured at BL1-5, which is equipped with a Huber Kappa goniometer (φ-axis perpendicular to θ-axis) and a Rayonix MAR345 image plate detector. The Gd/Pt(111) crystal was brought to BL7-2, which has a Huber six-circle (4+2) diffractometer and a Dectris Pilatus 300K pixel detector. Both diffractometer stages were equipped with goniometer heads that allowed the crystal surface normal to be aligned to the φ-rotation axis using a laser. All the data were acquired at a fixed incidence angle of 0.2° to maximise surface sensitivity, and the photon energy was set to 11 keV to avoid fluorescence background from Pt. A sketch of the geometry of the scattering experiment is shown in Figure 1. The acquired diffraction data was combined to form a 3 dimensional image of parts of the *Q*-space, and the intensity was corrected for the *Lorentz* factor, polarisation, and geometrical effects using our own MatLab scripts.

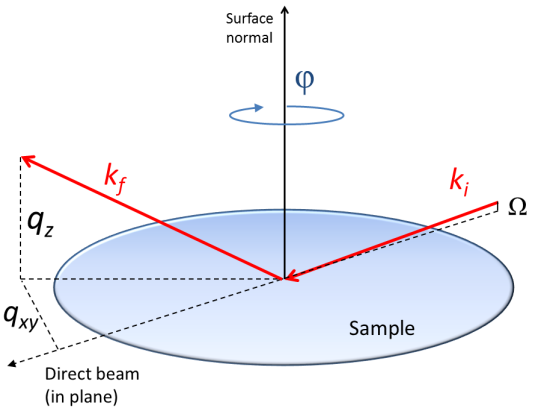

Figure 1: A sketch of the experimental setup used to acquire the X-ray diffraction data using an area detector. During all the experiments the incidence angle was kept at Ω=0.2˚ to maximise surface sensitivity. The sample was rotated in steps of 0.2˚ around the surface normal, and at each step an image was acquired. All the images were combined to form a 3-dimensional representation of the *Q*-space.

The electrochemical conditioning of the Gd/Pt(111) and the Y/Pt(111) samples was conducted at SSRL. For Gd/Pt(111), we performed 1461 cycles from -0.1 V to 0.8 V and 125 cycles from 0.0 V to 1.00 V, followed by 106 cycles from 0.0 V to 1.1 V and 98 cycles from 0.0 V to 1.20 V *vs*. RHE. The Y/Pt(111) was measured as-prepared, and after 175 cycles from -0.1 V to 0.8 V and 189 cycles from 0.05 V to 1.05 V, followed by 261 cycles from 0.05 to 1.20 V and 202 cycles from 0.05 V to 1.30 V *vs*. RHE. All the diffraction data was acquired *ex-situ.* The electrochemical potential cycling at the synchrotron facility was performed using a standard 3-electrode setup with a Ag/AgCl reference electrode (Innovative Instruments, Inc. LF-1.6, 3.4 M AgCl) and a glassy carbon counter electrode. The two samples were measured at different beam times; two different reference electrodes were used. Due to safety reasons it was not possible to calibrate the RHE scale at the beamtime, as we were unable to saturate our electrolytes with H_2. Following the beamtime, during our analysis of the data, we used the onset of hydrogen evolution to estimate the RHE scale. We came to realise that there was a ~0.05 V offset between the onset of hydrogen evolution between the two reference electrodes. Consequently, the potential window for the Y/Pt(111) measurements is offset positively by 0.05 V, relative to Gd/Pt(111)

measurements. The cell is a hanging meniscus type, also described elsewhere.[42] The electrolyte was N_2 saturated 0.1M $HClO_4$ surrounded by a humidified N_2 atmosphere.

3 Results

3.1 Electrochemical experiments and X-ray photoelectron spectroscopy characterisation

The Gd/Pt(111) and Y/Pt(111) samples were transfered directly from the UHV setup to the electrochemical cell. The samples were exposed to the laboratory air for up to 45 min, whilst it was unmounted from the UHV chamber. The RRDE was immersed into the electrochemical cell under potential control of 0.1 V *vs.* RHE into N_2-saturated 0.1 M $HClO_4$. CVs between 0.05 and 1.00 V *vs.* RHE at 50 mV s^{-1} were recorded in N_2-saturated electrolyte. The cycling removes adventitious contamination accumulated on the surface during the transfer from the UHV chamber to the electrochemical cell. Figure 2 shows a negative potential shift for both Gd/Pt(111) and Y/Pt(111) in the H adsorption region (between 0.45 and 0.05 V *vs*. RHE), as well as a positive shift in the OH adsorption region (between 0.55 V and 0.85 V *vs*. RHE), relative to Pt(111). The potential shifts (in absolute values) for both the OH and H adsorption regions, $|\Delta U_{HO^*M/Pt(111)}| = |U_{HO^*Pt(111)} - U_{OH^*M/Pt(111)}|$ and $|\Delta U_{H^*M/Pt(111)}| = |U_{H^*Pt(111)} - U_{H^*M/Pt(111)}|$, where M is Gd or Y, are shown in Table 1. These values indicate the shift in the potential required to adsorb 1/8, 1/6, 1/4 and 1/3 monolayers (MLs) of OH (HO^*) and H (H^*), that is 30, 40, 60 and 80 μC cm^{-2}[43]. These shifts are in agreement with a Pt overlayer under compressive strain.[44]

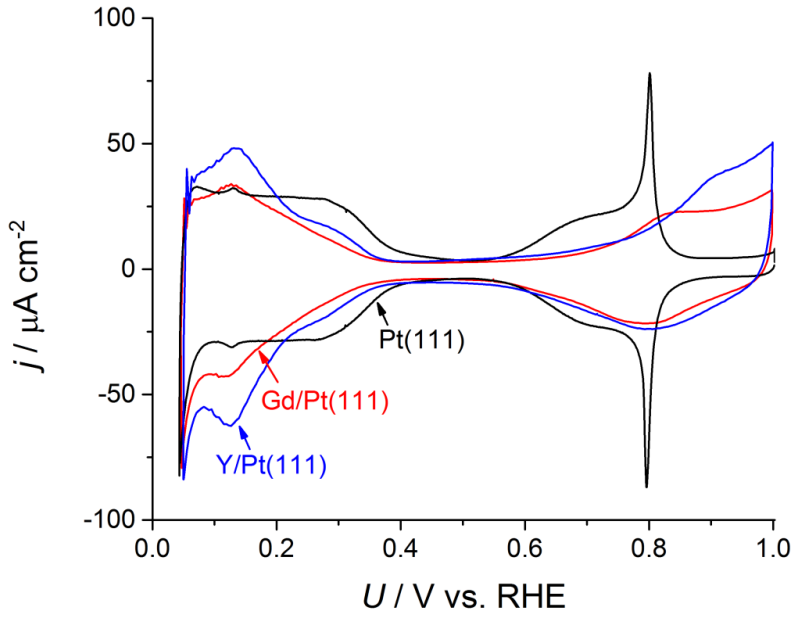

Figure 2: Stable (R)RDE based cyclic voltammograms in N_2-saturated 0.1 M $HClO_4$ at 50 mV s^{-1} and 23 °C of Gd/Pt(111), Y/Pt(111) and Pt(111) electrodes. The sharpness of the butterfly peak at ~0.8 V in comparison to the literature [45] indicates that the crystal is highly ordered,[46] validating our preparation procedure.

Table 1: Potential shifts (in absolute values) required to adsorb the charge *Q*, corresponding to coverages of OH and H adsorption of 1/8, 1/6, 1/4 and 1/3 ML. They have been obtained from the CVs in Figure 2 and shown for Gd/Pt(111) and Y/Pt(111) relative to Pt(111).

Q / µC cm^{-2}	$\lvert\Delta U_{HO^*\ Gd/Pt(111)}\rvert$ / V	$\lvert\Delta U_{H^*\ Gd/Pt(111)}\rvert$ / V	$\lvert\Delta U_{HO^*\ Y/Pt(111)}\rvert$ / V	$\lvert\Delta U_{H^*\ Y/Pt(111)}\rvert$ / V
30	0.107	0.074	0.099	0.054
40	0.104	0.075	0.099	0.057
60	0.110	0.073	0.095	0.050
80	0.136	0.062	0.107	0.036

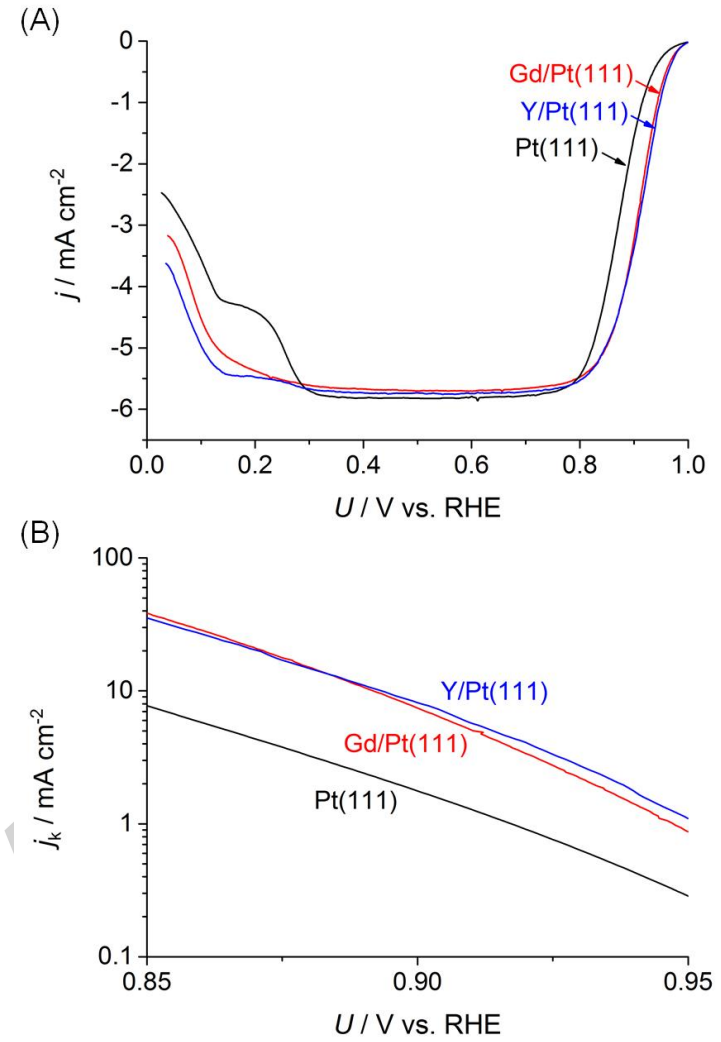

Figure 3: (A) Rotating ring disk electrode polarisation curves for the ORR on Gd/Pt(111), Y/Pt(111) and Pt(111). (B) Tafel plots showing the kinetic current density of Gd/Pt(111), Y/Pt(111) and Pt(111) as a function of the potential. The measurements were performed in O_2-saturated 0.1 M $HClO_4$ at 50 mV s^{-1}, 1600 rpm and 23 °C.

The oxygen reduction reaction activity of Gd/Pt(111), Y/Pt(111) and Pt(111) electrodes was measured in O_2-saturated 0.1 M $HClO_4$ once stable CVs in N_2-saturated electrolyte were obtained (see Supplementary Material (S.M.) Figures 1 and 2 for intial and stable CVs). The oxygen reduction values for Pt(111) are marginally higher than other data elsewhere in the literature;[18, 45] we can account for this marginal difference on the basis that we correct our data for Ohmic losses. The kinetic current density, j_k, *i.e.* the current density in the absence of any mass-transfer effects, was calculated by the *Koutecky-Levich* equation, $j_k=(j_l \cdot j)/(j_l - j)$, where j_l is the diffusion limited current density and j the measured current density. The *Tafel* plots (j_k as a function of the potential, U) are shown in Figure 3 for both electrodes. The kinetic current density of Gd/Pt(111) at 0.9 V *vs.* RHE is $j_{k,Gd/Pt(111)} = 7.3 \pm 1.4$ mA cm^{-2}, exhibiting a 4-fold ORR activity enhancement over Pt(111) ($j_{k,Pt(111)}$ 1.73 ± 0.07 mA cm^{-2} at 23 °C). This enhancement is similar to that measured on Y/Pt(111)[39] ($j_{k,Y/Pt(111)}$ = 7.9 mA cm^{-2} at 60 °C), presenting a near 4-fold improvement over Pt(111) as $j_{k,Pt(111)}$ 1.93 mA cm^{-2} at 60 °C. Moreover, it approaches the improvement of polycrystalline Pt_5Gd and Pt_3Y over polycrystalline Pt.[22, 31]

We performed AR-XPS, before and after the electrochemical testing; from these measurements we produced the depth profiles shown in Figure 4. Consistent with the other alloys tested at our laboratory, including polycrystalline Pt_5Gd,[31] Pt_xY nanoparticles[32] and Y/Pt(111),[39] the thickness of the Pt overlayer has increased significantly to ~10 Å after the electrochemical treatment, suggesting that the Gd has leached out from the surface layer. See S.M. Figure 4 for a depth profile on the Y/Pt(111) crystal after XRD measurements.

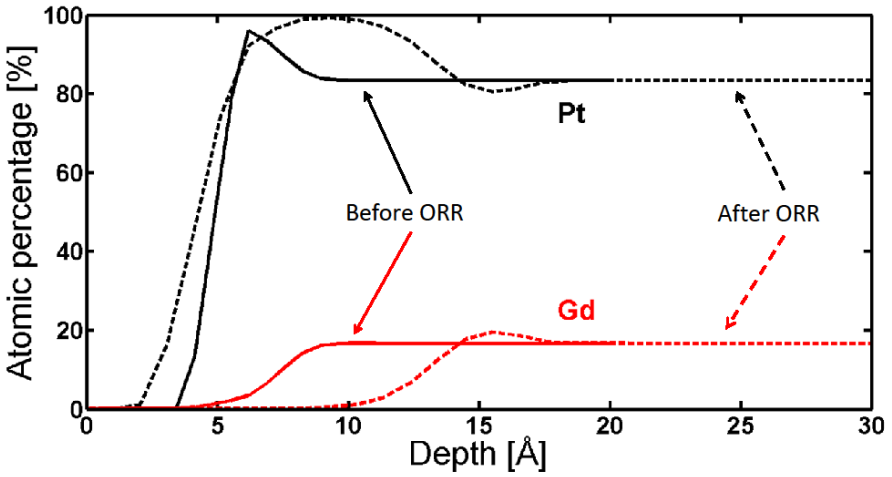

Figure 4: AR-XPS depth profiles of the Gd/Pt(111) sample before (solid lines) and after (dashed lines) the electrochemical treatment. These measurements have been performed in another UHV setup, and hence during the transfer the sample has been exposed to atmospheric air prior to these measurements. O and C signals were seen as a result from exposure to air, but have been omitted here for clarity. The depth profile including the surface contamination of O and C may be seen in S.M. Figure 3.

3.2 X-ray diffraction experiments

Figure 5 shows the X-ray diffraction pattern for the Pt_5M alloy phase, as prepared, *i.e.* before electrochemical conditioning. The structure shows an in-plane compression compared to Pt(111), and it has a complicated stacking sequence. One of the most important structural features is the formation of so-called kagomé layers, in which a pure Pt layer is compressed, and forms a (2x2) network of vacancies in order to accommodate a larger Gd atom in the layer above or below. Figure 6 shows a schematic of such a kagomé layer in the $CaCu_5$ structure; we consider this kagomé layer to be essential for the compression of the Pt-Pt distance relative to Pt(111).[38] We deduced that the red circled spot corresponds to the Pt(111) substrate. For a more convenient description in the context of the Pt(111) surface, the FCC structure of bulk Pt can be represented with a hexagonal unit cell with the unit cell vectors of the lengths a=b=2.775 Å parallel to the surface and c=6.797 Å for the unit cell vector along

the surface normal, α=β=90°, and γ=120°. Using this unit cell, the measured range of *Q*-space shows diffraction peaks from the Pt(111) substrate with a 3-fold in-plane symmetry at (*h*,*k*,*l*) positions (1,0,1), (1,0,4), and (0,1,2) and 120° rotations thereof; the (0,1,2) reflection appears in Figures 5c, 7c, and 8c. All other peaks originate from the alloy.

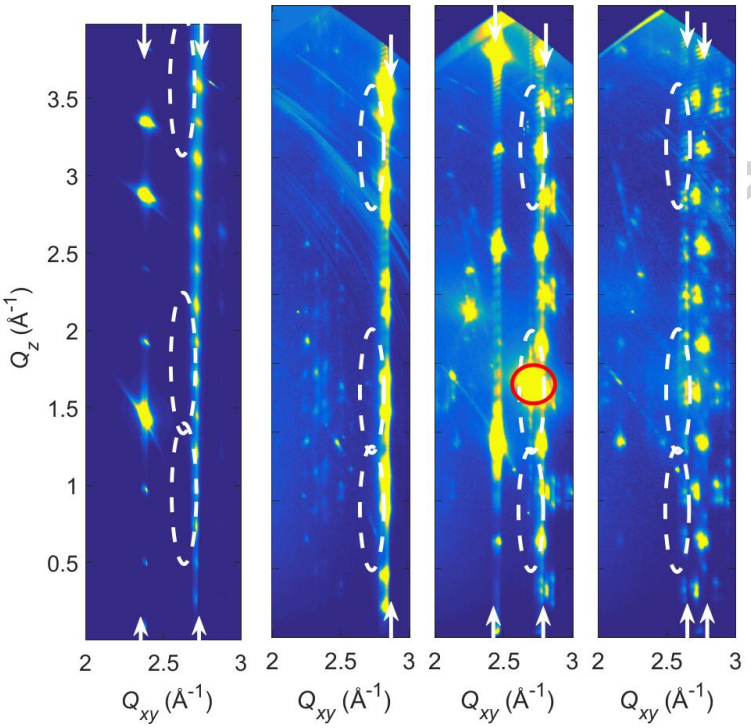

(a) Gd/Pt(111) 30° rotated overlayer.

(b) Y/Pt(111) 30° rotated overlayer.

(c) Y/Pt(111) unrotated overlayer.

(d) Y/Pt(111) ±5° rotated overlayer.

Figure 5: Diffraction images of Gd/Pt(111) and Y/Pt(111) taken before electrochemical potential cycling. (a) Gd/Pt(111), φ=28˚-32˚. (b)-(d) Y/Pt(111), (b) φ=28˚-32˚, (c) φ=-2˚-2˚, (d) φ=3˚-7˚. Locations for the overlayer diffraction spots in Figure 7 from the overlayers on the Gd/Pt(111) and Y/Pt(111) before electrochemical potential cycling are indicated by the dashed ellipses (spots not seen here since the thick overlayer has not been formed yet). With the exception of the (0,1,2) peak from the Pt substrate (red circle in (c)), all of the diffraction peaks are from the Pt_5M alloy phase, columns of *Bragg* peaks indicated by the arrows.

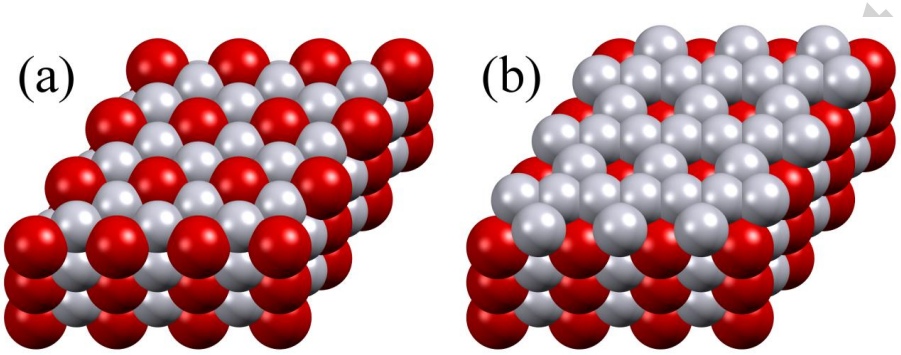

Figure 6: Schematic of the $CaCu_5$ structure, with Gd atoms shown in red and Pt atoms in grey. (a) shows the bulk structure terminated with the hexagonal layer with a Pt_2Gd stoichiometry, and (b) shows the bulk structure terminated with the pure Pt kagomé layer. The Pt-Pt distances in the kagomé layer is shorter than in bulk Pt, opening up room to accommodate the larger Gd atoms in the layers above and below.

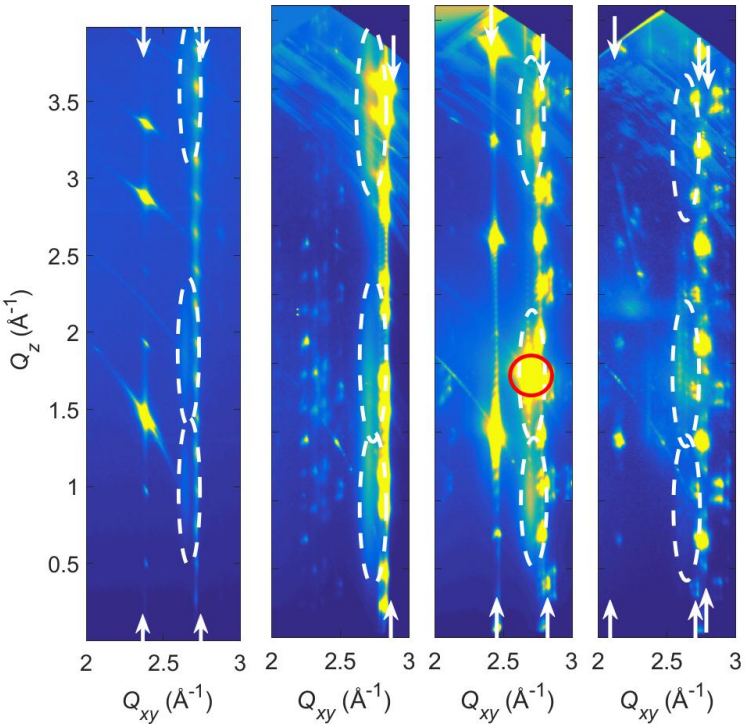

(a) Gd/Pt(111) 30° rotated overlayer. (b) Y/Pt(111) 30° rotated overlayer. (c) Y/Pt(111) unrotated overlayer. (d) Y/Pt(111) ±5° rotated overlayer.

Figure 7: Diffraction measurements of Gd/Pt(111) and Y/Pt(111) after cycling between 0.05 and 1.0 V. The same regions in reciprocal space are shown as in Figure 5. Three weak diffraction spots at $Q_{xy} \approx 2.64$ Å^{-1} and $Q_z \approx [0.9; 1.8; 3.6]$ Å^{-1} originate from the overlayer, as indicated by the dashed ellipses. The peak indicated by the red circle is from the Pt(111) substrate. All other peaks are from the Pt_5M bulk alloy.

Figure 7 shows the typical diffraction peaks that form on Y/Pt(111) and Gd/Pt(111) post-electrochemical potential cycling. All the features demarcated by the white dashed ellipsoids only appear after electrochemical measurements, suggesting that they are associated with the Pt overlayer; these features resemble those of the host Pt(111) substrate, although they are rotated by 30°; this rotation is identical to the orientation of the close-packed rows of Pt atoms within the kagomé layers of the Pt_5M alloy, as observed with LEED.[38, 39] For each in-plane vector of the overlayer, diffraction spots are

seen at L=1, L=2, and L=4, where the absence of the L=3 peaks indicate FCC structure like the Pt(111) substrate, but with two types of domains in the overlayer that are rotated 60° from each other. The image shows the intensity as a function of the in-plane (Q_{xy}) and out-of-plane (Q_z) components of scattering vector Q for the Gd/Pt(111) crystal after initial electrochemical potential cycling. In the figure the overlayer peaks at $Q_{xy} \approx 2.64$ Å^{-1} and $Q_z \approx [0.9; 1.8; 3.6]$ Å^{-1} are weak and quite broad, especially in the *z*-direction, indicating that the overlayer is very thin.[47] The other diffraction peaks in the image originate from the Pt_5Gd alloy phase (see Figure 5). Figures 7b and c show the overlayer peaks from the Y/Pt(111) crystal; there are two different sets of overlayer peaks, one set that is rotated 30° from the Pt(111) substrate, and one set that is unrotated from the substrate.

In the second set of electrochemical experiments we cycled Gd/Pt(111) up to 1.20 V *vs*. RHE and Y/Pt(111) up to 1.30 V *vs*. RHE, following which we repeated the diffraction experiments. As shown in Figure 8a, for the Gd/Pt(111) crystal there were no significant changes as only one overlayer was still observed at 30° rotation. In case of the Y/Pt(111) crystal, the overlayer rotated 30° disappeared completely, see Figure 8b, but the unrotated overlayer was still visible, as seen in Figure 8c. Furthermore, a new overlayer seems to appear at ±5° rotation from the Pt(111), although very weak; this overlayer feature is shown in Figure 8d. This slightly rotated layer was not visible after the first electrochemical cycling between 0.05 V and 1.0 V, as seen in Figure 7d.

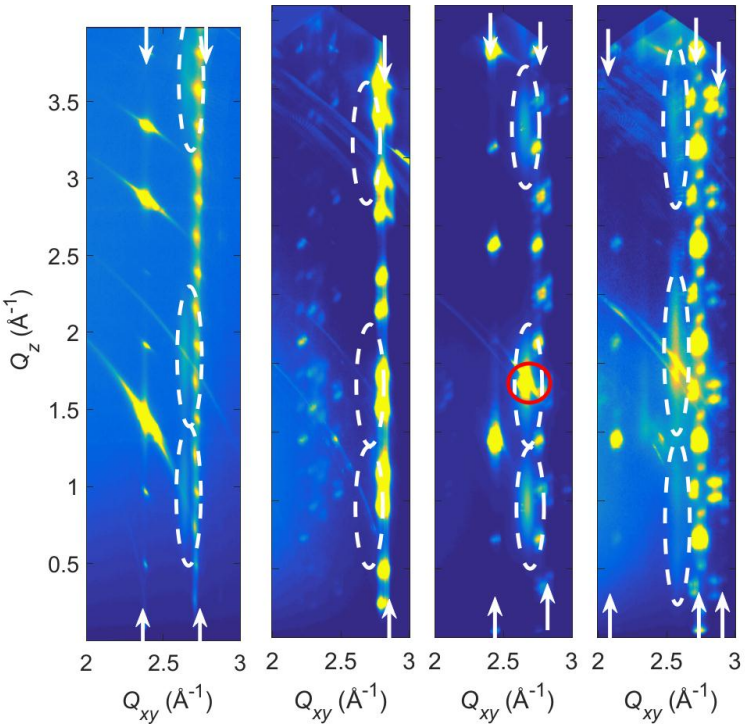

(a) Gd/Pt(111) 30° rotated overlayer.

(b) Y/Pt(111) 30° rotated overlayer.

(c) Y/Pt(111) unrotated overlayer.

(d) Y/Pt(111) ±5° rotated overlayer.

Figure 8: Diffraction measurements of Gd/Pt(111) and Y/Pt(111) after the second electrochemical potential cycling between 0.05 V and 1.2 V. The same regions in reciprocal space are shown as in Figures 5 and 7. The 3 weak spots seen at $Q_{xy} \approx 2.64$ Å^{-1} and $Q_z \approx [0.9; 1.8; 3.6]$ Å^{-1} are from the overlayer, marked by the dashed ellipses. The remaining peaks are from the Pt_5Gd alloy phase, columns of Bragg peaks indicated by the arrows, except one Pt(111) substrate peak on unrotated overlayer from the Y/Pt(111) crystal, shown by the red circle.

The diffraction pattern of the overlayer suggests that the Pt overlayer has an FCC structure, similar to bulk Pt, albeit with different lattice parameters. By comparing the positions of the overlayer peaks and the Pt(111) substrate peaks, we can determine the strain in both the in-plane and out-of-plane directions. Furthermore, we can estimate the thickness and lateral domain size using *Scherrer's* formula with a shape factor of 0.886.[48] The positions and widths of the overlayer diffraction peaks were determined

by fitting a sum of a 2D Gaussian and Lorentzian, and the resulting structural parameters are shown in Figure 9 and in Table 2. Only the 30° rotated and unrotated layers on the two crystals were fitted. The ±5° rotated overlayer was too weak in its diffracted intensity to fit; moreover, upon visual inspection of the diffraction image its structure also appears to be different from the FCC structure that we found on the other overlayers.

To further investigate the structure of the overlayer, we made a number of simulations of the overlayer peaks, considering an FCC and an HCP structure, which differ from each other only in terms of layer stacking. The simulation results in S.M. Figures 5 and 6 show the diffraction patterns from a varying number of atomic layers from 1 to 9. A visual comparison to Figure 7 suggests that the overlayer on Gd/Pt(111) crystal has about 5 atomic layers and the overlayer on the Y/Pt(111) crystal only has 3 layers. This is consistent with the thickness inferred from the peak widths, as well as the AR-XPS results on the polycrystalline samples of same composition. We can also conclude that the structure of the overlayer does not have HCP stacking.

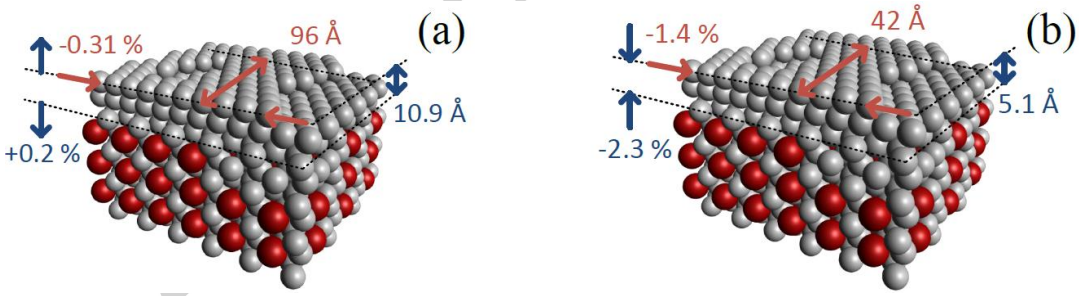

Figure 9: Schematic illustration of a pure Pt overlayers on Pt_5X alloy substrates. (a) A 30° rotated Pt overlayer on Gd/Pt(111). (b) A 30° rotated Pt overlayer on Y/Pt(111). Fitting results for the strain and domain sizes along in-plane (red) and out-of-plane directions (blue) are indicated for the two samples.

Table 2: Fitting results showing the strain and domain sizes of the overlayers on the Gd/Pt(111) and Y/Pt(111) crystal after two different electrochemical treatments.

Gd/Pt(111) 30°	U_{max} = 1.00 V *vs*. RHE	U_{max} = 1.20 V *vs*. RHE
Strain *xy* (%)	-0.31±0.05	-0.07±0.07
Strain *z* (%)	0.2±0.4	1.1±0.7
d *xy* (Å)	96±5	105±3
d *z* (Å)	10.9±0.3	10.8±0.3
Y/Pt(111) 30°	U_{max} = 1.05 V *vs*. RHE	U_{max} = 1.30 V *vs*. RHE
Strain *xy* (%)	-1.4±0.2	-
Strain *z* (%)	-2.3±0.9	-
d *xy* (Å)	42±3	-
d *z* (Å)	5.1±0.1	-
Y/Pt(111) 0°	U_{max} = 1.05 V *vs*. RHE	U_{max} = 1.30 V *vs*. RHE
Strain *xy* (%)	-0.5±0.2	0.2±0.5
Strain *z* (%)	-3±4	-1.4±2.6
d *xy* (Å)	61±1	75±5
d *z* (Å)	9.7±0.1	16±0.6

By estimating the domain size using the Scherrer equation, we implicitly neglect any peak broadening due to microstrain, *i.e.* inhomogeneous interatomic Pt-Pt distance in the overlayer. However, we do anticipate that the localised strain might vary significantly, which could also lead to peak broadening. Even so, we cannot distinguish the two possibilities on the basis of the XRD. Nonetheless, we can calculate a minimum and maximum value of strain. For the Gd/Pt(111) crystal the in-plane strain ranges from -1.39 % to +0.79 % after the first electrochemical cycling between 0.05 V and 1.05 V and -1.06 % to +0.94 % after the second electrochemical cycling between 0.05 V and 1.30 V. For the 30° rotated overlayer on the Y/Pt(111) crystal the in-plane strain ranges from -3.78 % to +1.02 % after the first electrochemical cycling between 0.05 V and 1.05 V; the in-plane strain in the unrotated layer ranges from -2.17 % to +1.20 % after the same treatment. After the second electrochemical cycling between

0.05 V and 1.30 V it ranges from -1.19 % to +1.61 %. These values of strain have been calculated by adding or subtracting half of the peak width at half height (HWHM) to the peak center position.

4. Theoretical Calculations

On a completely homogeneous surface, the difference in OH binding energies on Pt(111) and Gd/Pt(111) can be obtained from the electrochemical experiments, according to equation (1) [26]

$$\Delta E_{Gd/Pt(111)*OH} - \Delta E_{Pt*OH} = e(\Delta U_{*OH}) \quad (1)$$

where e is the elemental charge, $\Delta E_{Gd/Pt(111)*OH}$ and ΔE_{Pt*OH} are the OH binding energies on Gd/Pt(111) and Pt(111), respectively. ΔU_{*OH} is the difference in potential of Gd/Pt(111) relative to Pt(111) for adsorbing a fixed amount of charge corresponding to a given coverage of OH. By integrating charge in the cyclic voltammogram shown in Figure 2, we estimate a shift of around 0.1 V in U_{*OH} for Gd/Pt(111), relative to Pt(111) (see Table 1). We can also estimate the change in binding energy for H using a similar relationship

$$\Delta E_{H*Gd/Pt(111)} - \Delta E_{H*Pt} = -e(\Delta U_{*H}) \quad (2)$$

where $\Delta E_{H*Gd/Pt(111)}$ and ΔE_{Pt*H} are the binding energies of H on Gd/Pt(111) and Pt(111), respectively, and ΔU_{*H} is the shift in potential at a given coverage of H. The potential shift for hydrogen adsorption is around 0.07 V at 1/4 ML. Based on earlier DFT calculations,[49] the shift in OH binding would correspond to a strain of -3.5 %, whereas the shift in H binding would correpsond to a strain of -3.0 %. Both values are significantly greater than the strain we measured in the overlayer. See S.M. Section 4 for more details regarding these calculations.

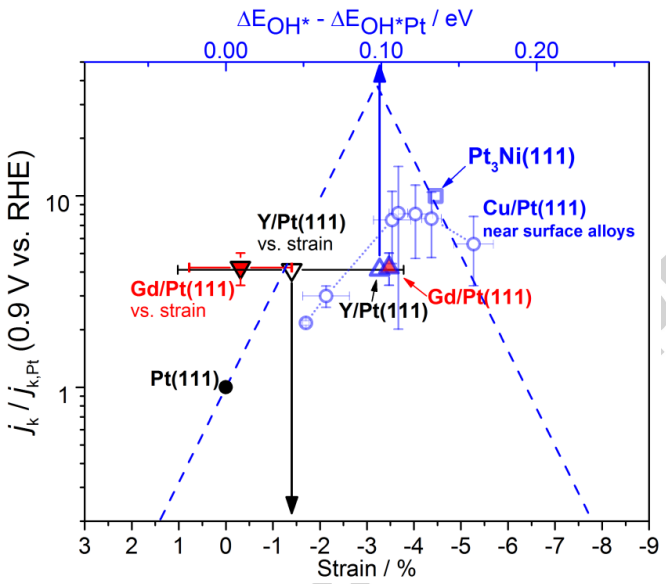

Figure 10: Oxygen reduction volcano as a function of lateral strain (lower *x*-axis) and OH binding energy (upper *x*-axis), relative to Pt(111). The relation between the strain and shift in OH binding energy is based on DFT calculations.[49] The blue dashed line is the thermodynamic Sabatier analysis, representing the upper limit to activity, neglecting additional kinetic barriers.[50] The activity of Y/Pt(111) and Gd/Pt(111) are plotted *versus* their measured strain on the bottom axis (down-triangles with black edge), and *versus* the voltametric shift on the top axis (up-triangles with blue edge). The error bar in the strain corresponds to the microstrain. For comparison, the blue circles represent the activity of the Cu/Pt(111) near surface alloys[26] and the square vacuum annealed $Pt_3Ni(111)$,[18] both plotted as a function of voltammetric shift for OH adsorption, which we assume to be equal to the shift in OH binding. The Gd/Pt(111) activity enhancement is based on several activity measurements of both Gd/Pt(111) and Pt(111) at 23 ˚C, whereas the Y/Pt(111) activity enhancement is based on a single measurement of Y/Pt(111) and Pt(111) at 60 ˚C.

5 Discussion

Evidently, for Gd/Pt(111) and Y/Pt(111) a vacuum annealed Pt overlayer structure is not stable when exposed to the electrolyte. This clearly contrasts with the smooth, monolayer-thick annealed Pt overlayers formed on $Pt_3Ni(111)$[18] and Cu/Pt(111) near-surface alloys,[26] which were stable under ORR conditions. This could partially be due to the increased interactions between adsorbed HO^* and O^*, and the solute metal in the second surface layer on the rare earth alloys, Y and Gd. Moreover, the greater degree of compressive strain in the bulk of Pt_5Gd and Pt_5Y, relative to those other alloys, could facilitate leaching from the subsurface layer.[39]

Our observation that the Pt overlayer on the dealloyed single crystal surfaces is under compressive strain is consistent with our EXAFS experiments on Pt_xGd and Pt_xY nanoparticles, post-electrochemistry. [32, 33] The mean value of the strain on the overlayer of Gd/Pt(111), at -0.31 %, is very low in comparison to the compression of the nearest-neighbour distance in the bulk of the alloy layer, and at 2.665 Å this is equivalent to 3.9 % compression. Likewise, on the overlayer of the unrotated Y/Pt(111), it is -0.5 %. Based on Table 2, it also seems that the strain is correlated with the thickness of the overlayer. Thus, we can conjecture that the strain relaxes further as the thickness increases. This interpretation is consistent with observations on single crystals based on Cu and Pt.[37, 51] On the other hand, on the Y/Pt(111) overlayer rotated by 30°, the compression is -1.4 %. As we suggested in Section 4, above, the measured strain is lower than we would expect if we were to assume that the shift in the voltammogram is purely due to compressive strain.

Figure 10 shows a volcano plot, where the oxygen reduction activity, relative to Pt(111) is plotted as function of both OH binding energy (upper *x*-axis), and lateral strain (lower *x*-axis), by virtue of the linear relationship between OH binding and strain.[49] The open circles represent the activity of the Cu/Pt(111) near-surface alloy[26] and the open square represents that of $Pt_3Ni(111)$,[18] both plotted as a function of the voltammetric shift in OH peak as an estimate of the OH binding energy, equation (1). We have also plotted the thermodynamic Sabatier-volcano[50] (note that the lower magnitude of the experimental enhancement over Pt(111), relative to that predicted by the theoretical thermodynamic Sabatier-volcano, is likely due to kinetic effects[50, 52]). We have located the position of the Gd/Pt(111) points and Y/Pt(111) data points on the *x*-axis according to (a) the voltammetric shift in OH adsorption,

ΔU_{*OH}, shown as up-triangles with a blue outline, and (b) the measured strain, shown as down-triangles with a black outline. On the basis of the voltammetric shift, and comparing our data to the earlier experimental data on other alloys, the activity of Y/Pt(111) and Gd/Pt(111) is lower than we would expect. [18, 26] On the other hand, comparing the activity with the measured strain in the overlayer, it is evident that the activity of Y/Pt(111) and Gd/Pt(111) is higher than we would expect.

We can account for this offset between our expectations and the actual enhancement on several accounts. The relationship between OH binding energy and voltammetric shift from equation (1) only holds for homogenous surfaces, such as Cu/Pt(111) near-surface alloys[26] and $Pt_3Ni(111)$,[18] as shown on the plot. Although the acid-leached overlayers are crystalline, they are likely to be somewhat heterogeneous. Such heterogenity is consistent with the large microstrain we estimate in the overlayer on Y/Pt(111) and Gd/Pt(111), represented as error bar in the *x*-axis on Figure 10. We note that the oxygen reduction activity will be dominated by the sites with the closest to optimum OH binding, whereas the voltammetric shift and the strain in the overlayer are more representative of the entire surface. We also acknowledge that in terms of catalysis, it is the actual surface layer which controls the activity, whereas we are probing the overall strain in the overlayer. Ideally, we would probe the surface layer, post-electrochemistry using UHV based techniques such as LEED[38, 39] or scannning tunnelling microscopy.[53-55] However, our current setup precludes this possibility: the transfer from the electrochemical cell to the UHV chamber through the laboratory air builds up a layer of adventitious contamination. To this end, we are currently in the process of building an electrochemical cell which is directly attached to an UHV chamber. It would be of particular interest to probe whether the oxygen reduction activity might be related to defects such as surface steps[56-58] or surface cavities,[59] in addition to compressive strain.

Finally, it is worth perusing upon the complete relaxation of the strain and loss of order in the overlayer exposed to more positive potentials. This observation explains our data on polycrystalline Pt_5Gd, where upon cycling to 1.2 V, the catalytic activity degraded rapidly.[31] Presumably the cause of this is due to subsurface oxide formation and its subsequent reduction.[60, 61]

6 Conclusion

In summary, we have fabricated Y/Pt(111) and Gd/Pt(111) by vacuum deposition. Subsequent ORR activity measurements show an enhancement over Pt(111) by a factor of 4. The single crystals show overlayers of 3-5 atomic layers upon exposure to electrolyte. We confirm that the overlayers are compressed. Upon electrochemical potential cycling between 0.1 V *vs.* RHE and >1.2 V *vs.* RHE, the strain in the overlayer is strongly reduced, which should result in a signficant decrease in ORR activity. Peak broadening suggests that some of the domains may have a distribution of strain; we expect that the most strained regions will dominate the oxygen reduction activity. Future studies in this direction will aim to elucidate the actual structure of the first surface layer.

Acknowledgments

We gratefully acknowledge EU PF7's initiative Fuel Cell and Hydrogen Joint Undertaking's project CathCat (GA 303492), as well as the Strategic Research's project NACORR (12-133817) for funding this work. MEE acknowledges the Danish Council for Independent Research for the Sapere Aude: DFF Research Talent Grant. The use of the Stanford Synchrotron Radiation Lightsource, SLAC National Accelerator Laboratory, is supported by the U.S. Department of Energy, Office of Science, Office of Basic Energy Sciences under Contract No. DE-AC02-76SF00515. We also thank Apurva Mehta and Chad Miller for invaluable assistance with both synchrotron data acquisition and processing. AFP also thanks the Danish Ministry of Higher Education and Science is acknowledged for an EliteForsk travel grant making an extended stay at SLAC possible. Ifan Stephens is the recipient of Peabody Visiting Associate Professorship from the Department of Mechanical Engineering at Masscachusetts Institute of Technology.

Highlights

Investigation of Gd/Pt(111) and Y/Pt(111) for oxygen reduction

Crystalline compressed pure Pt overlayer is formed

Overlayer is 3-5 monolayers thick

[1] O. Groger, H.A. Gasteiger, J.P. Suchsland, J. Electrochem. Soc., 162 (2015) A2605-A2622.
[2] M.K. Debe, Nature, 486 (2012) 43-51.
[3] H.A. Gasteiger, N.M. Markovic, Science, 324 (2009) 48-49.
[4] F.T. Wagner, B. Lakshmanan, M.F. Mathias, J. Phys. Chem. Lett., 1 (2010) 2204-2219.
[5] S. Mukerjee, S. Srinivasan, M.P. Soriaga, J. McBreen, J. Electrochem. Soc., 142 (1995) 1409-1422.
[6] T. Toda, H. Igarashi, H. Uchida, M. Watanabe, J. Electrochem. Soc., 146 (1999) 3750-3756.
[7] C. Chen, Y.J. Kang, Z.Y. Huo, Z.W. Zhu, W.Y. Huang, H.L.L. Xin, J.D. Snyder, D.G. Li, J.A. Herron, M. Mavrikakis, M.F. Chi, K.L. More, Y.D. Li, N.M. Markovic, G.A. Somorjai, P.D. Yang, V.R. Stamenkovic, Science, 343 (2014) 1339-1343.
[8] B.H. Han, C.E. Carlton, A. Kongkanand, R.S. Kukreja, B.R. Theobald, L. Gan, R. O'Malley, P. Strasser, F.T. Wagner, Y. Shao-Horn, Energy Environ. Sci., 8 (2015) 258-266.
[9] N. Todoroki, T. Kato, T. Hayashi, S. Takahashi, T. Wadayama, Acs Catalysis, 5 (2015) 2209-2212.
[10] F. Maillard, L. Dubau, J. Durst, M. Chatenet, J. Andre, E. Rossinot, Electrochemistry Communications, 12 (2010) 1161-1164.
[11] F. Hasche, M. Oezaslan, P. Strasser, J. Electrochem. Soc., 159 (2012) B25-B34.
[12] S. Chen, H.A. Gasteiger, K. Hayakawa, T. Tada, Y. Shao-Horn, J. Electrochem. Soc., 157 (2010) A82-A97.
[13] K.J.J. Mayrhofer, V. Juhart, K. Hartl, M. Hanzlik, M. Arenz, Angew. Chem.-Int. Edit., 48 (2009) 3529-3531.
[14] K. Sasaki, H. Naohara, Y.M. Choi, Y. Cai, W.F. Chen, P. Liu, R.R. Adzic, Nat. Commun., 3 (2012).
[15] X.Q. Huang, Z.P. Zhao, L. Cao, Y. Chen, E.B. Zhu, Z.Y. Lin, M.F. Li, A.M. Yan, A. Zettl, Y.M. Wang, X.F. Duan, T. Mueller, Y. Huang, Science, 348 (2015) 1230-1234.
[16] L. Dubau, M. Lopez-Haro, L. Castanheira, J. Durst, M. Chatenet, P. Bayle-Guillemaud, L. Guetaz, N. Caque, E. Rossinot, F. Maillard, Appl. Catal. B-Environ., 142 (2013) 801-808.
[17] G.A. Tritsaris, J. Greeley, J. Rossmeisl, J.K. Nørskov, Catal. Lett., 141 (2011) 909-913.
[18] V.R. Stamenkovic, B. Fowler, B.S. Mun, G.F. Wang, P.N. Ross, C.A. Lucas, N.M. Markovic, Science, 315 (2007) 493-497.
[19] D.G. Li, C. Wang, D.S. Strmcnik, D.V. Tripkovic, X.L. Sun, Y.J. Kang, M.F. Chi, J.D. Snyder, D. van der Vliet, Y.F. Tsai, V.R. Stamenkovic, S.H. Sun, N.M. Markovic, Energy Environ. Sci., 7 (2014) 4061-4069.
[20] H. Lv, D. Li, D. Strmcnik, A.P. Paulikas, N.M. Markovic, V.R. Stamenkovic, Nano Energy.
[21] J.K. Nørskov, J. Rossmeisl, A. Logadottir, L. Lindqvist, J.R. Kitchin, T. Bligaard, H. Jonsson, Journal of Physical Chemistry B, 108 (2004) 17886-17892.
[22] J. Greeley, I.E.L. Stephens, A.S. Bondarenko, T.P. Johansson, H.A. Hansen, T.F. Jaramillo, J. Rossmeisl, I. Chorkendorff, J.K. Nørskov, Nature Chemistry, 1 (2009) 552-556.
[23] V.R. Stamenkovic, B.S. Mun, K.J.J. Mayrhofer, P.N. Ross, N.M. Markovic, J. Am. Chem. Soc., 128 (2006) 8813-8819.
[24] L.J. Wan, T. Moriyama, M. Ito, H. Uchida, M. Watanabe, Chemical Communications, (2002) 58-59.
[25] J.R. Kitchin, J.K. Nørskov, M.A. Barteau, J.G. Chen, J. Chem. Phys., 120 (2004) 10240-10246.
[26] I.E.L. Stephens, A.S. Bondarenko, F.J. Perez-Alonso, F. Calle-Vallejo, L. Bech, T.P. Johansson, A.K. Jepsen, R. Frydendal, B.P. Knudsen, J. Rossmeisl, I. Chorkendorff, J. Am. Chem. Soc., 133 (2011) 5485-5491.
[27] M. Mavrikakis, B. Hammer, J.K. Nørskov, Physical Review Letters, 81 (1998) 2819-2822.
[28] U. Grønbjerg Vej-Hansen, J. Rossmeisl, I.E.L. Stephens, J. Schiøtz, Physical Chemistry Chemical Physics, accepted (2015).

[29] I.E.L. Stephens, A.S. Bondarenko, L. Bech, I. Chorkendorff, Chemcatchem, 4 (2012) 341-349.
[30] P. Malacrida, M. Escudero-Escribano, A. Verdaguer-Casadevall, I.E.L. Stephens, I. Chorkendorff, Journal of Materials Chemistry A, 2 (2014) 4234-4243.
[31] M. Escudero-Escribano, A. Verdaguer-Casadevall, P. Malacrida, U. Grønbjerg, B.P. Knudsen, A.K. Jepsen, J. Rossmeisl, I.E.L. Stephens, I. Chorkendorff, J. Am. Chem. Soc., 134 (2012) 16476-16479.
[32] P. Hernandez-Fernandez, F. Masini, D.N. McCarthy, C.E. Strebel, D. Friebel, D. Deiana, P. Malacrida, A. Nierhoff, A. Bodin, A.M. Wise, J.H. Nielsen, T.W. Hansen, A. Nilsson, I.E.L. Stephens, I. Chorkendorff, Nature Chemistry, 6 (2014) 732-738.
[33] A. Velázquez-Palenzuela, F. Masini, A.F. Pedersen, M. Escudero-Escribano, D. Deian, P. Malacrida, T.W. Hansen, D. Friebel, A. Nilsson, I.E.L. Stephens, I. Chorkendorff, J. Catal., *in press DOI:* 10.1016/j.jcat.2014.12.012 (2015).
[34] W. Bronger, Journal of the Less-Common Metals, 12 (1967) 63-&.
[35] W.P. Zhou, X.F. Yang, M.B. Vukmirovic, B.E. Koel, J. Jiao, G.W. Peng, M. Mavrikakis, R.R. Adzic, J. Am. Chem. Soc., 131 (2009) 12755-12762.
[36] T. Wadayama, N. Todoroki, Y. Yamada, T. Sugawara, K. Miyamoto, Y. Iijama, Electrochemistry Communications, 12 (2010) 1112-1115.
[37] R. Yang, J. Leisch, P. Strasser, M.F. Toney, Chem. Mat., 22 (2010) 4712-4720.
[38] E.T. Ulrikkeholm, A.F. Pedersen, U.G. Vej-Hansen, M. Escudero Escribano, I.E.L. Stephens, A. Mehta, J. Schiøtz, R.K. Feidenhans'l, A. Nilsson, I. Chorkendorff, Surf. Sci., in press (2016).
[39] T.P. Johansson, E.T. Ulrikkeholm, P. Hernandez-Fernandez, M. Escudero-Escribano, P. Malacrida, I.E.L. Stephens, I. Chorkendorff, Physical Chemistry Chemical Physics, 16 (2014) 13718-13725.
[40] Y. Gründer, C.A. Lucas, Nano Energy, *in press* (2016).
[41] J. Clavilier, R. Faure, G. Guinet, R. Durand, J. Electroanal. Chem., 107 (1980) 205-209.
[42] D. Friebel, D.J. Miller, C.P. O'Grady, T. Anniyev, J. Bargar, U. Bergmann, H. Ogasawara, K.T. Wikfeldt, L.G.M. Pettersson, A. Nilsson, Physical Chemistry Chemical Physics, 13 (2011) 262-266.
[43] N.M. Marković, P.N. Ross, Surf. Sci. Rep., 45 (2002) 117.
[44] H.E. Hoster, O.B. Alves, M.T.M. Koper, ChemPhysChem, 11 (2010) 1518-1524.
[45] A.M. Gomez-Marin, J.M. Feliu, Catal. Today, 244 (2015) 172-176.
[46] J. Clavilier, A. Rodes, K. Elachi, M.A. Zamakhchari, Journal De Chimie Physique Et De Physico-Chimie Biologique, 88 (1991) 1291-1337.
[47] D.-M. Smilgies, Journal of Applied Crystallography, 46 (2013) 286-286.
[48] D.M. Smilgies, Journal of Applied Crystallography, 42 (2009) 1030-1034.
[49] M. Escudero Escribano, P. Malacrida, M.H. Hansen, U.G. Vej-Hansen, A. Velazquez-Palenzuela, V. Tripkovic, J. Schiøtz, J. Rossmeisl, I.E.L. Stephens, I. Chorkendorff, Science, 352 (2016) 73-76.
[50] J. Rossmeisl, G.S. Karlberg, T. Jaramillo, J.K. Nørskov, Faraday Discussions, 140 (2008) 337-346.
[51] P. Strasser, S. Koh, T. Anniyev, J. Greeley, K. More, C.F. Yu, Z.C. Liu, S. Kaya, D. Nordlund, H. Ogasawara, M.F. Toney, A. Nilsson, Nature Chemistry, 2 (2010) 454-460.
[52] H.A. Hansen, V. Viswanathan, J.K. Nørskov, J. Phys. Chem. C, 118 (2014) 6706-6718.
[53] A.K. Engstfeld, S. Brimaud, R.J. Behm, Angew. Chem.-Int. Edit., 53 (2014) 12936-12940.
[54] N. Todoroki, Y. Asakimori, T. Wadayama, Physical Chemistry Chemical Physics, 15 (2013) 17771-17774.
[55] M. Mercer, H. Hoster, Nano Energy, accepted (2016).
[56] A. Kuzume, E. Herrero, J.M. Feliu, J. Electroanal. Chem., 599 (2007) 333-343.
[57] A. Hitotsuyanagi, M. Nakamura, N. Hoshi, Electrochimica Acta, 82 (2012) 512-516.
[58] K. Kodama, R. Jinnouchi, N. Takahashi, H. Murata, Y. Morimoto, J. Am. Chem. Soc., 138 (2016) 4194-4200.
[59] F. Calle-Vallejo, J. Tymoczko, V. Colic, Q.H. Vu, M.D. Pohl, K. Morgenstern, D. Loffreda, P. Sautet, W. Schuhmann, A.S. Bandarenka, Science, 350 (2015) 185-189.
[60] H. You, D.J. Zurawski, Z. Nagy, R.M. Yonco, J. Chem. Phys., 100 (1994) 4699-4702.
[61] M. Wakisaka, S. Asizawa, H. Uchida, M. Watanabe, Physical Chemistry Chemical Physics, 12 (2010) 4184-4190.

Paper III

Investigating the coverage dependent behavior of CO on Gd/Pt(111)
Elisabeth T. Ulrikkeholm, Martin Hangaard Hansen , Jan Rossmeisl, Ib Chorkendorff (2016), Submitted.

Journal Name

ARTICLE TYPE

Cite this: DOI: 10.1039/xxxxxxxxxx

Investigating the coverage dependent behaviour of CO on Gd/Pt(111)†

Elisabeth Therese Ulrikkeholm,*[a] Martin Hangaard Hansen,[a,b] Jan Rossmeisl[b] and Ib Chorkendorff[a]

Received Date
Accepted Date

DOI: 10.1039/xxxxxxxxxx

www.rsc.org/journalname

Gd modified Pt(111) single crystals have been prepared in ultra high vacuum. By vacuum deposition of ≈ 100 Å Gd on a sample heated to 800 °C, a Pt_5Gd alloy terminated by a single atomic layer of Pt was formed. Subsequently the surfaces were characterized using low energy electron diffraction (LEED), showing that a highly ordered crystal structure had appeared. To study the molecular dynamics on this surface a detailed study of the CO adsorption on the surface were made using temperature programmed desorption (TPD) of CO. The TPD spectra show a desorption peak shifted down in temperature. The shape of the desorption peak and the desorption temperature were strongly dependent on the CO coverage of the surface. A systematic investigation of CO desorption temperature as a function of coverage was performed. A simple simulation of the TPD spectra was carried out, based on adsorption energies from density functional theory (DFT). This simulation reproduces the shift and the narrowing of the desorption spectrum from the experiments and the DFT calculations suggest that the sharp shape is from cooperative adsorbate interactions, caused by subtle reconstructions occurring at coverages above 1/3 ML CO, whereas the temperature shift comes from weaker CO binding due to contraction of the Gd/Pt(111) surface.

1 Introduction

Bimetallic alloys based on platinum and lanthanides have attracted much attention due to their magnetic and catalytic properties. For example these alloys have interesting properties within electrocatalysis, where they can be used as new electrode materials which can reduce the platinum loading needed in polymer membrane fuel cells (PEM fuel cells) [1–4]. Especially Pt_xGd exhibit an exceptionally high activity for oxygen reduction, both as single crystals, in the polycrystalline form, and the nanoparticulate form [5,6]. Due to their large, negative heat of formation, these alloys will not be prone to electrochemical dealloying [3,7]. The crystal structure of Gd modified Pt(111) single crystals have been investigated to understand the origin of this enhanced activity [8,9]. We deposited 100 Å Gd to mimic the behavior of a bulk single crystal. These experiments revealed that these samples were terminated by a compressed platinum layer. To our knowledge, this is the first time bulk like alloy of platinum and a lanthanide has been investigated.

One of the central issues in heterogeneous catalysis is to obtain an understanding of the interactions between adsorbates and catalytic surfaces on an atomic level [10]. For this purpose, CO molecules are often used as a test molecule because of its relevanse in many chemical reactions such as CO oxidation and Fisher-Trops. In this article we focus on how the compressive strain on platinum surface effects the reactivity of the surface and describe how adsorbed molecules can interact. Temperature programmed desorption (TPD) has been used to study the reactivity of platinum surface during the last decades [11–16]. In this paper we present a detailed study of the behaviour of CO molecules on a Gd/Pt(111) surface. The study is carried out using temperature programmed desorption, (TPD), low energy electron diffraction, (LEED), and density functional theory, (DFT), calculations are used to make an atomic scale model for the observed trends. Strain effects for CO-Pt(111) systems have previously been studied by DFT by several groups [17,18]. In the present study, the strain is varied from 0% to −6% in steps of 1%, and at several coverages. Simulated TPD spectra are presented on the basis of adsorption energies from the DFT calculations, which show effects from subtle surface reconstructions due to strain, in addition to the well known strain effects of strain predicted by the d-band model [19,20].

[a] Department of Physics, Center for Individual Nanoparticle Functionality, Building 312, Technical University of Denmark, 2800 Lyngby, Denmark. Fax: +45 4593 2399; Tel: +45 4525 3344; E-mail: eltu@fysik.dtu.dk

[b] Department of Chemistry, Nano-Science Center, Univerisity of Copenhagen, Universitetsparken 5, 2100, Copenhagen, Denmark.

† Electronic Supplementary Information (ESI) available: Simulated TPD spectra and adsorption free energies are included for various strains. XPS and ISS data are included. See DOI: 10.1039/b000000x/

2 Experimental setup

The experiemts were performed in a vacuum chamber with a base pressure of $1.0{\cdot}10^{-10}$ Torr. The chamber is equipped with standard UHV surface science techniques; X-ray photoelectron spectroscopy (XPS), ion scattering spectroscopy (ISS), low energy electron diffraction, and a quadrupole mass spectrometer for temperature programmed desorption (TPD). ISS is performed using He^+ ions accelerated over an acceleration voltage of 1.25 kV. The XPS experiments were performed using K_α radiation from a Mg anode (1253.4 eV).

The sample, a Pt(111) single crystal, 5 mm in diameter and 3 mm thick, was supplied by MaTecK, GmbH, Germany. The sample was mounted in a hairpin shaped tungsten wire which is then mounted onto the feed-through on the manipulator end. The temperature is measured using a type K thermocouple. The sample can be resistively heated using a PID controller, and cooled to $T =$ -190 °C using liquid nitrogen. The main chamber is equipped with a water cooled metal Gd evaporator and a Quartz Crystal Microbalance (QCM), which makes it possible to evaporate Gd on the surface of the sample at a well known evaporation rate. The evaporator was made by cutting flakes of a Gd foil and attaching them to a coil shaped 0.25 mm 99.95 % tungsten wire. The Gd flakes were cut from a 0.127 mm 99.9 % Gd foil supplied by Alfa Aesar.

2.1 Sample preparation

The sample was prepared by vacuum deposition of Gd on a sputtercleaned, annealed Pt(111) sample. Prior to the Gd deposition, the Pt(111) sample was characterized with ISS and XPS to verify the cleanliness of the sample, and with CO TPD and LEED to verify that the crystal is single crystalline. A thick layer of (20 ± 5) nm Gd was deposited on a Pt(111) sample, heated to 800 °C. Earlier experiments have shown that Gd migrates to the subsurface region and that Pt form an overlayer when the sample is heated to temperatures above 500 °C[8]. By doing the evaporation on a sample heated to a temperature well above the mobility temperature, we anticipate that a Pt overlayer will be formed instantaneously. This Pt overlayer can protect the Gd from oxidation.

After the Gd deposition, ISS was performed to measure the composition of the surface layer, and XPS was used to evaluate the atomic composition, see supplementary information B.1 and C.1. These experiments showed that a Pt_5Gd alloy terminated with a Pt overlayer had been formed. The thickness of this prepared alloy corresponds to roughly 100 nm, and we anticipate that this sample will mimic the behavior of a bulk single crystal. A detailed description of the sample preparation can be found elsewhere[8].

3 Experimental results

We evaluated the crystal structure of the prepared surface using LEED, see Figure 1. The diffraction pattern of the prepared alloy is represented together with the diffraction pattern of the clean, Pt(111) surface. The position of the diffraction spots could be determined within an uncertainty of 2 %. It could be seen from the LEED pattern that a (1.90×1.90) structure was formed, corresponding to a (2×2) structure with 5.2 % compressive strain. Gd/Pt(111) samples have been prepared using this procedure several times, and a 30° rotation with respect to the Pt substrate was observed approximately 50 % of the time. This indicates that these two configuration are equivalent or really close in energy.

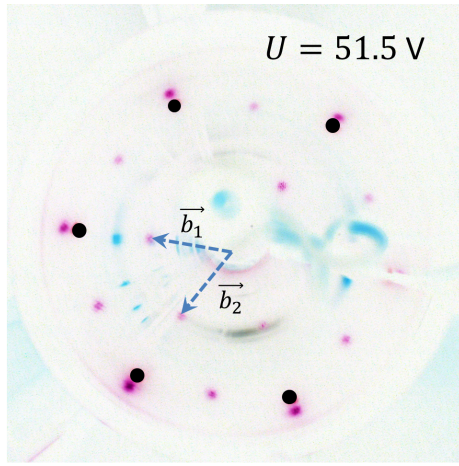

Fig. 1 *LEED before and after Gd deposition. The black dots represent the position of the diffraction spots from the Pt(111) sample before the Gd deposition. The arrows represent the reciprocal lattice vectors the the structure.*

To evaluate the reactivity of the prepared Gd/Pt(111) sample, CO TPD measurements were performed on the prepared Gd/Pt(111) surface. The sample was heated to $T = 1000$ °C and annealed for 60 s to ensure that it was completely clean and that no contamination was adsorbed on the surface. $2.0{\cdot}10^{-7}$ Torr CO was dosed for 35 min while the sample was cooled from $T = 1000$ °C to $T = -190$°C. This corresponds to a dosage of 420 L and we assume that the surface is saturated after this exposure. The sample was heated at a constant heating rate of 2 °C/s during the TPD experiments. The CO TPD can be seen in Figure 2 where it is compared with a CO TPD made on a clean, annealed Pt(111) sample. The CO TPD experiment was repeated several times, showing a high degree of reproducibility. The high temperature limit for the desorption peak of Pt(111) will be used in the comparison, since it corresponds to to the desorption temperature from a sample with a low coverage(Find ref.). From the CO TPDs it can be seen that the Gd/Pt(111) surface binds CO significantly weaker than on Pt(111) with a change in desorption temperature of $\Delta T = 200$ °C. , The CO binding energy can be evaluated from the desorption temperature using the Redheat method[21,22], see Table 1.

The CO desorption peak located at $T =$ -10 °C is extremely sharp, indicating strong attractive interactions between the CO molecules adsorbed on the surface. However, since CO molecules

	T_{max}	$E_{des;CO}$	ΔE_{des}
Gd/Pt(111)	-10 °C	0.71 eV	0.56 eV
Pt(111)	190 °C	1.27 eV	0.00 eV

Table 1 The CO desorption temperature and the corresponding desorption energy from Gd/Pt(111) and Pt(111).

behave like dipoles, we expect to observe repulsive dipole-dipole interactions, and hence this result is quite contra intuitive.

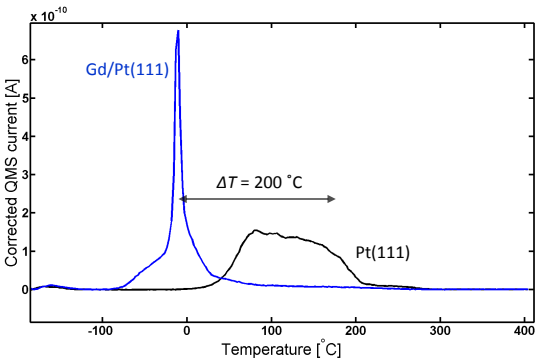

Fig. 2 *Temperature Programmed Desorption on a saturated Gd/Pt(111) compared with a CO TPD made on a Pt(111) surface. The measurements have been made using a heating rate of 2 °C/s.*

To investigate the origin of this further, CO TPDs at different levels of CO coverage were performed on the Gd/Pt(111) sample. In Figure 3, TPDs made with low CO doses of 0.01 L, 0.05 L, 0.10 L, 0.25 L, and 0.50 L are shown together with a CO TPD of a saturated surface. Before the CO was dosed, the sample was heated to $T = 1000$ °C and then cooled rapidly using liquid nitrogen. CO was dosed when the sample had reached a temperature of T =-190 °C. For the low dosages the surface is far from being covered with CO, and hence the interaction between the adsorbed CO molecules is weak. It can be seen, that as the exposure increases, the position of the maximum of the desorption peaks shift to a lower temperature, indicating a weakening of the CO binding energy. This is expected since the repulsive dipole-dipole interactions between CO molecules will lower the effective binding energy.

In Figure 4 slightly higher doses of CO have been used; 0.75 L, 1.0 L, and 1.5 L. In this coverage regime the shape of the desorption peak starts to change, indicating the presence of interactions between the CO molecules on the surface. It should be noted that the desorption temperature increases with the degree of coverage, in contrast to in the low coverage regime where the desorption temperature decreases with the degree of coverage. This indicates that CO molecules are bound stronger as the surface is getting covered with CO.

We evaluated the coverage of the sample after the dosing of CO

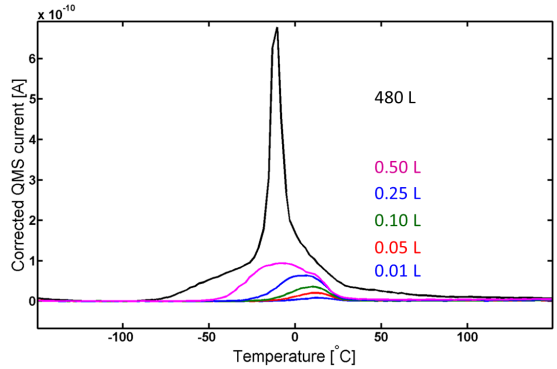

Fig. 3 *Temperature Programmed Desorption of the Gd/Pt(111) surface for low doses of CO. The measurements have been made using a heating rate of 2 °C/s.*

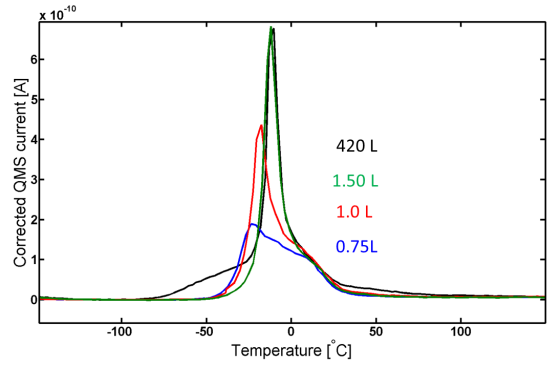

Fig. 4 *Temperature Programmed Desorption on the Gd/Pt(111) surface at different doses of CO. The measurements have been made using a heating rate of 2 °C/s.*

from the integrated area of the desorption peaks, and comparing it with the desorption peak from the CO saturated Pt(111) surface where the saturation coverage has been measured and determined to be $\theta = 0.6$, where $\theta = n/N$, is the coverage, where n is the number of CO molecules, and N is the number of surface atoms[23]. The coverage as a function of the dose can be seen in Figure 5. We could observe that the sample became saturated with CO after an exposure of 1.5 L. The relative uncertainty on the small doses is high because of the CO background pressure in the UHV chamber.

The temperature where maximum of the desorption peak appears can be seen as a function of CO coverage in Figure 6. It can be seen that the desorption temperature is lowest for a coverage of 0.28 ML CO, indicating that the weakest binding occur when the coverage is close to $\theta = 1/4$ ML. The trend exhibit higher and near constant desorption temperatures at higher doses corresponding to $\theta > 1/3$ ML. A high dose of CO may drive occupation of neighbouring sites which may yield a more

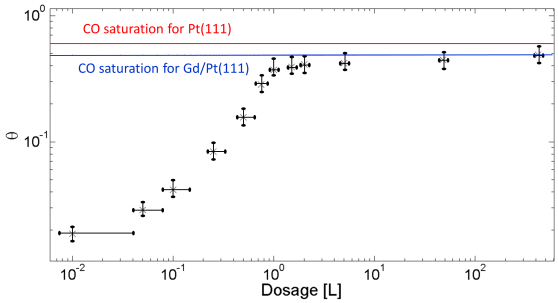

Fig. 5 *The coverage as a function of the CO dose. The surface becomes saturated with CO around 1.5 L. Due to the CO background the relative uncertainties on the CO dosages are high for the lowest coverages.*

stable surface configuration than at lower coverages. Thus a cooperative adsorbate interaction exist for CO on the Gd/Pt(111) at higher coverages.

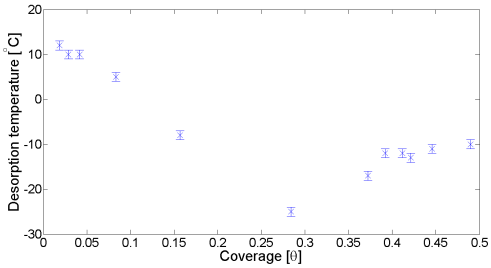

Fig. 6 *The desorption temperature of CO on the Gd/Pt(111) surface for different CO coverages. A minimum can be seen at a coverage around θ = 0.28 ML of CO.*

LEED experiments were performed on the surfaces after dosing 1 L of CO. These images suggest that a reconstruction appear. This reconstruction could be induced by high doses of CO and it might provide the stabilizing effect on adsorption that are indicated by Figure 6. The LEED signal, however, is too weak to be conclusive, see supplementary info.

To further study the origin of this behaviour we initiated a density functional theory study of the strain effects on the system. The details and results of the DFT calculations are presented in the following.

4 DFT calculations

In this section, computer simulations of the TPD spectra are presented on basis of density functional theory (DFT) calculations. First the DFT calculations are presented and then the method for the simulations of TPD spectra is introduced.

The adsorption/desorption energies of CO was calculated on Pt(111) at various coverages, θ, and with various lattice strain. The strain was in the range from -6% to 0%, and the CO coverages were 1/9, 1/6, 2/9, 1/4, 1/3, 4/9, 1/2, 5/9 and 2/3 monolayers.

The atomic structures were set up using the atomic simulation environment (ASE)[24]. The Pt(111) surfaces were represented with non-orthogonal 3×3, 2×2, or orthogonal or non-orthogonal 3×2 super cells. Several possible adsorbate surface arrangements were checked for the coverages 2/9, 1/3 and 4/9. The DFT calculations were carried out using GPAW[25,26], which uses projector augmented wave functions to represent atomic core electrons. The single electron Kohn-Sham[27] wave functions were represented using plane-waves with an energy cut-off of at least 500 eV, (800 eV for all super cells smaller than 3×3), and a k-point sampling[28] of 8×8, 6×6, or 6×8 depending on the super cell size. Exchange and correlation contributions were approximated with the RPBE functional[29]. All structures were relaxed until the maximum forces were below 0.05 eV/Å. In all cases, the CO was placed initially on top sites and not constrained. Although DFT is known to over-estimate the stability of CO in the hollow sites relative to the top sites[30], the top site is a local minimum, and in most cases the molecules stayed there, with the exception of the 4/9 ML, 3/6 ML and 5/9 ML configurations, where one CO molecule moved to a bridge or hollow site. See supplementary information for views of the $\theta = 0.5$ ML structures at various strains.

The differentiated adsorption energy, $E^{diff}(\theta)$, and the integral adsorption energy, $E^{int}(\theta)$, are defined by

$$E^{diff}(\theta) = N\frac{\partial E_{int}(n,N)}{\partial n} = \frac{\partial E_{int}(\theta)}{\partial \theta} \quad (1)$$

$$E^{int}(\theta) = [E(n,N) - E(n=0,N) + n\cdot(\Delta ZPE_{CO} - E_{CO(g)})]/N \quad (2)$$

E, are the potential energies at 0K calculated using DFT and $\theta = n/N$ is the coverage, where n is the number of CO molecules and N is the number of surface atoms. The difference in zero-point energy, ΔZPE, was 0.06 eV using the harmonic approximation with a vibration frequency from Feibelman et al.[30] for CO on top sites and a CO molecule in vacuum.

Surface configurations with integral free energy $E^{int}(\theta)$ above a line between the energy of any two other configurations, will be replaced by domains of those two surface configurations. The relevant integral adsorption energies are therefore found using the convex hull of the calculated integral adsorption energies. The calculated $E^{int}(\theta)$ from DFT (See equation 2) are shown in Figure 7 together with an interpolation of the convex hull of $E^{int}(\theta)$.

In order to simulate the TPD spectra, the desorption energy was calculated as minus the differential adsorption energy, i.e $E^{des}(\theta) = -E^{diff}(\theta)$. The desorption energy (See Figure 7, lower panel) was calculated by differentiating the interpolated convex hull of $E^{int}(\theta)$.

Simulated TPD spectra are shown in Figure 8 for the unstrained and the most strained configurations in this study.

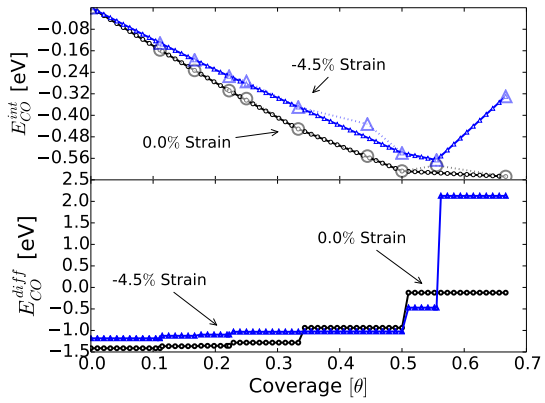

Fig. 7 *The CO binding energies calculated by DFT for a relaxed and a Pt(111) surface under -4.5% strain. The upper panel shows integral adsorption energy $E^{int}(\theta)$ from DFT (large markers) and the linear interpolation of the convex hull of $E^{int}(\theta)$ (small markers). The lower panel shows the differentiated linear interpolation of the convex hull (See equation 1). Notice in the low coverage limit that the CO is more stable on the relaxed surface than on the contracted surface. Notice also how the coverage $\theta = 0.5$ ML is relatively stable on the contracted surface, compared to lower coverages.*

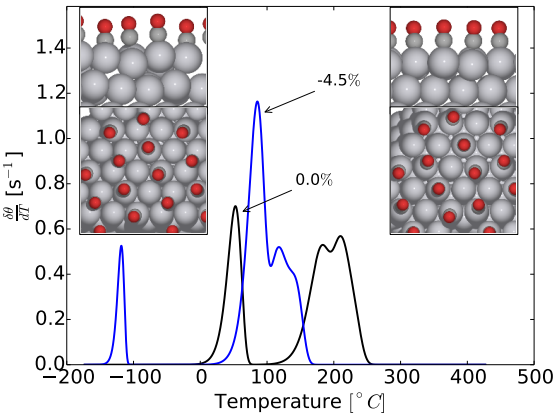

Fig. 8 *Simulated TPD curves for CO on a relaxed Pt(111) surface and a Pt(111) surface under -4.5% compressive strain. The insets show side views of the atomic structure at $\theta = 0.5$ ML, for the compressed surface on the left and the relaxed lattice on the right. Notice how the row of Pt atoms, on which CO is adsorbed, is drawn out of the plane, and that one CO molecule moved to the bridge site on the contracted surface.*

The TPD spectra simulate first order desorption described by

$$-\frac{d\theta_s}{dT} = \frac{\nu}{\beta}\exp[-E_{des}/kT]\theta_s \tag{3}$$

where β is the ramp rate (2 K / s) and ν is the attempt frequency, which is $\frac{k_B T}{h}$. The simulated spectra are the result of the summed contribution from each coverage, treated as distinct sites. The per site coverage, θ_s, is a function of the temperature, which it enters as[31]:

$$\theta_s = \exp[F(T)] \tag{4}$$

$$F(T) = \frac{\nu}{\beta}\int_0^T \exp[-E_{des}/kT]dT \tag{5}$$

The presented simulations of TPD spectra are based on the simplest first order desorption model based on adsorption energies from DFT. The energies, from which the TPD spectra are simulated do not contain contributions from configurational entropy. Most simulations of CO-TPD use lattice Monte Carlo simulations[32–34] to include the effects of configurational entropy. The main effect from entropy is a broadening of each of the desorption peaks, after which the simulated spectra resemble experiments. However, lattice Monte Carlo simulations rely on constant adsorption energies with added pair potentials for neighbouring adsorbates. It is not trivial to include the reconstruction effect consistently in such pair-potentials. In the present study it proved to be possible to capture the overall trends from experiments without using a lattice Monte Carlo model and without configurational entropy. In the following section the results of the TPD simulations are discussed in relation to the experimental TPD spectra.

5 Discussions and conclusions

In this article we have investigated behavior of CO molecules on Gd/Pt(111) under UHV conditions. Earlier experiments have shown that this surface is terminated by a single layer of Pt with a compressive strain of 5 %[8]. By studying this surface, we can investigate how compressive strain effects change the behaviour of CO molecules adsorbed to strained Pt surfaces. Our experimental work has been supported by DFT calculations.

First, the results from DFT calculations on relaxed Pt(111) are discussed: The experimental TPD spectrum shows a broad feature peaking around 80 °C and ending around 190 °C. The simulated TPD spectrum, based on the DFT calculations, is split into two main features. The low temperature peak is at 53 °C and correspond to coverages higher than 1/3 ML, where occupied neighbouring top sites are present. This peak most likely corresponds to the one at 80 °C in the experiment and thus the simulation predicts slightly too unstable adsorption energies. It is possible, that the adsorbate interactions are overestimated, or that a more stable configurations exist, which are not included in the calculations. The high temperature feature ends around 250 °C, corresponding to desorption of CO from the low coverage configuration. Thus, the absolute value for the desorption temperature is 60 °C too high, corresponding to a binding energy in the simulations which is slightly too stable compared to experiments. The error may be attributed to the entropy of the desorbed state, which is unknown in the experiment and neglected in the calculations. Thus, the simulated spectrum for relaxed Pt(111) shows a broader spectrum with more separate narrow peaks than the experimental observations. In the following, the results of the Gd/Pt(111) alloy is discussed

in relation to the DFT calculated strain effects.

By comparing the CO TPD made on saturated surfaces we notice two significant differences between the Pt(111) and the Gd/Pt(111) surfaces; the desorption temperature has shifted with approximately 200 °C and the shape of the desorption peak has become much more well defined. Similar results have been observed prior on other alloys of platinum and lanthanides; sharp desorption features have been observed earlier by Vermang et al. who have been studying Ce/Pt(111) surfaces[35], by Ramstad et al. who have been studying La/Pt(111)[36], and by Kildemo et al. who have studied Tm/Pt(111)[37]. Common for these samples is that they were all prepared by depositing monolayers of the lanthanide metal on a sputter cleaned Pt(111) surface. On these alloys is apparent that they have several desorption peaks, in contrast to Gd/Pt(111) where we only observed one peak. This difference can be a consequence of the different preparation procedures; if only a thin layer of the lanthanide metal is deposited, there might not be enough to produce a homogeneous layer of Pt_5Ln, which is the most platinum rich of the alloys.

The compressive strain imposed on the Gd/Pt(111) surface, as indicated by the LEED experiments, makes the surface less reactive in accordance with the d-band model[19,20]. The temperature shift of 200 °C compared to regular Pt(111), that was observed in the TPD experiments is equivalent to a destabilization of the adsorbates by around 0.56 eV compared to regular Pt(111). This was evaluated assuming the desorption process was first order[21]. The present DFT calculation show a shift in binding energy of just 0.32 eV at the lowest coverages at -6% strain, compared to the surface with a relaxed lattice constant. It could be possible that DFT underestimates the effect of strain on surface reactivity. In contrast to that, previous reports show a smaller strain effect in experiments than in calculations, where the experimental system was contracted Pt monolayers on Ru(0001)[18]. It is more likely that the ligand effects from Gd cause a shift, which is not accounted for in the present study, since only strain effects were addressed in the calculations.

Now the change in shape of the TPD spectra is discussed in relation to the DFT calculations. As the contraction increases from 0% towards 5%, the desorption peaks at high temperature move down and merge with the desorption peak at lower temperature as seen in 8 for -0% and -4.5% strain (Simulated spectra for the intermediate strain values are available in the supplementary information). The trend of narrowing is explained by the integral energy, which develop a minimum around 0.5 ML. The surfaces with a contracted lattice push out Pt atoms, as seen in the insets in Figure 8. These reconstructions are especially stabilized in the $\theta = 0.5$ configuration, where CO can adsorb in lines on top of rows of pushed-out atoms, but also at coverages including 4/9 and up. This is a cooperative effect between adsorbates, that develops more as surfaces are become more contracted, because contraction makes it favourable to draw out Pt-atoms from the surface plane, but mostly if one or two Pt-neighbours are also drawn out. At strains, where a high coverage configuration is more stable than configurations with lower coverages, domains or connected rows form. This results in identical desorption energies for a larger coverage range and for a larger portion of the adsorbates. In the case of connected rows, addition of CO molecules essentially costs the adsorption energy of the middle atoms and not the ends of the rows. The consequence of domain or row formation is identical adsorption energies for a larger fraction of the adsorbates, which result desorption in a narrower temperature range that are observed as sharper peaks in the TPD spectra. This is in good agreement with the general trend from the TPD experiments. In addition, the simulated TPD spectra at -4.5% strain and -5% strain show very sharp features due to the 0.5 ML state in agreement with experimental TPD from Y/Pt(111)[38] and Gd/Pt(111). These peaks also have small trailing satellites due to the lowest coverage configurations in the simulated spectra, which indicate that isolated adsorbates are still more stable than adsorbates in the bulk of the domains or rows.

In summary, the TPD simulations based on DFT calculations produces a narrowing of the TPD spectra and also a downward temperature shift from more contracted Pt surfaces, and thus reproduces the main trends from the experiments. The calculated temperature shift is due to the weaker binding of the contracted Pt(111) surface compared to the unstrained Pt(111) surface, while the narrowing of the simulated spectrum is due to the relative stabilisation of the high coverage configurations, compared to lower coverages. This relative stabilization is due to a subtle restructuring of the Pt(111) facet where Pt-atoms are drawn out of the plane by CO adsorbates, which is a cooperative adsorbate effect.

6 Acknowledgements

The work was funded by the Technical University of Denmark and by the Danish Council for Strategic Research *via* the NACORR project no. 12-132695.

References

1 I. E. L. Stephens, A. S. Bondarenko, U. Grønbjerg, J. Rossmeisl and I. Chorkendorff, *Energy Environ. Sci.*, 2012, **5**, 6744–6762.

2 S. J. Yoo, S. J. Hwang, J.-G. Lee, S.-C. Lee, T.-H. Lim, Y.-E. Sung, A. Wieckowski and S.-K. Kim, *Energy Environ. Sci.*, 2012, **5**, 7521–7525.

3 P. Malacrida, M. Escudero-Escribano, A. Verdaguer-Casadevall, I. E. L. Stephens and I. Chorkendorff, *J. Mater. Chem. A*, 2014, **2**, 4234–4243.

4 M. Escudero-Escribano, A. Verdaguer-Casadevall, P. Malacrida, U. Grønbjerg, B. P. Knudsen, A. K. Jepsen, J. Rossmeisl, I. E. L. Stephens and I. Chorkendorff, *J. Am. Chem. Soc.*, 2012, **134**, 16476–16479.

5 A. Velázquez-Palenzuela, F. Masini, A. F. Pedersen, M. Escudero-Escribano, D. Deiana, P. Malacrida, T. W. Hansen, D. Friebel, A. Nilsson, I. E. L. Stephens and

I. Chorkendorff, *J. Catal.*, 2015, **328**, 297–307.
6 M. Escudero-Escribano, P. Malacrida, M. H. Hansen, U. G. Vej-Hansen, A. Velázquez-Palenzuela, V. Tripkovic, J. Schiøtz, J. Rossmeisl, I. E. L. Stephens and I. Chorkendorff, *Science*, 2016, **352**, 73–76.
7 U. G. Vej-Hansen, J. Rossmeisl, I. E. L. Stephens and J. Schiøtz, *Phys. Chem. Chem. Phys.*, 2016, **18**, 3302–3307.
8 E. T. Ulrikkeholm, A. F. Pedersen, U. G. Vej-Hansen, M. Escudero-Escribano, I. E. Stephens, D. Friebel, A. Mehta, J. Schiøtz, R. K. Feidenhansl, A. Nilsson and I. Chorkendorff, *Surf. Sci.*, 2016, DOI: 10.1016/j.susc.2016.02.009.
9 A. F. Pedersen, E. T. Ulrikkeholm, M. Escudero-Escribano, T. P. Johansson, P. Malacrida, C. M. Pedersen, M. H. Hansen, K. D. Jensen, J. Rossmeisl, D. Friebel, A. Nilsson, I. Chorkendorff and I. E. Stephens, *Nano Energy*, 2016, DOI: 10.1016/j.nanoen.2016.05.026.
10 C.-M. Chan, R. Aris and W. Weinberg, *Appl. Surf. Sci. (1977-1985)*, 1978, **1**, 360 – 376.
11 G. Ertl, M. Neumann and K. M. Streit, *Surf. Sci.*, 1977, **64**, 393–410.
12 E. K. Vestergaard, P. Thostrup, T. An, E. Laegsgaard, I. Stensgaard, B. Hammer and F. Besenbacher, *Phys. Rev. Lett.*, 2002, **88**, 259601.
13 J. C. Davies, R. M. Nielsen, L. B. Thomsen, I. Chorkendorff, A. Logadottir, Z. Lodziana, J. K. Norskov, W. X. Li, B. Hammer, S. R. Longwitz, J. Schnadt, E. K. Vestergaard, R. T. Vang and F. Besenbacher, *Fuel Cells*, 2004, **4**, 309–319.
14 S. R. Longwitz, J. Schnadt, E. K. Vestergaard, R. T. Vang, I. Stensgaard, H. Brune and F. Besenbacher, *J. Phys. Chem. B*, 2004, **108**, 14497–14502.
15 G. Ertl, M. Neumann and K. Streit, *Surf. Sci.*, 1977, **64**, 393–410.
16 G. Rupprechter, T. Dellwig, H. Unterhalt and H.-J. Freund, *J. Phys. Chem. B*, 2001, **105**, 3797–3802.
17 L. Grabow, Y. Xu and M. Mavrikakis, *Phys. Chem. Chem. Phys.*, 2006, **8**, 3369–3374.
18 A. Schlapka, M. Lischka, A. Groß, U. Käsberger and P. Jakob, *Phys. Rev. Lett.*, 2003, **91**, 016101.
19 B. Hammer and J. Nørskov, *Adv. Catal.*, 2000, **45**, 71–129.
20 M. Mavrikakis, B. Hammer and J. K. Nørskov, *Phys. Rev. Lett.*, 1998, **81**, 2819–2822.
21 P. Redhead, *Vacuum*, 1962, **12**, 203 – 211.
22 I. Chorkendorff and H. Niemantsverdriet, *Concepts in modern catalysis and kinetics*, Wiley-VCH, 2003.
23 H. Steininger, S. Lehwald and H. Ibach, *Surf. Sci.*, 1982, **123**, 264–282.
24 S. R. Bahn and K. W. Jacobsen, *Comput. Sci. Eng.*, 2002, **4**, 56–66.
25 J. Enkovaara, C. Rostgaard, J. J. Mortensen, J. Chen, M. Dulak, L. Ferrighi, J. Gavnholt, C. Glinsvad, V. Haikola and H. A. Hansen, *J. Phys.: Condens. Matter*, 2010, **22**, 253202.
26 J. J. Mortensen, L. B. Hansen and K. W. Jacobsen, *Phys. Rev. B*, 2005, **71**, 035109.
27 W. Kohn and L. J. Sham, *Phys. Rev.*, 1965, **140**, A1133–A1138.
28 H. J. Monkhorst and J. D. Pack, *Phys. Rev. B*, 1976, **13**, 5188–5192.
29 B. Hammer, L. B. Hansen and J. K. Nørskov, *Phys. Rev. B*, 1999, **59**, 7413–7421.
30 P. J. Feibelman, a. J. K. N. B. Hammer, F. Wagner, M. Scheffler, R. Stumpf, R. Watwe, and J. Dumesic, *J. Phys. Chem. B*, 2001, **105**, 4018–4025.
31 Y.-H. Hu, H.-L. Wan, K.-R. Tsai and C.-T. Au, 1996, **274**, 289–301.
32 S. Raaen and A. Ramstad, *Energy*, 2005, **30**, 821 – 830.
33 N. Petrova and I. Yakovkin, *Surf. Sci.*, 2005, **578**, 162 – 173.
34 J.-S. McEwen, S. Payne, H. Kreuzer, M. Kinne, R. Denecke and H.-P. Steinrück, *Surf. Sci.*, 2003, **545**, 47 – 69.
35 J. Tang, J. M. Lawrence and J. C. Hemminger, *Phys. Rev. B*, 1993, **48**, 15342–15352.
36 A. Ramstad and S. Raaen, *Phys. Rev. B*, 1999, **59**, 15935–15941.
37 A. Kildemo, A. Juel and S. Raaen, *Surf. Sci.*, 2005, **581**, 133–141.
38 T. P. Johansson, E. T. Ulrikkeholm, P. Hernandez-Fernandez, M. Escudero-Escribano, P. Malacrida, I. E. L. Stephens and I. Chorkendorff, *Phys. Chem. Chem. Phys.*, 2014, **16**, 13718–13725.

Paper IV

Widely available active sites on Ni_2P for electrochemical hydrogen evolution – insights from first principles calculations

Martin H. Hansen, Lucas-Alexandre Stern, Ligang Feng, Jan Rossmeisl and Xile Hu

Physical Chemistry Chemical Physics, (**2015**), 17, 10823

PCCP

PAPER

View Article Online
View Journal | View Issue

Cite this: *Phys. Chem. Chem. Phys.*, 2015, **17**, 10823

Widely available active sites on Ni_2P for electrochemical hydrogen evolution – insights from first principles calculations†

Martin H. Hansen,[ab] Lucas-Alexandre Stern,[b] Ligang Feng,[b] Jan Rossmeisl*[a] and Xile Hu*[b]

Received 20th February 2015,
Accepted 16th March 2015

DOI: 10.1039/c5cp01065a

www.rsc.org/pccp

We present insights into the mechanism and the active site for hydrogen evolution on nickel phosphide (Ni_2P). Ni_2P was recently discovered to be a very active non-precious hydrogen evolution catalyst. Current literature attributes the activity of Ni_2P to a particular site on the (0001) facet. In the present study, using Density Functional Theory (DFT) calculations, we show that several widely available low index crystal facets on Ni_2P have better properties for a high catalytic activity. DFT calculations were used to identify moderately bonding nickel bridge sites and nickel hollow sites for hydrogen adsorption and to calculate barriers for the Tafel pathway. The investigated surfaces in this study were the $(10\bar{1}0)$, $(\bar{1}\bar{1}20)$, $(11\bar{2}0)$, $(11\bar{2}1)$ and (0001) facets of the hexagonal Ni_2P crystal. In addition to the DFT results, we present experiments on Ni_2P nanowires growing along the ⟨0001⟩ direction, which are shown as efficient hydrogen evolution catalysts. The experimental results add these nanowires to a variety of different morphologies of Ni_2P, which are all active for HER.

1. Introduction

Water splitting by electrolysis or photocatalysis is attracting attention as a prospective sustainable source of hydrogen for energy storage applications.[1–3] The hydrogen evolution reaction (HER) is the cathode half reaction:

$$H^+(aq) \rightarrow 1/2H_2(g)$$

The most active and stable catalysts in acid environments for HER are currently based on precious metals.[4] At low over-potentials, HER from Pt(111) is dominated by the Volmer–Tafel mechanism[5–7] which can be written as:

$$H^+(aq) \rightarrow H^* \quad (1)$$

$$2H^* \rightarrow H_2(g) \quad (2)$$

This requires two H atoms to be adsorbed in proximity for fast diffusion and recombination. Alternatively the reaction may take place *via* a Volmer step (1), followed by the Heyrovski step:

$$H^+(aq) + H^* + e^- \rightarrow H_2(g) \quad (3)$$

Reaction (3) is considered to be relevant at high over-potentials only.[7]

In the last decade, several classes of non-precious materials have been found to be active catalysts for the HER. MoS_2 was proven as a promising non-precious HER catalyst material, which is stable in a wide pH range. However MoS_x catalysts are not as active as platinum and they are only active at under-coordinated edge sites.[8–11] Hydrodesulfurization (HDS) catalysts such as Mo_2C and MoB have recently attracted attention as hydrogen evolution catalysts with good stability in both acid and alkaline solution.[12,13] Ni_2P has also previously been subjected to experimental and theoretical studies for the catalysis of hydrodesulfurisation[13–16] water-gas-shift,[17] and more recently for hydrogen evolution in acid.[18–20] The active sites and the details of the mechanism remain unknown for several of the newly discovered HER catalysts including Ni_2P. The observed Tafel slopes of the Ni_2P catalysts are similar to what is observed for MoS_2 edges, and the specific activity is one of the highest of the non-precious catalysts. Further experimental and theoretical studies can yield new insights for further design of electro-catalysts, which is the motivation of this study. In this paper, density functional theory (DFT) calculations are combined with experiments on high aspect ratio crystalline Ni_2P nanowires to understand the mechanism of HER from Ni_2P.

The trends in hydrogen evolution activity over various transition metals,[21,22] and various metal- and non-metal combinations have been investigated using DFT. The free energy of hydrogen

[a] *Department of Physics, Technical University of Denmark, Fysikvej, Building 307, Office 242 DK-2800 Kgs, Lyngby, Denmark. E-mail: Jan.Rossmeisl@fysik.dtu.dk*
[b] *Laboratory of Inorganic Synthesis and Catalysis, Institute of Chemical Sciences and Engineering, École Polytechnique Fédérale de Lausanne (EPFL), ISIC-LSCI, BCH 3305, 1015 Lausanne, Switzerland. E-mail: xile.hu@epfl.ch*

† Electronic supplementary information (ESI) available. See DOI: 10.1039/c5cp01065a

adsorption, ΔG_{H^*}, has been established as a descriptor for predicting the exchange current density,[21–24] of transition metal catalysts. The best catalysts have free binding energies close to 0.0 eV, which is explained by the Sabatier principle;[25] stronger binding results in hydrogen poisoning, leaving no free sites for adsorption. Weaker binding results in a high overpotential needed to adsorb protons. Transition metal catalysts have binding energies that are slightly coverage dependent. On Pt(111) the binding energy calculated with DFT varies from −0.12 eV at low coverage to 0.04 eV at one monolayer coverage.[21] In addition, it has been shown by DFT calculations that platinum has no significant diffusion barrier between the adsorbing hollow sites on the (111) facet.[26]

Liu and Rodriguez have published several studies on DFT calculations of hydrogen binding energies on the $Ni_2P(0001)$ surface. In 2005, they predicted the hydrogen evolution activity of Ni_2P to be comparable to that of hydrogenase based on trends in adsorption energies. The ensemble of phosphor atoms available as proton acceptors next to moderately binding metal hollow sites and a weak binding Ni–P bridge is proposed to facilitate HER catalysis.[18] The binding energies can be compared with the trends in HER exchange current density calculated by Nørskov *et al.*[21] In these studies, the binding free energies are presented, which means that the calculated potential energy is corrected by +0.24 eV accounting for entropy and differences in zero point energy. When comparing the binding energies at the relevant coverage,[7,27] one observes that the metal hollow sites on Ni_2P will be fully occupied and that the Ni–P sites will need an overpotential of at least 0.31 V. This does not agree with the very high activity observed in new studies of hollow and multifaceted Ni_2P nanoparticle catalysts.[19,20,28,29] Another active site may therefore exist, and we investigate this using more detailed DFT calculations. In addition we report experiments showing that nano wires grown along the (0001) direction are highly active for HER, supporting the results of the present DFT calculations.

Calculation methods

Calculations were carried out using the GPAW code with projector augmented wave functions on a real space grid and ultra soft pseudopotentials.[30] The RPBE[31] functional was used for the exchange–correlation contribution. The Ni_2P crystal structure[32] was copied from The Materials Project,[33] and imported to The Atomic Simulation Environment (ASE).[34] Bulk lattice constants were converged to a = 5.151 Å and c = 3.408 Å using a third order polynomial fit to the energy *versus* the lattice constant.[35]

A 1 × 1 supercell was used for the (0001) and $(11\bar{2}1)$ surfaces, a 3 × 1 supercell was used for the $(10\bar{1}0)$ surface and a 1 × 2 supercell was used for the $\pm(11\bar{2}0)$ surfaces. The (0001) surface had five atomic layers, the $(11\bar{2}1)$ and $(10\bar{1}0)$ slabs had four atomic layers, and the $\pm(11\bar{2}0)$ surfaces had three atomic layers. The dipoles across the unit cells were all less than 0.10 V.

A Monkhorst–Pack[36] sampling of 2 × 2 × 1 k-points was used for the large $(11\bar{2}1)$ surfaces, 2 × 3 × 1 k-points were used for the $\pm(11\bar{2}0)$ surfaces, 3 × 2 × 1 k-points for the $(10\bar{1}0)$ slabs and for the (0001) surface a 3 × 3 × 1 k-point sampling was used. The grid spacing was 0.18 Å in all calculations.

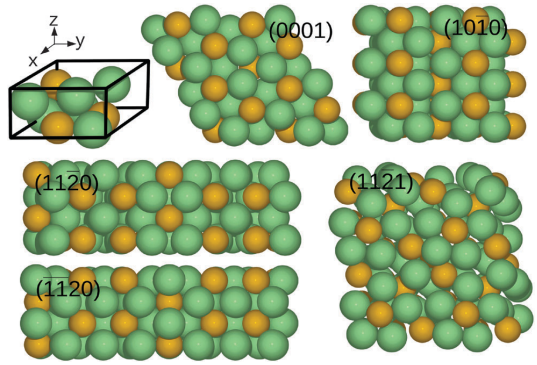

Fig. 1 The Ni_2P unit cell and top views of the low index surfaces used in this study. The surface unit cells have been repeated once in the X and Y directions, apart from the $(10\bar{1}0)$ direction, for which a 2 × 3 supercell is shown. Nickel atoms are represented by green spheres and phosphor atoms by yellow spheres.

The slabs were relaxed using the Broyden–Fletcher–Goldfarb–Shanno LineSearch algorithm within ASE until the forces were below 0.01 eV Å^{-1}. A recalculation was later carried out with double the k-point sampling and a grid spacing of 0.12 Å for the most interesting slabs and adsorbate configurations. The resulting differences in adsorption energies did not exceed 0.02 eV, which is below the accuracy usually attributed to DFT.

The choice of facets and surface termination were based on calculations of the minimum energy configuration of all different ways to cut the crystal into the lowest index planes. Several STM and LEED studies[37–40] show that the Ni_2P surfaces can have a stable phosphor termination, but under the hydro-thermal treatment before testing, it is expected that they lose the phosphor layer and expose active metal sites, as on the structures investigated in our calculations. The chosen structures are $(10\bar{1}0)$, $(11\bar{2}0)$, $(\bar{1}\bar{1}20)$, $(11\bar{2}1)$ and the Ni_3P terminated (0001), as shown in Fig. 1 along with their (hkjl) indices from a top view.

The free adsorption energies are found from calculated potential energies by correcting for the gas phase entropy $\Delta S = -S_0(H_2)$ and the difference in zero point energy ΔZPE using the equation

$$\Delta G = \Delta E - T\Delta S + \Delta \mathrm{ZPE}$$

where E denotes the ground state energy at 0 K obtained from DFT. The correction for ZPE and entropy makes an addition of 0.24 eV to the adsorption energy of a hydrogen atom.[21,41]

The calculation of adsorption free energies and adsorbate coverages was carried out using the self consistent scheme as in the work reported by Skulason *et al.*[7] The integral adsorption energy $G_{\mathrm{int}}(n)$ is

$$G_{\mathrm{int}} = (G(N,n) - G(N,0) - n\mu_{\mathrm{H}}), \quad \text{where } \mu_{\mathrm{H}} = 1/2G_{\mathrm{H_2}} - eU$$

where $G(N,n)$ is the free energy of a surface which includes N nickel atoms in the top layer and n adsorbed hydrogen atoms. Thus we use a definition of the coverage $\theta = n/N$, where n is the number of hydrogen adsorbates and N is the number of Ni

atoms on the surface. The configuration which is relevant at a given chemical potential of protons and electrons is the one with the minimum integral adsorption energy ($G_{int}(n)$). Using the computational hydrogen electrode approach[41] with self-consistent coverage and adsorption free energies,[27] the adsorption phase diagram was calculated for every facet. The required over-potential to favor an intermediate step is given through the differential binding energy, which is given by:

$$\Delta G_{diff}(n) = (G_{int}(n) - G_{int}((n-1)))$$

We apply $\eta = \Delta G_{diff}(n)/e$ to find the minimum required over-potential to adsorb the intermediate,[41] which enables a surface recombination reaction (the Tafel step). The barriers were calculated using the nudged elastic band (NEB) method with a climbing image.[42]

2. Experimental methods

Materials

The commercially available materials were used as received: nickel acetylacetonate ($Ni(acac)_2$ for synthesis, VWR), oleic acid (suitable for cell culture, BioReagent, Aldrich), oleylamine (OA approximate C18-content 80–90%, Acros), trioctylphosphine (TOP 90%, technical grade, AcroSeal®, Acros), ethanol (absolute alcohol without additive ≥99.8%, Aldrich), *n*-hexane (HiPerSolv CHROMANORM® for HPLC 97%, VWR), sulfuric acid (H_2SO_4 volumetric 1 M, Aldrich), and Nafion® (117 solution, Aldrich). Water was first purified using a Millipore Milli-Q® Integral water purification system (18.2 MΩ cm resistivity). All syntheses were performed under strict air-free conditions using glove-box and Schlenk line techniques unless stated otherwise.

Synthesis of nickel phosphide nanowires

The synthesis was performed following a previous report.[43] A stock solution containing 0.75 mmol of $Ni(acac)_2$, 1.8 mmol of oleic acid and 10 mL of OA was heated at 120 °C. Then the stock solution was very slowly injected (0.05 mL min^{-1}) using a syringe pump into a stirred mixture containing 5 mL of OA and 2.4 mmol of TOP heated at 320 °C under reflux. The reaction mixture was kept at 320 °C under reflux until the stock solution was used up. Over the course of the reaction, the mixture color changes from transparent to dark yellow, orange and finally black. After cooling to room temperature, the products were washed using a mixture of hexane and ethanol, and separated by centrifugation. The supernatant was discarded and the washing step was repeated two more times. After the supernatant was discarded the nanowires were collected on a watch glass and dried in an oven at 50 °C overnight.

Physical characterization

X-ray diffraction (XRD) was carried out on a X'Pert Philips diffractometer in Bragg–Brentano geometry with Cu $K_{\alpha 1}$ radiation (λ = 0.1540 nm) and a fast Si–PIN multi-strip detector. The tube source was operated at 45 kV and 40 mA. The Scherrer equation was used to calculate the average crystallite size of the powder. The diffraction pattern was analyzed and compared with references in the international center of diffraction data (ICDD). Transmission electron microscope (TEM) images were taken on a Philips (FEI) CM12 with a LaB_6 source operated at 120 kV accelerating voltage. Specimens were prepared by ultrasonic dispersion of the samples in ethanol. The suspension was mixed with a micropipette by several suction–release cycles to ensure a representative and reproducible TEM sample is obtained. A few drops of the mixed suspension were deposited onto the carbon-coated grid.

Electrochemical measurements

Electrochemical measurements were recorded using a Gamry Instruments Reference 3000™ potentiostat. A traditional three-electrode configuration was used. For polarization and electrolysis measurements, a platinum wire was used as the auxiliary electrode and a double-junction Ag/AgCl (KCl saturated) electrode was used as the reference electrode. Both counter and reference electrodes were rinsed with distilled water and dried with compressed air prior to measurements. Potentials were referenced to a reversible hydrogen electrode (RHE) by adding a value of (0.2 + 0.059 × pH) V. The current was normalised over the geometric surface area of the electrode. Ohmic drop was corrected using the current interrupt method. A total electrolyte volume of ~50 mL was used to fill the glass cell. All potentials were converted and referred to the RHE unless stated otherwise. The electrolyte used throughout all electrochemical experiments was a 1 M H_2SO_4 solution. During electrochemical experiments, the electrolyte was agitated using a magnetic stirrer rotating at 300 rpm. For all electrochemical experiments a glassy carbon electrode (~0.071 cm^2) was used as the working electrode. The cyclic voltammetry (CV) experiments were conducted in 1 M H_2SO_4 at 25 °C using a scan-rate of 5 mV s^{-1} across a potential window of −0.3 to +0.1 V *vs.* RHE.

Pretreatment of the working electrode

Prior to loading of the catalyst, the working electrode was pretreated to achieve a better performance.[44] First, the electrode was manually polished using alpha alumina powder (CH Instruments, Inc.) with decreasing grain sizes (typically 0.3 and 0.05 μm) on a 73 mm diameter nylon polishing pad (MasterTex, Buehler). Between each polishing step the electrode was rinsed with deionized water and ultrasonicated in distilled water for 10 seconds. Then the electrode was dried using compressed air. This ultrasonication and drying cycle was repeated two more times: once in absolute ethanol and a second time with distilled water. This polishing process resulted in a shiny mirror finish. The bare working electrode was subjected to a constant potential of 2 V *vs.* RHE in 1 M H_2SO_4 under vigorous stirring at 25 °C over 1 hour. Then, the pretreated electrode was rinsed with absolute ethanol and dried with compressed air prior to catalyst deposition.

Electrode preparation

Before being deposited on the working electrode, the nanowires were annealed at 450 °C for 4 hours under 5% H_2/N_2 gas in order to remove any surfactant present on the nanowire surface.[19,43]

The catalyst was loaded on a pretreated working electrode *via* drop-casting of 10 μL of the catalyst ink, equivalent to a loading of 1.42 mg cm^{-2}. The catalyst suspension was a 500 μL solution consisting of 5 mg of the catalyst, 400 μL of distilled water, and 100 μL of absolute ethanol. The slurry was ultrasonicated for 5 hours and mixed with a micropipette by several suction–release cycles prior to deposition to ensure that a representative and reproducible catalyst sample is obtained. The temperature of the ultrasonic bath was kept below 45 °C at all times to avoid any undesired heating effect. The nanowires are ultra-sonicated for 5 h to minimize aggregation. Once the catalyst was deposited, the electrode was dried in an oven at 50 °C for 10 minutes. 5 μL of 0.2% Nafion® solution in absolute ethanol was then drop-casted on the glassy carbon surface and the electrode was dried in air for 5 minutes prior to electrochemical measurements.

3. Results and discussion

XRD measurements were conducted on the annealed Ni_2P nanowires (Fig. 2). According to Scherrer's equation, the average crystallite size of the nanowires is 11 nm. Ni_2P is the predominant species in the sample, while small amounts of $Ni_{12}P_5$ and NiO are also present. Recently, Zhang *et al.* reported that pure $Ni_{12}P_5$ has a similar activity to that of Ni_2P for HER in acid.[45] We showed earlier that NiO is less active than Ni_2P; furthermore, NiO tends to dissolve at a reductive potential in acid. Thus, the HER activity of the nanowires (see below) can be mostly attributed to Ni_2P.

The transmission electron microscope (TEM) image and selected area electron diffraction (SAED) patterns of the nanowires are shown in Fig. 2a–d. The nanowires are rather uniform and the width of the nanowires observed by TEM is in agreement with the crystallite size calculated from the XRD pattern.

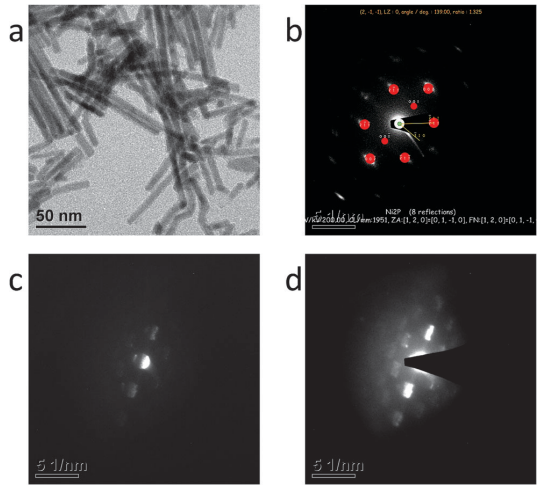

Fig. 2 (a) Representative TEM image of the annealed Ni_2P nanowires. (b) Focused SAED of nanowire crystallites indexed using JEMS© software. (c) and (d) Unfocused SAED patterns whose complementary information served to identify the growth direction of the nanowires.

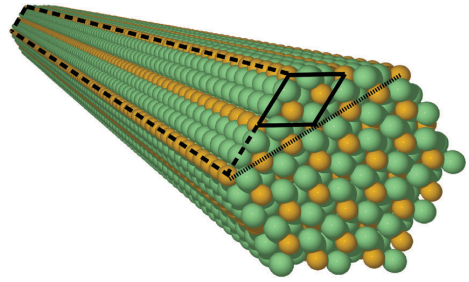

Fig. 3 Model of a nanowire crystal. This illustrates the exposed facets. The (0001) plane of the unit cell is shown with solid lines, the coarsely dashed lines show a $(10\bar{1}0)$ surface, and the finely dashed line shows the $\pm(11\bar{2}0)$ planes. Ni atoms are shown in green and phosphor atoms in yellow.

The focused SAED pattern (Fig. 2b) was indexed using the JEMS software program (P. Stadelmann, JEMS, EPFL). The line linking the $(000n)$ spots is the (0001) direction. The nanowire can be observed on the SAED pattern when the focus is reduced (Fig. 2c and d). Comparison between the indexed (Fig. 2b) and unfocused SAED patterns (Fig. 2c and d) allows the determination of the growth direction. The results indicate that the nanowires grow along the *c*-axis, *i.e.*, the $\langle 0001 \rangle$ direction.

Thus, the nanowires do not expose many (0001) facets, since the $(000n)$ planes exist only in their cross section (see Fig. 3). The low index facets $\pm(11\bar{2}0)$ and $(10\bar{1}0)$ are assumed to be widely available on the samples. These morphologies would be expected to exhibit a less than optimal performance if the ensemble on the Ni_3P terminated (0001) facet was the only active site.

Fig. 4 shows the HER activity of the Ni_2P nanowires in 1 M H_2SO_4. The nanowires are excellent HER catalysts. This result combined with the calculations (see below) does not indicate that the (0001) ensemble is the only active site of HER from Ni_2P, although it is not possible to separate contributions from the various facets and sites in the experiments. The overpotential to drive a current density of 10 mA cm^{-2} is 133 mV (Fig. 4a). Two Tafel slopes are observed. At $\eta < 125$ mV, the Tafel slope is about 60 mV dec^{-1}, while at $\eta \approx 125$–275 mV, the Tafel slope is 126 mV dec^{-1} (Fig. 4b). Despite the difference in sample preparation and morphology, the catalytic activity of the Ni_2P nanowires is very similar to the activity of hollow and multi-faceted Ni_2P nanoparticles reported by Schaak *et al.*,[19] that of polydispersed Ni_2P nanoparticles reported by our group[20] and that of high surface area Ni_2P nanoflakes reported by Han *et al.*[29] This suggests that widely available facets or sites of Ni_2P are active. This is contrary to MoS_x, where only specific morphologies are efficient because the edge sites need to be exposed.[8] The facets with $(ab\ -(a+b)\ 0)$ indices are propagating along the growth direction of the nanowires (see Fig. 3), and are thus expected to be abundant in the sample.

The DFT calculations show that the most strongly binding sites tend to be nickel bridge sites or nickel 3-fold hollow sites. The nickel bridge sites are found in continuous rows on the $(10\bar{1}0)$ and $(\bar{1}\bar{1}20)$ facets and adjacent to nickel hollow sites on the $(11\bar{2}1)$ facet. (see ESI,† for geometries and adsorption

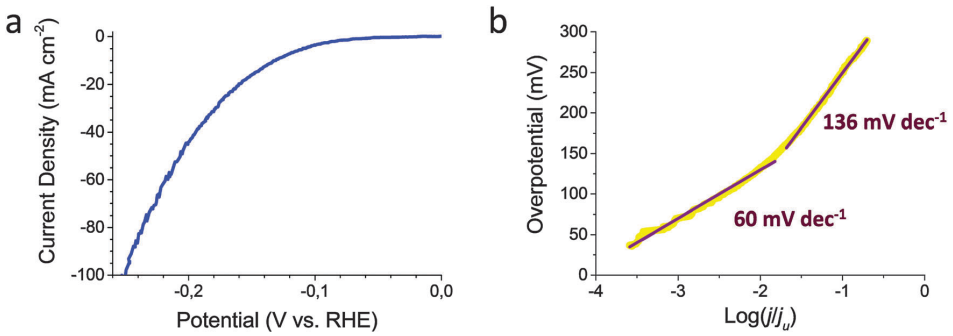

Fig. 4 (a) Polarization curve of Ni_2P nanowires in 1 M H_2SO_4 at 25 °C at a scan rate of 5 mV s^{-1}. (b) Tafel analysis of the polarization curve.

energies.) Adsorption on Ni–P sites and on top P atoms was generally 0.2 eV to 0.4 eV less stable than the metal sites. Thus, adsorption on Ni–P sites and on top P atoms would require a higher over-potential.

It takes a high over-potential to favor a high coverage of atomic hydrogen on all the facets. Thus, Ni_2P is on the weak binding side of the Sabatier volcano. Adsorbates on Ni_2P interact strongly leading to a steeper increase in binding energy with increasing coverage (see ESI,† for the surface phase diagrams), compared to most transition metals including platinum.

The (0001) facet has the hollow site occupied at equilibrium, but as shown in Fig. 6, it requires a large over-potential of 0.41 V to stabilize the initial Ni–P bridge state for the Tafel step. It is also improbable that adsorbates from separate hollow sites on (0001) can combine since they are not neighbouring. This was confirmed by calculating the diffusion barriers on the (0001) and the $(10\bar{1}0)$ facets (see ESI†). The $(10\bar{1}0)$, $(\bar{1}\bar{1}20)$ and $(11\bar{2}1)$ facets only require an over-potential of 0.0 V, 0.06 V and 0.19 V, respectively, to stabilise neighbouring H* or H*, which are mobile in the row of nickel atoms. These results suggest that H* in Ni hollow sites on the (0001) facet do not contribute to the HER rate at low over-potentials. To investigate further, the barriers for the Tafel step were calculated as described in the following.

Previous calculations on Pt(111) suggest that the Tafel pathway is faster than the Heyrovski pathway at low over-potentials. If proton transfer is faster to H*(Ni_2P) than to H*(Pt(111)), it is possible that isolated metal hollow sites on the (0001) facet play a role. In the following, it is assumed that the surface coverage is in equilibrium with protons in solution, which means that the Tafel step is rate limiting. Calculation of the barrier for proton transfer (Volmer or Heyrovski step) is out of the scope of this paper, since it requires very precise information on the interfacial structure.[46]

As shown in Fig. 5, the rate limiting HER barrier is G^{TS}, where G^{TS} is the energy of the transition state relative to the $2(H^+ + e^-)$ state. The initial states were the most stable configurations at the lowest possible over-potential according to the surface phase diagrams. As shown from calculations presented in Fig. 5, G^{TS} can be lowered by further increasing the over-potential

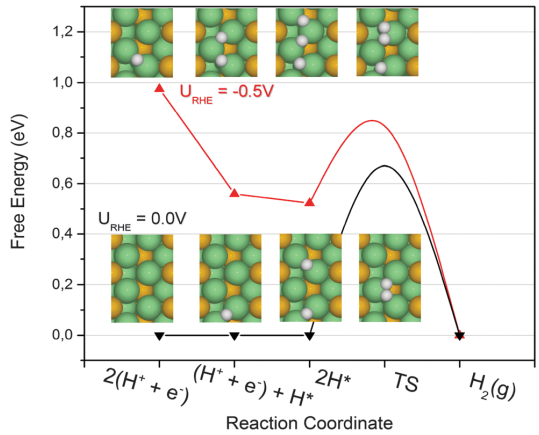

Fig. 5 Free energy pathway of the Volmer–Tafel reaction on the $(10\bar{1}0)$ facet. The configuration of every point is shown by the insets, where Ni is shown in green, P in yellow and H in white. The energy of the transition states is shown by the peak of the splines. These were calculated using the nudged elastic band method with a climbing image.[41] This shows how G^{TS} is reduced by applying a higher over-potential.

until the free energy of protons in solution are at the Tafel transition state level. This agrees well with the exchange current density being a good indication for the activity at higher over-potentials.

The results for a Tafel pathway are summarized in Fig. 6, with comparison between the studied facets. The adsorption energies, which are easy to calculate, are usually a good descriptor, since they are expected to scale with the transition state energies. In the case of a Tafel pathway, it is more accurate to use calculated G^{TS} to compare the activity from the different facets, since it is the highest barrier in the reaction pathway, which limits the rate.

Observing the calculated G^{TS} in Fig. 6 for the Tafel steps, it is clear that the $(\bar{1}\bar{1}20)$ facet and the $(11\bar{2}1)$ facet should have the highest exchange current density and thus be the most active facets. The reason why these sites have the lowest combination barrier may be found in the geometry of the Ni atom binding

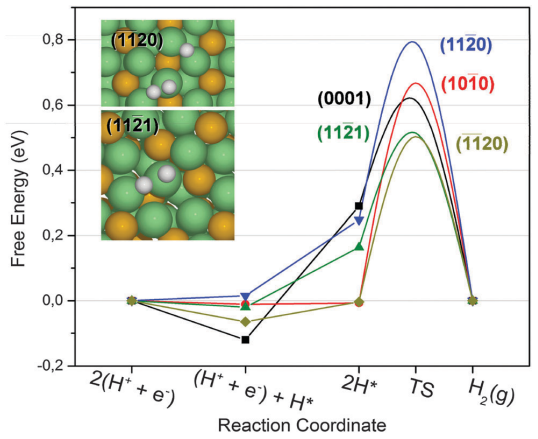

Fig. 6 Free energy diagram assuming a Tafel mechanism. Calculated barriers for the Tafel step are shown by the peak of the splines for the configurations, which are most stable at 0 V *vs.* RHE. The insets show transition states of the two facets with the lowest Tafel barriers. Ni atoms are shown in green, P in yellow and H in white.

the transition state. The transition states for ($\bar{1}\bar{1}$20) and (11$\bar{2}$1) are presented in the insets in Fig. 6. The atomic hydrogen moves from stable bridge sites on top of the nickel atom, which on these two facets is coordinated to six nickel atoms and two or three phosphor atoms. It is possible to imagine that a few defect sites, not investigated here, could be participating in the catalysis. However, the most active sites investigated in this study have binding energies very close to the optimal value and they are calculated to be very active. Other sites such as corners or kinks would only be relevant if they have a much higher activity than the low index facets. Furthermore, we expect that sites with lower coordination will bind too strongly, thus being less active according to the Sabatier principle.

4. Conclusion

In summary, the DFT calculations have shown that phosphor stabilized Ni-bridge sites found on several available facets of Ni_2P nanowires provide moderate binding to hydrogen atoms. The sites with highest exchange current density estimated from the Tafel transition state energy appear to be the Nickel bridge sites on either the ($\bar{1}\bar{1}$20) facet or the (11$\bar{2}$1) facet. The high activity measured from nanowires grown along the ⟨0001⟩ direction suggests that the active site of Ni_2P is unlikely the (0001) facet as previously speculated.[18] Thus the experiments support the calculations, although contributions from various sites or facets cannot be completely isolated in the electrochemical measurements.

This work shows that Ni_2P has many very active sites for HER, which explains the good performance. An interesting outlook is the calculation of other metal phosphor compounds, to look for sites with slightly stronger hydrogen binding energies or less adsorbate repulsion, which could be promising candidates for new catalyst materials.

Acknowledgements

The work at EPFL is supported by EPFL and a grant from the Competence Center for Energy and Mobility (CCEM) in the framework of the Hytech project. At DTU, the work is funded by the Catalysis for Sustainable Energy (CASE) initiative and the Danish Council for Strategic Research *via* the NACORR project no. 12-132695.

References

1 A. Züttel, *Hydrogen as a Future Energy Carrier*, Wiley-VCH Verlag GmbH & Co. KGaA, 2008, pp. 1–6.
2 N. S. Lewis and D. G. Nocera, *Proc. Natl. Acad. Sci. U. S. A.*, 2006, **103**, 15729–15735.
3 M. G. Walter, E. L. Warren, J. R. McKone, S. W. Boettcher, Q. Mi, E. A. Santori and N. S. Lewis, *Chem. Rev.*, 2010, **110**, 6446–6473.
4 S. Trasatti, *J. Electroanal. Chem. Interfacial Electrochem.*, 1972, **39**, 163–184.
5 J. X. Wang, T. E. Springer and R. R. Adzic, *J. Electrochem. Soc.*, 2006, **153**, A1732–A1740.
6 K. Kunimatsu, T. Senzaki, M. Tsushima and M. Osawa, *Chem. Phys. Lett.*, 2005, **401**, 451–454.
7 E. Skulason, G. S. Karlberg, J. Rossmeisl, T. Bligaard, J. Greeley, H. Jonsson and J. K. Norskov, *Phys. Chem. Chem. Phys.*, 2007, **9**, 3241–3250.
8 B. Hinnemann, P. G. Moses, J. Bonde, K. P. Jørgensen, J. H. Nielsen, S. Horch, I. Chorkendorff and J. K. Norskov, *J. Am. Chem. Soc.*, 2005, **127**, 5308–5309.
9 T. F. Jaramillo, K. P. Jørgensen, J. Bonde, J. H. Nielsen, S. Horch and I. Chorkendorff, *Science*, 2007, **317**, 100–102.
10 J. Kibsgaard, Z. Chen, B. N. Reinecke and T. F. Jaramillo, *Nat. Mater.*, 2012, **11**, 963–969.
11 J. R. McKone, B. F. Sadtler, C. A. Werlang, N. S. Lewis and H. B. Gray, *ACS Catal.*, 2013, **3**, 166–169.
12 H. Vrubel and X. Hu, *Angew. Chem., Int. Ed.*, 2012, **51**, 12703–12706.
13 C. G. Morales-Guio, L.-A. Stern and X. Hu, *Chem. Soc. Rev.*, 2014, **43**, 6555–6569.
14 P. Liu, J. A. Rodriguez, T. Asakura, J. Gomes and K. Nakamura, *J. Phys. Chem. B*, 2005, **109**, 4575–4583.
15 G. H. Layan Savithra, E. Muthuswamy, R. H. Bowker, B. A. Carrillo, M. E. Bussell and S. L. Brock, *Chem. Mater.*, 2013, **25**, 825–833.
16 S. T. Oyama, T. Gott, H. Zhao and Y.-K. Lee, *Catal. Today*, 2009, **143**, 94–107.
17 P. Liu, J. A. Rodriguez, Y. Takahashi and K. Nakamura, *J. Catal.*, 2009, **262**, 294–303.
18 P. Liu and J. A. Rodriguez, *J. Am. Chem. Soc.*, 2005, **127**, 14871–14878.
19 E. J. Popczun, J. R. McKone, C. G. Read, A. J. Biacchi, A. M. Wiltrout, N. S. Lewis and R. E. Schaak, *J. Am. Chem. Soc.*, 2013, **135**, 9267–9270.
20 L. Feng, H. Vrubel, M. Bensimon and X. Hu, *Phys. Chem. Chem. Phys.*, 2014, **16**, 5917–5921.

21 J. K. Nørskov, T. Bligaard, A. Logadottir, J. Kitchin, J. Chen, S. Pandelov and U. Stimming, *J. Electrochem. Soc.*, 2005, **152**, J23–J26.
22 M. E. Bjorketun, A. S. Bondarenko, B. L. Abrams, I. Chorkendorff and J. Rossmeisl, *Phys. Chem. Chem. Phys.*, 2010, **12**, 10536–10541.
23 J. O. Bockris, A. K. Reddy and M. Electrochemistry, *Electrodics in Chemistry, Engineering, Biology, and Environmental Science*, Springer, 2000.
24 J. Greeley, J. K. Nørskov, L. A. Kibler, A. M. El-Aziz and D. M. Kolb, *ChemPhysChem*, 2006, **7**, 1032–1035.
25 R. Parsons, *Trans. Faraday Soc.*, 1958, **54**, 1053–1063.
26 G. W. Watson, R. P. K. Wells, D. J. Willock and G. J. Hutchings, *J. Phys. Chem. B*, 2001, **105**, 4889–4894.
27 J. Rossmeisl, J. K. Nørskov, C. D. Taylor, M. J. Janik and M. Neurock, *J. Phys. Chem. B*, 2006, **110**, 21833–21839.
28 Y. Pan, Y. Liu, J. Zhao, K. Yang, J. Liang, D. Liu, W. Hu, D. Liu, Y. Liu and C. Liu, *J. Mater. Chem. A*, 2015, **3**, 1656–1665.
29 A. Han, S. Jin, H. Chen, H. Ji, Z. Sun and P. Du, *J. Mater. Chem. A*, 2015, **3**, 1941–1946.
30 J. J. Mortensen, L. B. Hansen and K. W. Jacobsen, *Phys. Rev. B: Condens. Matter Mater. Phys.*, 2005, **71**, 035109.
31 B. Hammer, L. B. Hansen and J. K. Nørskov, *Phys. Rev. B: Condens. Matter Mater. Phys.*, 1999, **59**, 7413–7421.
32 E. Larsson, *Ark. Kemi*, 1965, **23**, 335–365.
33 A. Jain, G. Hautier, C. J. Moore, S. P. Ong, C. C. Fischer, T. Mueller, K. A. Persson and G. Ceder, *Comput. Mater. Sci.*, 2011, **50**, 2295–2310.
34 S. R. Bahn and K. W. Jacobsen, *Comput. Sci. Eng.*, 2002, **4**, 56–66.
35 A. B. Alchagirov, J. P. Perdew, J. C. Boettger, R. C. Albers and C. Fiolhais, *Phys. Rev. B: Condens. Matter Mater. Phys.*, 2003, **67**, 026103.
36 H. J. Monkhorst and J. D. Pack, *Phys. Rev. B: Solid State*, 1976, **13**, 5188–5192.
37 D. Kanama, S. T. Oyama, S. Otani and D. F. Cox, *Surf. Sci.*, 2004, **552**, 8–16.
38 M. G. Moula, S. Suzuki, W.-J. Chun, S. Otani, S. T. Oyama and K. Asakura, *Surf. Interface Anal.*, 2006, **38**, 1611–1614.
39 Q. Li and X. Hu, *Phys. Rev. B: Condens. Matter Mater. Phys.*, 2006, **74**, 035414.
40 D. Guo, Y. Nakagawa, H. Ariga, S. Suzuki, K. Kinoshita, T. Miyamoto, S. Takakusagi, K. Asakura, S. Otani and S. T. Oyama, *Surf. Sci.*, 2010, **604**, 1347–1352.
41 J. K. Nørskov, J. Rossmeisl, A. Logadottir, L. Lindqvist, J. R. Kitchin, T. Bligaard and H. Jónsson, *J. Phys. Chem. B*, 2004, **108**, 17886–17892.
42 G. Henkelman and H. Jónsson, *J. Chem. Phys.*, 2000, **113**, 9978.
43 Y. Chen, H. She, X. Luo, G.-H. Yue and D.-L. Peng, *J. Cryst. Growth*, 2009, **311**, 1229–1233.
44 L.-A. Stern and X. Hu, *Faraday Discuss.*, 2014, **176**, 363–379.
45 Z. Huang, Z. Chen, Z. Chen, C. Lv, H. Meng and C. Zhang, *ACS Nano*, 2014, **8**, 8121–8129.
46 J. Rossmeisl, K. Chan, R. Ahmed, V. Tripković and M. E. Björketun, *Phys. Chem. Chem. Phys.*, 2013, **15**, 10321–10325.

Paper V

Extract of:

Water at Interfaces

Olle Bjorneholm; Martin Hansen; Andrew Hodgson; Li-Min Liu, David Limmer, Angelos Michaelides, Philipp Pedevilla, Jan Rossmeisl, , Huaze Shen, Gabriele Tocci, Eric Tyrode, Marie-Madeleine Walz, Josephina Werner, Hendrik Bluhm

Chemical Reviews, Accepted, (**2016**)

3. BULK WATER/METAL INTERFACES

After the discussion of low coverage and monolayer (ML) water adsorption at low temperatures and under ultra high vacuum conditions we now turn our attention to bulk aqueous solution/metal interfaces, which are of paramount importance to a broad range of scientific and technological areas, including electrochemistry, heterogeneous catalysis and energy storage.[53,54,55,56,57,58] Consequently these interfaces have been investigated for more than 100 years using both experimental and theoretical approaches. While a thorough discussion of the current literature about all water/metal interfaces is outside the scope of this review, Refs. 9, 59, 60, 61, and 62 offer relevant recent reviews.

At ambient conditions, when metal interfaces are in contact with liquid water, the molecular structure of the interface is no longer directly accessible like it is at monolayer coverages and ultrahigh vacuum conditions. Thus, indirect measurements and theory are needed. A number of recent experimental methods have recently provided important insight into water-metal interfaces. For instance, with the help of temperature programed desorption of ice-metal interfaces a weakly interacting first monolayer of water suggestive of a mostly in-plane hydrogen bonding geometry was uncovered.[45] Similar weak interactions have been inferred from altered wetting behavior either with un-dissociated water molecules[31] or in mixed water-hydroxyl overlayers.[9] The importance of surface hydroxyl groups for the wettability has been demonstrated for a metal under ambient conditions of relative humidity and temperature: While Cu(110) is covered by a mixed hydroxyl/water layer at a RH of 5%, Cu(111) does not show the presence of molecular water at the same RH, due to the higher dissociation barrier of water on the less reactive (111) surface.[62,63] Electrochemical kinetic measurements with simple kinetic modeling have unveiled that relaxation times in some cases can be unexpectedly long,[64] which is also consistent with recent probes of electronic relaxation.[65] Recently, X-ray absorption experiments were performed at water-gold interfaces under bias, and have unveiled an altered interfacial water structure.[66] Together with first principles modeling, it was determined that applied voltage can shift the number of molecules that are bound to the interface, losing hydrogen bonds to the liquid.

Absent more direct experimental probes, our understanding of liquid water-metal interfaces comes from theory and molecular simulation. Modeling extended water-metal interfaces at a molecular level is difficult for a number of reasons that make modeling water a challenging task in general, such as accurate description of the potential energy surface, as well as many specific problems arising from the structure and dynamics of water at the interface as a result of the subtle balance of water-water and water-substrate interactions. This balance is manifested already at monolayer coverages on simple planar metal surfaces, where STM experiments have exposed a rich variety of two-dimensional hydrogen bonding structures, as discussed in the previous section. Even at ambient temperature, where entropic effects mix many of these nearly degenerate configurations, this balance is also evident and can result in a wide range of wetting behaviors from hydrophobic to hydrophilic.[45,61,67] While the intermolecular interactions between water molecules are notoriously difficult to capture[68], a coherent picture of the forces acting on a single molecule on a closed-packed planar surface has emerged over the last 10 years[18,69,70,71,72], but the influence of step edges (e.g., on higher indexed surfaces) and other defects are largely unknown and unexplored.

Apart from the specifics of the intermolecular interactions, the statistical nature of the liquid state in contact with the metal necessitates an adequate treatment of thermal fluctuations in order to accurately compute thermodynamic expectation values. This means that the phase space must be appropriately sampled, requiring a way of generating many independent configurations that populate an appropriate Boltzmann distribution. Independent configurations are typically generated using molecular dynamics simulations, which can be hampered by long correlation times common for liquids in heterogeneous environments.[73] For most systems of interest the appropriate ensemble fixes the temperature, volume, particle number, and importantly, the applied electric potential within the metal. In practice, molecular dynamics simulations of water near metal interfaces have come in two varieties, either *ab initio* from electronic structure theory or with empirical force fields. In the former, forces are computed "on the fly", typically with DFT.[74] While this approach affords minimal assumptions as to the form of interactions among water molecules, and between water, the metal surface and solutes, the relatively high computational expense limits the system size, although calculations involving thousands of molecules are

possible for short times.[75] These two types of simulations are illustrated in Figure 5, shown to scale in the characteristic sizes feasible with current computational and algorithmic resources. The figure highlights the benefits of DFT based simulations in describing bond breaking and bond making as in the transfer of a proton between hydrogen bonded water molecules, while sacrificing the large lengths scales and long time scales approachable by force field based methods.

The aim of *ab initio* calculations has, however, primarily been to model chemical bonds and reactions

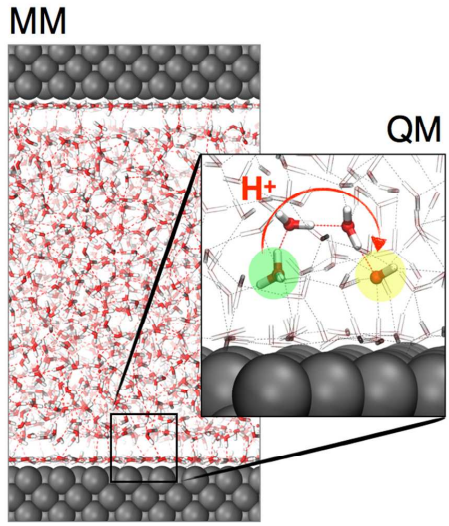

Figure 5. Characteristic snapshots taken from molecular dynamics simulations of the water-platinum interface. These two molecular renderings illustrate roughly the current state of the art with regard to simulation sizes approachable with empirical molecular mechanics (MM) and *ab initio* forces (QM). Empirical models are capable of simulating 10^4-10^5 molecules over hundreds of ns, while *ab initio* models are capable of following 10^2-10^3 molecules over 10-100 ps. However, only the latter is able to capture chemical bonding rearrangements necessary for a complete description of electrochemically relevant phenomena. *The figure is only schematic and does not represent the actual embedding of QM regions into MM environments.*

rather than dynamic properties of interfacial water. *Ab initio* models have previously suffered difficulties in the numerical description of water due to the strong non-bonding interactions. The numerical description of the interaction of water molecules on a metal surface has traditionally met more success.[74,76] Differences in adsorption energies on metal surfaces appear to be generally well described by

DFT with standard GGA functionals such as PBE[77] and RPBE[78], which are computationally relatively inexpensive compared to hybrid functionals or wave function methods. For example, ground state structures predicted at this level of theory for monolayer and sub-monolayer coverages are typically in good agreement with those observed in low-temperature STM experiments as described in Section 2.[10,79,80] However, various functionals which account for van der Waals dispersion forces have recently been developed and applied to water/solid interfaces.[81,82,83,84] These functionals are expected to provide a more balanced description of water-water versus water-surface interactions and have been shown to improve the wetting properties of water monolayers on metals.[50] Most importantly, *ab initio* calculations of water/metal interfaces are able to describe instances of dissociative adsorption and mixed water-hydroxide or water-hydride interfaces. Many recent studies have exploited that benefit as well as exploring the structure and dynamics of aqueous water-/metal interfaces, although relatively small system sizes and/or short dynamical trajectories are possible with current computational resources.[74,85,86,87,88,89,90]

The modeling of electrochemical reactions for small systems containing a metal-water interface requires the exchange of species like protons or counter ions, which is not straightforward in molecular dynamics simulations.[91] In addition, the modeling of electrochemical interfaces poses additional challenges related to the applied potential[66] and the electrochemical environment.[92] In recent years, a several advances have been made towards *ab initio* models that include these features.[85,93,94,95] Grand canonical ensembles with continuously varying numbers of electrons have been consistently formulated within a DFT framework[96,97,98,99], however, these methods have not yet garnered widespread use, largely due to difficulties in the implementation and because they do not account for the chemical potentials of ions.[92] Other more practical methods have been developed specifically aimed at static electrochemistry. These methods use an *a posteriori* mapping from fixed charged calculations to a Grand Canonical ensemble. They use the electron work function as an absolute electrode potential scale.[88,100,101,102]

These systems are still not in equilibrium with the ionic chemical potentials, since the number of ions is kept constant. Nevertheless, it is possible to measure pH and potentials in a simulation using the work function as potential scale and a variable number of protons in the simulation cell. By doing so it has been

observed that changing the pH at a fixed driving force can cause water to reorient at the interface.[86] Electrochemical reactions including charge transfer across the water-metal interface and its dependence on the interfacial water structure can now be calculated with *ab initio* models. Such studies have started to appear within the last decade.[85,95] It still largely remains to be shown how well these methods reproduce experimental results. Another chapter in DFT calculations of metal water interfaces is combining surface models with continuum dielectric theory, in the form of Poisson-Boltzmann theory. Using such an approach, Jinnouchi and Anderson[100] were able to accurately compute the potential of zero charge of the water-platinum electrode. Combination with dielectric continuum models promises some remedy to the problem of limited system sizes in DFT.

While most *ab initio* calculations of liquid water near extended metal interfaces are fairly recent, there is a long history of studies using classical molecular dynamics simulations based on empirical force fields. These studies typically use static electronic structure calculations to parameterize intermolecular potentials and are able to handle systems of 10^4 to 10^5 molecules and trajectories of 10-100 ns. While many intermolecular potentials for water exist, only a few different potentials for the water-metal interface are routinely used.[88,103] These potentials usually recover the single molecule binding energies and diffusion barriers with good accuracy.[88,104] However, they are mostly unable to reproduce the complex ground state structures of single monolayers, unlike *ab initio* models which accurately describe both water-water and water-metal interactions.[67,105] Moreover, most classical models are also not flexible enough to easily incorporate bond breaking and charge transfer, though there has been success in adapting Empirical Valence Bond models[106,107] to describe the dynamics of excess protons near the water-metal interface through multi-state approaches.[108,109,110,111,112] The utility of a force-field based approach is that collective effects from the correlated dynamics of many molecules can be sampled and subsequently thermodynamic properties can be computed with reasonable assurance as to their statistical convergence. This has enabled studies of water orientational dynamics[108,113,114], ionic adsorption[112,115,116] and solvation[67,117,118] within and near the interface. These studies have been largely limited to defect-free low

index fcc surfaces due to the complexity of the interactions at defect sites. Further, they have also been largely constrained to instances where dissociative adsorption does not occur.

The relevance of these studies for a better understanding of electrochemical reactions has been increased by methods that sample a constant electric potential ensemble and combine that with rare event methods.[119] One of the most versatile methods for sampling a classical constant potential ensemble was developed by Seipmann and Sprik[105] for studying interactions between water adlayers with an STM tip and was adapted to electrochemical cell calculations by Madden and coworkers.[120] In this treatment the charge distribution on each electrode changes dynamically, subject to a constraint of a fixed electrostatic potential. Using the Johnson-Nyquist equation that relates charge fluctuations on an electrode to its electrochemical response allows for the facile calculation of the capacitance of the cell[121,122]. These calculations are capable of recovering known capacitances and potential drops across the interface and have also provided a useful means for testing fundamental assumptions about the mechanisms, driving forces and timescales of electron transfer and liquid reorganization.[123,124] Specifically, by computing vertical energy gaps for standard redox couples at various distances from the electrode, Willard *et al*. have shown that energy gaps are Gaussian as expected from Marcus theory, and that the reorganization energy includes terms from the solvent dielectric as well as unscreened image charges on the electrode.[125] Limmer *et al*. have found that constraints on strongly adsorbed interfacial water can result in a hierarchy of timescales of solvent motion, ranging from the ps relaxation times of bulk density fluctuations to 10-100 ns for dipolar fluctuations of water within the adlayer.[67] These fluctuations are important to the chemistry at metal/solution interfaces, as slow polarization fluctuations within the solvent couple to charge reorganization; simulation approaches that are not able to reach these relaxation times lead to results that are difficult to interpret.

There are a number of efforts to combine the accuracy provided by *ab initio* methods in describing water-metal interfaces, including bond formation and breaking as well as charge transfer, with the computational tractability afforded by classical molecular dynamics, in particular their ability to describe long range correlations and slow dynamical processes. Recently Golze *et al*. have implemented a method

for hybrid quantum mechanics/molecular mechanics simulations of adsorbate-metal systems.[108] This method provides a density functional theory treatment of liquid water, combined with an empirical force model for the water-platinum interaction that includes polarization fluctuations on the metal with the correct constant potential ensemble. This method mitigates the complexity associated with the electronic structure of the metal, while allowing for bond-breaking within the liquid, though still faces the same difficulty in describing water-metal interactions appropriately as other empirical models. Voth and co-workers have employed force matching to parameterize reactive models of water that include excess protons and hydroxide, which could be used together with generalized water-metal potentials to study dissociative adsorption.[126] An attractive avenue for further pursuit is to generate potentials using neural networks[127] or other machine learning approaches [128] or many-body expansions[129] which offer a higher degree of flexibility over standard force field approaches and could be used to parameterize molecular forces fields for a description of water-metal interactions with higher level electronic structure theory than used previously. These mixed quantum classical calculations may offer the potential to advance the modeling of water-metal interfaces in the short term, while full *ab initio* descriptions for now are confined to limited system size.

Paper VI

Towards first principles modeling of electrochemical electrode–electrolyte interfaces

Malte Nielsen, Mårten E. Björketun, Martin H. Hansen, Jan Rossmeisl

Surface Science 631 (2015) 2–7

Surface Science 631 (2015) 2–7

Contents lists available at ScienceDirect

Surface Science

journal homepage: www.elsevier.com/locate/susc

Towards first principles modeling of electrochemical electrode–electrolyte interfaces

Malte Nielsen, Mårten E. Björketun, Martin H. Hansen, Jan Rossmeisl *

Center for Atomic-scale Materials Design, Department of Physics, Technical University of Denmark, DK-2800 Kgs. Lyngby, Denmark

ARTICLE INFO

Available online 17 August 2014

Keywords:
Atomic scale modeling
Electrochemical interface
Density functional theory

ABSTRACT

We present a mini-perspective on the development of first principles modeling of electrochemical interfaces. We show that none of the existing methods deal with all the thermodynamic constraints that the electrochemical environment imposes on the structure of the interface. We present two directions forward to make the description more realistic and correct.

1. Introduction

Electrocatalysis has many potential applications that can revolutionize energy conversion and storage. However, the best catalysts are made from rare and expensive metals of which only a few tons are mined and produced per year [1]. The global power consumption is measured in TW and this combined with a very small annual production of, e.g., Pt, Ru and Ir represents the largest challenge for electrocatalysis. The activity of each metal atom has to be increased with at least an order of magnitude compared to today's technologies. This calls for atomic scale insight into the processes and reactions taking place at the electrocatalyst surface and within the electrochemical interface. To put it differently, for electrocatalysis to play a role on the global scale, atomic scale insight is needed.

Electrochemical measurements on electrocatalysts are normally done at a macroscopic level, measuring, e.g., current versus voltage, and offer no direct information about the atomic-scale properties of the interface. Measurements revealing the atomic structure, such as STM, cannot easily be performed in aqueous electrolytes, and even if performed will not reveal the water structure.

First principles simulations seem well suited to provide the required fundamental understanding of the structure of the electrochemical interface. However, as the title of this paper—taken from an ACS symposium in New Orleans in 2013 where three back-to-back talks had similar titles [2]—indicates, first principles modeling of the electrochemical interface is far from trivial. Actually, we will argue that the electrochemical solid–liquid interface represents one of the frontiers in first principles modeling.

So far, simulated interfaces have differed significantly from real catalysts, and it is of great importance to bridge the gap between the model systems used in computer simulations and true catalysts, exposed to realistic operating conditions. Resolving this issue is not just a matter of adding more atoms to the simulations in order to make the molecular model more realistic; it is actually a fundamental challenge.

Normally, calculations are carried out with a fixed charge and number of atoms, while experiments are performed at constant electrochemical potential. This may seem as a small problem—it is still possible to set up an atomic structure and minimize the energy or perform dynamics. Simulations of this type may provide some insight related to, e.g., water on metal surfaces, but they do not necessarily describe the electrochemical interface [3].

The real electrochemical interface and reactions taking place across it are very complicated and hence challenging to model. There is a potential difference between the two electrodes, a chemical potential of protons (or other charge carriers) and counter-ions in solution, and, importantly, the electrochemical reactions occur at fixed electrochemical potentials. This means that the electrochemical system is an open system with a source of electrons, at a constant potential, for cathode reactions and a sink of electrons, at a constant potential, for anode reactions. It is therefore crucial to include the potential in the simulations.

It must be clear from the above discussion that the energy directly obtained from a first principles calculation is not representative of the system at constant chemical potential, and this is the biggest challenge when trying to bridge between simulations and experiments. For example, consider a proton that is transferred across an electrochemical interface. The reaction energy will be proportional to the difference in potential between the electrolyte and the electrode surface. In the real system, this potential difference will be proportional to the potential difference between the working electrode and a reference electrode. In atomic scale simulations, where the potential relative to a reference electrode is not controlled, the reaction energy is proportional to the dipole of the interface. This difference is dependent on, among other things, the electrode material as the work function differs between different materials. In the real system, on the other hand, the work function will be determined by the potential relative to the reference

* Corresponding author.
E-mail address: jross@fysik.dtu.dk (J. Rossmeisl).

http://dx.doi.org/10.1016/j.susc.2014.08.018
0039-6028/

electrode and is thus material independent. This means that simulations of reactions involving charged ions are qualitatively wrong if the electrochemical potential is not controlled.

Furthermore, the forces that are used to move the atoms in simulations will not keep the chemical potential constant. By applying the energy and forces from constant charge simulations, generally the chemical potentials are changed during an atomic step. This means that the effective electrode potential and pH may change during a simulation.

In principle, what is needed is a method that feeds the operating conditions—such as pH and potential—into a model simulation and then extracts from the simulation the relevant structure of the atoms at the interface, the charge on the slab and the number of, e.g., protons. This would allow theoretical investigations to answer questions about the interface that are very hard to answer by experimental methods, such as Is the water on the electrode surface ice-like or fluid-like? How is this structure affected by potential, pH, ions and material? However, no such computational method exists today.

In this paper, we give a perspective on first principles modeling of electrochemical interfaces; we discuss the state of the art and propose directions towards more realistic first principles modeling. In Section 2, we start out by introducing two fundamentally different strategies for dealing with pH and electrode potential. This includes a brief discussion of some recent and past works in the field. Section 3 goes into further detail on how to model the interface at a given potential and how to extract potential dependent information. In Section 4, we then analyze recent attempts to include the effect of pH. Finally, in Section 5, we discuss a desired future path and developments needed to improve the methodology in this field.

2. Strategies

As we see it, there are two possible strategies for obtaining the structure of the interface at constant chemical potentials. Strategy I is the dream scenario, a method that keeps the chemical potentials constant during structural optimization or during dynamic simulations. Strategy II is to first perform normal constant-charge simulations and then afterwards "measure" potential and pH of the obtained interface structure. The two strategies are illustrated in Fig. 1, where the upper arrow represents the measuring approach (strategy II) and the lower arrow is the dream method (strategy I), which is still to be developed.

2.1. Strategy I

Let us start out by considering the type of calculations represented by the lower arrow. Here the big challenge is to find a correct and still practical way of performing grand canonical modeling of the electrochemical interface. Density functional theory (DFT) has proven a useful and efficient research tool in many areas of materials science, e.g., for heterogeneous catalysis, but has mostly been carried out for a constant number of particles, i.e., microcanonically. N. David Mermin formulated grand canonical DFT already back in 1964 [4], but difficulties in the implementation prevented widespread use of the theory for a long time. During the last decades, considerable progress has, however, been made and the grand canonical strategy has been applied to a number of systems, albeit none of the current methods is fully compatible with the constraints of electrochemical interfaces.

One of the first successful attempts to implement grand canonical DFT for electrodes was proposed by Lozovoi et al. [5]. What was proposed was a way to treat the electrons grand canonically, thus keeping the chemical potential of the electrons fixed. They introduced a slab and then controlled the chemical potential of the electrons by charging the slab and adding a counter-charge of some shape. This helps keep the cell charge neutral, a requirement in periodic DFT simulations. More recently, a scheme for conducting first principles molecular dynamics simulations at constant electrode potential has been developed [6]. A fictitious force drives the system towards a preset electron chemical potential by allowing exchange of charge between the system and an external potentiostat. In the above methods, electrons are dealt with grand canonically, but real electrochemical systems are open also with respect to protons, something they do not account for.

In addition, it is possible to introduce a constant bias in a simulation via non-equilibrium Greens functions [7]. Accordingly, two different leads can have different Fermi-levels. This is important for calculating electronic conductivity through single-molecule contacts [7]. However, this approach is also difficult to extend to a thermodynamically correct treatment of protons.

2.2. Strategy II

In contrast to Strategy I, a significant amount of work has been done along the lines of Strategy II, starting from a given atomic structure and then calculating (measuring) the electrode potential and other macroscopic variables. As a measure of the absolute electrode potential, one normally uses the work function of the electrons [8]. The main idea in most of these works is to vary the dipole of the interface and measure the corresponding change in the electron work function, where a change in work function corresponds to a change in electrode potential. In contrast to Strategy I, this approach is directly targeted towards electrochemical interfaces; it will probably not be useful as a general scheme for grand canonical simulations.

In Section 3, we will first see how calculate-and-measure (Strategy II) methods can be used to extract information about the interface and reactions taking place across it, at a given electrode potential. In Section 4, we will then see how these methods can be extended to account for pH effects.

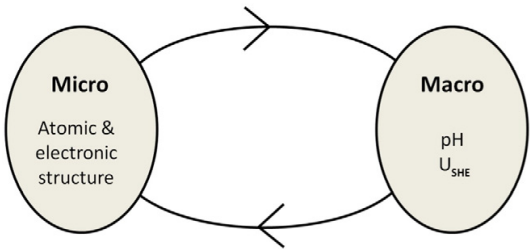

Fig. 1. Illustration of the connection between micro variables (charge, number of protons, structure) and macro variables (pH, potential). Ideally, the macro variables would control the micro (lower arrow), as is the case in real open systems (Strategy I). In strategy II the micro variables control the macro (upper arrow).

3. Extrapolation to constant potential

Once the interface energy has been calculated, it can be plotted against the work function. Having investigated multiple interface structures, spanning a range of potentials, one can thus construct a phase diagram by identifying the structure with the lowest energy at a given potential (see Fig. 2). Since the interface dipole changes locally during a charge transfer reaction, reaction energies for, for instance, a proton transfer process cannot be evaluated from a single barrier calculation, at least not if the simulation cell is small. However, as suggested by Fig. 2, given a set of structures with varying interface dipole, it is possible to estimate the reaction energy and reaction barrier at constant work function, and thereby constant electrode potential, by first constructing separate energy vs. work function curves for initial, transition and final states [9,10].

An alternative, but similar, approach to barrier calculations is to employ increasingly larger simulation cells and then extrapolate the result to the limit of infinite area. If the interface is assumed to behave as a

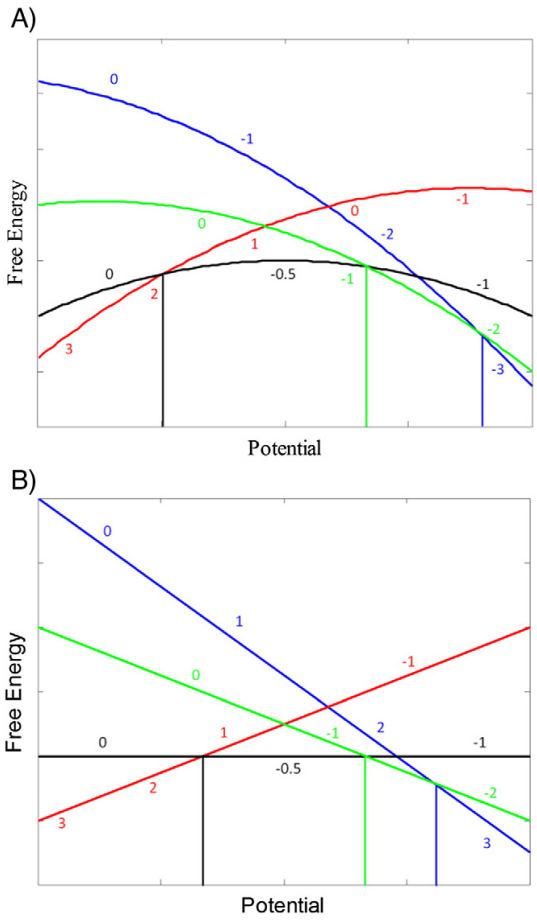

Fig. 2. Schematic plots showing the main idea behind strategy II. (A) Free energies obtained from constant charge calculations (the charge is indicated with numbers) for different states of the interface, plotted against the measured work function. The colors in the figure can either indicate different structures, coverages or transitions states. The relative energy between different states can be directly seen. (B) The same as panel A, but with a constant curvature removed from the free energy vs. potential functions.

perfect capacitor, a very limited number of calculations are needed [11]. This is a very promising way of dealing with the finite size problem. An appealing feature related to this approach is that the interface as a whole is charge neutral and that the counter-ions naturally are protons. Imagine that a proton is moved from the water layer to the electrode surface where it recombines with an electron. This reaction will obviously change the dipole of the interface and hence the absolute electrode potential. The bigger the area of the supercell, the smaller the change in dipole along the reaction path and in the limit of a simulation cell with infinite area the problem with varying dipole approaches zero. In fact, the varying dipole along charge transfer reaction path is a consequence of the simulations being performed at constant charge; however, it is not itself the entire problem. The whole structure and the driving force for the reaction are also determined by pH and potential.

In terms of how the interface dipole is varied, the above methods fall into three main categories, differing primarily in the description of the counter-charge compensating electrons added to the slab. The first type uses a homogenous background charge [12,13], the second introduces explicit protons in the electrolyte [14,15] and the third uses a compensating plane of charge [16]. In addition, there are a few examples of more elaborate descriptions of the distribution of the counter-charge and of the electrolyte in general [17–19]. In the following, we are going to expand a bit on the first two categories.

In an article by Filhol et al. [12], the authors use a method very similar to the method of Lozovoi et al. to predict the structure of water, OH^- and H_3O^+ on a metal surface. Their method relies on charging the surface of a slab and adding counter-charge homogeneously distributed across the system, to control the chemical potential of the electrons. The surface charge and counter-charge set up a field, and the water in the calculation reacts to this field and can change position and direction.

Another way of dealing with the counter-charge is to introduce protons in the electrolyte, e.g., in the water layer just outside the slab. One application of this approach is found in Ref. [11] where the authors calculate activation barriers for formation of hydrogen on a metal surface. It is of course impossible to add partial protons to the system and that creates problems when finite cell sizes are used in the calculation. In Ref. [11] the finite size problem is overcome by using cells of different size and extrapolating to the limit of infinite surface area as mentioned previously.

Strategy II approaches discussed so far all assume a one-to-one mapping between energy and electron work function, which is not generally true. If the water arrangement is changed this could affect the dipole of the interface, but not necessarily the energy of the system. This means that for the one-to-one mapping to hold, the above simulations have to be performed with a more or less constant water structure. Otherwise, one cannot expect the interface to behave as a capacitor or the interface energy to be a simple function of the work function. It also means that one is given a freedom in the choice of water structure when doing the simulations. In reality, the structure of the interface has to be completely determined by the electrochemical conditions so this freedom is artificial.

The artificial degree of freedom turns out to be related to the pH. The approaches described above assure constant chemical potential for electrons, but not necessarily constant pH. Hence, one cannot easily compare the structures even if they correspond to the same chemical potential of the electrons. Accounting for the effect of pH constitutes next level of sophistication in the calculate-and-measure type methods. In next section, we will discuss some recent attempts to include pH in electrochemical interface models.

4. Extrapolation to constant pH

4.1. Capacitor model

We first look at an extension of the third method—where the counter-charge is collected in a plane and placed some distance from the surface, essentially setting up a capacitor—to account for pH. An example of this method is presented in an article by Bonnet et al. [20]. In this article, the whole water layer is modeled by a continuous capacitor model, which means there are no explicit water molecules in the calculation. The capacitor model allows for including part of the effect of pH. A change in pH will also change the field across the double layer. The field will interact with surface species that have a dipole perpendicular to the surface, and therefore the adsorption energies become dependent on pH. A wide range of reaction intermediates do not have a significant dipole so for these the effect of pH is small. To align potential and field, the potential of zero field or zero charge is needed. This is experimental input, as are the capacitance and the work function of the standard hydrogen electrode. This scheme thus takes into account the interaction energy between the surface and the field, but not the energy related to the change in electrolyte structure needed to setup the field.

The Bonnet approach is related to a method from 2004 [21], where only the electrochemical potential of protons plus electrons was considered. The effect of the field was also estimated, but without having the

correct reference for the potential of zero field [22]. However, the 2004 method only considers the surface and not the interface as such, so even if it was very useful and computationally cheap it is out of the scope of this paper.

4.2. Thermodynamic approach

If we are to fully understand the effect of pH on the systems, we need to go beyond the method introduced in 2004 [21] and separate the chemical potentials of electrons and protons. To understand why, it is instructive to review the Born–Haber cycle for hydrogen oxidation. Fig. 3A shows a schematic figure of this cycle and Fig. 3B gives a physical interpretation of the various components.

The main point is that the change in energy for going from ½ $H_{2(g)}$ to H^+(solution) + e^- (electrode) is independent of whether we choose a clockwise or anticlockwise route through the Born–Haber cycle. Clockwise, the hydrogen is dissociated and ionized in vacuum, and the resulting proton is moved from rest in vacuum, through a water surface, to the bulk of the solution. The energy change associated with the last step is equivalent to the negative of a proton work function, $-\phi_{H+}$. The same is done for the electron; it is moved through the electrochemical interface to the Fermi level of the electrode. The energy of this step is the negative of the work function of the electron, $-\phi_{e-}$, and proportional to the absolute potential of the electrode. The chemical potential for protons and electrons combined is $\mu(H^+ + e^-)$, which is the potential vs. the reversible hydrogen electrode, RHE ($U_{RHE} = 0$ when $H^+ + e^- \leftarrow\rightarrow$ ½ H_2 is in equilibrium at room temperature and $p_{H2} = 1$ bar), and the free energy compared to hydrogen in the gas phase (see Fig. 3B).

Since the dissociation energy, $\Delta_d G$, and the ionization energy, $\Delta_i G$, are constant no matter the electrochemical environment, there are three interdependent variables—$\mu(H^+ + e^-)$, ϕ_{H+} and ϕ_{e-}. However, as $\mu(H^+ + e^-)$ has to be the same no matter the route there are only two independent variables. Thus, if two of the three variables are controlled, the last variable is also defined.

In most experiments, the pH is constant and the potential is varied. In this mode, $\mu(H^+ + e^-)$ and ϕ_{e-} are the same, just shifted by a constant. This constant is given by $\Delta_d G$, $\Delta_i G$ and ϕ_{H+}, where only ϕ_{H+} is related to the electrochemical environment. The constant is difficult to calculate, but it has been determined experimentally. At room temperature, pH = 0, $p_{H2} = 1$ bar and $\mu(H^+ + e^-) = 0$ eV, it has been measured to be ~4.44 eV [8]. This is the work function for the standard hydrogen electrode, ϕ_{e-}^{SHE}, and it is the constant that connects $\mu(H^+ + e^-)$ and ϕ_{e-} given that ϕ_{H+} is measured at pH = 0. If pH is finite, the constant is changed by ϕ_{e-}^{SHE} + 0.059 eV/pH. The work function of the proton gets larger as pH is increased because the protons are more stable at high pH due to higher configurational entropy.

It is important to note that, thus far, nothing has been assumed. All relations are direct consequences of the Born–Haber cycle, and they can be used as a starting point for simulations of the electrochemical interface, thus putting the modeling on a firm foundation. Let us first ignore all ions in the electrolyte except for the protons. We assume that the protons at the interface have the same chemical potential as protons in the bulk electrolyte, which means that the work function for a proton moved from rest in vacuum to the interface should be the same as ϕ_{H+} for a proton in the solution.

As noted above, Fig. 3 reveals that the chemical potential (work function) of the electrons is only one of three variables. When only considering this single variable, there is no way of controlling the other two, namely, the work function of protons in the electrolyte and the combined electrochemical potential of protons and electrons. Consequently, in most methods (those that only control the electron work function), $\mu(H^+ + e^-)$ and ϕ_{H+} could in principle change during a simulation. This is clearly far from an ideal situation as the experiments we try to compare with are typically done at constant pH, i.e., constant ϕ_{H+}. Nevertheless, some of these studies may still be physically relevant since ϕ_{H+} might be fortuitously kept almost constant as a result of the water structure being kept almost fixed. However, if we manage to control both $\mu(H^+ + e^-)$ and ϕ_{e^-} at the same time, the chemical potential of the protons, which in turn gives us the pH, will also be controlled.

The ideal solution would obviously be to impose constant pH and potential on the simulations, i.e., to go from right to left in Fig. 1. Currently, there is no method for doing this. It is possible to do it for electrons (potential) only since it is easy to introduce fractions of a charge in a simulation so that the charge can be varied continuously, but it is not possible to do it in the same direct manner for protons. However, the number of protons per electrode surface area can be varied more or less continuously by performing simulations on supercells of different sizes describing the same situation. If the water is periodically well structured, this could be an interesting way to pursue.

On the other hand, a method for mapping from left to right in Fig. 1, measuring both pH and potential of a given interface structure, has recently been developed [23]. The idea is to calculate the relative energy of a given structure as a function of the number of hydrogen atoms, ϕ_{e^-} and $\mu(H^+ + e^-)$. ϕ_{e^-} can be calculated directly with the DFT code, and the relative energy of two structures, A and B, with the same number of atoms and electrons and with the same work function is calculated according to the following equation: $\Delta G / N = (G(A) - G(B)) / N$. We divide by the number of surface atoms, N, to get the relative energy normalized to electrode area. The challenge is to compare structures that do not have the same charge or number of atoms. In this case, the simulations are carried out on different structures with different number of hydrogen atoms added/removed to/from the water. Addition will result in hydrogen adsorbed on surface or in H^+(water) + e^-(electrode), and removal will result in HO, O adsorbed on the electrode surface or in HO^-(water)-e^-(electrode). If ϕ_{e^-} and the number of hydrogen atoms are the same in two simulations, then, as before, the energies are

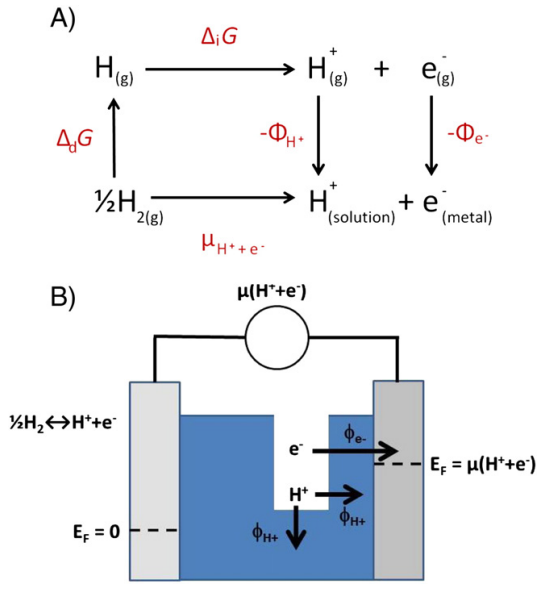

Fig. 3. (A) The Born–Haber cycle for hydrogen insertion into an electrochemical interface. (B) Schematic figure of an electrochemical cell, showing the different energy variables. The left-hand side electrode is a reference electrode, and the right-hand side is the working electrode.

directly comparable. The energy of the interface will depend on what chemical potential the hydrogen added to the interface comes from. For a single structure, this energy is given by

$$G_{\mathrm{Int}} = (G(n,N) - G(0,N))/N - n\mu\left(H^+ + e^-\right)/N \quad (1)$$

For any simulation, G_{int} can be calculated and plotted vs. ϕ_{e^-}. As seen in Eq. (1), G_{int} is also a linear function of $\mu(H^+ + e^-)$ and the slope is n/N, which is the coverage of hydrogen atoms that have been added to the interface relative to the reference structure $G(0,N)$. This means that when simulations have been performed on a set of systems, G_{int} can be presented as a function of $\mu(H^+ + e^-)$ and ϕ_{e^-} (see Fig. 4A). In order to establish the pH-potential phase-diagram (Pourbaix diagram), one has to first map G_{int} on constant-pH planes for a range of pHs. pH is constant as long $\Delta\Phi_{e^-} = \Delta\mu(H^+ + e^-)$, so vertical planes (gray plane in Fig. 4A) that fulfill this represents constant pH. Generating the Pourbaix diagram then becomes a matter of picking out the lowest-energy intercepts of G_{int} with the various constant pH planes (Fig. 4B).

5. Future developments

5.1. Structural optimization at constant work function

What is described above provides a method for analyzing data, but not a scheme to systematically search for relevant structures. In first principles calculations, the lowest energy structure is normally found by moving the atoms according to the Hellman–Feynman forces. However, in general, the ionic minimization will change ϕ_{e^-}, which in our case means that the system's (G_{int}'s) position along the ϕ_{e^-} axis will change. Furthermore, the number of hydrogen atoms will be constant. Thus, one has to search for structures that minimize G_{int} with respect to the ionic structure without changing ϕ_{e^-}.

So far, the best of the interface methods assume some structure or attribute of the water layer and then calculates the corresponding operating conditions (going from left to right in Fig. 1). While this is fine for benchmarking and comparing to experiment, the information obtained by being able to go the other way (right to left) would be much more valuable. In that case, it would be possible to choose the operating conditions of an experiment and on the basis of calculations directly predict the atomic structure, potentially radically expanding our understanding of the electrochemical interface. This type of search would require methods of grand canonical DFT, which means keeping fixed electrochemical potential and pH during a calculation and is a challenge yet to overcome.

Somehow the structures should be relaxed under the constraint that the electron work function stays constant, while controlling $\mu(H^+ + e^-)$. This is different from the approach by Lozovoi et al. [5] where the chemical potential of electrons is constant; however, $\mu(H^+ + e^-)$ is not controlled. The chemical potential is held constant by adding electrons to the calculation, which complicates controlling $\mu(H^+ + e^-)$. If protons and electrons are not added to the simulations together, it is difficult to control $\mu(H^+ + e^-)$. We suggest developing a method to relax structures with constant electron work function and charge, where only the ionic and electronic structures are allowed to relax.

One could think of different ways of accomplishing this. However, the most straightforward solution would probably be to measure the electron work function after each ionic relaxation step and add a penalty in terms of a field acting back on the structure for deviations from the preset (target) work function, similar to the approach in [6]. This will require a second self-consistency loop, where the work function is calculated and compared with the preset value, the corresponding field is

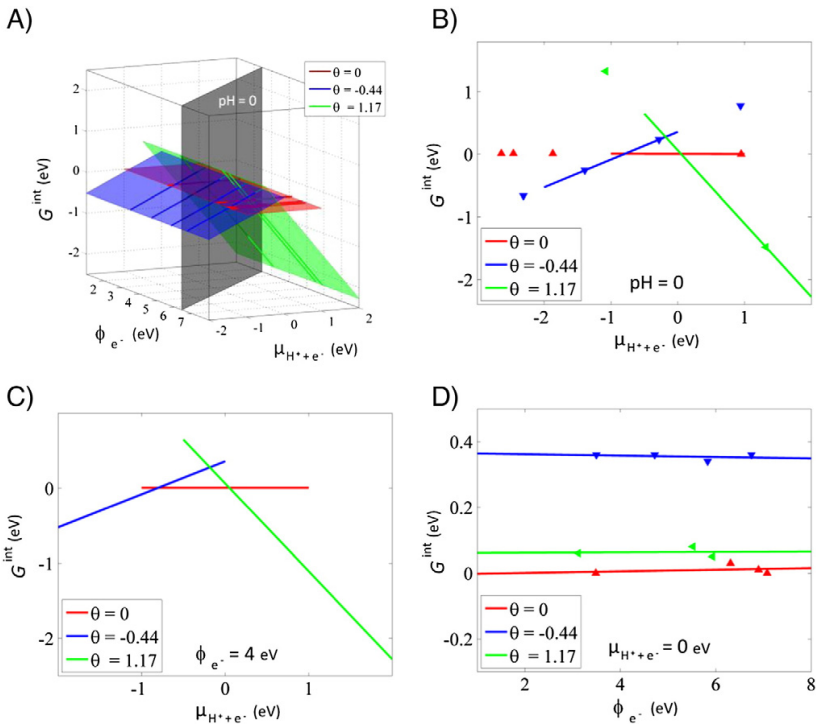

Fig. 4. Plot of the interface free energy for three different structures of water with varying amount of hydrogen: (A) in 3D, (B) projected onto the pH = 0 plane, (C) projected onto the f_{e^-} = 4 eV plane and (D) projected onto the $\mu(H^+ + e^-) = 0$ eV plane.

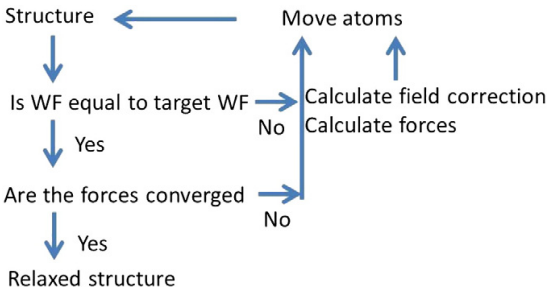

Fig. 5. The proposed scheme for performing calculations at constant work function. The check of the work function occurs before the force convergence. This ensures that if a non-relaxed structure with the target work function is found, it will subject to further relaxation. This scheme has some flexibility in how the field correction due to non-target work function is calculated. This correction is however not part of the converged result.

calculated and added to the Hellman–Feynman forces, and the atoms are moved according to the new forces, see Fig. 5. The water has a very high number of local minima structures and if supercell is large the lowest energy structure for most work functions is such a minimum. In that case (most cases), the field will not be present when the desired (target) work function is reached and hence not interfere in an artificial manner with the end result.

In order to avoid unwanted metal–field interactions where we end up charging the surface of the metal, the application of the penalty field could be limited to only the electrolyte part of the structure.

The main challenge is that the water structures will have a zoo of local minima structures, and relaxation with the above scheme will just bring the structure to the closest minimum. Therefore, the scheme has to be combined with a method for searching the different structures. This could be an algorithm for perturbing the interface structure and accepting the change if it brings the work function closer to the target value. The scheme could then minimize the energy and/or be combined with a genetic algorithm where the dipole orientation of the water is a fitness criterion.

5.2. Including ions

So far, all ions except protons (or OH^-) have been ignored. We have thus implicitly assumed that those ions do not interact with the interface. This is generally not the case in a liquid electrolyte. In principle, the ions should therefore be included in the same manner as hydrogen atoms. This amounts to calculating G_{int} (Gibbs adsorption isotherm) for different amounts of neutral molecules of the ions in the simulations (e.g. Cl if the anion is Cl^-), according to the following equation:

$$G_{\mathrm{Int}} = (G(n,x,N) - G(0,N))/N - n\mu\left(H^+ + e^-\right)/N - x\mu(Cl^- - e^-)/N, \quad (2)$$

where x is the number of Cl atoms added to the interface. In experiments, the anions do not represent another degree of freedom. Given a specific acid of a specific concentration, the activities of the anions and the protons are both defined and mutually dependent. In the simulations, however, the anions introduce yet another parameter that has to be varied. In this case, Fig. 4A becomes a four dimensional figure with $\mu(Cl^- - e^-)$ being the fourth axis.

For a solid–solid interface, the analysis is a bit easier as the counter-ions are immobile, which means that one to a good approximation can use the bulk concentration of counter-ions in the interface region as well (micro canonical). In the liquid electrolyte where the system is open for exchanging counter-ions with the bulk the chemical potential of these ions should match the pH.

6. Conclusions

The fact that electrochemical systems are open systems, where the reaction free energy for any reaction is determined by chemical potentials, implies that thermodynamic driving forces obtained directly (without correction) from normal first principles simulations, with fixed number of electrons, can be qualitatively wrong. Different approaches to tackle this issue have started to appear, but none of them include all the thermodynamic constraints imposed on the interface structure by the electrochemical environment. In this mini-perspective, the thermodynamics has been analyzed, and we have suggested a methodology for simulating the electrochemical interface including potential, pH and counter-ions. Furthermore, we have outlined a scheme for optimizing interface structures at constant work function without varying the charge. In the future, such a methodology would enable us to study the atomic-scale nature of electrochemical interfaces.

Acknowledgments

We want to acknowledge Michiel Sprik for useful discussions. The Catalysis for Sustainable Energy (CASE) initiative and the Danish Council for Strategic Research via the NACORR project nr. 12-132695 are acknowledged for funding.

References

[1] P.C.K. Vesborg, T.F. Jaramillo, R. Soc. Chem. Adv. 2 (2012) 7933.
[2] "Theory and Simulation in Energy and Fuel Production and Utilization" at the 245th ACS National Meeting, 2013.
[3] S. Schnur, A. Gross, New J. Phys. 11 (2009) 125003.
[4] N.D. Mermin, Phys. Rev. 137 (1965) A1441.
[5] A.Y. Lozovoi, A. Alavi, J. Kohanoff, R.M. Lynden-Bell, J. Chem. Phys. 115 (2001) 1661.
[6] N. Bonnet, T. Morishita, O. Sugino, M. Otani, Phys. Rev. Lett. 109 (2012) 266101.
[7] M. Brandbyge, J.-L. Mozos, P. Ordejón, J. Taylor, K. Stokbro, Phys. Rev. B 65 (2002) 165401.
[8] S. Trasatti, Pure Appl. Chem. 58 (1986) 955.
[9] C. Taylor, R.G. Kelly, M. Neurock, J. Electrochem. Soc. 154 (2007) F55.
[10] S.A. Wasileski, M.J. Janik, Phys. Chem. Chem. Phys. 10 (2008) 3613.
[11] J. Rossmeisl, E. Skúlason, M.E. Björketun, V. Tripkovic, J.K. Nørskov, Chem. Phys. Lett. 466 (2008) 68.
[12] J.-S. Filhol, M. Neurock, Angew. Chem. Int. Ed. 45 (2006) 402.
[13] C.D. Taylor, S.A. Wasileski, J.-S. Filhol, M. Neurock, Phys. Rev. B 73 (2006) 165402.
[14] E. Skúlason, G.S. Karlberg, J. Rossmeisl, T. Bligaard, J. Greeley, H. Jónsson, J.K. Nørskov, Phys. Chem. Chem. Phys. 9 (2007) 3241.
[15] E. Skúlason, V. Tripkovic, M.E. Björketun, S. Gudmundsdóttir, G.S. Karlberg, J. Rossmeisl, T. Bligaard, H. Jónsson, J.K. Nørskov, J. Phys. Chem. C 114 (2010) 18182.
[16] M. Otani, O. Sugino, Phys. Rev. B 73 (2006) 115407.
[17] R. Jinnouchi, A.B. Anderson, Phys. Rev. B 77 (2008) 245417.
[18] I. Hamada, O. Sugino, N. Bonnet, M. Otani, Phys. Rev. B 88 (2013) 155427.
[19] K. Letchworth-Weaver, T.A. Arias, Phys. Rev. B 86 (2012) 075140.
[20] N. Bonnet, N. Marzari, Phys. Rev. Lett. 110 (2013) 086104.
[21] J.K. Nørskov, J. Rossmeisl, A. Logadottir, L. Lindqvist, J.R. Kitchin, T. Bligaard, H. Jónsson, J. Phys. Chem. B 108 (2004) 17886.
[22] J. Rossmeisl, J.K. Nørskov, C.D. Taylor, M.J. Janik, M. Neurock, J. Phys. Chem. B 110 (2006) 21833.
[23] J. Rossmeisl, K. Chan, R. Ahmed, V. Tripkovic, M.E. Björketun, Phys. Chem. Chem. Phys. 15 (2013) 10321.

Paper VII

Finite Bias Calculations to Model Interface Dipoles in Electrochemical Cells at the Atomic Scale

Martin Hangaard Hansen, Chengjun Jin, Kristian S. Thygesen, Jan Rossmeisl

The Journal of Physical Chemistry C, (**2016**), Accepted.

Finite Bias Calculations to Model Interface Dipoles in Electrochemical Cells at the Atomic Scale

Martin Hangaard Hansen[a,b], Chengjun Jin[a], Kristian S. Thygesen[a], Jan Rossmeisl[b]

[a]Technical University of Denmark, Fysikvej Building 307, DK-2800 Kgs. Lyngby

[b]Department of Chemistry, University of Copenhagen, Universitetsparken 5, DK-2100 København Ø.

ABSTRACT: The structure of an electrochemical interface is not determined by any *external* electrostatic field, but rather by external chemical potentials. This paper demonstrates that the electric double layer should be understood fundamentally as an *internal* electric field set up by the atomic structure to satisfy the thermodynamic constraints imposed by the environment. This is captured by the generalized computational hydrogen electrode model, which enables us to make efficient first principles calculations of atomic scale properties of the electrochemical interface.

Introduction

Electrochemical energy storage and consumption in both the power sector and in transportation is gaining increased interest.[1-4] Batteries and fuel cells are being developed, demonstrated and applied on a growing scale[5]. Many important chemical reactions in electrochemical devices occur at the interface between electrode and electrolyte.[6,7] Understanding mechanisms for degradation and enhancement of stability is often the key to a successful electrochemical device, and so is efficient catalysis of the desired reactions. Simulating the interfaces between electrodes and electrolytes on the atomic scale has so far brought further understanding of catalytic *surfaces* and it is hoped that the same can be achieved for the *interface* between electrode and electrolyte. The possibility of doing rational design[8,9] of the electrolyte-electrode combination is of high interest and creates a demand for atomic scale modeling of the interface.

Numerous approaches[10-17] based on density functional theory (DFT) have been proposed to solve parts of the problem of calculating the atomic scale properties of the electrode/electrolyte interface. Accuracy limitations in the electronic structure calculations may be solved by a growth in available computational resources and algorithms. However, most models lack important thermodynamic constraints[18] from the electrochemical environment. These thermodynamic constraints include the pH-dependence of the work function. This is a consequence of the thermodynamic analysis[19] to solve this problem, which is revisited in the present paper. Finite bias transport calculations with non-equilibrium Greens functions[20] are then done, to include an explicit reference electrode. This is done to demonstrate that the electric double layer of the electrodes set up internal electric fields to satisfy the thermodynamic constraints from the environment. The internal dipole has previously been measured in slab calculations[13] for the same purpose. The finite bias calculations and the insight that the electric field in the double

layer is an *internal* field demonstrate that it is accurate to use the vacuum level as the reference in a slab calculation for modeling the electrochemical interface. The simple thermodynamic analysis in the *generalized computational hydrogen electrode*[19], combined with slab calculations, thus provide an efficient way to solve the problem with DFT.

Theory

To model the electrochemical interface as a microscopic system given a constant electrode potential and pH, the system should be considered in equilibrium with a reservoir of electrons and a reservoir of protons. The volume, temperature and chemical potentials are fixed, which prompts us to apply the grand canonical ensemble[21] as sketched in figure 1.

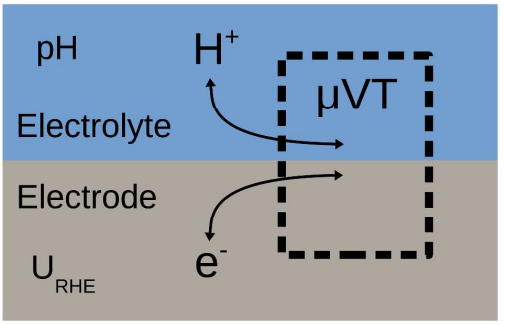

Figure 1: The electrochemical interface micro system in the grand canonical ensemble. The micro system has a fixed volume and it is in equilibrium with a reservoir at a constant chemical potential and temperature. The micro system is open to ions and electrons and the numbers of these inside the microsystem may fluctuate.

Any observable quantity, A, of the micro system can be obtained as an average over that property in all the micro states, weighted with respect to their probabilities.

$$\langle A \rangle = 1/Z \sum_i A_i * \exp(-\Delta G_i / kT)$$

where $Z = \sum_i \exp(-\Delta G_i / kT)$ is the grand partition function, the index, *i,* denote a state, and ΔG_i is the free energy of the state *i* relative to a reference state, eg. $\Delta G_i = G_i - G_{ref}$. Every state is characterized by a set of atomic positions and it has some number of protons and electrons.

To determine <A> at a given pH and electrode potential, the key is to know ΔG_i of every state as a function of pH and electrode potential. In the following it is shown how ΔG_i is calculated.

The micro system, (sketched in figure 1), is open to protons and electrons and every micro state could have any number of those particles. However the electrode and the electrolyte both conduct electrons and ions, respectively. The interface must therefore be charge neutral on the macroscopic scale. The micro system is modeled with periodic boundary conditions and must also be charge neutral. It is therefore a practical issue, when modeling, that the micro system is large enough, that total charge fluctuations can be neglected. In the present model, the system only exchanges protons and electrons in equal numbers.

$$n_{i,H^+} = n_{i,e^-} = n_i$$

where n_{i,H^+} is the number of protons, is the n_{i,e^-} number of electrons and n_i is the number of hydrogen atoms in state *i*. In the grand canonical ensemble, the relative free energy of the i^{th} state is

$$\Delta G_i = \Delta E_i + \Delta ZPE_i - T\Delta S_i - n_i(\mu_{H^+} + \mu_{e^-}) \quad (1)$$

where ΔE_i is the difference in internal energy of state *i* relative to the reference state, eg. $\Delta E_i = E_i - E_{ref}$, and $n_{ref} = 0$. ΔZPE_i, is the difference in zero-point energy, $T\Delta S_i$ is the difference in entropy and μ_{H^+} and μ_{e^-} are the chemical potentials of the proton and electron reservoirs, respectively. It does not matter to the last term in equation (1), where in the micro system, the proton and the electron are located – the references are the same reservoirs. The difference in

energy between protons and adsorbed hydrogen only enters in the first three terms of equation (1). To relate the energy of the reservoir of electrons and protons to something observable, a reference electrode is introduced. The reversible hydrogen electrode (RHE) is defined by the equilibrium $\frac{1}{2}H_2$ (g) $\leftrightarrow$ H^+ (aq) + e^- (s), where the electrons are at the Fermi level of the reference electrode, $\mu^{ref}_{e^-}$, and protons are present in the electrolyte and H_2 is present at 1 atm[22]. This means[21]

$$\mu^{ref}_{H^+} + \mu^{ref}_{e^-} = \mu_{H_2(g)} / 2 \qquad (2)$$

μ_{H^+} is assumed to be the same for the working and reference electrodes, since the both electrodes are in contact with the proton reservoir through the electrolyte, which is in equilibrium, so $\mu^{ref}_{H^+} = \mu_{H^+}$. The position of μ_{e^-} relative to $\mu^{ref}_{e^-}$ can be measured, since $-eU_{RHE} = \mu_{e^-} - \mu^{ref}_{e^-}$, where U_{RHE} is the voltage between the electrodes. Inserting this into equation (2) leads to

$$\mu_{H^+} + \mu_{e^-} = \mu_{H_2(g)}/2 - eU_{RHE}$$

The chemical potential, $\mu_{H_2(g)}$, of H_2 in the gas phase can be obtained from standard thermodynamic tables. This is inserted into (1) to get ΔG_i as a function of U_{RHE}:

$$\Delta G_i = E_i(n) - E_{ref}(n=0) + \Delta ZPE_i - T\Delta S_i - n(\mu_{H_2(g)}/2 - eU_{RHE})$$

where $E_i(n)$ is the internal energy of state i, and $E_{i=0}(n=0)$ is the internal energy of a reference state of the interface. This is the Computational Hydrogen Electrode[23,24] (CHE) scheme, where $-eU_{RHE}$ is usually written as a chemical potential relative to H_2 at standard conditions, i.e. $\mu_{H^+ + e^-} = -eU_{RHE}$.

U_{RHE} is defined at arbitrary pH, so the effect of pH cannot be separated from the effect of electrode potential in the framework of the CHE.

To understand the effect of pH on the micro system, it is therefore necessary to generalize the CHE to unfold the effects of the pH and U_{RHE}, on the ensemble of states and the free energies ΔG_i. This was done previously[19], in line with Trasatti's[25] absolute hydrogen electrode, and it is reviewed in the following.

To understand the relation between pH and $\mu_{H^+ + e^-}$, it is helpful to consider the Born-Haber cycle in figure 2 for insertion of $H^+ + e^-$ into the micro system.

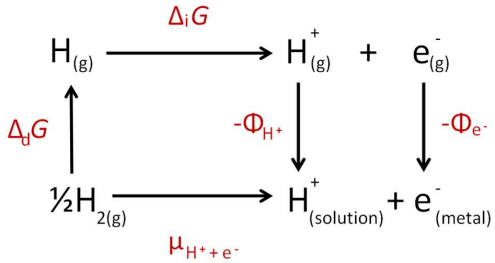

Figure 2: Born-Haber cycle for $H^+ + e^-$ insertion into the electrochemical interface (see figure 1). The H_2 molecule can either react electrochemically to $H^+ + e^-$ or it can go through dissociation, ionization in vacuum followed by insertion onto the interface. $\Delta_d G$ is the free energy of H_2 dissociation, $\Delta_d G$ is the free energy of H ionization, φ_{e^-} and φ_{H^+} is the free energy of insertion of electrons and protons respectively, into the interface.

As shown in figure 2, energy conservation implies that $\mu_{H^+ + e^-}$ equals the sum of the dissociation free energy, $\Delta_d G$, the ionization potential, $\Delta_i G$, and the free energies, φ_{e^-} and φ_{H^+}, of insertion of electrons and protons into the interface.

$$\mu_{H^+ + e^-} = \Delta_d G + \Delta_i G - \varphi_{e^-} - \varphi_{H^+} \quad (3)$$

For convenience, the vacuum level in figure 2 is chosen to be the near field vacuum level, where a charged particle is in vicinity of the infinite extended surface. This is convenient, because φ_{e^-} is then the near field work function of the working electrode, which can be obtained from a DFT calculation. The thermodynamic analysis would give the same result, if the vacuum level was the one infinitely far away in space.

The chemical potential of protons is constant throughout the equilibrated electrolyte. In a conductive medium, any electric fields are screened out at the interfaces, in water within a distance of up to around 1µm. That means there can be no difference in the near field vacuum

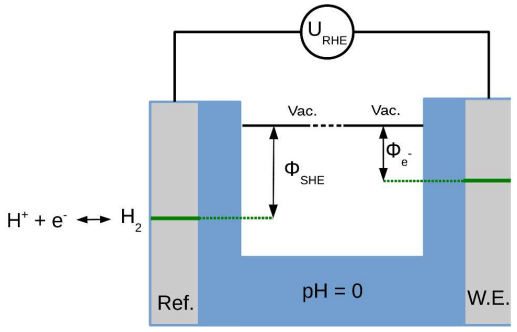

Figure 3: Sketch of an electrochemical cell with thermodynamic variables. The working electrode is shown on the right and the reference electrode is shown on the left. At pH 0, $U_{SHE} = U_{RHE}$.

level for protons (and thereby also electrons) outside the two electrodes, as shown in figure 3.

If pH = 0 and $U_{RHE} = 0$, then

$$0 = \Delta_d G + \Delta_i G - \varphi_{SHE} - \varphi^0_{H^+} \quad (4)$$

where $\varphi^0_{H^+}$ is the work function for the proton at pH = 0, and φ_{SHE} is the work function of the standard hydrogen electrode, which is between 4.44 eV and 4.85 eV according to experiments[25]. The free energy of the proton in aqueous solution is stabilized by 2.3 k T per pH unit, thus

$$\varphi_{H^+} - \varphi^0_{H^+} = 2.3\ k\ T\ pH \quad (5)$$

Adding φ_{H^+} to equation (4) gives:

$$\varphi_{H^+} = \Delta_d G + \Delta_i G - \varphi_{SHE} - \varphi^0_{H^+} + \varphi_{H^+}$$

Inserting equation (5):

$$\varphi_{H^+} = \Delta_d G + \Delta_i G - \varphi_{SHE} + 2.3\ k\ T\ pH$$

And inserting that into equation (3) gives the final result at all pH and U_{RHE}:

$$\mu_{H^+ + e^-} = \varphi_{SHE} - \varphi_{e^-} - 2.3\ k\ T\ pH \quad (8)$$

In the case of pH = 0, we have $\mu_{H^+ + e^-} = -eU_{RHE} = -eU_{SHE}$ and:

$$eU_{SHE} = \varphi_{e^-} - \varphi_{SHE}$$

If one specifies a constant pH and U_{RHE}, it is clear from equation (8) and figure 2, that a constraint is imposed on the work function of the interface. The physical consequence of this is that a variation in pH, while at a constant U_{RHE} changes φ_{e^-} and thus changes the dipole of the water in the interface layer[19]. Variation in pH manifests itself in the double layers as a variation in dipole and thereby atomic structure. The uncertainty to φ_{SHE} does not cancel out, when relating individual atomic structures to electrode potential and pH, but if trends depend only on differences in work function, then the error cancels out. One may now write up a partition function, $Z(pH, \varphi_{e^-})$, for a given pH and φ_{e^-} and the free energy of a state can be written $\Delta G_i = \Delta G^{int}(pH, \varphi_{e^-})$, following the notation from previous papers[26]. In the following, density functional theory (DFT) calculations are presented to understand the consequence which this thermodynamic analysis has on the behavior of the interface.

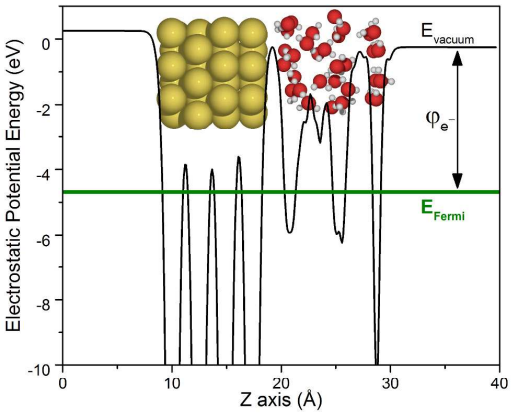

Figure 4: The electrostatic potential energy, E_H, of a metal water interface structure averaged in the XY dimension and plotted versus the position out-of plane to the surface (Z). The near field work function of the electrode, φ_{e^-}, is φ in the vacuum beyond the water layer minus the Fermi level, which is shown in green. The inset shows the atomic-scale Au(111) | water interface. Au atoms are golden colored, O atoms are red and H atoms are white.

$\Delta G^{int}(pH, \varphi_{e^-})$ may be obtained from DFT calculations for any given micro state as a function of pH and electrode potential. Any microscopic property, <A>, of the electrochemical interface, may then be calculated if all relevant states are considered. The near field work function φ_{e^-} can be obtained for a given micro state using a DFT calculation by taking the difference between the near field vacuum level and the Fermi level in a half cell configuration as shown in figure 4. This calculation has periodic boundary conditions in the plane. Non-periodic boundary conditions were used in the out-of-plane direction with a dipole correction[27].

The relative free energies, ΔG_i, of an interface structure at a known pH and U_{RHE} can then be calculated from DFT using[26]

$\Delta G^{int}(pH, \varphi_e\text{-}) = (E(n, \varphi_e\text{-}) - E(n=0)) + \Delta ZPE_i - T\Delta S_i - nG^0_{H2}/2 - n\mu_{H^+ + e^-}$

The first five terms, $(E(n, \varphi_e\text{-}) - E(n=0, \varphi_e\text{-})) + \Delta ZPE_i - T\Delta S_i - nG^0_{H2}/2$, are the relative free energies of each state at standard conditions and 0 V vs RHE.

In the following, it is shown how the net dipole of the interface is constrained by the chemical potentials of the environment.

Results & Discussion

The electrostatic potential for a full electrochemical cell under finite bias is calculated for three situations, which are explained in this section. **1)** Both electrodes are at the equilibrium potential of the standard hydrogen electrode, **2)** a bias is applied without changing the atomic structure of the interface, and **3)** the same bias is applied while the atomic structure has been changed to satisfy the constraints imposed by the external chemical potentials.

The finite bias calculation is carried out using non-equilibrium Green's functions and DFT (NEGF+DFT), implemented in the Transiesta[20,28,29] code. This type of calculations is frequently applied for nano-electronics. In NEGF-DFT calculations, the electrodes are semi-infinite, meaning the boundary conditions of the left and right side of the full cell structure are calculated from a NEGF-DFT calculation of the infinite continuation of the outermost three atomic layers, (in this case Au(111)). The bias is defined as $U = (\mu_L - \mu_R)/e$ where $\mu_{L/R}$ denotes the electronic chemical potential of the left/right electrode. These electronic chemical potentials set the boundary conditions for the electrostatic potential. Thus $U = U_{RHE}$. In the central region (the full cell structure), NEFG-DFT calculations uses Green's functions instead of wave functions. The Green's functions, $f_G(E)$, for the central region can be written

$$f_G(E) = [E\,S - H_C - \Sigma_L(E) - \Sigma_R(E)]^{-1}$$

Where E is the energy, S is the overlap and H_C is the Hamiltonian of the central region and $\Sigma_{L/R}$ are the sums of the lead self-energies. The Greens's function are converged equivalently to the usual self-consistency cycle: f_G -> n(r) -> v(r) -> H_C -> f_G. A set of slab/water structures were initially calculated with standard DFT, as shown in figure 4, with varying water orientations and varying net dipoles. The parameters and details for the DFT calculations can be found in the supplementary material. For each slab calculation, a full cell system was set up with the slab/water system as the working electrode on the right, while the left electrode was kept constant as a half cell structure with a work function of φ_{SHE} = 4.44 eV, representing the reference electrode. Atomic structures for the full cell calculations were made by interfacing the two half-cell systems including the 20Å of vacuum between the electrolyte layers as shown in figure 5, but excluding the vacuum on the backside. Let us first consider an electrochemical cell with U = 0. The planar averaged electrostatic potential is calculated as

$$\overline{E}_H(Z) = \int_{X,Y} E_H(X,Y,Z)dXdY$$

from the NEGF-DFT calculations using the Macroave code from Junquera et al.[30,31] and is shown in figure 5 together with the Hartree potentials from half-cell calculations. In system **1)** with U = 0 V, the net dipole moments in the z direction on the two electrodes are identical. Identical atomic structures to set up those identical dipole moments and the Hartree potentials plotted with each electrode are from the same half cell calculation.

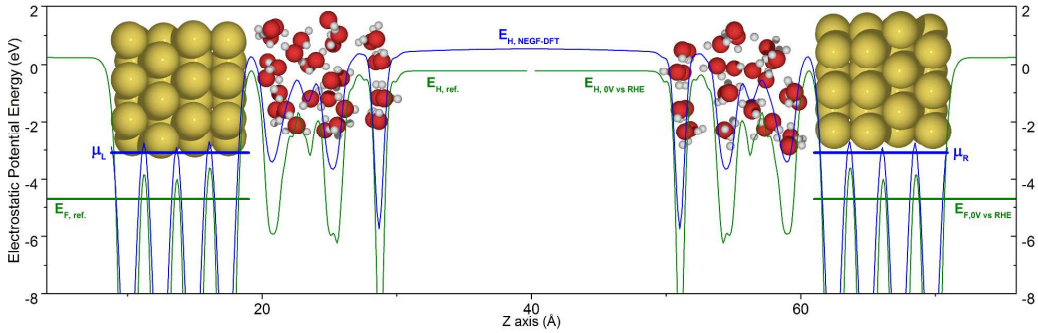

Figure 5: Situation **1)** The electrostatic potentials, E_H, of the full cell NEFG-DFT calculation (blue line), and the reference half cell calculations (green lines, left and right). The Fermi levels is shown for each electrode with a thick line. The two electrodes are the same atomic structure which has a work function of 4.44 eV. The absolute positions of the Transiesta Fermi levels are plotted with reference to the deformation potential, δV, averaged in a single atomic layer in the left electrode[41]. $\delta V = E_H - E_{NA}$, where E_H is the electrostatic potential and E_{NA} is the neutral atom potential extracted from Transiesta.[41,30]

The Fermi levels on either electrode are at the same level, and the field in the vacuum is zero. If a voltage is now applied to this atomic structure, situation **2)** arises, which is shown in figure 6.

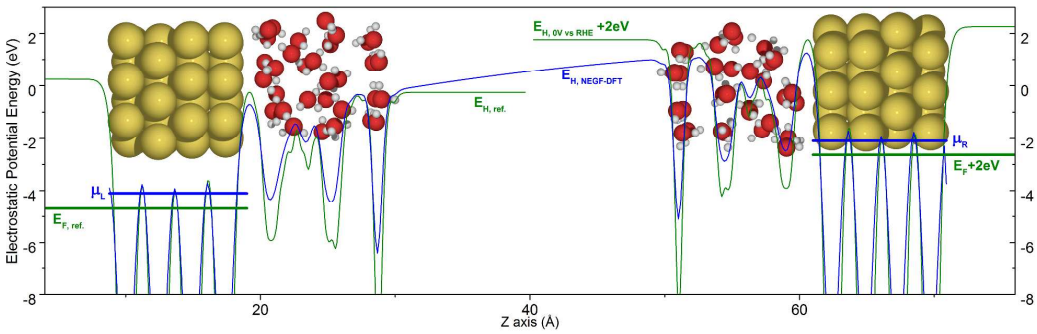

Figure 6: Situation **2)** The same full cell atomic structure and half cell calculations as in figure 5. However the bias in the full cell calculation is now U = -2.01 V. As observed on the electrostatic potential of the NEGF-DFT calculation (blue line), a non-zero electric field therefore remains between the electrodes due to the difference in Fermi levels (shown as thick horizontal lines). The position of the potentials of the working electrode half cell (right) is such that the Fermi level (thick green line) is 2.01 eV higher than on the reference.

In situation **2)** shown in figure 6, the field in the vacuum is no longer zero. Thus the near field vacuum levels are different on the two electrodes. In this situation, the protons are therefore not at the same chemical potential outside the two electrodes. Any atomic interface structure with φ_{e^-} different from 4.44 eV - eU_{RHE} results in a non-zero field, as shown by comparing NEGF-DFT calculations with slab calculations (See figure 5, 6 and 7). The only way for the field to be zero in the vacuum, is the fulfillment of equation (8)

$$U = (\varphi_{e^-} - \varphi_{SHE})/e \quad (8)$$

Situation **3)** is such an equilibrated state. This is shown in figure 7, in which the atomic structure of the working electrode has been exchanged to one with a work function of 2.43 eV, so equation (8) is fulfilled.

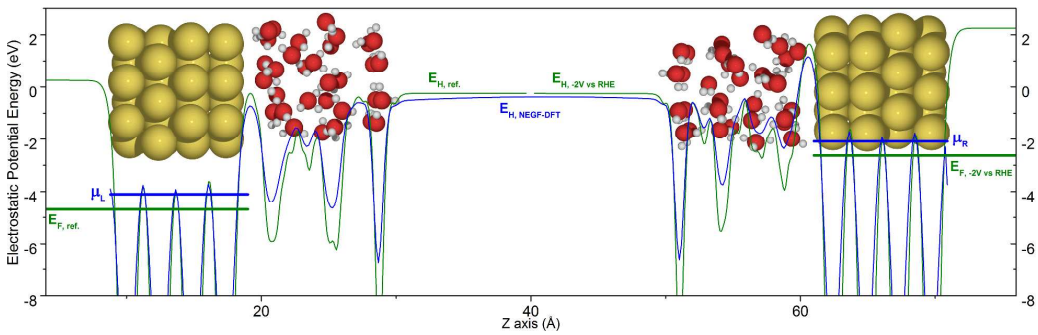

Figure 7: Situation **3)** The planar averaged electrostatic potentials, V_H, of the full cell calculation (blue line), and of the separate half cell calculations (green lines, left and right). The half cell electrostatic potentials are aligned to each other at the vacuum level outside the water layer. The Fermi levels are shown with thick horizontal lines for each structure. The working electrode (left) has a work function of 2.43 eV, whereas the reference electrode (right) has a work function of 4.44 eV. When applying $U_{transiesta}$=-2.01 V, there is practically no electric field in the vacuum in this full cell calculation.

Thus, as shown in figure 7, the vacuum levels are again aligned, and the protons outside either electrode are in equilibrium. The physical consequence of this is that equation (8) is a condition on the work function, which the interface can only obey by redistributing charges internally by reorganizing the atomic structure. All states where equation 8 is not fulfilled correspond to a state that is not in thermodynamic equilibrium. It is therefore reasonable to construct the thermodynamic ensemble, only of states obeying this constraint. Slab/water calculations, where the work function is calculated are therefore sufficient to model the effect of electrode potential and pH. This is fortunate, since they are much more computationally efficient than full cell NEGF-DFT calculations. As seen in figures 5, 6 and 7, the vacuum levels in the Transiesta NEGF-DFT calculations consistently come out lower than in the GPAW slab calculations, compared to the respective Fermi levels. In both codes, the basis sets are the default double zeta

polarized, but they are likely not identical since the cutoff radii of the basis functions can be different. A too small cut off radius can cause the work function to be underestimated because the electronic spillout is too small. However, differences in work function seem to come out identical, since there is consistency between applied bias in NEGF-DFT calculations and slab calculations, and this consistency would not otherwise be there.

The physical consequence from this model is that the electric double layer sets up an *internal* electric field due to the constraints from the chemical potentials. Influences of the *external* electric field should be omitted for the following reason: Typical voltages between electrodes in electrochemistry are on the order of 1 V, and dimensions of the electrolyte phase are typically in centimeters and at least microns. A molecule, aligning to such an external electric field therefore only gains a reorientation energy in the order of 1e * 1 Å * (1 V / 1 μm) = 10^{-4} eV, which is ~2 orders of magnitude smaller than kT. Furthermore, by applying the dipole correction into the periodic DFT simulation, a much larger external field is set up, still with negligible effect on the energies.

Under increasing cathodic polarization, the internal dipole fulfilling equation 8 could be set up by water molecules pointing H more *away* from the surface. An increasingly anodic polarization would have the opposite effect. This is because the half cell interface with cathodic polarization has a *small* work function compared to the reference electrode. Anodic polarization would result in a half cell structure with a larger work function and water pointing H *towards* the surface. The effect of ions and electrons on the internal dipole of the interface may however be huge, and it is elaborated further upon in the following.

Introduction or removal of one $H^+ + e^-$ in the system adds much larger change to the net dipole moment than the reorientation of one water molecule. In the half cell DFT calculation, an excess hydrogen atom present in the electrolyte layer, causes approximately one electronic charge to appear on the metal, while the proton in the electrolyte layer has a positive charge. In the same manner, creating a hydrogen deficient system results in electrons being transferred to a solvated hydroxide from the electrode. These are the most stable solutions to the electronic structure problem and this effect is captured by DFT[32], as long as the electrolyte band gap straddles the Fermi level[33]. An extra proton and electron yields a dipole pointing *away* from the surface and a smaller work function, like the water molecule pointing H *away* from the surface. The opposite is the case if an OH^- is present in the electrolyte. Charge neutrality of the interface system is always conserved due to the assumption of a conductive electrode and conductive electrolyte. In figure 8, equivalent NEFG-DFT calculations to the above is as presented for an added proton+electron in the working electrode interface.

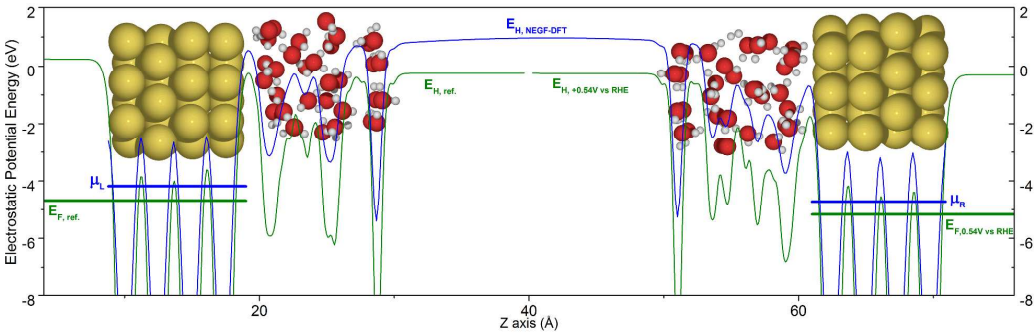

Figure 8: Planar averaged electrostatic potentials, V_H, of the electrochemical cell (blue line), the reference half cell system (green line, left), and the right hand half cell, which has a proton in the electrolyte (green line, right). The work function of the right half cell is 4.98 eV, and U = +0.54 V. The Fermi levels are shown for each structure with a thick horizontal line.

Since the introduction of a $H^+ + e^-$ is stabilized by cathodic potentials, the proton may provide a large enough net dipole to counter the dipole moment of several water molecules pointing H towards the surface. This, along with attraction from the excess surface electron, may yet again yield the result that water molecules are stable in an orientation with hydrogen towards the surface under cathodic potentials, as has been suggested by some experiments[34]. This orientation is not due to an excess free charge in the present model and it is not due to any external electric field. It is rather due to a thermodynamically more stable distribution of the total charge including protons+electrons or other neutral ion and electron combinations.

Conclusions

In summary it has been demonstrated that the electric double layer has an *internal* electric field, set up by the interface atomic structure that keep the electrolyte in equilibrium. This is a thermodynamic consequence in the generalized computational hydrogen electrode model. The model was revisited in this paper and derived from statistical physics, definitions of the

electrochemical standard and reversible hydrogen electrodes and the assumption that the conductive electrode and conductive electrolyte keep equilibrium within the electrolyte and within the electrodes, and that they keep the micro system charge neutral. Finite bias NEGF-DFT calculations on a full electrochemical cell setup have been compared with half cell calculations to demonstrate that the internal electric field, set up in the double layer must be self consistent with the electrode potential. This demonstrates that half cell calculations with the generalized computational hydrogen electrode analysis is an efficient and effective method for the purpose of calculating properties of the electrochemical interface on the atomic scale.

AUTHOR INFORMATION

Corresponding Author

E-mail: jan.rossmeisl@chem.ku.dk

Notes

The authors declare no competing financial interests.

Supporting Information

Details of the DFT calculations and the NEGF-DFT calculations.

ACKNOWLEDGMENT

The work is funded by the Technical University of Denmark, by the Danish Council for Strategic Research via the NACORR project nr. 12-132695 and by the Department of Chemistry, University of Copenhagen.

REFERENCES

(1) Yang, P.; Tarascon, J.-M. Towards Systems Materials Engineering. *Nat. Mater.* **2012**, *11*, 560–563.

(2) Díaz-González, F.; Sumper, A.; Gomis-Bellmunt, O.; Villafáfila-Robles, R. A Review of Energy Storage Technologies for Wind Power Applications. *Renewable Sustainable Energy Rev.* **2012**, *16*, 2154–2171.

(3) Chalk, S. G.; Miller, J. F. Key Challenges and Recent Progress in Batteries, Fuel Cells, and Hydrogen Storage for Clean Energy Systems. *J. Power Sources* **2006**, *159*, 73–80.

(4) Armand, M.; Tarascon, J.-M. Building Better Batteries. *Nature* **2008**, *451*, 652–657.

(5) Cheng, M.; Sun, L.; Buja, G.; Song, L. Advanced Electrical Machines and Machine-Based Systems for Electric and Hybrid Vehicles. *Energies* **2015**, *8*, 9541.

(6) Markovic, N. M. Electrocatalysis: Interfacing Electrochemistry. *Nat. Mater.* **2013**, *12*, 101–102.

(7) Katsounaros, I.; Cherevko, S.; Zeradjanin, A. R.; Mayrhofer, K. J. J. Oxygen Electrochemistry as a Cornerstone for Sustainable Energy Conversion. *Angew. Chem. Int. Ed.* **2014**, *53*, 102–121.

(8) Nørskov, J. K.; Bligaard, T.; Rossmeisl, J.; Christensen, C. H. Towards the Computational Design of Solid Catalysts. *Nat. Chem.* **2009**, *1*, 37–46.

(9) J. Greeley; J. K. Nørskov; Mavrikakis, M. Electronic Structure and Catalysis on Metal Surfaces. *Annu. Rev. Phys. Chem.* **2002**, *53*, 319–348.

(10) Taylor, C. D.; Wasileski, S. A.; Filhol, J.-S.; Neurock, M. First Principles Reaction Modeling of the Electrochemical Interface: Consideration and Calculation of a Tunable Surface Potential from Atomic and Electronic Structure. *Phys. Rev. B* **2006**, *73*, 165402.

(11) Filhol, J.-S.; Neurock, M. Elucidation of the Electrochemical Activation of Water over Pd by First Principles. *Angew. Chem., Int. Ed.* **2006**, *45*, 402–406.

(12) Taylor, C.; Kelly, R. G.; Neurock, M. Theoretical Analysis of the Nature of Hydrogen at the Electrochemical Interface between Water and a Ni (111) Single-Crystal Electrode. *J. Electrochem. Soc.* **2007**, *154*, F55–F64.

(13) Rossmeisl, J.; Skúlason, E.; Björketun, M. E.; Tripkovic, V.; Nørskov, J. K. Modeling the Electrified Solid–liquid Interface. *Chem. Phys. Lett.* **2008**, *466*, 68–71.

(14) Wasileski, S. A.; Janik, M. J. A First-Principles Study of Molecular Oxygen Dissociation at an Electrode Surface: A Comparison of Potential Variation and Coadsorption Effects. *Phys. Chem. Chem. Phys.* **2008**, *10*, 3613–3627.

(15) Jinnouchi, R.; Anderson, A. B. Electronic Structure Calculations of Liquid-Solid Interfaces: Combination of Density Functional Theory and Modified Poisson-Boltzmann Theory. *Phys. Rev. B* **2008**, *77*, 245417.

(16) Otani, M.; Sugino, O. First-Principles Calculations of Charged Surfaces and Interfaces: A Plane-Wave Nonrepeated Slab Approach. *Phys. Rev. B* **2006**, *73*, 115407.

(17) Hamada, I.; Sugino, O.; Bonnet, N.; Otani, M. Improved Modeling of Electrified Interfaces Using the Effective Screening Medium Method. *Phys. Rev. B* **2013**, *88*, 155427.

(18) Nielsen, M.; Björketun, M. E.; Hansen, M. H.; Rossmeisl, J. Towards First Principles Modeling of Electrochemical Electrode–electrolyte Interfaces. *Surf. Sci.* **2015**, *631*, 2–7.

(19) Rossmeisl, J.; Chan, K.; Ahmed, R.; Tripkovic, V.; Bjorketun, M. E. pH in Atomic Scale Simulations of Electrochemical Interfaces. *Phys. Chem. Chem. Phys.* **2013**, *15*, 10321–10325.

(20) Brandbyge, M.; Mozos, J.-L.; Ordejón, P.; Taylor, J.; Stokbro, K. Density-Functional Method for Nonequilibrium Electron Transport. *Phys. Rev. B* **2002**, *65*, 165401.
(21) H. Gould and J. Tobochnik: Statistical and Thermal Physics. *J. Stat. Phys.* **2010**, *140*, 1022–1023.
(22) A. J. Bard and L. R. Faulkner, Electrochemical Methods: Fundamentals and Applications, New York: Wiley, 2001, 2nd Ed. *Russ. J. Electrochem.* **2002**, *38*, 1364–1365.
(23) Nørskov, J. K.; Rossmeisl, J.; Logadottir, A.; Lindqvist, L.; Kitchin, J. R.; Bligaard, T.; Jónsson, H. Origin of the Overpotential for Oxygen Reduction at a Fuel-Cell Cathode. *J. Phys. Chem. B* **2004**, *108*, 17886–17892.
(24) Rossmeisl, J.; Nørskov, J. K.; Taylor, C. D.; Janik, M. J.; Neurock, M. Calculated Phase Diagrams for the Electrochemical Oxidation and Reduction of Water over Pt(111). *J. Phys. Chem. B* **2006**, *110*, 21833–21839.
(25) Trasatti, S. The Absolute Electrode Potential: An Explanatory Note (Recommendations 1986). *Pure and applied chemistry* **1986**, *58*, 955–966.
(26) Tripkovic, V.; Björketun, M. E.; Skúlason, E.; Rossmeisl, J. Standard Hydrogen Electrode and Potential of Zero Charge in Density Functional Calculations. *Phys. Rev. B* **2011**, *84*, 115452.
(27) Bengtsson, L. Dipole Correction for Surface Supercell Calculations. *Phys. Rev. B* **1999**, *59*, 12301.
(28) Ordejón, P.; Artacho, E.; Soler, J. M. Self-Consistent Order-N Density-Functional Calculations for Very Large Systems. *Phys. Rev. B* **1996**, *53*, R10441–R10444.
(29) José M Soler and Emilio Artacho and Julian D Gale and Alberto García and Javier Junquera and Pablo Ordejón and Daniel Sánchez-Portal. The SIESTA Method for Ab Initio Order- N Materials Simulation. *J. Phys.: Condens. Matter* **2002**, *14*, 2745.
(30) Junquera, J.; Zimmer, M.; Ordejón, P.; Ghosez, P. First-Principles Calculation of the Band Offset at $BaOBaTiO_3$ and $SrOSrTiO_3$ Interfaces. *Phys. Rev. B* **2003**, *67*, 155327.
(31) J. Junquera and M. H. Cohen and K. M. Rabe. Nanoscale Smoothing and the Analysis of Interfacial Charge and Dipolar Densities. *J. Phys.: Condens. Matter* **2007**, *19*, 213203.
(32) Skúlason, E.; Tripkovic, V.; Björketun, M. E.; Gudmundsdottir, S.; Karlberg, G.; Rossmeisl, J.; Bligaard, T.; Jónsson, H.; Nørskov, J. K. Modeling the Electrochemical Hydrogen Oxidation and Evolution Reactions on the Basis of Density Functional Theory Calculations. *J. Phys. Chem. C* **2010**, *114*, 18182–18197.
(33) Björketun, M. E.; Zeng, Z.; Ahmed, R.; Tripkovic, V.; Thygesen, K. S.; Rossmeisl, J. Avoiding Pitfalls in the Modeling of Electrochemical Interfaces. *Chem. Phys. Lett.* **2013**, *555*, 145–148.
(34) Velasco-Velez, J.-J.; Wu, C. H.; Pascal, T. A.; Wan, L. F.; Guo, J.; Prendergast, D.; Salmeron, M. The Structure of Interfacial Water on Gold Electrodes Studied by X-Ray Absorption Spectroscopy. *Science* **2014**, *346*, 831–834.
(35) Bahn, S. R.; Jacobsen, K. W. An Object-Oriented Scripting Interface to a Legacy Electronic Structure Code. *Comput. Sci. Eng.* **2002**, *4*, 56–66.
(36) Larsen, A. H.; Vanin, M.; Mortensen, J. J.; Thygesen, K. S.; Jacobsen, K. W. Localized Atomic Basis Set in the Projector Augmented Wave Method. *Phys. Rev. B* **2009**, *80*, 195112.
(37) Mortensen, J. J.; Hansen, L. B.; Jacobsen, K. W. Real-Space Grid Implementation of the Projector Augmented Wave Method. *Phys. Rev. B* **2005**, *71*, 035109.

(38) Enkovaara, J.; Rostgaard, C.; Mortensen, J. J.; Chen, J.; Dułak, M.; Ferrighi, L.; Gavnholt, J.; Glinsvad, C.; Haikola, V.; Hansen, H. A. Electronic Structure Calculations with GPAW: A Real-Space Implementation of the Projector Augmented-Wave Method. *J. Phys.: Condens. Matter* **2010**, *22*, 253202.
(39) Monkhorst, H. J.; Pack, J. D. Special Points for Brillouin-Zone Integrations. *Phys. Rev. B* **1976**, *13*, 5188–5192.
(40) Perdew, J. P.; Burke, K.; Ernzerhof, M. Generalized Gradient Approximation Made Simple. *Phys. Rev. Lett.* **1996**, *77*, 3865–3868.
(41) X. Zhong. Electron Transport in Low-Dimensional Nanostructures - Theoretical Study with Application. Dissertation, Michigan Technological University, 2013.

TOC GRAPHICS

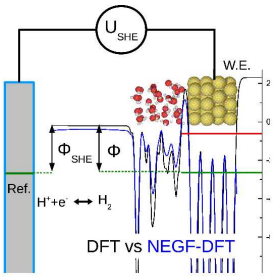

Paper VIII

Grand Canonical Statistics of an Aqueous Electrochemical Interface from Dynamic Atomic-scale Calculations

Martin Hangaard Hansen, Jan Rossmeisl

In preparation.

Grand Canonical Statistics of an Aqueous Electrochemical Interface from Dynamic Atomic-scale Calculations

Martin Hangaard Hansen

*Center for Atomic-scale Materials Design, Department of Physics, Technical University of Denmark, 2800 Kgs. Lyngby, Denmark**

Jan Rossmeisl

Nano Science Center, Department of Chemistry, University of Copenhagen, Universitetsparken 5, 2100 Copenhagen, Denmark

(Dated: June 2, 2016)

Abstract

A method for ab initio simulations of the aqueous electrochemical interfaces on the atomic scale is presented as a proof of concept. This simulation unfolds the effects of pH and electrode potential using a generalized computational hydrogen electrode. The liquid structures of the solvent is included with the use of molecular dynamics, to sample an ensemble of thousands of micro states. A Metropolis Monte Carlo algorithm is applied to calculate the probability weight function at constant pH and electrode potential from the ensemble. Several atomic-scale quantities are calculated for our model system, water / Au(111), as averages over the grand canonical ensemble. The only inputs to the model are the fundamental assumptions of an equilibrated solvent and the dimensions of the micro system and unit cell. As outputs, the model gives potentials of zero charge, potentials of maximum entropy, Frumkin isotherms and differential capacities as a functions of pH and electrode potential. It produces the Nernstian pH-behaviour of the potential of zero total charge and non-Nernstian behaviour for the potential of zero free charge, which is observed experimentally from cyclic voltammetry on single crystals. These results demonstrates the potential usefulness of the generalized computational hydrogen electrode analysis with density functional theory to study liquid / metal electrochemical interfaces.

INTRODUCTION

Electrochemical energy conversion and storage will become an increasingly important part of the future energy system. The actual energy conversion occurs in the electrochemical reactions on the interface between the electrolytes and electrodes. Being able to determine the properties of the electrochemical interface from first principles is therefore of high interest in the electrochemistry community. Understanding the interfaces in ever greater detail has been a challenge for electrochemistry for decades[1, 2]. It is known that macroscopic properties such as pH and concentrations of ions govern reaction rates through changes happening in the interface on the molecular scale[3–5]. However, the structure of the atomic scale metal water interface is very difficult to obtain information about from experiments, since the observables in electrochemical experiments are primarily the current and voltage, which only provides indirect information.

The present work presents and tests a scheme using density functional theory to reproduce pH dependent behaviour of the aqueous electrochemical interface, with water / Au(111) as the case study. First, the theory of the generalized computational hydrogen electrode is reviewed, secondly a simple method for sampling of the interface partition functions is presented, and finally, observables calculated as weighted averages are evaluated and compared to experiments.

THEORY

Observables or quantities from the micro system can be calculated as averages over all the states, the micro system can be in. The probability weight function in this sampling is the Boltzmann factor. For a quantity of interest, A, this is written

$$< A > = \sum_i A_i p_i \tag{1}$$

$$p_i = \frac{\exp\left[-G_i/k_B T\right]}{Z} \tag{2}$$

$$Z = \sum_i \exp\left[-G_i/k_B T\right] \tag{3}$$

where Z is the grand partition function, p_i is the probability of state i and ΔG_i is the free energy of the state. If an ensemble containing all relevant states is known and if the free

energy of all the states is known at the given pH and electrode potential surrounding the interface, then $< A >$ can be calculated. The interface micro system can be modelled as an extended metal/water slab with variable numbers of protons and electrons[6]. In the slab model, periodic boundary conditions are used in the plane, while the slab is surrounded by vacuum in the out-of-plane dimension, and non-periodic boundary conditions are used with a dipole-correction[7], (See figure 1).

The integral free energy, G^{int}, of each state is according to the usual Computation Hydrogen

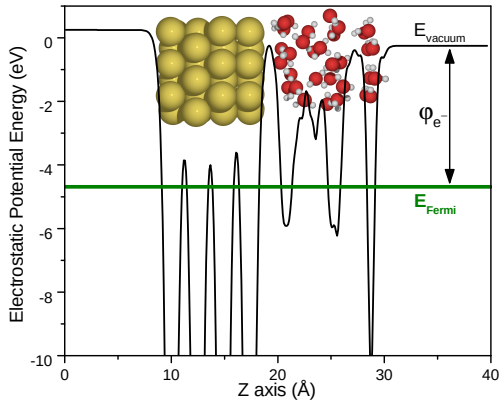

FIG. 1: *Snapshot from molecular dynamics simulation plotted with the Hartree potential (black line) and the Fermi level (green line). The work function is the difference between the vacuum level on the right side and the Fermi level.*

Electrode[8] scheme:

$$G^{int} = E(n) - E(n=0) + ZPE - TS - n(G^0_{H_2} - eU_{RHE}) \tag{4}$$

where $E(n)$ is the energy obtained from the density functional theory, n is a number of hydrogen atoms added to the interface. $G^0_{H_2}$ is the free energy of H_2 (g) at standard conditions, obtained from a DFT calculation and thermodynamic tables. Three assumptions are made in the original Computational Hydrogen Electrode:

1 The bulk electrolyte is in equilibrium.

2 The interfaces are in equilibrium with the bulk electrodes and the electrolyte surrounding them.

3 The relative free energy of each state is independent of pH and electric fields[9].

If G^{int} is dependent on electric fields, as in the case of water structures, the Generalized Computational Hydrogen Electrode must be used.[10] This replaces assumption 3 with assumption 4

4 The interface region is charge neutral and large enough to screen charges.

Macroscopically, it is trivial, that the interface region is charge neutral, since it is surrounded by and in equilibrium with charge conducting media. Then it is a practical question to use sufficiently large models in the computations, to allow sufficient room for charges and counter charges. Assumptions 1,2 a 4 leads to a constraint on the interface and that leads to:

$$eU_{RHE} = \phi - \phi_{SHE} + 2.303k_BT \cdot pH \tag{5}$$

where ϕ, is the work function and ϕ_{SHE} is the work function of the electrode at pH = 0 and U_{SHE} = 0V. The reader is referred to these recent papers for the derivation.[10, 11] Equation 5 also reflects the connection between work function and electrode potential, which is well known in the experimental literature[12, 13] as an absolute electrode potential. From simulations, the work function can be obtained from the planar averaged electrostatic potential and the Fermi level using:

$$\phi = < \Phi_{x,y}(z_{max}) > -E_F \tag{6}$$

$$< \Phi_{x,y}(z) > = \int_{x,y} \Phi(x,y,z)dxdy \tag{7}$$

where $\Phi(x,y,z)$ is the electrostatic potential, which can be calculated for each micro state by DFT, (See figure 1). Inserting equation (5) into (4), the free energy of a micro state is written

$$G^{int} = E(n) - E(n=0) + ZPE - TS - n(G^0_{H_2} + \phi_{SHE} - \phi - 2.303k_BT \cdot pH) \tag{8}$$

In reality, equation 5 acts as a constraint on the macroscopic interface, so in the limit of large unit cells, it must hold. In the present work, it was not possible to evaluate the effects of unit cell size, so the rest of the analysis assumes, that the unit cell is large enough.

METHOD

To create an ensemble of structures, and to calculate the grand partition function, Z, Ab Initio Molecular Dynamics (AIMD) was employed. Trajectories containing from -6 to +6 extra hydrogen atoms were made. The hydrogens were included as specifically adsorbed H* and with and without one solvated proton. The electrode surface was represented by a four atomic layer Au(111) slab in a 3×4 orthogonal super cell. The electrolyte layer included 24 water molecules $\pm$ the above mentioned hydrogen atoms. In addition, the vacuum interface was kept by a constrained layer of 8 water molecules in a hexagonal structure with close to zero net dipole moment out of the plane.

Figure 2 shows the free energy of all the individual snapshots sampled from molecular dynamics at pH 0 and pH 14. The integral free energy, G^{int} is calculated using equation (8). The value for ϕ_{SHE} is between 4.44 eV and 4.85 eV according to experiments[13, 14]. Capturing work functions accurately using DFT requires that the electron spill-out from the interface is well described. In the present calculations, it was most feasible to use localized basis sets which resulted in underestimated the work functions for all the structures. Therefore a lower value of 3.9 eV was used for ϕ_{SHE}. This choice will be evaluated further in the discussion.

The time step for the dynamics was 0.5 fs and a Berendsen thermostat was employed with characteristic time constant of 1000 fs, to keep the temperature at 300K in all trajectories. A total number of 90000 states were generated. The electronic structure in every time step was calculated by density functional theory using the GPAW[15, 16] code. To reduce the total energy oscillations, the convergence criteria for the density was tightened to $2 \cdot 10^{-5}$ Å^3, which ensured higher self-consistency in calculation of the forces, still without compromising efficiency too much. The exchange-correlation contribution to the energy was represented using the RPBE functional[17]. Single electron wave functions were expanded in localized atomic orbitals (LCAO) with the double-zeta-polarized basis set[18]. The k-point sampling was $3 \times 3 \times 1$. In the out-of-plane direction, the boundary conditions were non-periodic and the Bengtsson dipole correction[7] was used for the electrostatic potential.

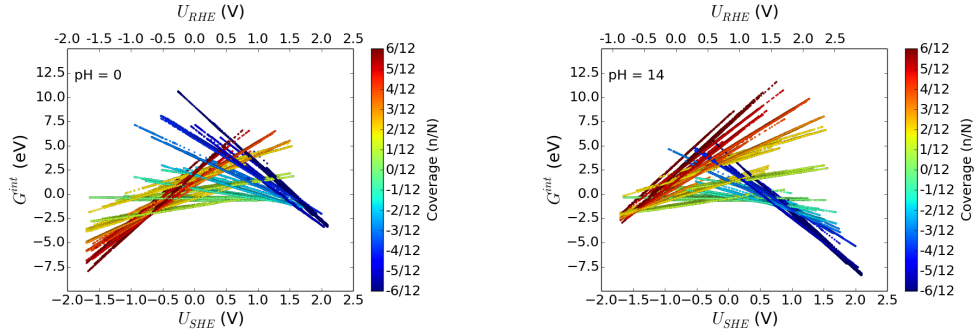

FIG. 2: *Calculated ΔG^{int} versus U_{SHE} and U_{RHE} (bottom and top axis respectively) for all atomic structure states, sampled from molecular dynamics. n/N denotes the number of H atoms added to the neutral water system, and this value is shown for every state by color as indicated by the colorbar. The two plots show projections of ΔG^{int} onto pH 0 (left panel), and pH 14 (right panel).*

In the following, it is shown how the pH-dependent grand canonical averages were obtained from the molecular dynamics trajectories.

A Posteriori Analysis

Calculating any atomic-scale quantity requires an ensemble with the correct averages of surface coverage and proton excess, at any given electrode potential and pH. This is not already achieved by averages of a raw ensemble, consisting of all states from the trajectories. It is our choice how long simulation time is given to each trajectory and thereby how many states are tried at each coverage. Our solution to this problem is to calculate the probability weight function using a grand canonical Metropolis Monte Carlo algorithm that walks around in all the states that are sampled. The probability, π_{ij}, to walk from an accepted state j to a trial state i, and add i to the new ensemble is a piecewise function of the difference in free energy:

$$\Delta G_{ij}^{int} \leq 0 \Rightarrow \pi_{ij} = 1 \tag{9}$$

$$\Delta G_{ij}^{int} > 0 \Rightarrow \pi_{ij} = \exp\left(-\Delta G_{ij}^{int}/k_B T\right) \tag{10}$$

where $\Delta G_{ij}^{int} = \Delta G_i^{int} - \Delta G_j^{int}$. By moving between trajectories, the trial step can add or remove 0, 1, 2 or 3 protons+electrons or adsorbed H, all at equal attempt probabilities. Such a set of trial steps yield at least a quasi ergodic Markov chain[19], and therefore it gives the correct relative probabilities of occurrence for the states in the annealed ensemble. ΔG^{int} of each state is only calculated relative to states with the same work function. This is achieved by binning the states according to the ϕ_{e^-} value, resolved in 256 bins. In essence, $\Delta G_i^{int}(\phi_i) = \Delta G_i^{int}(\phi_i) - min(\Delta G^{int}(\phi_i))$, where $min(\Delta G^{int}(\phi_i))$ is the lowest free energy of any state in the bin with work function ϕ_i. Annealed ensembles are generated for each pH value, and the free energies should ideally follow a Boltzmann distribution. An example of a distribution of ΔG^{int} after annealing is shown in figure 3 for pH = 14.

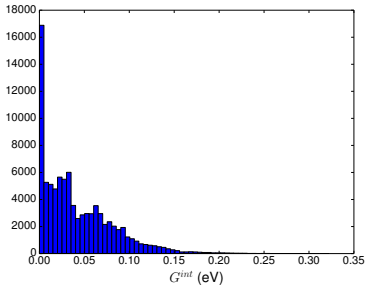

FIG. 3: Histogram of free interface energies in the annealed ensemble at 300K.

The distribution in figure 3 is not far from the ideal Boltzmann distribution, but a notable deviation is visible: The first bin is much higher than the rest of the distribution, which indicate that trial the Monte Carlo algorithm too often ends up the minimum energy states. The free energy is also plotted versus electrode potential for ensembles resulting from the annealing in figure 4, (a) for pH = 0 and (b) for pH = 14.

Comparing figure 4 with figure 2, an overview is obtained over which states remains after the Metropolis Monte Carlo annealing. As an example, consider that states with high number of hydrogens at a very anodic potential are non-existent in the annealed ensemble, as would be expected in the real system. The Monte Carlo annealing effectively filters away all states, which are irrelevant or improbable, because they are unstable, at that pH and potential.

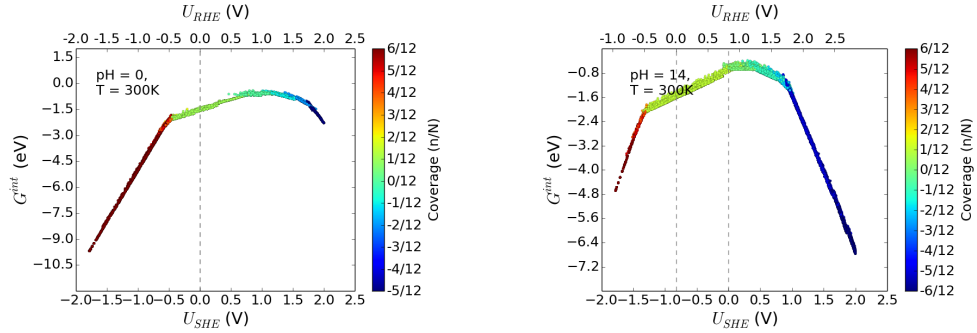

FIG. 4: *Calculated G^{int} versus U_{SHE} and U_{RHE} (bottom and top axis respectively) for all atomic structure states, sampled from molecular dynamics and annealed to 300K with a Grand Canonical Monte Carlo sampling. n/N denotes the number of H atoms added to the neutral water system, and this value is shown for every state by color as indicated by the colorbar. The two plots show projections of G^{int} onto pH = 0 (left panel) and pH = 14 (right panel).*

As explained in previous papers[10, 11], the pH effect enters through the relevant set of states at a given electrode potential. E.g., states at 0V versus RHE and pH=0 have a calculated work function of 3.9 eV, while states at 0V vs RHE at pH = 14 have a work function of $3.9 + 2.3k_BT \cdot 14 \approx 4.7$ eV. If energies of some structures depend on the work function, they will be more or less likely to appear in the annealed ensemble lower or higher pH's. In addition, relative frequencies of occurrence in the dynamics simulation carry over in the Monte Carlo annealing, thereby capturing any entropy dependence on the interface dipole and the work function. Water structures and surface species that are field dependent on the atomic scale, are thereby pH-dependent in grand canonical macroscopic scale.

Any static atomic-scale properties of the interface, as a function of pH and electrode potential, can now be calculated from the annealed ensembles. Properties that are dynamic and dependent on the trajectories cannot currently be calculated.

RESULTS

Simulations of several experimentally observable quantities are presented and the trends are compared to experiments. These include the Gibbs isotherms, differential capacitances, the potentials of zero charge and potential of maximum entropy. They are all evaluated as grand canonical averages based on equation (1).

First, the Gibbs isotherms are presented. They are calculated as the average value of n/N from the annealed ensemble. This is from the equivalent to:

$$< n/N >= \frac{1}{Z} \sum_i \frac{n_i}{N_i} \exp\left(-G_i^{int}(pH, \phi_{e^-})/k_B T\right) \tag{11}$$

The surface coverages for hydrogen, θ_H, or oxide species, θ_{OH}, or the proton excess, Γ_{H^+}, may be inserted instead of n/N to calculate their respective isotherm. The proton excess is plotted in figure 5a, and the OH coverage is plotted in figure 5b. An equivalent plot of the hydrogen surface coverage can be found in the supplementary information, but it is virtually identical at all pH values from 0 to 14.

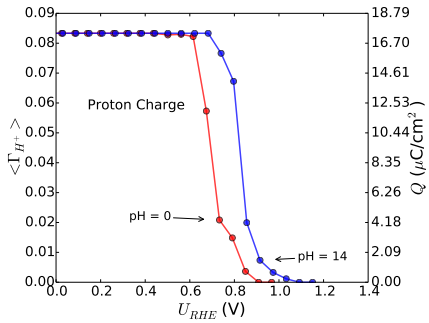

(a) Simulated proton charge isotherms at pH=0 and 14.

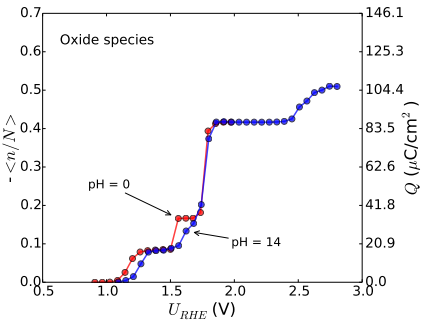

(b) Oxide species isotherm at pH=0 and pH=14.

FIG. 5: Simulated Gibbs isotherms, calculated using equation 11.

The isotherms are not directly observable in experiments. They are inferred from cyclic voltametry (CV) by calculating the differential capacitance from the current, j, and the scan

speed, v:

$$C = \frac{j}{v} \tag{12}$$

Integrating the experimental differential capacity from the point of zero total charge, $(PZTC)$, to U, leads the total charge, $\sigma_{Total}(U)$. This is written:

$$\sigma_{Total}(U) = \int_{PZTC}^{U} C dU \tag{13}$$

The differential capacity, C, may be evaluated from the present calculations using:

$$Q = e < n/N > \tag{14}$$

$$C = \| \frac{dQ}{dU} \| \tag{15}$$

where e is the unit charge. C is plotted for three different pH values in figure 6a. In figure 6b, C is plotted for pH = 8 together with experimental data in neutral solution.

Including the differential capacitance of protons + electrons in the simulations corresponds to an apparent electro-valency of 1 for proton insertion in experiments.

DISCUSSION

Simulated Cyclic voltammetry

The isotherms contain three distinct plateaus, which are due to either hydrogen species, no species or oxide species. A wide potential range of zero proton excess and zero surface coverage is observed. On the RHE scale, the proton excess exhibit pH dependent behaviour with a clear shift towards higher potential as the pH is increased. However, the surface adsorption isotherms are almost identical at pH = 0 and pH = 14.

Experimental cyclic voltammograms on Au(111) shows an oxidation region, which is asymmetric in the potential axis[22–24], and a hydrogen evolution region. No underpotential deposition of hydrogen is observed on Au(111)[23]. Experimentally, the hydrogen evolution reaction shows pH-dependence on several transition metals[4]. Recent electrochemical studies also suggest, that underdeposited hydrogen is stabilised by higher pH[25] on these transition metals.

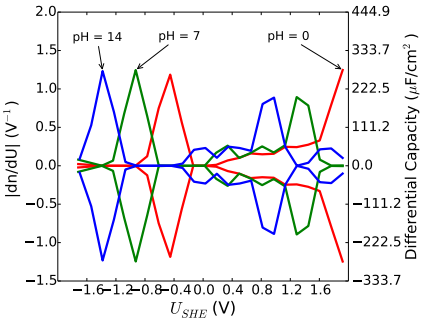

(a) *Specific capacities plotted against potential versus SHE at various pH. Three main capacities appear. The first indicates equilibrium potential of adsorbed H, the second is proton charge, and the third indicates *OH formation.*

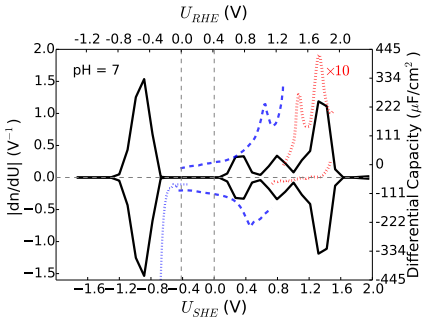

(b) *Black lines: Simulated specific capacity at pH 7. Blue dashed lines: Experimental differential capacitances from CV's in 0.1M $NaClO_4$ by Hamelin et al.[20] in the oxidising region, and in the HER region by Wang et al.[21] measured in 0.5M H_2SO_4, plotted on the RHE axis. The high potential regions, marked by red dotted lines are very large and are therefore divided by 10 in the plot.*

FIG. 6: *Specific capacities, calculated from numerical differentials of* $< n/N >$.

Observing the OH adsorption region, OH starts to adsorb at around +0.8V vs. RHE. Chemisorption of OH has been reported not to appear in the ORR region in alkaline.[26] Comparing to the CV's by Climent et al.[27], the features also seem well reproduced. However, differences in the CV's depending on cations are significant, and they are not captured by this simulation, because no states with cations were included.

To understand the Gibbs isotherms and the simulated cyclic voltammograms in better detail, it is useful to consider the free energies of adsorption. Integral free energies are first calculated by averaging $G^i nt$ from the constant n subsets that were sampled from the dynamics simulations, i.e:

$$< G^{int} > (n, \phi_{e^-}, pH) = \frac{1}{Z} \sum_i G^i nt_i \exp\left(G_i^{int}(n, \phi_{e^-}, pH)/k_B T\right) \tag{16}$$

The reference for the integral free energies is set to be the averaged G^{int} of the subset with a clean surface:

$$< \Delta G^{int} > (n, \phi_{e^-}, pH) =< G^{int} > (n, \phi_{e^-}, pH) - < G^{int} > (n = 0, \phi_{e^-}, pH) \qquad (17)$$

The differences are taken to get the differential free energies:

$$< \Delta G^{diff} > (n, \phi_{e^-}, pH) =< G^{int} > (n, \phi_{e^-}, pH) - < G^{int} > (n - 1, \phi_{e^-}, pH) \qquad (18)$$

In figure 7, the average free energies of hydrogen adsorption and of OH adsorption are shown at 0 V versus RHE.

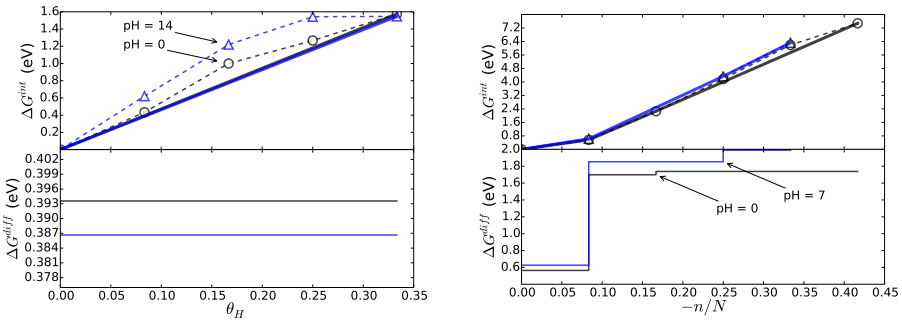

(a) Free energies of hydrogen chemisorption, with one proton in the double layer.

(b) Free energies of removing hydrogen from the system, forming oxide species on the surface.

FIG. 7: The integral free energies in the top panels and differential free energies in the bottom panels. They are calculated from the wieghted averages of ensembles generated by molecular dynamics.

For hydrogen, the differential free energies are constant around 0.3 eV, which may be compared to the previously reported values of 0.2 eV at 1/4 ML to 0.4 eV at 1 ML.[28] Observing the integral free energies from $\theta_H = 1/12$ to $\theta_H = 3/12$, the values are somewhat higher than those of the clean surface and the $\theta_H = 4/12$ ML, and thus these low to intermediate coverage structures are not stable. Not stabilizing adsorbate interaction is expected for chemisorbed hydrogen. The differential adsorption energies of removing hydrogen go up to 1.7 to 1.9 eV depending on the pH. Looking at snapshots from the MD, it was observed

that the trajectories from $-n/N = 1/12$ ML to $-n/N = 2/12$ formed OH on the surface, while those with $-n/N = 3/12$ ML and $-n/N = 4/12$ ML had 1 and 2 atomic oxygen on the surface, respectively. Previously the OH adsorption energies have been reported at 1.5 eV.[29] There may be several reasons for the discrepancy on the OH adsorption energy: The surface is not allowed to relax, and that may introduce some destabilizing effect on adsorbates. However, the most likely reason for the discrepancies is that the water structures are not well enough equilibrated.

The various results that are obtained as averages are more or less dependent on very well equilibrated ensembles. The free energies of adsorption or proton insertion are particularly affected by how well the individual trajectories are equilibrated, while other properties may be less dependent on that. Currently, it is demanding on time and computational resources to obtain sufficiently good ensembles with molecular dynamics to capture very accurate free energy differences, while also describing the electronic structure with satisfying accuracy. Alternatives to using molecular dynamics, such as a combination of Monte Carlo or MD methods with classical potentials and subsequent DFT calculations, may or may not be more efficient. Hopefully such sampling methods can be tested with this methodology in the future, but for now MD was chosen to make this proof of concept.

Returning to the comparison of simulated cyclic voltammetry with experiments, there are some additional contributions to the total charge, that are discussed in the following.

Total charge and free charge

The total charge, σ_{Total}, which is can be quantified from experiments using equation 13, can be divided into several contributions:

$$\sigma_{Total} = \sigma_F - F\theta_H + F\theta_{OH} \tag{19}$$

where $F\theta_s$ is charge attributed to electrosorption of species s. The free charge is σ_F, which is observed in CV experiments as the capacitive current from metal electrode is aqueous

media. In the present work, we choose to divide the free charge into two contributions:

$$\sigma_F = \sigma_{dl} + \sigma_{dip} \tag{20}$$

σ_{dl} is electronic surface charge, screening ions in the double layer and thus $\sigma_{dl} = F\Gamma_{OH^-} - F\Gamma_{H^+}$, due to the assumption of charge conservation. States containing solvated OH^-, were not put into the dynamics, so the calculated Γ_{OH^-} is 0 in the present study. In the simulated cyclic voltammograms, the only contribution that is not included is σ_{dip}.

σ_{dip} is attributed to relocation of image charges in the electrode, that screen water dipoles in the double layer. σ_{dip} is therefore a smaller contribution, but it is not quantified in the simulation, and thus it is not counted in the calculated differential capacitance, C, (shown in figure 6a). However, the potential where σ_{dip} is zero may be captured, as will be explained in the following.

Potentials of Zero charge and maximum entropy

The potential of zero free charge ($PZFC$) and the potential of zero total charge ($PZTC$) are both quantities of interest to interpret cyclic voltammetry experiments. Experimentally, the $PZTC$ and the $PZFC$ show Nernstian behaviour (a potential shift of $\approx 2.3k_BT/e$ per pH unit on the RHE potential scale).[30]

The PZFC has been correlated closely with the potential of maximum entropy (PME)[27, 30]. The explanation of this may be found in the distribution of work functions and interface dipoles sampled by the molecular dynamics.

The net dipole moment of the water layer is the result of the integrated dipole moment in the direction normal to the surface, which is set up by the orientation of water molecules. The molecular dynamics does not include any external fields, and thus it accesses all of configuration space of up and down orientation of the molecules. The work function varies on a rather short timescale, indicating reorientation happens often and with negligible energy barriers. Therefore the net dipole moment of the water behave like a random walk[31]. The

distribution of dipole moments projected onto the axis normal to the surface is reflected in the distribution of work functions, shown in figure 8.

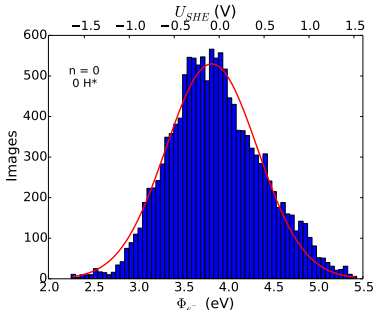

FIG. 8: *Histogram of calculated work functions in the* $\Gamma_{H^+} = 0, \theta_H = 0$ *subset of structures obtained directly from the molecular dynamics simulation.*

The peak of the distribution shows which micro state of the net dipole moment has the highest multiplicity. This may explain the observation of a potential of maximum entropy (PME) in electrochemical experiments by Climent et al.[27, 32]. In these experiments, a very small heating of the interface is induced by a laser pulse on the order of micro seconds, resulting in a shift towards a higher entropy macro state. This shift is observed as a small transient in the measured potential. From the electrocapillary equation the following relation can be derived for an ideal polarizable electrode[33, 34]:

$$\frac{\partial U}{\partial T}_q = -\frac{\partial \Delta S}{\partial q}_T \tag{21}$$

where q is charge and U is the electrode potential. Measuring ΔU, equation 21 is then used to identify the potential of zero potential transient with the potential of maximum entropy. Since the micro state with the highest entropy is found at a certain potential, an electrochemical system already in this state will show no shift and thus no potential transient. A cathodic potential results in a cathodic potential transient and vice versa according to the the PME experiments[27, 32]. An interface at cathodic potentials has a small work function and a net dipole pointing up. It would see an increase in work function, corresponding to a net dipole reorientation towards hydrogen down, i.e. positive down, negative up. To screen this, image charge electrons would flow away from the surface. As long as the out-of-equilibrium reorientation persists, the voltmeter would feel a higher Fermi

level, which is the same as a cathodic potential transient.

In the present model, the PME is linked directly to the SHE potential scale because the work function is linked directly to the SHE scale (See equation 5). Therefore the PME has perfect Nernstian behaviour, assuming constant coverage. The calculated work function of maximum entropy is not completely independent of coverage, but varies from 3.15 eV at $\theta_H = 5/12$ to 3.3 eV at $\theta_H = 0$, while there is one proton in the double layer. Relating the work function of maximum entropy to the potential is done using $eU_{SHE} = \phi - \phi_{SHE}$. The DFT calculations with LCAO basis sets consistently underestimate the calculated work functions by 0.3 to 0.5 eV, when comparing a few structures calculated with the incomplete LCAO basis sets and the more complete grid based basis sets. Therefore it is argued that the structure corresponding to 0 V versus SHE should have a work function 0.3 to 0.5 smaller than the conventional 4.44 eV. Estimating $\phi_{SHE} = 3.9$ corresponds to a potential of maximum entropy up to -0.6 V versus SHE.

The PME evaluated self-consistently with the surface coverage at various pH is plotted in figure 9. The PME is in the region with high hydrogen coverage, and therefore the Nernstian behaviour is preserved. The experiments by Climent et al. concludes that the PME is around 0.2 V versus SCE, measured in 0.1 M $HClO_4$, so this is far more positive than predicted by the calculation. The discrepancy may be due to the presence of counter ions, which have not been included in the calculations. It is straightforward to do so within the current methodology, except for the demands on computations to expand the sample.

In figure 9, the potentials of proton insertion and hydrogen chemisorption are also plotted. The hydrogen surface coverage is completely independent of pH, (non-Nernstian). The insertion of protons show non-Nernstian or sub-Nernstian behaviour from pH = 0 to pH = 14. The proton insertion isotherm moves by approximately 0.15 V over this range in pH.

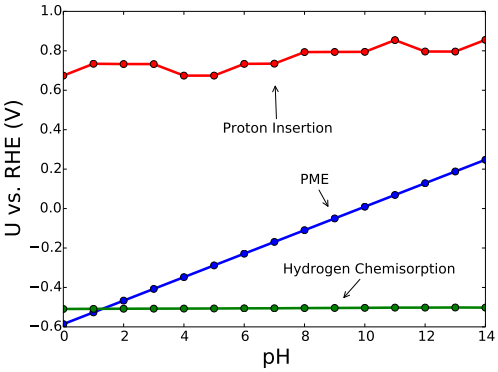

FIG. 9: *The potential of maximum entropy plotted versus pH, plotted together with the potential of hydrogen adsorption and proton insertion to the interface. The latter two were evaluated by taking the point closest to the intercept with zero of each isotherm.*

CONCLUSION

A grand canonical method for simulating the electrochemical interface on the atomic-scale, including Nernstian pH-dependence has been presented. The generalization of the Computational Hydrogen Electrode provided free energies of interface states as functions of pH and potential. Molecular dynamics simulations was used to sample states with various numbers of adsorbed OH, H and $(H^+ + e^-)$. This ensemble was used to calculate the static properties of the water / Au(111) interface as grand canonical averages. It is therefore a promising method for creating idealized theoretical simulations of electrochemical experiments and thus help identification of observed current-potential behaviour. The demand on computational resources for generating sufficiently large and well equilibrated ensembles is presently limiting for obtaining accurate results from the method.

Further developments in software and hardware will soon enable more accurate simulations of the interface including van der Waals forces and larger unit cells. This will enable more precise determination of the molecular structures at the interface with various electrolytes. The methodology and the generalized computational hydrogen electrode is hoped to yield a high impact on the understanding of electrochemical interfaces, for a wide range of applications.

The work is funded by the Catalysis for Sustainable Energy (CASE) initiative and by the Danish Council for Strategic Research via the NACORR project nr. 12-132695.

* mhah@dtu.dk

[1] S. Schnur and A. Groß, New Journal of Physics **11**, 125003 (2009).

[2] M. Nielsen, M. E. Björketun, M. H. Hansen, and J. Rossmeisl, Surface Science **631**, 2 (2015), surface Science and Electrochemistry - 20 years later.

[3] M. Gattrell, N. Gupta, and A. Co, Journal of Electroanalytical Chemistry **594**, 1 (2006).

[4] J. Zheng, W. Sheng, Z. Zhuang, B. Xu, and Y. Yan, Science Advances **2** (2016), 10.1126/sciadv.1501602, http://advances.sciencemag.org/content/2/3/e1501602.full.pdf.

[5] A. S. Varela, W. Ju, T. Reier, and P. Strasser, ACS Catalysis **6**, 2136 (2016), http://dx.doi.org/10.1021/acscatal.5b02550.

[6] E. Skulason, G. S. Karlberg, J. Rossmeisl, T. Bligaard, J. Greeley, H. Jonsson, and J. K. Nørskov, Phys. Chem. Chem. Phys. **9**, 3241 (2007).

[7] L. Bengtsson, Physical Review B **59**, 12301 (1999).

[8] J. K. Nørskov, J. Rossmeisl, A. Logadottir, , L. Lindqvist, J. R. Kitchin, T. Bligaard, and H. Jónsson, The Journal of Physical Chemistry B **108**, 17886 (2004), http://dx.doi.org/10.1021/jp047349j.

[9] J. Rossmeisl, J. K. Nørskov, C. D. Taylor, M. J. Janik, and M. Neurock, The Journal of Physical Chemistry B **110**, 21833 (2006).

[10] J. Rossmeisl, K. Chan, R. Ahmed, V. Tripkovic, and M. E. Björketun, Physical Chemistry Chemical Physics **15**, 10321 (2013).

[11] K. S. T. J. R. M. H. Hansen, C. Jin, Journal of Physical Chemistry C (2016).

[12] D. M. Kolb, Angewandte Chemie International Edition **40**, 1162 (2001).

[13] Trasatti, Sergio, Pure and Applied Chemistry **58**, 955 (1986).

[14] E. Kötz, H. Neff, and K. Müller, Journal of Electroanalytical Chemistry and Interfacial Electrochemistry **215**, 331 (1986).

[15] J. J. Mortensen, L. B. Hansen, and K. W. Jacobsen, Physical Review B **71**, 035109.

[16] J. Enkovaara, C. Rostgaard, J. J. Mortensen, J. Chen, M. Dulak, L. Ferrighi, J. Gavnholt,

C. Glinsvad, V. Haikola, and H. A. Hansen, Journal of Physics: Condensed Matter **22**, 253202.

[17] B. Hammer, L. B. Hansen, and J. K. Nørskov, Physical Review B **59**, 7413.

[18] A. H. Larsen, M. Vanin, J. J. Mortensen, K. S. Thygesen, and K. W. Jacobsen, Phys. Rev. B **80**, 195112 (2009).

[19] J. P. Valleau and L. K. Cohen, The Journal of Chemical Physics **72**, 5935.

[20] A. Hamelin, Journal of Electroanalytical Chemistry and Interfacial Electrochemistry **210**, 303 (1986).

[21] T. Wang, L. Liu, Z. Zhu, P. Papakonstantinou, J. Hu, H. Liu, and M. Li, Energy Environ. Sci. **6**, 625 (2013).

[22] P. Rodriguez, J. M. Feliu, and M. T. Koper, Electrochemistry Communications **11**, 1105 (2009).

[23] J. Perez, , E. R. Gonzalez, and H. M. Villullas, The Journal of Physical Chemistry B **102**, 10931 (1998), http://dx.doi.org/10.1021/jp9831987.

[24] A. Chen and J. Lipkowski, The Journal of Physical Chemistry B **103**, 682.

[25] W. Sheng, Z. Zhuang, M. Gao, J. Zheng, J. G. Chen, and Y. Yan, Nature communications **6** (2015).

[26] S. Štrbac and R. Adžié, Journal of Electroanalytical Chemistry **403**, 169 (1996).

[27] V. Climent, B. A. Coles, and R. G. Compton, The Journal of Physical Chemistry B **106**, 5258 (2002).

[28] J. K. Nørskov, T. Bligaard, A. Logadottir, J. Kitchin, J. Chen, S. Pandelov, and U. Stimming, Journal of The Electrochemical Society **152**, J23 (2005).

[29] J. Rossmeisl, A. Logadottir, and J. Nrskov, Chemical Physics **319**, 178 (2005), molecular Charge Transfer in Condensed Media - from Physics and Chemistry to Biology and Nanoengineering in honour of Alexander M. Kuznetsov on his 65th birthday.

[30] N. García-Aráez, V. Climent, and J. M. Feliu, Electrochimica Acta **54**, 966.

[31] H. Gould and J. Tobochnik, *Statistical and Thermal Physics: With Computer Applications* (Princeton University Press, 2010).

[32] V. Climent, B. A. Coles, and R. G. Compton, The Journal of Physical Chemistry B **105**, 10669 (2001).

[33] J. Harrison, J. Randles, and D. Schiffrin, Journal of Electroanalytical Chemistry and Inter-

facial Electrochemistry **48**, 359 (1973).

[34] V. Benderskii and G. Velichko, Journal of Electroanalytical Chemistry and Interfacial Electrochemistry **140**, 1 (1982).